

DISSERTATION

submitted to the

Combined Faculty of Mathematics, Engineering and Natural  
Sciences

of Heidelberg University, Germany

for the degree of

Doctor of Natural Sciences

Put forward by

Ning Yuan

born in Zhangye, China

Oral examination: 04.07.2024





High-Pressure Single Crystal Growth and  
Magnetization Studies  
on Correlated Electron Systems

Referees: Prof. Dr. Rüdiger Klingeler  
Prof. Dr. Maurits W. Haverkort



# Abstract

This work presents the high-pressure single crystal growth and the magnetic properties of the rare-earth indates  $\text{GdInO}_3$  and  $\text{TbInO}_3$ , the Ruddlesden-Popper trilayer nickelates  $\text{La}_4\text{Ni}_3\text{O}_{10}$ , as well as the rare-earth orthochromites  $\text{ErCrO}_3$ ,  $\text{GdCrO}_3$ , and  $\text{SmCrO}_3$ . All single crystals were grown by the floating zone method under the pressure over 20 bar. The challenges of single crystal growth are discussed and the corresponding growth parameters are presented. The magnetic properties of the materials under study are primarily characterized through magnetization measurements at temperatures down to 0.4 K and in magnetic fields up to 14 T.  $\text{GdInO}_3$  is a frustrated magnet which develops long-range magnetic order below  $T_N = 2.1$  K. Specifically, a broad 1/3 plateau indicative of the up-up-down spin configuration appears for magnetic fields  $B||c$  but is absent for  $B||ab$ . A discontinuous transition into a high-field phase is found and the magnetic phase diagram is established. For  $\text{TbInO}_3$ , no long-range order is observed down to 1.8 K which combined with previous reports suggests a potential spin liquid ground state. The Ruddlesden-Popper nickelates  $\text{La}_4\text{Ni}_3\text{O}_{10}$  show a unique metal-to-metal transition. The different single crystal growth and post-annealing processes result in two distinct structure modifications  $P2_1/a$  and  $Bmab$  in which the metal-to-metal transitions occur at 136 K and 152 K, respectively. All single crystals of the rare-earth orthochromites  $\text{ErCrO}_3$ ,  $\text{GdCrO}_3$ , and  $\text{SmCrO}_3$  exhibit significant magnetic anisotropy.  $\text{ErCrO}_3$ ,  $\text{GdCrO}_3$ , and  $\text{SmCrO}_3$  develop long-range magnetic order below  $T_N = 132$  K, 167 K, and 192 K respectively, and the magnetization processes for different crystal-axis orientations clearly demonstrate the spin reorientation transition of these three materials. The presence of spin switching (magnetization reversal) in  $\text{GdCrO}_3$  is investigated. The work at hand illustrates that growth of novel correlated magnetic materials by means of sophisticated methods is a precondition for the detailed investigation and understanding of their magnetic properties.



# Kurzzusammenfassung

In der vorliegenden Arbeit werden die Hochdruck-Einkristallzucht sowie magnetische Messungen der Seltenerd-Indate  $\text{GdInO}_3$  und  $\text{TbInO}_3$ , der Ruddlesden-Popper-Dreischicht-Nickelate  $\text{La}_4\text{Ni}_3\text{O}_{10}$  und der Seltenerd-Orthochromite  $\text{ErCrO}_3$ ,  $\text{GdCrO}_3$  und  $\text{SmCrO}_3$  untersucht. Alle Einkristalle wurden durch das Zonenschmelzverfahren beim Drücken über 20 bar gezüchtet. Die Bedingungen der erfolgreichen Zucht werden diskutiert und die zugehörigen Wachstumsparameter aufgelistet. Die magnetischen Eigenschaften der Materialien werden hauptsächlich durch Magnetisierungsmessungen für Temperaturen ab 0,4 K und in Magnetfeldern von bis zu 14 T untersucht.  $\text{GdInO}_3$  ist ein magnetisch frustriertes System, welches unterhalb von  $T_N = 2,1$  K eine langreichweitige antiferromagnetische Ordnung ausbildet. Für Magnetfelder  $B||c$  tritt ein breites 1/3-Plateau in der Magnetisierung auf, welches auf eine up-up-down-Spinkonfiguration hinweist. Hingegen wird das Plateau für  $B||ab$  nicht beobachtet. Des Weiteren zeigt sich ein diskontinuierlicher Übergang in eine Hochfeldphase. Für  $\text{TbInO}_3$  ist oberhalb von 1,8 K keine langreichweitige magnetische Ordnung zu beobachten. Dies deutet in Übereinstimmung mit früheren Arbeiten auf einen potenziellen Spinflüssigkeits-Grundzustand hin. Im Falle von  $\text{La}_4\text{Ni}_3\text{O}_{10}$  wurden durch variierende Zuchtprozesse sowie Wärmebehandlungen Einkristalle mit unterschiedlichen Kristallstrukturen  $P2_1/a$  und  $Bmab$  hergestellt. Diese weisen einen Metall-Metall-Übergang bei 136 K bzw. 152 K auf. Die Einkristalle  $\text{ErCrO}_3$ ,  $\text{GdCrO}_3$  und  $\text{SmCrO}_3$  zeigen eine signifikante magnetische Anisotropie. Magnetische Ordnung tritt in den Systemen bei  $T_N = 132$  K ( $\text{ErCrO}_3$ ), 167 K ( $\text{GdCrO}_3$ ) bzw. 192 K ( $\text{SmCrO}_3$ ) auf. Außerdem zeigen sich in allen drei Systemen Spin-Reorientierungsübergänge. Das Auftreten einer *Spin Switching* bzw. *Magnetization Reversal* ist dahingegen nur in  $\text{GdCrO}_3$  zu beobachten. Im Allgemeinen verdeutlicht die vorliegende Arbeit, dass die Züchtung neuer einkristalliner korrelierter magnetischer Materialien eine Voraussetzung für die detaillierte Untersuchung und das Verständnis ihrer magnetischen Eigenschaften ist.



# Table of Contents

<b>Abstract</b>	<b>V</b>
<b>Abstrakt</b>	<b>VII</b>
<b>1 Introduction and Background</b>	<b>1</b>
1.1 Introduction . . . . .	3
1.2 Theoretical Background . . . . .	5
1.2.1 Single-Atom Hamiltonian . . . . .	6
1.2.2 Hund's Rules . . . . .	7
1.2.3 Spin-Orbit Coupling . . . . .	8
1.2.4 Atom in a Magnetic Field . . . . .	9
1.2.5 Brillouin Function . . . . .	9
1.2.6 Magnetic Order . . . . .	11
1.2.7 Magnetic Interactions . . . . .	12
1.2.8 Energy Conditions for Crystallization . . . . .	18
<b>2 Experimental Method</b>	<b>21</b>
2.1 Synthesis . . . . .	23
2.1.1 Solid State Reaction Method . . . . .	23
2.1.2 Ball Milling Method . . . . .	24
2.1.3 Single Crystal Growth by Floating Zone Method . . . . .	25
2.1.4 The Challenges of Single Crystal Growth of $R\text{InO}_3$ ( $R = \text{Gd}, \text{Tb}$ ), $\text{La}_4\text{Ni}_3\text{O}_{10}$ , and $R\text{InO}_3$ ( $R = \text{Er}, \text{Gd}, \text{Sm}$ ) . . . . .	27
2.2 Characterization . . . . .	30
2.2.1 X-ray Diffraction (XRD) and Refinement . . . . .	30
2.2.2 Back-reflection Laue Method . . . . .	32
2.2.3 Magnetometry . . . . .	33
<b>3 Rare-Earth Indates</b>	<b>35</b>
3.1 1/3 Plateau and 3/5 Discontinuity in the Magnetization and the Magnetic Phase Diagram of Hexagonal $\text{GdInO}_3$ . . . . .	37
3.2 $\text{TbInO}_3$ . . . . .	56
3.2.1 Crystal Growth and Structural Characterization of $\text{TbInO}_3$ . . . . .	56
3.2.2 Magnetic Susceptibility of $\text{TbInO}_3$ . . . . .	59
3.2.3 Summary . . . . .	60

<b>4</b>	<b>Ruddlesden–Popper Trilayer Nickelates <math>\text{La}_4\text{Ni}_3\text{O}_{10}</math></b>	<b>63</b>
<b>5</b>	<b>Rare-Earth Orthochromites</b>	<b>77</b>
5.1	Introduction of $R\text{CrO}_3$ . . . . .	79
5.2	$R\text{CrO}_3$ Sample Details . . . . .	83
5.3	Magnetization . . . . .	87
5.3.1	$\text{ErCrO}_3$ . . . . .	87
5.3.2	$\text{GdCrO}_3$ . . . . .	95
5.3.3	$\text{SmCrO}_3$ . . . . .	105
5.4	Summary . . . . .	121
<b>6</b>	<b>Overall Summary</b>	<b>123</b>
	<b>Appendix</b>	<b>129</b>
A.1	$\text{LiMn}_2\text{O}_4$ . . . . .	129
A.2	Additional Tables . . . . .	132
	<b>List of Tables</b>	<b>133</b>
	<b>List of Publications</b>	<b>135</b>
	<b>Bibliography</b>	<b>137</b>



# 1

## Introduction and Background

This chapter provides general remarks on this work and presents the basic theoretical background for analyzing magnetic materials characterized by multiple interactions.



---

## 1.1 Introduction

Strongly correlated materials are a class of material systems in which electron-electron repulsive interactions play an essential role [1, 2]. These interactions give rise to intriguing physical properties, such as Mott insulator [3], spin fluctuations [4], etc. In the advancement of this research field, the exploration of new materials has always been a crucial aspect. One significant technique in this exploration is the floating zone method, which dates back to the 1960s [5]. Developed over decades, the floating zone method has not only been industrialized to enhance the preparation of conventional materials but has also played a crucial role in exploring novel quantum materials. This technique provides crucial experimental samples for a profound understanding of their physical properties, thereby enhancing our comprehension of strongly correlated electron systems. The floating zone method is commonly employed for the preparation of superconducting materials, including conventional copper-based superconductors  $\text{La}_{2-x}\text{Sr}_x\text{CuO}_4$  [6],  $\text{PrBa}_2\text{Cu}_3\text{O}_x$  [7], etc. Additionally, it is widely utilized in the synthesis of the geometrically frustrated magnet  $\text{Yb}_2\text{Ti}_2\text{O}_7$  [8], topological insulator  $\text{Bi}_2\text{Se}_3$  [9], spin ice  $\text{Pr}_2\text{Zr}_2\text{O}_7$  [10], spin liquid  $\text{YbMgGaO}_4$  [11–13] and  $\text{Tb}_2\text{Ti}_2\text{O}_7$  [14], magnetic skyrmions  $\text{Fe}_{0.5}\text{Co}_{0.5}\text{Si}$  [15] and  $\text{Gd}_3\text{Ru}_4\text{Al}_{12}$  [16] and other materials. Moreover, the floating zone method plays a vital role in preparing the perovskite rare-earth oxides, represented by the nominal composition  $R\text{BO}_3$  ( $R$  = rare-earth ion,  $B$  = cations), forming a multi-functional class of materials that are central to current research in condensed matter physics and materials science. This class of materials exhibits remarkable phenomena, including metal-insulator transitions in rare-earth nickelates [17–19], spin-phonon coupling in rare-earth orthoferrites [20], colossal magnetoresistance, phase separation, and charge (orbital) order in manganates [21–24], as well as multiferroicity in  $R\text{MnO}_3$  [25–27].

The first class of material discussed in this work is the rare-earth indates ( $R\text{InO}_3$ ,  $R$  = rare-earth ion)  $\text{GdInO}_3$  and  $\text{TbInO}_3$ , which crystallize in the  $P6_3cm$  space group [28, 29]. Its centered honeycomb lattice structure makes  $R\text{InO}_3$  a well-suited platform for studying geometrically frustrated magnets. For example,  $\text{GdInO}_3$  is a Heisenberg-like frustrated system with small anisotropy [30, 31]. Particularly,  $\text{GdInO}_3$  presents a 1/3 magnetization plateau in the isothermal magnetization curves at 1.8 K [30], which is a typical feature of the up-up-down (uud) phase in triangular antiferromagnets [32–35].  $\text{GdInO}_3$  also features ferroelectricity, confirmed by the observation of  $P(E)$  hysteresis loop and a  $Z_6$  vortex topological domain structure. Additionally,  $\text{TbInO}_3$  is considered a candidate for quantum

spin liquid behavior and has also shown ferroelectric behavior [36, 37].

Secondly, this work investigates the properties of Ruddlesden–Popper trilayer nickelates  $\text{La}_4\text{Ni}_3\text{O}_{10}$ . The electronic similarity between  $\text{Ni}^{1+}$  and  $\text{Cu}^{2+}$  configurations makes nickelates prime analogs to high-temperature superconducting cuprates. The significance of nickelates is further underscored by the recent discovery in superconductivity of infinite-layer nickelates [38–45]. The crystal structure of trilayer nickelates like  $\text{La}_4\text{Ni}_3\text{O}_{10}$  is commonly depicted as an alternating arrangement of perovskite-like and rock-salt-like layers [46, 47], often considered quasi-two-dimensional (2D). It features a mixture of  $\text{Ni}^{2+}$  and  $\text{Ni}^{3+}$  ions with an average valence of +2.67 [48]. Additionally,  $\text{La}_4\text{Ni}_3\text{O}_{10}$  shows an unusual metal-to-metal transition (MMT) [48–55], characterized by intertwined charge and spin orders emerging at MMT temperature [56].

The third class of material explored in this work is rare-earth orthochromites ( $R\text{CrO}_3$ )  $\text{ErCrO}_3$ ,  $\text{GdCrO}_3$ , and  $\text{SmCrO}_3$ , which adopt a distorted perovskite structure and display three main types of magnetic interactions: those between the  $3d$  moments of  $\text{Cr}^{3+}$ , between the  $4f$  moments of  $R^{3+}$ , and between the  $3d$  and  $4f$  moments. Canted antiferromagnetic ordering of the  $\text{Cr}^{3+}$  moments, involving the weak ferromagnetic component due to Dzyaloshinskii-Moriya (DM) interactions, has been verified through numerous investigations [57–59]. Consequently,  $R\text{CrO}_3$  exhibits intricate phenomena arising from the intertwining of two different magnetic subsystems, such as the spin reorientation [60, 61], spin switching [62, 63], etc.

The structure of this work is outlined below:

- Chapter 1 provides general remarks about this work and presents the basic theoretical background for analyzing magnetic materials characterized by multiple interactions.
- Chapter 2 outlines the experimental methods, including sample synthesis and the challenges of obtaining single crystals discussed in this work. It also covers the method for structural characterization and magnetization measurement.
- Chapter 3 examines two hexagonal rare-earth indates,  $\text{GdInO}_3$  and  $\text{TbInO}_3$ . Specifically, section 3.1 presents experimental results of magnetization and specific heat measurement of single crystal  $\text{GdInO}_3$ . The signal of long-range magnetic order evolution at  $T_N = 2.1$  K has been determined and  $\text{GdInO}_3$  shows significant magnetic frustration. The system exhibits remarkable magnetization behavior, including a broad  $1/3$  plateau indicative of the up-up-down (uud) spin configuration for magnetic fields aligned with the  $c$  axis, reorientation processes, and a discontinuous transition

---

into a high-field phase. The magnetic phase diagrams in the temperature regime down to 400 mK and in magnetic fields up to 14 T have been constructed. Additionally, the possible spin configurations of  $\text{GdInO}_3$  have been discussed. Section 3.2 presents magnetization measurements of single crystal  $\text{TbInO}_3$ . There is no signal of long-range ordering observed down to 1.8 K.

- Chapter 4 details the single crystal growth and magnetic properties of Ruddlesden–Popper nickelates  $\text{La}_4\text{Ni}_3\text{O}_{10}$ . Two distinct phases, namely  $Bmab$  and  $P2_1/a$ , influenced by the post-annealing process under pressure, are discussed. In both structures, the metal-to-metal transition occurs at 152 K and 136 K, respectively, as determined by magnetization and heat capacity measurements.
- Chapter 5 investigates three rare-earth orthochromites:  $\text{ErCrO}_3$ ,  $\text{GdCrO}_3$ , and  $\text{SmCrO}_3$ . All three single crystals display significant magnetic anisotropy and spin reorientation transition.  $\text{ErCrO}_3$ ,  $\text{GdCrO}_3$ , and  $\text{SmCrO}_3$  exhibit long-range antiferromagnetic order below  $T_N = 132$  K, 167 K, and 192 K, respectively. In this chapter, the evolution of their magnetic ordering states along various crystallographic axis have been discussed. Additionally, the magnetic phase diagram of  $\text{SmCrO}_3$  in the temperature regime down to 1.8 K and in magnetic fields up to 7 T have been presented.
- Chapter 6 serves as the conclusion of this dissertation.

## 1.2 Theoretical Background

This section lays out the fundamental theoretical groundwork for this study. Subsections 1.2.1–1.2.6 are primarily derived from “Magnetism in Condensed Matter” by S. Blundell [64], “Magnetism and Magnetic Materials” by J. Coey [65], and “The Oxford Solid State Basics” by S. Simon [66]. Subsection 1.2.7 draws from “Introduction to Many-Body Physics” authored by P. Coleman [67], “Modern Magnetic Materials: Principles and Applications” by R. O’Handley [68], as well as the book authored by S. Blundell [64] and J. Coey [65]. Additionally, this section also refers to the presentation of “Frustration” in the review articles [69–73]. Lastly, subsection 1.2.8 is derived from “Principles of Physical Chemistry” by R. Rosenberg [74].

### 1.2.1 Single-Atom Hamiltonian

The atoms constituting macroscopic matter contain electrons and nuclei, both with certain magnetic moments. However, since the electronic magnetic moment is 3-4 orders of magnitude larger than that of the nucleus, the magnetic moment of macroscopic matter is mainly determined by electrons. For a system containing  $N$  electrons, the total Hamiltonian should include five parts: the kinetic energy of the electrons, the kinetic energy of nuclei, the Coulomb interaction between electrons, the Coulomb interaction between nuclei, and the Coulomb interaction between electrons and nuclei. Therefore, solving this complex many-body system is highly challenging. The energy band theory is an important theoretical foundation that allows dealing with this complex many-body problem, employing three approximate treatments:

- Born-Oppenheimer approximation: Considering that the nuclei are much heavier than the electrons (the proton-to-electron mass ratio  $\approx 1836$ ), for the same interaction, the motion of the electrons is much faster than that of the nuclei. Thus, from the perspective of the electrons, the nuclei are approximately stationary, and the kinetic energy term of the nuclei can be neglected. When considering the interaction of the nuclei attracting the electron, only the electron coordinates vary, while the coordinates of the nuclei appear as parameters. Finally, the interaction term between nuclei appears as a constant. From the perspective of the nuclei, the nuclei cannot “feel” the exact position of a particular electron, instead it only receives the average force. Eventually, the motion of the electrons and that of the nuclei can be treated separately, and the state of the electrons does not change with the motion of the nuclei. This simplifies the complex many-body problem to a many-electron problem.
- Hartree-Fock (Mean-Field) approximation: In the many-electron system the motions of all electrons are correlated due to interactions. Considering the interaction of the surrounding electrons on one electron equivalent to a mean field that does not vary with time, the complex many-electron problem is simplified to a single-electron problem.
- Periodic potential approximation: Each electron experiences an exactly periodic potential field, so the motion of each electron can be considered separately.

Therefore, based on the above approximations, the complex many-body problem becomes a single-electron problem in a periodic potential field, and the Hamiltonian of the system

---

becomes the sum of the single-electron Hamiltonian. The single-electron Hamiltonian is given by:

$$\mathcal{H} = \frac{p^2}{2m_e} - \frac{Ze^2}{r} \quad (1.1)$$

with the momentum operator  $p$ , the electron mass  $m_e$ , the proton number  $Z$ , and the distance from the nucleus for electron  $r$ .

The Hamiltonian of  $N$  electrons moving around the nucleus:

$$\mathcal{H} = \sum_{i=1}^N \left( \frac{p_i^2}{2m_e} - \frac{Ze^2}{r_i} + V_i(r_i) \right) \quad (1.2)$$

with the momentum operator for the  $i$ th electron  $p_i$ , the distance from the nucleus for the  $i$ th electron  $r_i$ , and the effective electrostatic potential for the  $i$ th electron  $V_i(r_i)$ .

The eigenfunction  $\psi$  of Eq. 1.2:

$$\psi_{n,l,m_l,m_s}(r,\theta,\phi) = R_{n,l}(r)Y_l^{m_l}(\theta,\phi)\chi(m_s) \quad (1.3)$$

with the principal quantum number  $n = 1, 2, \dots$  (positive integer), the angular momentum quantum number  $l = 0, 1, \dots, n - 1$ , the magnetic quantum number  $m_l = 0, \pm 1, \pm 2, \dots, \pm l$ , and the spin quantum number  $m_s = \pm 1/2$ .  $R_{n,l}(r)$  quantifies the radial part of the wave function, the angular part of the wave function is constructed from the spherical harmonics  $Y_l^{m_l}(\theta,\phi)$ , and  $\chi(m_s)$  is the spin part.

## 1.2.2 Hund's Rules

The ground state electronic configuration of an atom or an isolated ion is dictated by Hund's rules, which encompass three requirements:

1. Without violating the Pauli exclusion principle, the total spin quantum number  $S$  takes the maximum value for the lowest energy state.
2. Given the spin  $S$ , the state where the total orbital quantum number  $L$  takes the maximum value has the lowest energy.
3. If the shell is less than half-filled, the total angular momentum quantum number  $J$  is determined by  $J = |L - S|$ ; if the shell is more than half-filled,  $J = |L + S|$ ; if the shell is half-filled,  $L = 0$  and  $J = S$ .

### 1.2.3 Spin-Orbit Coupling

In Hund's rules,  $J$  arises from the relativistic spin-orbit coupling (SOC) interaction, which represents the relativistic influence of electron spin on the electron's orbital motion. The SOC Hamiltonian is expressed as:

$$\mathcal{H}_{SOC} = \lambda \mathbf{L} \cdot \mathbf{S} \quad (1.4)$$

where the coupled orbital moment  $\mathbf{L} = \sum_{i=1}^N \mathbf{l}(i)$ , the coupled spin moment  $\mathbf{S} = \sum_{i=1}^N \mathbf{s}(i)$ , and  $\lambda$  denotes the SOC constant.

The Landé  $g$ -factor  $g_J$  is given by:

$$g_J = \frac{3}{2} + \frac{S(S+1) - L(L+1)}{2J(J+1)} \quad (1.5)$$

As a result, in the case of  $L = 0$  and  $J = S$ ,  $g_J = 2$ . Conversely, for  $S = 0$  and  $J = L$ ,  $g_J = 1$ . The orbital angular momentum  $L$ , the spin angular momentum  $S$ , and total angular momentum  $J$  after coupling are shown in Fig. 1.1.

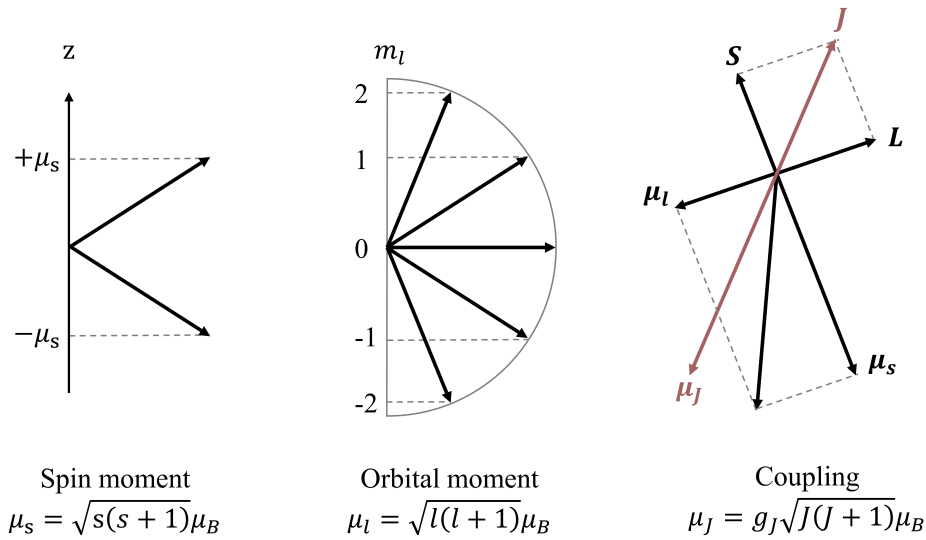


**Figure 1.1:** Schematic of the orbital angular momentum  $L$ , the spin angular momentum  $S$ , and total angular momentum  $J$ . After [65].



---

## 1.2.4 Atom in a Magnetic Field

Introducing a magnetic field  $\mathbf{B}$  acting on the many-electron system:  $\mathbf{B} = \nabla \times \mathbf{A}$ , where  $\mathbf{A}$  is the magnetic vector potential:

$$\mathbf{A}(\mathbf{r}) = \frac{\mathbf{B} \times \mathbf{r}}{2} \quad (1.6)$$

Hence the perturbed Hamiltonian is given by:

$$\hat{\mathcal{H}} = \sum_{i=1}^Z \left( \frac{[\mathbf{p}_i + e\mathbf{A}(\mathbf{r}_i)]^2}{2m_e} + V_i \right) + g\mu_B \mathbf{B} \cdot \mathbf{S} \quad (1.7)$$

where  $g\mu_B \mathbf{B} \cdot \mathbf{S}$  is the Zeeman-term, and Eq. 1.7 can be simplified to:

$$\hat{\mathcal{H}} = \sum_i \left( \frac{p_i^2}{2m_e} + V_i \right) + \mu_B (\mathbf{L} + g\mathbf{S}) \cdot \mathbf{B} + \frac{e^2}{8m_e} \sum_i (\mathbf{B} \times \mathbf{r}_i)^2 \quad (1.8)$$

$$= \hat{\mathcal{H}}_0 + \mu_B (\mathbf{L} + g\mathbf{S}) \cdot \mathbf{B} + \frac{e^2}{8m_e} \sum_i (\mathbf{B} \times \mathbf{r}_i)^2 \quad (1.9)$$

$\hat{\mathcal{H}}_0$  represents the original Hamiltonian, the second and third terms correspond to the paramagnetic and diamagnetic moment respectively.

## 1.2.5 Brillouin Function

The classical theory of paramagnetism was first introduced by Paul Langevin. In this theory, it is assumed that the interactions between atomic magnetic moments (e.g., the influence of magnetic dipole interactions on the system are very weak compared to thermal energy at room temperature) can be neglected, resulting in the orientation of the magnetic moments being disordered at equilibrium, thus exhibiting no magnetic moment in the absence of an external magnetic field. However, when an external magnetic field is applied, the magnetic moments align with the field direction, leading to paramagnetism. The magnetization in the system is expressed as:

$$M = n\mu \left( \coth y - \frac{1}{y} \right) = n\mu L(y) \quad (1.10)$$

$$y = \frac{\mu B}{k_B T} \quad (1.11)$$

where  $n$  is the number of magnetic moments per unit volume,  $k_B$  is the Bohr magneton,  $T$  is temperature, and  $L(y)$  is the Langevin function.

In small magnetic field, the paramagnetic susceptibility is denoted as:

$$\chi = \frac{n\mu_0\mu^2}{3k_B T} \quad (1.12)$$

When the magnetic field is strong enough, the saturation magnetization  $M_S$  is denoted by:

$$M_S = n\mu \quad (1.13)$$

$$\frac{M}{M_S} = \frac{\mu B}{3k_B T} \quad (1.14)$$

However, considering that the total magnetic moment of an atom is quantized in its orientation within the external magnetic field, the  $z$  component of the magnetic moments  $m_J = \pm 1/2$ . For a system with  $J = 1/2$ , the magnetic moments can take values of  $-\mu_B$  or  $\mu_B$ . Therefore, the Brillouin function is used to estimate the magnetization of an ideal paramagnet:

$$B_J(y) = \frac{2J+1}{2J} \coth\left(\frac{2J+1}{2J}y\right) - \frac{1}{2J} \coth\left(\frac{y}{2J}\right) \quad (1.15)$$

$$y = \frac{g_J\mu_B JB}{k_B T} \quad (1.16)$$

The susceptibility for low magnetic fields is given by

$$\chi = \frac{n\mu_0\mu_{\text{eff}}^2}{3k_B T} \quad (1.17)$$

The effective magnetic moment is given by:

$$\mu_{\text{eff}} = g_J \sqrt{J(J+1)} \quad (1.18)$$

When the magnetic field is strong enough:

$$M_S = ng_J\mu_B J \quad (1.19)$$

$$M = M_S B_J(y) \quad (1.20)$$

---

When  $J = \infty$ , Brillouin function is equal to Langevin function:

$$B_{\infty}(y) = L(y) \quad (1.21)$$

When  $J = 1/2$ , Brillouin function is equal to the tanh function:

$$B_{\frac{1}{2}}(y) = \tanh(y) \quad (1.22)$$

The relation between magnetic susceptibility and temperature is described by the extended Curie-Weiss (CW) Law:

$$\chi = \frac{C}{T - \Theta} + \chi_0 \quad (1.23)$$

where  $C$  is the Curie constant,  $\chi_0$  is the temperature independent term and  $\Theta$  is the Weiss temperature, with  $\Theta > 0$  for the ferromagnet and  $\Theta < 0$  for the antiferromagnet. The origin of the molecular field in Weiss model is explained by the exchange interaction proposed by physicist Werner Heisenberg, see section 1.2.7.

## 1.2.6 Magnetic Order

Research on the theory of ferromagnetism begun in the early 20th century with the Weiss model introduced by the physicist Pierre Weiss, employing the following assumptions:

- Molecular field assumption: A strong “molecular field” exists inside ferromagnetic materials. In the absence of an external magnetic field, spontaneous magnetization occurs within the material. The role of the external magnetic field is to align the magnetic moments of different regions with the direction of the external field.
- Magnetic domain assumption: The spontaneous magnetization of ferromagnetic materials can be divided into different regions called magnetic domains. Each domain exhibits spontaneous saturation of magnetization. In the absence of an external magnetic field, the magnetic moments within each domain are randomly oriented, resulting in the absence of macroscopic magnetism.

Therefore, the contribution of the molecular field is incorporated into Eq. 1.16:

$$y = \frac{g_J \mu_B J (B + \lambda M)}{k_B T} \quad (1.24)$$

where  $\lambda$  represents a constant that characterizes the magnitude of the molecular field as a function of magnetization.  $\lambda > 0$  for the ferromagnet and  $\lambda < 0$  for the antiferromagnet.  $\lambda M$  term represents a molecular field. The critical transition temperature from the ferromagnetic state to the paramagnetic state is denoted by the Curie temperature:

$$T_C = \frac{g_J \mu_B (J + 1) \lambda M_S}{3k_B} = \frac{n \lambda \mu_{\text{eff}}^2}{3k_B} \quad (1.25)$$

The critical transition temperature from the antiferromagnetic state to the paramagnetic state is denoted by the Néel temperature:

$$T_N = \frac{g_J \mu_B (J + 1) |\lambda| M_S}{3k_B} = \frac{n |\lambda| \mu_{\text{eff}}^2}{3k_B} \quad (1.26)$$

## 1.2.7 Magnetic Interactions

### 1.2.7.1 Magnetic Dipole-Dipole Interaction

For two magnetic dipoles  $\mu_1$  and  $\mu_2$ , separated by a distance  $\mathbf{r}$ , there exists magnetic dipole coupling between them. The corresponding coupling energy is given by:

$$E = \frac{\mu_0}{4\pi r^3} \left[ \mu_1 \cdot \mu_2 - \frac{3}{r^2} (\mu_1 \cdot \mathbf{r})(\mu_2 \cdot \mathbf{r}) \right] \quad (1.27)$$

where  $\mu_0$  is the vacuum permeability.

### 1.2.7.2 Exchange Interaction

By considering two electrons with wave functions denoted as  $\psi_1$  and  $\psi_2$ , the position of the  $i^{\text{th}}$  electron is  $\mathbf{r}_i$ , and its spin component is denoted by  $\chi_i$ , the state in which the two electrons have opposite spins resulting in total  $S = 0$  is known as the singlet state:

$$\Psi_S = \frac{1}{\sqrt{2}} [\psi_a(\mathbf{r}_1)\psi_b(\mathbf{r}_2) + \psi_a(\mathbf{r}_2)\psi_b(\mathbf{r}_1)] \chi_S \quad (1.28)$$

the state in which the spins of the two electrons are parallel, resulting in the total  $S = 1$ , is known as the triplet state:

$$\Psi_T = \frac{1}{\sqrt{2}} [\psi_a(\mathbf{r}_1)\psi_b(\mathbf{r}_2) - \psi_a(\mathbf{r}_2)\psi_b(\mathbf{r}_1)] \chi_T \quad (1.29)$$

The difference between the singlet and triplet states can be parameterized as  $\mathbf{S}_1 \cdot \mathbf{S}_2$ . For a singlet state,  $\mathbf{S}_1 \cdot \mathbf{S}_2 = -\frac{3}{4}$ , while for a triplet state,  $\mathbf{S}_1 \cdot \mathbf{S}_2 = \frac{1}{4}$ .

The energy difference between the triplet and singlet states can be expressed as:

$$E_S - E_T = 2 \int \psi_a^*(\mathbf{r}_1)\psi_b^*(\mathbf{r}_2)\hat{\mathcal{H}}\psi_a(\mathbf{r}_2)\psi_b(\mathbf{r}_1)d\mathbf{r}_1d\mathbf{r}_2 \quad (1.30)$$

$J$  is defined as the exchange constant:

$$J = \frac{E_S - E_T}{2} = \int \psi_a^*(\mathbf{r}_1)\psi_b^*(\mathbf{r}_2)\hat{\mathcal{H}}\psi_a(\mathbf{r}_2)\psi_b(\mathbf{r}_1)d\mathbf{r}_1d\mathbf{r}_2 \quad (1.31)$$

Hence, the spin term in the Hamiltonian can be written as:

$$2 \text{ spins} : \hat{\mathcal{H}}^{spin} = -2J\mathbf{S}_1 \cdot \mathbf{S}_2 \quad (1.32)$$

For  $J > 0$ ,  $E_S > E_T$ , indicating that the system is in the triplet state. Conversely, for  $J < 0$ ,  $E_S < E_T$ , indicating that the system is in the singlet state. Thus, the interaction between all neighboring atoms in the macroscopic system can be expressed as:

$$N \text{ spins} : \hat{\mathcal{H}} = -2 \sum_{i>j} J_{ij} \mathbf{S}_i \cdot \mathbf{S}_j \quad (1.33)$$

where  $J_{ij}$  is the exchange constant between  $i^{th}$  and  $j^{th}$  spins. When the two electrons are on the same atom,  $J > 0$  and the triplet state is of lower energy. Conversely, if the two electrons are on neighboring atoms,  $J < 0$  and the singlet state is of lower energy.

### 1.2.7.3 Spin Waves

Spin waves are the low-energy excitations of the exchange-coupled magnetic lattice. The magnon is defined as the elementary excitation of a spin waves. According to the Heisenberg model, when one spin flips, the spin on the adjacent lattice point also flips due to the exchange interaction, and it attempts to return the flipped spin to its pre-flip state, propagating this spin flip throughout the lattice in the form of the wave, known as spin waves. Considering a spin chain based on Eq. 1.33, the Hamiltonian reduces to:

$$\hat{\mathcal{H}} = -2J \sum_j \mathbf{S}_j \cdot \mathbf{S}_{j+1} \quad (1.34)$$

When solving, fluctuations are assumed to be transverse and small, i.e., the following approximation  $S_j^x = S_j^y \ll S$ ,  $S_j^z \approx S$  are considered:

$$S_j^x = Ae^{i(qja-\omega t)} \quad (1.35)$$

$$S_j^y = Be^{i(qja-\omega t)} \quad (1.36)$$

where  $q$  is the wave vector,  $A$  and  $B$  are constants,  $a$  is the interatomic spacing, and  $\omega$  is the frequency of the spin waves. This yields the dispersion relation:

$$\hbar\omega = 4JS(1 - \cos qa) \quad (1.37)$$

when  $qa \ll 1$ , at the limit of small wave vectors the dispersion relation is:

$$\hbar\omega \approx 2JSa^2q^2 \quad (1.38)$$

i.e, for small values of  $q$ , the ferromagnet's spin waves have a quadratic dispersion.

The antiferromagnet spin waves dispersion relation is given by:

$$\hbar\omega = 4JS \sin qa \quad (1.39)$$

at the limit of small wave vectors the dispersion relation is:

$$\hbar\omega \approx 4JSaq \quad (1.40)$$

i.e, for small values of  $q$ , the antiferromagnet's spin waves have a linear dispersion.

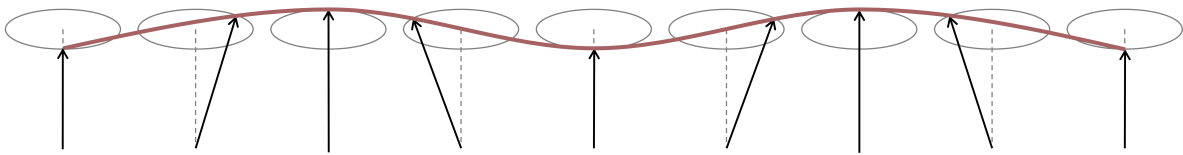


**Figure 1.2:** Illustrates the spin waves. After [64].

---

### 1.2.7.4 Magnetic Anisotropy

When an external magnetic field is applied along different crystal-axis directions, the ease with which the material becomes magnetized varies, resulting in magnetic anisotropy. Crystal field is one of the sources of induced anisotropy, achieved by lowering the symmetry of electron orbital motion. Magnetic anisotropy also originates from SOC and dipolar interactions, while any process that breaks symmetry can also contribute to additional magnetic anisotropy. The two main types of magnetic anisotropy are:

- Magnetocrystalline anisotropy is intrinsic to the material and arises from interactions between spin, orbit, and lattice. For example, the orientation of the orbit is strongly fixed to the lattice. Due to SOC, an external magnetic field attempts to reorient the spin, but the orbit is strongly coupled to the lattice and resists efforts to reorient the spin. As a result, magnetocrystalline anisotropy overcomes this resistance originating from SOC.

In addition, in exchange interactions, if the components of the spin in the  $x$ ,  $y$ , and  $z$  three directions are considered, the interaction can be one- (Ising model), two- (XY model) or three-dimensional (Heisenberg model), and the Hamiltonian Eq. 1.33 can be written as:

$$\mathcal{H} = - \sum_{ij} \left( J_x S_i^x S_j^x + J_y S_i^y S_j^y + J_z S_i^z S_j^z \right) \quad (1.41)$$

where  $S_i^x$ ,  $S_i^y$ ,  $S_i^z$ , and  $S_j^x$ ,  $S_j^y$ ,  $S_j^z$  are the  $x$ ,  $y$ , and  $z$  components of the spin operators at lattice points  $i$  and  $j$ , respectively. The anisotropy is expressed by  $J_x$ ,  $J_y$ , and  $J_z$ .

- Shape anisotropy arises from the geometry of the sample. During magnetization, an internal demagnetizing field forms within the material, causing the internal magnetic field to be weaker than the external field. The energy of this demagnetizing field is determined by a parameter known as the demagnetization factor  $N$ , which depends on the sample's shape. Consequently, shape anisotropy is particularly significant for thin film materials.

### 1.2.7.5 Hubbard Model

Energy band theory is based on the single-electron approximation, where interactions between electrons are considered in the form of a mean field. However, when the electron interactions in a system are very strong (e.g.,  $3d$  electrons for transition metals, and

4*f* electrons for rare-earth ions), the system exhibits a series of very complex behaviors, and this class of systems is known as strongly correlated electron systems, such as Mott insulators [75], high-temperature superconductors [76], and quantum spin liquids [71]. One of the fundamental models describing this category of systems is the Hubbard model [77]. The Hubbard model is based on the idea that when an electron moves from one localized atomic orbital to another, it is necessary to take into account whether the latter is occupied by other electrons. If it is already occupied, adding the Coulombic interaction between two electrons situated around the same atom will result in a significant change in the state of the energy bands. In the basic scenario, an atom has only one energy level, which can be occupied by at most two electrons with opposite spins. The Hubbard Hamiltonian is given by:

$$\mathcal{H} = -t \sum_{i,j,\sigma} c_{i\sigma}^\dagger c_{j\sigma} + U \sum_i n_{i\uparrow} n_{i\downarrow} - \mu \sum_{i,\sigma} n_{i\sigma} \quad (1.42)$$

where  $c_{i\sigma}^\dagger$  is the creation operator which creates an electron of spin  $\sigma$  on lattice site  $i$ ,  $c_{j\sigma}$  is the annihilation operator,  $n_{i\sigma} = c_{i\sigma}^\dagger c_{i\sigma}$  is the number operator with spin up ( $\uparrow$ ) or spin down ( $\downarrow$ ).

The first term represents the kinetic energy, indicating the electron's movement from one site to its neighbors (hopping), where  $t$  controls the scale of this hopping energy. The second term represents the interaction energy. If the atom has zero or only a single electron, then the Coulomb interaction is zero. However, if the atom has two electrons, an energy  $U$  is added to the second term. There is no interaction between electrons on different sites. The final term represents the chemical potential.

### 1.2.7.6 Magnetic Frustration

Magnetic frustration is a crucial concept, especially in the study of quantum spin liquids [71]. In general magnetic materials, thermal fluctuations decrease with decreasing temperature, causing the spins to form long-range order states at low temperatures to minimize the free energy of the system. However, in the presence of magnetic frustration, the energy levels of individual magnetic ground states become very close to each other, resulting in ground-state degeneracy. Consequently, even at very low temperatures, the system remains disordered with strong quantum fluctuations [69]. Geometric frustration is currently a highly discussed scenario of magnetic frustration.



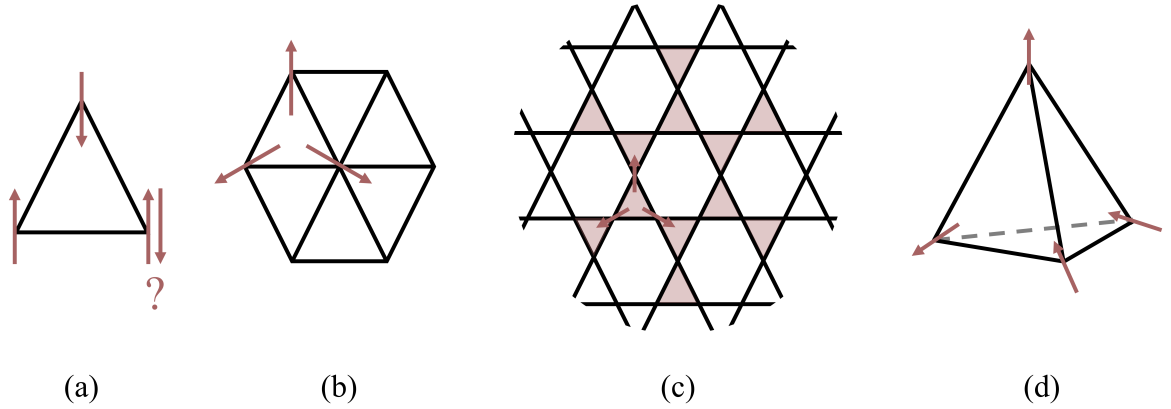


**Figure 1.3:** (a) Schematic of the geometrical frustration on a single triangle within the triangular Ising lattice. (b) The spins on the triangular-lattice Heisenberg antiferromagnet are oriented at angles of 120 degrees to each other. (c) Schematic of the geometrical frustration in the Kagome lattice and (d) on a single tetrahedron in the pyrochlore lattice. After [69, 71].

Geometric frustration arises in specific lattice geometries due to competing antiferromagnetic (AFM) interactions. Representative examples of geometrically frustrated structures include the triangular lattice, the Kagome lattice, and the 3D co-vertex tetrahedral (Pyrochlore) lattice, as shown in the Fig. 1.3. Taking the triangular lattice as an example, when nearest-neighbor (NN) interaction is the AFM interaction, two spins on the triangular lattice align antiparallel to each other below the transition temperature. However, regardless of the direction chosen, the third spin cannot satisfy the condition of being antiparallel to both of the other two spins. In considering only the NN interactions, the ground state of the antiferromagnetic system based on a triangular lattice exhibit three spin directions at 120 degrees to each other, as depicted in Fig. 1.3(b). Based on the Weiss temperature as given in Eq. 1.23, the strength of frustration is quantified by the frustration factor:

$$f = \frac{|\Theta|}{T_N} \quad (1.43)$$

It is typically assumed that a system exhibits frustration when  $f > 5 - 10$ , and a system with frustration necessarily exists degeneracy.

### 1.2.8 Energy Conditions for Crystallization

Crystal growth can occur with the gas, liquid, or solid as the parent phase and is a typical first-order phase transition process. The Gibbs free energy of the system can be expressed as a relation between the internal energy  $E$ , the pressure  $V$ , the absolute temperature  $T$ , and the entropy  $S$ :

$$G = E + pV - TS \quad (1.44)$$

For isothermal processes, the following equation applies, where  $H = E + pV$  is the enthalpy of the system:

$$\Delta G = \Delta H - T\Delta S \quad (1.45)$$

The requirements for crystal growth satisfy the second law of thermodynamics, i.e., the free energy reduction principle. The temperature at which the material begins to crystallize is always below the melting point of the material, which is known as the supercooling degree  $\Delta T = T_M - T$ . The greater degree of supercooling, the higher number of nuclei, and the finer grain size after crystallization.

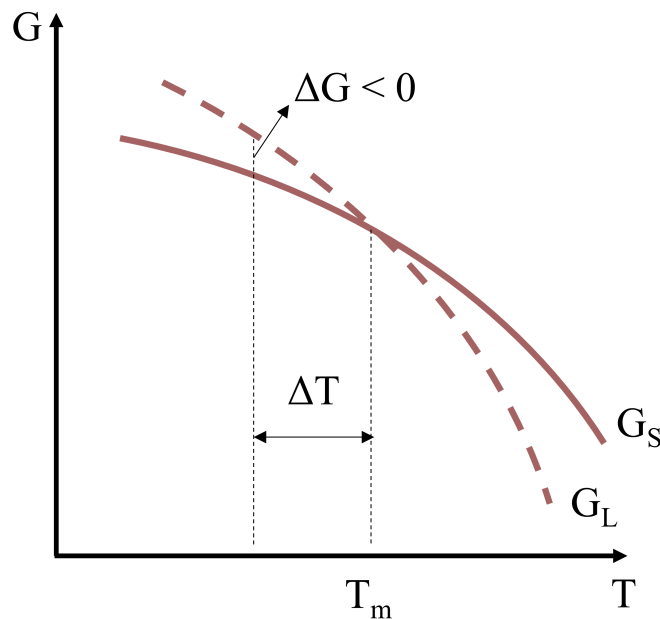


**Figure 1.4:** Schematic illustration of the  $G - T$  curve for solid-phase and liquid-phase systems. After [74].

Fig. 1.4 illustrates the temperature dependence of the free energy in both liquid and solid

---

phases. Since the degree of order in liquid atoms is lower than that in solid atoms, and the entropy value of the liquid is greater than that of the solid, the free energy curves of the two phases are bound to intersect at the melting point  $T_m$ . The process of crystallization is achieved by the movement of the crystalline interface to the parent phase. The driving force  $\Delta G_V$  for crystallization per unit volume is proportional to the supercooling degree:

$$\Delta G_V = \Delta H_m \frac{\Delta T}{T_m} \quad (1.46)$$

where  $\Delta H_m$  is the enthalpy of melting at temperature  $T_m$ .



# 2

## Experimental Method

High quality samples are prerequisite for the successful performance of the experiments. This work involves the preparation of single crystals  $R\text{InO}_3$  ( $R = \text{Gd}, \text{Tb}$ ),  $\text{La}_4\text{Ni}_3\text{O}_{10}$ , and  $R\text{InO}_3$  ( $R = \text{Er}, \text{Gd}, \text{Sm}$ ) using the high-pressure optical floating zone method. This chapter outlines the experimental methods, covering the sample synthesise, structural characterization, and magnetization measurements.



---

## 2.1 Synthesis

### 2.1.1 Solid State Reaction Method

Polycrystalline samples are typically prepared using the conventional solid state reaction (SSR) method, characterized by the absence of solvents and the simplicity of the experimental process. The SSR method involves the chemical reaction of two or more solid state chemical compounds, resulting in the formation of a new solid state product [78]. The SSR usually requires long reaction times. For the samples discussed in this work, the sintering temperature and time are provided in Table 2.1. Oxide powders are commonly selected as the initial reactants, and a list of chemicals utilized in this work can be found in Table A.3 in the appendix. The specific experimental procedure is outlined as follows:

- Investigate the synthesis conditions of the samples to be prepared by checking the melting points of the reactants, their volatility and the possible changes in the valence states of the elements during the reaction. Calculate the mass of reagents required according to the chemical equation, taking into account the purity of the reagents.
- Pre-heating: The reagents for the SSR are pre-heated in separate alumina crucibles in order to eliminate possible quality errors due to the water absorption and volatile impurities of the reagents. After pre-heating, the oxide powders are accurately weighed and mixed. The box muffle furnace Nabertherm-LHT 02/17 was used for sintering in this work.
- Grinding-sintering cycle: The mixed powder is placed in an agate mortar, along with appropriate amounts of isopropanol (or anhydrous ethanol). The mixture is thoroughly ground until the isopropanol is completely volatilized. Subsequently, the powder mixture undergoes sintering at temperatures ranging from 1300 °C to 1500 °C, with a sintering duration selected between 24 to 72 hours. To ensure thorough reaction and the uniformity of powder particles, the "grinding-sintering" process is cycled, maintaining the same temperature and duration for each sintering process. This cycle was repeated three times for the samples presented in this work.
- Rod pressing: The powder, having undergone multiple sintering cycles, is pressed into rods with a controlled diameter of approximately 5 mm. The mold and rubber tube used for rod pressing are depicted in Fig. 2.1. It is essential to note that the condensity and uniformity of the rods directly influence the efficiency and success of

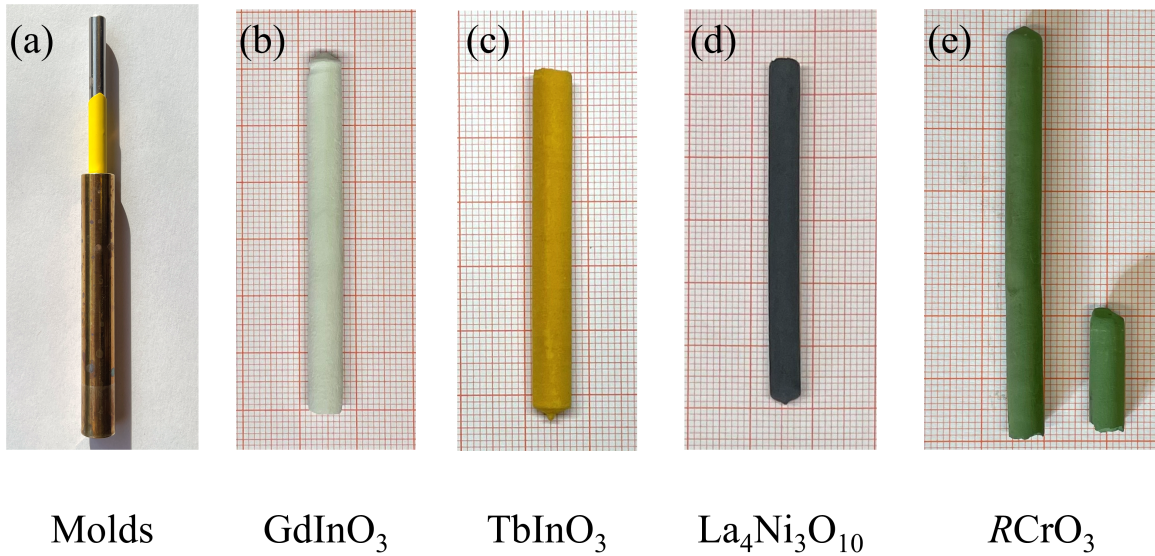


**Figure 2.1:** (a) The schematic of mold for preparing polycrystalline rods. (b)-(e) The polycrystalline rods prepared in this work.

the subsequent single crystal growth process described in the following subsection. Therefore, ensuring the uniformity of the rods is crucial, achieved by thoroughly milling the powder into a fine consistency without any granularity before commencing the rod pressing. The rods were isostatically pressed at 60-70 MPa.

- Rod sintering: Following the pressing and molding stages, the rods undergo another round of sintering. The sintering temperature of the rods can be elevated by approximately 50 °C, and the sintering duration can be extended based on experimental requirements to ensure the desired condensity of the rods.

### 2.1.2 Ball Milling Method

In cases where there is a significant disparity in the particle size among the various powders, the ball milling technique can be combined with the SSR method. This combination ensures the production of powders with uniform particle sizes, thoroughly mixed to facilitate an adequate SSR. Alternatively, ball milling can precede the rod pressing step to enhance the densification of the rods. Ball milling is a mechanical method utilized to grind powders into fine particles or to prepare composite material, offering a simple and cost-effective way to synthesize composites. In this work, the Retsch Planetary Ball Mill PM-100 was employed for ball milling, comprising a rotating chamber that generates centrifugal force, grinding



jars with varying volumes, and grinding balls. Dry or wet grinding can be applied during the synthesise process based on the final product requirements. In this work,  $ZrO_2$  balls with a diameter of 1 mm were utilized, and the ratio of  $ZrO_2$  to the raw material, along with the duration and rotation speed of the ball milling process, were adjusted according to the specific circumstances. Following the ball milling process, the sample was cleaned with isopropanol, collected, and dried.

### 2.1.3 Single Crystal Growth by Floating Zone Method

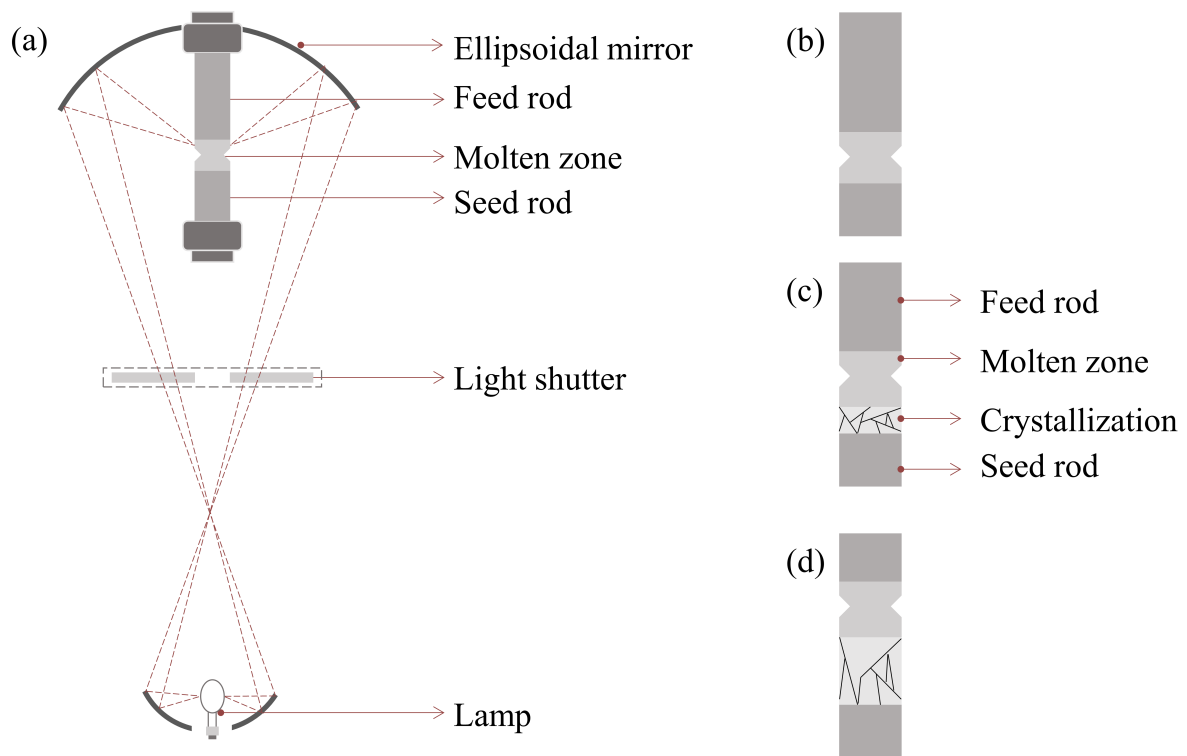


**Figure 2.2:** (a) The structure schematic of the optical floating zone furnace HKZ. The schematic of the melting zone at stages for (b) docking, (c) the beginning of crystallization, and (d) grain in specific directions continues to enlarge. After [79].

Crystal growth techniques are mainly categorized into four groups based on the type of phase transition utilized during crystal growth: growth from melt, solution, vapor, and solid state [81]. Among these, the floating zone method, which involves crystal growth from the melt, was invented in the early 1960s [5, 82]. Compared to traditional crystal growth methods from the melt such as the bridgman method, the most notable feature of the floating zone method is its freedom from the limitation of crucibles. This characteristic

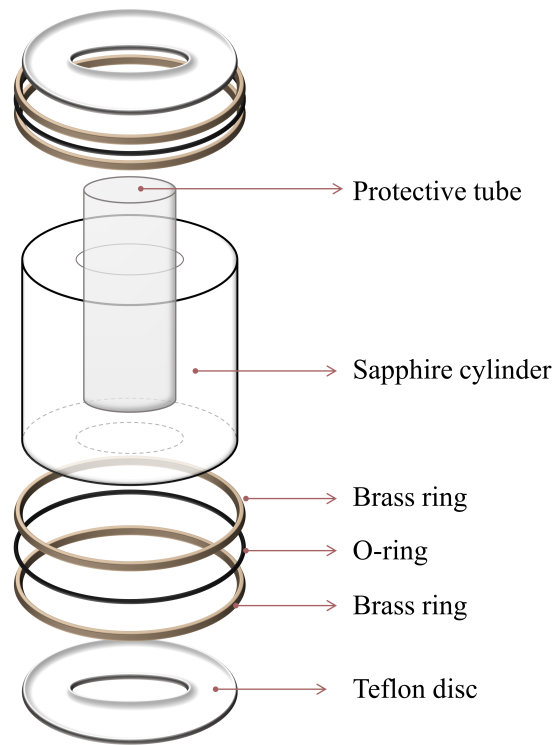


**Figure 2.3:** Schematic diagram of the HKZ growth chamber. After [80].

makes it suitable for growing single crystal of substances with higher melting points while minimizing the risk of contamination [79]. In the optical floating zone method, two rod-shaped polycrystalline samples are prepared: feed rod and seed rod <sup>1</sup>. Different heat sources can be used to melt the rods. Usually, a light source with high energy density, such as a halogen lamp, xenon lamp, or laser beam, is used to focus the light on the sample by utilizing curved mirrors. The crystal growth process begins with the melting of the tops of feed and seed, causing them to cluster together and form a floating zone between the feed and seed (refer to Fig. 2.2(b)). As this method does not utilize a crucible, the connection between the feed and seed relies on the balance between gravity and surface tension of the melt. For oxide melts, convection in the molten zone plays an important role in heat transport, with forces such as surface tension, buoyancy, and centrifugal force influencing fluid motion within the melt [83]. The rods are rotated in opposite directions to ensure thorough fusion. The recrystallization process in the optical floating zone method is achieved through the relative motion of the light source and the sample. In the case of spontaneous nucleation with polycrystalline rods as seed, the melted seed contains small multi-directional grains (Fig. 2.2(c)). During the growth process, grain in specific directions

<sup>1</sup> Using the single crystal rods as seed is a better choice for improving the crystallization efficiency.

---

continue to enlarge, leading to the re-crystallization of the melted rods along those specific directions (Fig. 2.2(d)).

The high-pressure optical floating zone furnace HKZ (SciDre) was used to prepare single crystals in this work [84–86]. It adopts a vertical mirror setup, as shown in the schematic structure in Fig. 2.2(a). In this work, 5 kW or 7 kW Xenon arc lamps were employed as a heat source with melting temperatures of up to 3000°C. The HKZ is equipped with a two-color pyrometer for stroboscopic measurement near the melting zone and a high-resolution CCD camera, enabling real-time monitoring of the temperature and status of the melting zone during the growth process. Furthermore, one significant advantage of this device is the ability to work with different gases and mixtures in the growth chamber at pressures up to 150 bar [80]. An enlarged view of the growth chamber is shown in Fig. 2.3. The chamber is divided into two layers: the outer layer is a sapphire cylinder (weighing approximately 1.0 kg), used as a pressure vessel to ensure pressures up to 150 bar, and the inner layer is a protection tube with a volume of approximately 23 ml.

#### **2.1.4 The Challenges of Single Crystal Growth of $R\text{InO}_3$ ( $R = \text{Gd}, \text{Tb}$ ), $\text{La}_4\text{Ni}_3\text{O}_{10}$ , and $R\text{InO}_3$ ( $R = \text{Er}, \text{Gd}, \text{Sm}$ )**

In the floating zone method, the stability of the melt zone during growth is crucial. Factors such as compound decomposition during crystal growth, surface tension of the melt, segregation effects, low/high-temperature phase transitions, variation rate of gas flow, and vacuum of the growth chamber all impact the stability of the melting zone [5, 79, 87]. The preparation of single crystals of  $R\text{InO}_3$  ( $R = \text{Gd}, \text{Tb}$ ),  $\text{La}_4\text{Ni}_3\text{O}_{10}$ , and  $R\text{InO}_3$  ( $R = \text{Er}, \text{Gd}, \text{Sm}$ ) discussed in this work are challenging. For instance,  $\text{GdInO}_3$  undergoes decomposition during growth, leading to the loss of  $\text{In}_2\text{O}_3$  due to volatilization. This loss results in an imbalance of the stoichiometric ratio, and the volatiles adhering to the inner wall of the protection tube affect the focusing of the light source (see Fig. 2.4). Common methods to mitigate this issue include employing high-pressure growth environment, adding a small amount of  $\text{In}_2\text{O}_3$  to the feed rod, or using the gas with higher molecular mass (such as Ar instead of  $\text{N}_2$ ) to reduce the rate of volatilization. In this work, 30 bar Ar atmosphere was applied and the Ar flow rate was maintained at 0.1 l/min, which significantly slowed down the volatilization of  $\text{In}_2\text{O}_3$ . Fig. 2.5(a) illustrates the orientation of  $\text{GdInO}_3$  single crystal at the early stage of growth, where crystals gradually begin to orient after being docked and grown for 1.5 cm, accompanied by an evident color change. Additionally, a

large number of cracks are observed in the  $\text{GdInO}_3$  crystals after growth, as depicted in Fig. 2.5(d). These cracks are attributed to the presence of large temperature gradients in the crystal, which can typically be mitigated by reducing the growth rate [79].

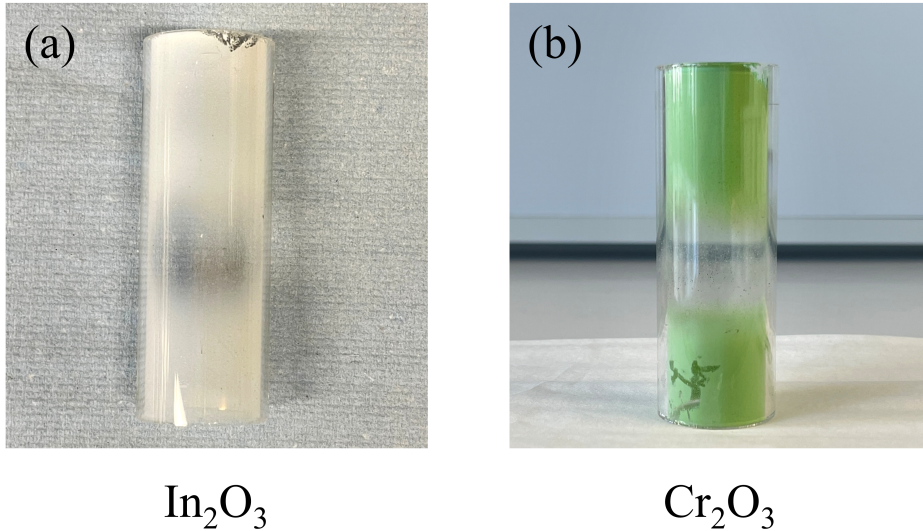


**Figure 2.4:** The protective tube with volatiles (a)  $\text{In}_2\text{O}_3$ , and (b)  $\text{Cr}_2\text{O}_3$  attached to the inner wall.

Secondly, for  $\text{TbInO}_3$ , it faces the same issue of  $\text{In}_2\text{O}_3$  volatilization as  $\text{GdInO}_3$ , which can be mitigated by pressurization. However, a significant number of bubbles were observed within the melt zone during the growth of  $\text{TbInO}_3$  (see Fig. 2.5(c) and (e)). These bubbles gradually expanded until they burst, causing the volume of the melt zone to shrink rapidly. This sudden change in volume led to a variation in light absorption, resulting in rapid fluctuations in temperature within the melt zone. In severe cases, this phenomenon directly caused the melt to fall onto the top of the feed and the detachment of the melt zone. Previous reports have suggested several reasons for bubble formation [5, 79, 87]: 1. Bubbles that nucleate homogeneously at the solid-liquid interface may be retained in the post-growth crystals (micro-pores); 2. Segregation effect or gaseous impurities; 3. Poor densification of the feed rod or inhomogeneity of the rods. While ensuring that there were no impurity effects, this work employed an increased sintering temperature of the feed rods, as well as a reduced growth rate to alleviate the bubble formation during growth. Additionally, varying the relative rotation rate of the feed and seed, adjusting the pressure in the range of 30-50 bar, and adding an additional 10% of  $\text{In}_2\text{O}_3$  of the stoichiometric ratio to the feed rod did not have a significant effect on bubble generation.

Thirdly, in the single crystal growth of  $\text{La}_4\text{Ni}_3\text{O}_{10}$ , using the same velocities for both rods

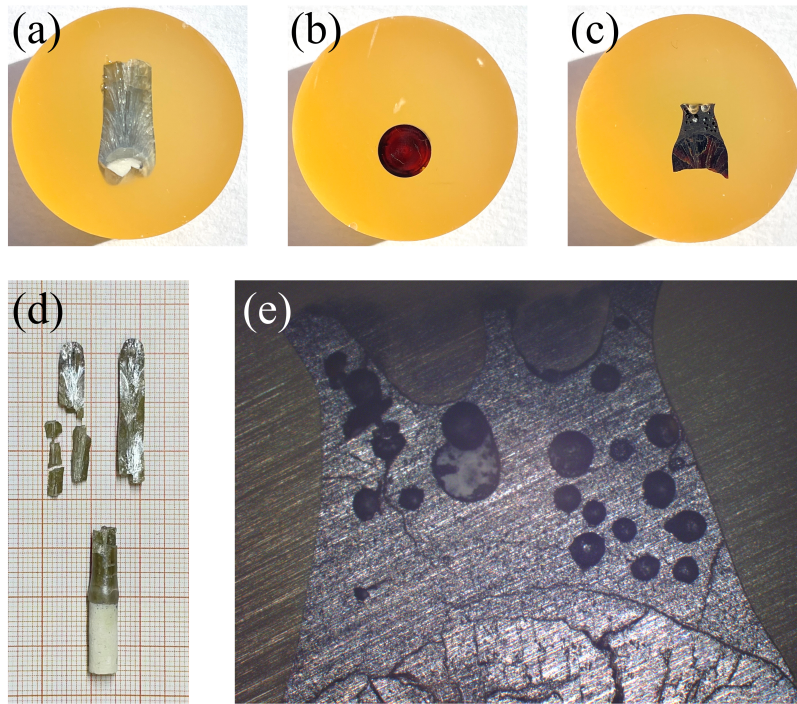


**Figure 2.5:** (a) Longitudinal section along the growth direction of  $\text{GdInO}_3$  in the early stages of growth. (b) Cross section of as-grown  $\text{TbInO}_3$ . (c) Longitudinal section of  $\text{TbInO}_3$  melt zone along the growth direction, solidified melt zone obtained by rapid cooling at the end of growth. (d) Natural cleavage surface of as-grown  $\text{GdInO}_3$  single crystal along the  $[001]$  direction. (e) Enlarged schematic of the bubble-rich melt zone for  $\text{TbInO}_3$ .

resulted in the depletion of liquid in the melting zone, similar to what was observed for  $\text{LaNiO}_3$  [17]. Inconsistent velocity settings resulted in a wider diameter of the as-grown single crystal compared to the feed (see Fig. 2.6(b)) and, in general, entailed an increase in cracks. As mentioned above, cracking usually occurs due to the large temperature gradients during growth [79]. Additionally, cracks are prone to occur when there is a low-temperature to high-temperature phase transition during the growth (eg.  $\text{Li}_3\text{VO}_4$  [88]). Reducing the growth rate is one of the method to suppress the appearance of cracks [79]. Finally, single crystal preparation of  $\text{RCrO}_3$  faces the challenge of  $\text{RCrO}_3$  decomposing during growth and losing  $\text{Cr}_2\text{O}_3$  due to volatilization. Pressurization is an effective way to mitigate volatilization; however, due to the high melting point of  $\text{RCrO}_3$ , increasing the pressure will further raise its melting point, reaching the upper limit of the equipment's operating temperature. Therefore, an Ar pressure setting of 30-80 bar and adding the additional  $\text{Cr}_2\text{O}_3$  of 10% of the stoichiometric ratio to the feed rod were attempted in this work to suppress the volatilization of  $\text{Cr}_2\text{O}_3$ . All the growth parameters of single crystals

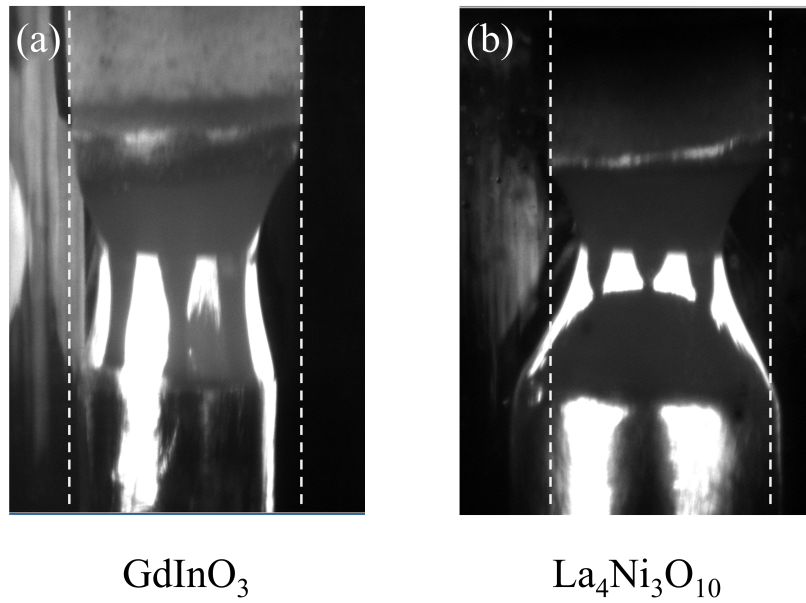


**Figure 2.6:** (a) The state of the melting zone when  $\text{GdInO}_3$  is growing steadily, with the crystallized part below the melting zone showing a normal diameter. (b) The state of the melt zone during the growth of  $\text{La}_4\text{Ni}_3\text{O}_{10}$ , and the wider diameter of the as-grown crystal. Dashed lines are guides to the eye.

discussed in this work are listed in Table 2.1.

**Table 2.1:** The synthesize temperatures and growth parameters of the single crystal samples prepared in this work.

Material	Powder sintering (air, ambient)	Rods sintering (air, ambient)	Melting zone Temp.(K)	Growth rate (mm/h)	Gaseous	Pressure (bar)	Gas flow (l/min)
$\text{GdInO}_3$	1350°C for 24 h	1400°C for 36 h	~1750°C	10	$\text{O}_2$	30	0.1
$\text{TbInO}_3$	1300°C for 24 h	1400°C for 36 h	~1820°C	10	$\text{O}_2$	30	0.1
$\text{La}_4\text{Ni}_3\text{O}_{10}$	1050°C for 24 h	1400°C for 24 h	~1650°C	6(feed)+4(seed)	$\text{O}_2$	20	0.1
$\text{ErCrO}_3$	1350°C for 48 h	1500°C for 48 h	~2300°C	10	Ar	45	0.1
$\text{GdCrO}_3$	1350°C for 48 h	1500°C for 48 h	~2300°C	10	Ar	45	0.1
$\text{SmCrO}_3$	1350°C for 48 h	1500°C for 48 h	~2300°C	10	Ar	30	0.1

## 2.2 Characterization

### 2.2.1 X-ray Diffraction (XRD) and Refinement

The phase purity of the resulting materials was assessed using powder X-ray diffraction (XRD). X-ray diffraction is a non-destructive method applicable to fully or partially



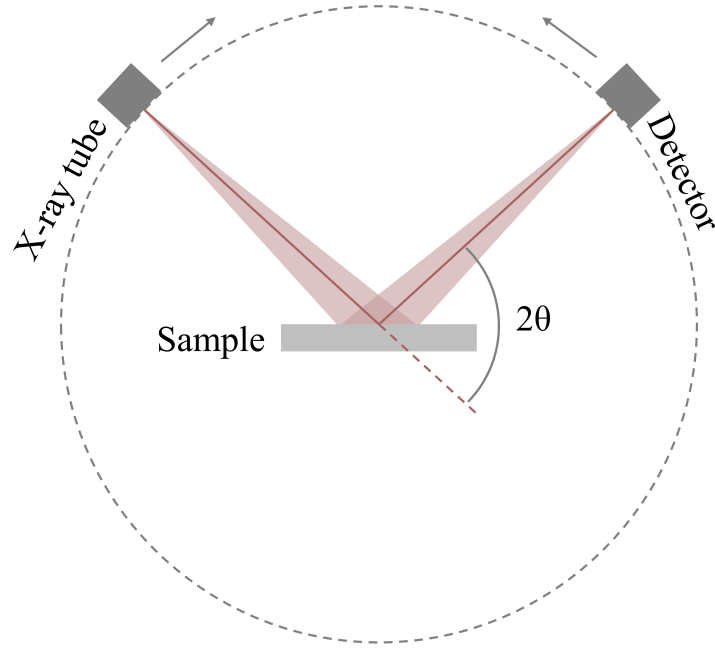


**Figure 2.7:** XRD schematic based on Bragg-Brentano geometry. After [89].

crystallized materials [90]. Monochromatic X-rays are directed onto the sample and scattered by atoms within the lattice. Since the atoms are arranged periodically within the crystal, certain scattering directions exhibit reinforcement of scattered waves. To probe the microstructure of crystals effectively, the X-ray wavelength should be proportional to the atomic spacing (approximately 0.1 nm) [91]. Bragg equation 2.1 defines the fundamental condition required for X-ray diffraction in a crystal:

$$2d \sin \theta = n\lambda. \quad (2.1)$$

Where  $d$  represents the interplanar crystal spacing,  $\theta$  is the incident angle (the angle between the incident ray and the scattering plane),  $\lambda$  denotes the wavelength of the X-rays, and  $n$  signifies the diffraction order, the diffraction angle is given by  $2\theta$ . The XRD schematic based on Bragg-Brentano geometry is show in Fig. 2.7. Since powdered materials exhibit random orientations, scanning in the range of  $2\theta = 10^\circ - 90^\circ$  allows for the collection of all possible diffraction directions of the lattice, resulting in the distribution of diffraction intensities as a function of  $2\theta$ . The arrangement of atoms within each crystal is unique, leading to a distinct diffraction pattern. The distribution of the diffraction peaks is determined by the size, shape, and orientation of the crystal cell, while the intensity of the diffraction peaks is influenced by the type of atoms and their positions in the crystal

cell [91]. The broadening of the diffraction peaks is associated with the grain size and can be characterized using Scherrer equation 2.2:

$$D = \frac{K\lambda}{\beta \cos \theta}. \quad (2.2)$$

where  $D$  represents the mean size of the ordered crystallite domains,  $K$  is the Scherrer constant,  $\lambda$  denotes the wavelength of the X-ray,  $\beta$  represents the full width at half maximum of the peak, and  $\theta$  is the Bragg angle. In addition, the Rietveld method is utilized to fit (refine) the full spectrum of XRD data. Rietveld refinement relies on the assumption of a crystal structure model and structural parameters [92, 93]. It combines these parameters with peak shape functions to calculate the polycrystalline diffraction spectrum, which is then adjusted using the least squares method for factors such as zero shift, lattice parameters, asymmetry, and preferred orientation etc. These adjustments ensure that the structural model aligns with the experimental data.

The XRD data in this work were performed at room temperature by means of a Bruker D8 Advance ECO diffractometer using Cu- $K\alpha$  radiation ( $\lambda = 1.5418 \text{ \AA}$ ). The data was collected in the  $2\theta$  range of  $10 - 90^\circ$  with  $0.02^\circ$  step-size. All the data were measured by Ilse Glass at the Institute of Earth Sciences, Heidelberg University. All XRD refinements in this work were conducted using the FULLPROF SUITE software [93], with the peak shape function selected as Pseudo-Voigt function <sup>2</sup>.

### 2.2.2 Back-reflection Laue Method

The grown crystals were checked by the Laue back-reflection diffraction experiment to confirm their single crystal nature and to orient the crystals. Following Bragg equation 2.1, the fixed crystal was irradiated by X-rays with continuously varying wavelengths, resulting in a two-dimensional diffraction pattern of the fixed crystal surface. The Laue diffraction patterns utilized in this work were obtained using a high-resolution X-ray Laue camera manufactured by Photonic Science. Single crystal samples were securely mounted on a goniometer stage, and the diffraction patterns were generated using white X-rays emitted by a standard tungsten X-ray tube. Operating parameters typically included an acceleration voltage ranging from 25 to 30 kV and a tube current of 15 to 20 mA. Acquisition times of 300 to 500 seconds were employed to ensure the capture of high-quality images.

---

<sup>2</sup> Pseudo-Voigt function is a linear combination of Lorentzian and Gaussian functions [93].



---

### 2.2.3 Magnetometry

The DC susceptibility data were measured using a magnetic property measurement system (MPMS3, Quantum Design) device, which employs a superconducting quantum interference device (SQUID) magnetometer to measure the magnetic moment. The MPMS3 offers two acquisition modes of DC susceptibility signal [94]. 1. DC Mode: The DC susceptibility signal is acquired as the sample is gradually moved through the pick-up coils. 2. Vibrating Sample Magnetometer (VSM) Mode: The VSM mode operates based on the electromagnetic induction principle. In this mode, the sample vibrates at a fixed frequency and amplitude centered on pick-up coils. The signals generated from these vibrations are measured with a lock-in amplifier, allowing for the computation of the magnetic moment of the sample. This mode offers faster acquisition speeds and higher sensitivity, resulting in higher resolution data. For the measurement of magnetic susceptibility dependence on temperature, three different methods were employed in this work:

- Zero Field Cooling (ZFC): The sample is initially mounted at room temperature and then cooled down to the lowest measured temperature (e.g.,  $T = 1.8$  K) without applying a magnetic field. Subsequently, a magnetic field is applied, and the measurement is initiated during the warming process.
- Field-Cooled Cooling (FCC): The sample is mounted and magnetized at room temperature (e.g.,  $B = 1$  T), and the measurement is initiated during the cooling process.
- Field-Cooled Warming (FCW): The sample is mounted and magnetized at room temperature (e.g.,  $B = 1$  T), cooled down to the lowest measured temperature (e.g.,  $T = 1.8$  K), and the measurement is initiated during the warming process.

The MPMS3 system can provide magnetic fields up to 7 T in a temperature range between 1.8 K and 400 K. Additionally, with the specific  $^3\text{He}$  option provided by Quantum Design, this temperature range can be extended down to 400 mK.



# 3

## Rare-Earth Indates

This chapter presents two members of the hexagonal rare-earth indates,  $\text{GdInO}_3$  and  $\text{TbInO}_3$ . The centered honeycomb lattice structure makes  $R\text{InO}_3$  an excellent platform for studying geometrically frustrated magnets or potential spin liquid states. Section 3.1 has been published in Physical Review B [95].



---

### 3.1 1/3 Plateau and 3/5 Discontinuity in the Magnetization and the Magnetic Phase Diagram of Hexagonal GdInO<sub>3</sub>


The following section has been published: N. Yuan, A. Elghandour, W. Hergett, R. Ohlendorf, L. Gries, and R. Klingeler, “1/3 plateau and 3/5 discontinuity in the magnetization and the magnetic phase diagram of hexagonal GdInO<sub>3</sub>”, *Physical Review B*, vol. 108, no. 22, p. 224403, 2023 [95]. Copyright ©2023 American Physical Society. All rights reserved. The authors contribution are following:

- Single crystal samples were prepared by **N. Yuan**, including the orientation and cutting of single crystals.
- The data presented in the paper were measured and analyzed by **N. Yuan**, with the exception of the specific heat data (Fig. 4(a)). All figures and tables were made by **N. Yuan**.
- **A. Elghandour** measured the specific heat and participated in the discussion of these data.
- **W. Hergett** contributed to the discussions during the single crystal preparation session and provided technical support.
- **R. Ohlendorf** and **L. Gries** participated in the data discussion, and the analysis of the dipole-dipole interaction between Gd<sup>3+</sup> moments in this paper was done by **R. Ohlendorf** with reference to her master’s thesis [96].
- **R. Klingeler** was responsible for the project, supervised the measurements, supported the data analysis and finalization of the manuscript.
- The manuscript draft was written by **N. Yuan**. Together with **R. Klingeler**, she revised and finished the manuscript, and communicated with the reviewers.
- All authors proofread the manuscript.



# 1/3 plateau and 3/5 discontinuity in the magnetization and the magnetic phase diagram of hexagonal GdInO<sub>3</sub>

N. Yuan,<sup>\*</sup> A. Elghandour<sup>✉</sup>, W. Hergett, R. Ohlendorf<sup>✉</sup>, L. Gries, and R. Klingeler<sup>✉†</sup>  
*Kirchhoff Institute of Physics, Heidelberg University, INF 227, D-69120 Heidelberg, Germany*

 (Received 9 August 2023; revised 14 November 2023; accepted 15 November 2023; published 1 December 2023)

We report the high-pressure optical floating-zone growth of GdInO<sub>3</sub> single crystals and show its magnetic phase diagram down to the millikelvin regime as determined by magnetization measurements. The centered-honeycomb lattice structure shows considerable magnetic frustration ( $|\Theta|/T_N \simeq 5$ ) and develops long-range magnetic order below  $T_N = 2.1$  K from a short-range-ordered paramagnetic phase. Concomitantly, a small net magnetic moment evolves at  $T_N$  which points along the crystallographic  $c$  direction. Upon cooling, the net moment reorients at  $T^{**} \simeq 1.7$  K and  $T^* \simeq 1$  K. A broad 1/3 plateau indicative of the up-up-down (*uud*) spin configuration appears for magnetic fields  $B\parallel c$  but is absent for  $B\parallel ab$ , thereby suggesting easy-axis anisotropy. At  $T = 0.4$  K, a jump in magnetization at  $\simeq 3/5$  of the saturation magnetization signals a discontinuous transition to a high field phase and we find evidence for a possible tricritical point. Small energy and field scales in the accessible regimes render GdInO<sub>3</sub> a well-suited example to study the phase diagram of a semiclassical frustrated hexagonal lattice in the presence of weak easy-axis anisotropy of mainly dipolar origin.

DOI: [10.1103/PhysRevB.108.224403](https://doi.org/10.1103/PhysRevB.108.224403)

## I. INTRODUCTION

Due to a wealth of relevant physical properties, perovskite rare-earth (RE) oxides with the nominal composition  $RBO_3$  ( $R$  a RE ion) form a versatile class of materials and are a major topical research area in condensed-matter physics and materials science. Prominent examples of spectacular phenomena observed in this class of materials are metal-insulator transitions in rare-earth nickelates [1,2], colossal magnetoresistance, phase separation, or charge and orbital order in manganates [3–6] or multiferroicity in  $RMnO_3$  [7,8]. Similar to hexagonal  $RMnO_3$ , the hexagonal  $RInO_3$  ( $R = \text{Eu, Gd, Tb, Dy, and Ho}$ ) systems crystallize in the  $P6_3cm$  space group [9,10]. Their centered honeycomb lattice structure renders  $RInO_3$  a well-suited platform to study geometrically frustrated magnets. Prior to 2017, studies on  $RInO_3$  were limited to polycrystalline samples [11]. Accessibility of macroscopic single crystals such as GdInO<sub>3</sub> [12], TbInO<sub>3</sub> [13,14], and Mn-doped TbInO<sub>3</sub> [15] has boosted the field as, for example, ferroelectricity and spin-liquid-like behavior were found in TbInO<sub>3</sub> [13,14]. In comparison to the quantum spin liquid candidate TbInO<sub>3</sub>, the properties of GdInO<sub>3</sub> resemble more those of a Heisenberg-like frustrated system with only small anisotropy [16]. In particular, in Ref. [16] the presence of a 1/3 magnetization plateau is reported which was inferred from an anomaly in the isothermal magnetization curves at 1.8 K. The presence of an  $M_s/3$  plateau is a typical feature of the up-up-down (*uud*) phase in triangular antiferromagnets [17–20]. In addition, GdInO<sub>3</sub> features ferroelectricity as confirmed by observation of the

$P(E)$  hysteresis loop as well as a  $Z_6$  vortex topological domain structure [12].

Volatilization of In<sub>2</sub>O<sub>3</sub> has long been a major challenge for the preparation of GdInO<sub>3</sub> single crystals. In this work, we have mitigated this issue by employing the high-pressure optical floating-zone method and show that high-quality GdInO<sub>3</sub> single crystals are successfully grown when using a high oxygen pressure of 30 bar. Using the single crystals we have constructed the magnetic phase diagrams in the temperature regime down to 400 mK and in magnetic fields up to 14 T. In the zero magnetic field, distinct anomalies in the magnetization and specific heat signal the evolution of long-range magnetic order at  $T_N = 2.1$  K. Applying the magnetic fields parallel to the  $c$  axis yields a 1/3 magnetization plateau in the isothermal magnetization which is centered at about 3 T. This magnetization plateau behavior is absent when the field is applied along the  $ab$  plane. The system also exhibits a small net magnetic moment along the  $c$  axis, weak easy-axis anisotropy, reorientation processes both in the zero magnetic field and driven by the field, and a discontinuous transition into a high-field phase.

## II. EXPERIMENTAL METHODS

Polycrystalline GdInO<sub>3</sub> was synthesized by a standard solid-state reaction following Refs. [12,16]. Stoichiometric amounts of Gd<sub>2</sub>O<sub>3</sub> and In<sub>2</sub>O<sub>3</sub> powders were well mixed and calcined at 1350 °C for 24 h (air flow, ambient pressure). The resulting material was ground and sintered for three times to ensure a complete reaction. Polycrystalline rods were prepared by hydrostatically pressing the powders under a pressure of 60 MPa and annealing them for 36 h at 1400 °C. GdInO<sub>3</sub> single crystal was grown by using the high-pressure optical floating-zone furnace (HKZ, SciDre) as described

<sup>\*</sup>ning.yuan@kip.uni-heidelberg.de

<sup>†</sup>klingeler@kip.uni-heidelberg.de

TABLE I. Growth parameters and phase analysis from the Rietveld refinement of the room-temperature powder XRD data of GdInO<sub>3</sub> single crystals from the literature [12,16] and reported at hand (HKZ).

	Laser <sup>a</sup>	Two-mirror <sup>b</sup>	HKZ <sup>c</sup>
Atmosphere	O <sub>2</sub>	O <sub>2</sub>	O <sub>2</sub>
Flow rate (l/min)	0.1	0.2	0.1
O <sub>2</sub> pressure (bar)	9.5	9	30
Growth rate (mm/h)	5–10	10	10
Lattice parameter <i>a</i> (Å)	6.3301(4)	6.3433(3)	6.3451(3)
Lattice parameter <i>c</i> (Å)	12.3340(17)	12.3320(1)	12.3408(9)

<sup>a</sup>Grown by the laser floating zone furnace (Crystal Systems Inc.), see Ref. [12].

<sup>b</sup>Grown by a two-mirror optical floating zone furnace (IRF01-001-05, Quantum Design), see Ref. [16].

<sup>c</sup>Grown by the high-pressure optical floating zone furnace (HKZ, SCIDRE), this work.

below. The phase purity and crystallinity were studied by powder x-ray diffraction (XRD) and the back-reflection Laue method. XRD was performed at room temperature by means of a Bruker D8 Advance ECO diffractometer using Cu-K $\alpha$  radiation ( $\lambda = 1.5418 \text{ \AA}$ ). Data have been collected in the  $2\Theta$  range of  $10^\circ$ – $90^\circ$  with a  $0.02^\circ$  step size. Structure refinement was carried out using the FULLPROF SUITE by means of the Rietveld method [21]. Studies of DC magnetization at 1.8–300 K have been performed in a SQUID magnetometer (MPMS3, Quantum Design Inc.) and by employing the vibrating sample magnetometer option of a Physical Properties Measurement System (PPMS, Quantum Design Inc.). For studies at temperatures between 0.4 and 5 K, the iQuantum <sup>3</sup>He option of MPMS3 was used. A relaxation method was used to perform specific heat measurements in the PPMS.

### III. RESULTS

#### A. GdInO<sub>3</sub> single crystal growth

Heavy volatilization of In<sub>2</sub>O<sub>3</sub> and low surface tension of the melts challenges growth of macroscopic GdInO<sub>3</sub> single crystals. To suppress volatilization, the crystals reported here were grown under an oxygen pressure of 30 bar using the high-pressure floating-zone furnace (HKZ, SciDre) [22,23]. High pressure was maintained at an O<sub>2</sub> flow rate of 0.1 l/min. A xenon arc lamp operating at 5 kW was employed and the growth was performed inside a sapphire chamber. A relatively fast growth rate of 10 mm/h was chosen in order to further mitigate In<sub>2</sub>O<sub>3</sub> volatilization. At slower growth rates, we observed significant amounts of deposited In<sub>2</sub>O<sub>3</sub> volatiles (see Fig. S1(a) of the Supplemental Material (SM) [24]) adhering to the inner protection glass tube, thereby affecting the focusing of light and preventing stable growth.

Using an *in situ* temperature measurement by means of a two-color pyrometer [25,26], the temperature of the melting zone during the growth was determined to about 1750 °C. The feed and seed rods were counter-rotated at 20 rpm to improve homogeneity of the melt; both feed and seed rods were pulled at 10 mm/h. The obtained boule is shown in Fig. S1(b) in the SM [24]. Table I lists the growth parameters used in this

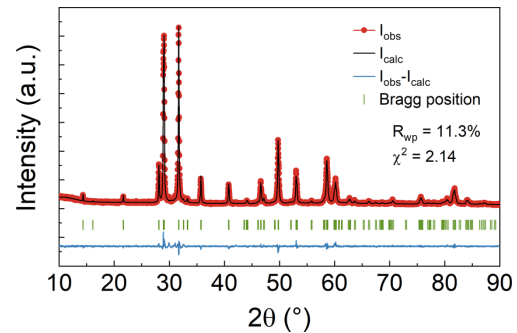


FIG. 1. Room-temperature XRD pattern and corresponding Rietveld refinement of powdered GdInO<sub>3</sub> single crystals grown at 30 bar O<sub>2</sub> pressure. The observed diffraction pattern is shown in red, the calculated one is shown in black, and the difference between them is shown in blue. Refinement is based on the hexagonal crystal system (space group  $P6_3cm$ , No. 185) of GdInO<sub>3</sub> as a main phase. The vertical green bars show the expected Bragg positions. The refinement converged to  $R_p = 12.0\%$ ,  $R_{wp} = 11.3\%$ , and  $\chi^2 = 2.14$ .

work and those in previous studies, as well as the refined lattice parameters and further characteristics of the respective crystals.

A powder x-ray diffractogram on a ground single crystal as well as an Rietveld refinement to the data is shown in Fig. 1. The result of the XRD refinement demonstrates that our sample is free of impurities, and the lattice parameters and the crystal structure match the reported crystals [12,16]. Refined structural parameters are shown as Table S1 in the SM [24]. The x-ray Laue diffraction in back-scattering geometry was used to confirm single crystallinity and orient the single crystals, which were then cut with respect to the crystallographic main directions using a diamond-wire saw. Figure S1(c) [24] shows the single crystal sample used for the magnetic and specific heat measurements. The Laue pattern in Fig. S1(d) [24] illustrates the high crystallinity of this sample. Laue diffraction performed at several other pieces of the GdInO<sub>3</sub> boule which were cleaved at room temperature confirm that the dominant growth direction is in the *ab* plane.

The crystal structure of GdInO<sub>3</sub> is shown in Fig. 2. It belongs to the hexagonal space group  $P6_3cm$  (No. 185), which alternately arranges corner-connected layered

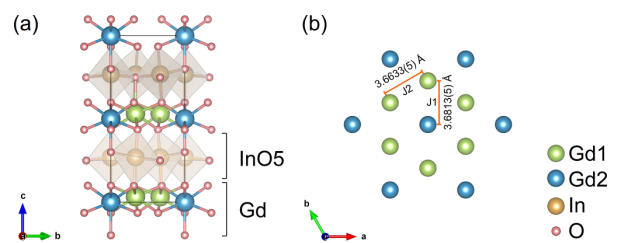


FIG. 2. (a) Schematic of the crystal structure of GdInO<sub>3</sub> along the [100] projection. (b) In-plane honeycomb arrangement of two inequivalent atomic sites of Gd<sup>3+</sup> ions.  $J_1$  and  $J_2$  represent two magnetic exchange interactions that are distinguished by symmetry (COD No. 7237332 [12,27]).



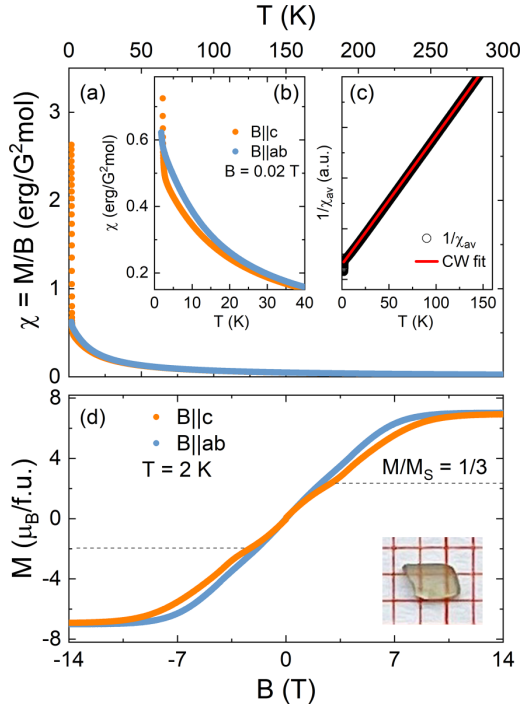


FIG. 3. (a) Temperature dependence of the static magnetic susceptibility  $\chi = M/B$ , obtained at  $B = 0.02$  T applied along the crystallographic  $c$  axis ( $B||c$ ) and in-plane ( $B||ab$ ), respectively; panel (b) highlights small anisotropy at low temperatures. (c) Inverse of the averaged susceptibility  $\chi_{av} = (\chi_c + 2\chi_{ab})/3$  and Curie-Weiss fit (red line; see also Fig. S2 in the SM [24]). (d) Isothermal magnetization at  $T = 2$  K for  $B||c$  and  $B||ab$ . The horizontal dashed line marks  $1/3$  of the saturation magnetization. The inserted picture shows the oriented single crystal under study on a millimeter grid.

InO<sub>5</sub> bipyramids and Gd layers. The structure features two inequivalent Gd sites in the Gd layers with Wyckoff positions 2a and 4b, respectively. The two types of Gd sites form an arc-like arrangement when viewed from the [100] direction [see Fig. 2(a)]. Hence, in the centered honeycomb layers formed by the Gd atoms in the plane perpendicular to the [001] axis, there are two slightly different Gd-Gd distances which may result in two distinct nearest-neighbor magnetic exchange parameters,  $J_1$  (Gd1-Gd2) and  $J_2$  (Gd1-Gd1) [see Fig. 2(b)] [11,16].

### B. Magnetization $M(T, B)$

The static magnetic susceptibility  $\chi = M/B$  obeys Curie-Weiss-like behavior down to about 50 K as shown in Figs. 3(a) and 3(c). At 300 K,  $\chi(B||ab)/\chi(B||c) \simeq 1.01$  signals purely paramagnetic behavior and negligible anisotropy of the  $g$  factor. Upon cooling below  $\sim 50$  K, a small anisotropy between  $\chi_c$  and  $\chi_{ab}$  evolves before an anomaly at  $T_N = 2.1$  K indicates the onset of long-range magnetic order [see Fig. 3(b)]. Fitting the averaged susceptibility well above  $T_N$  by an extended Curie-Weiss law, i.e.,  $(\chi_c + 2\chi_{ab})/3 = \chi_0 + N_A p_{\text{eff}}^2 / [3k_B(T - \Theta)]$  with the Avogadro number  $N_A$  and the Boltzmann constant  $k_B$  yields an excellent agreement with

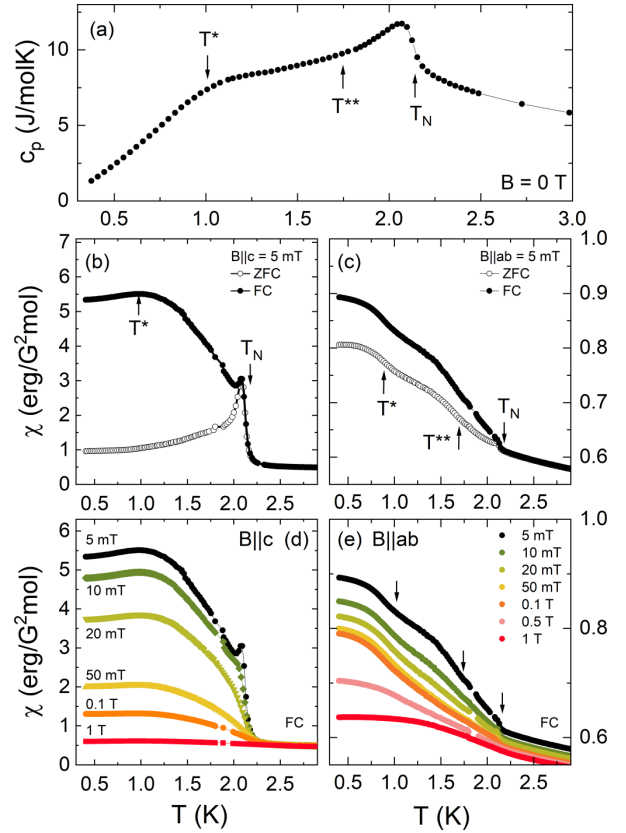


FIG. 4. (a) Specific heat at  $B = 0$  T and static magnetic susceptibility  $\chi = M/B$  in (b)  $B||c = 5$  mT and (c)  $B||ab = 5$  mT obtained in the field-cooled (FC) regime and the zero-field-cooled regime (ZFC) (black). (d, e) Static magnetic susceptibility (FC) at different external magnetic fields up to 1 T.  $T_N$ ,  $T^*$ , and  $T^{**}$  have been determined as described in the text.

the data [Fig. 3(c)]. The fit yields the Weiss temperature  $\Theta = -12(1)$  K and the effective magnetic moment  $p_{\text{eff}} = 7.9(1) \mu_B$  which agrees with the theoretical value of  $7.94 \mu_B$  for a free  $\text{Gd}^{3+}$  moment. The obtained negative Weiss temperature  $\Theta$  implies predominant antiferromagnetic interactions. We note the frustration parameter  $f = |\Theta|/T_N \simeq 5$ , which suggests considerable spin frustration in  $\text{GdInO}_3$ . Note that the experimental data deviate from the high-temperature Curie-Weiss fit below about 20 K as shown in Fig. S2 in the SM [24].

The onset of long-range antiferromagnetic (AF) order is associated with a clear anomaly in the specific heat shown in Fig. 4(a). Concomitantly and in agreement with the presence of a hysteresis in  $\chi$  vs  $T$ , there is a steep increase of  $\chi(B||c)$  at  $T_N$  and pronounced hysteresis between the data obtained after cooling in the magnetic field (field-cooled; FC) and in the zero magnetic field (zero-field-cooled; ZFC) [see Figs. 4(b) and 4(c)]. Upon cooling, the FC static susceptibility ( $\chi_{\text{FC}}$ ) increases further until a broad maximum develops around  $T^* \simeq 1$  K; below  $T^*$ , the magnetization  $\chi(B||c)$  slightly decreases. Concomitantly, there is a broad hump in the specific heat which has been interpreted as a signature of a second

antiferromagnetic phase appearing at  $T_{N2}$ , with  $T_{N2} = 1.05$  K as indicated by the associated maximum in  $c_p/T$  [16]. This hump is clearly visible in our data in Fig. 4(a), too. We note, however, that the hump neither signals an entropy jump nor is it  $\lambda$  shaped, and hence, there is no clear signature of a thermodynamic phase transition at  $T^*$ . If one would alternatively interpret the hump as a broad jump in  $c_p$ , an entropy-conserving construction would suggest  $T_{N2} \simeq 1.4$  K. At this temperature, however, there is no anomaly in the magnetization. As is discussed below, the observation of an anomaly in  $\chi$  vs  $T$  and a maximum of a broad hump in  $c_p$  at the same temperature  $T^*$  may, hence, be considered a signature of crossover associated with reorientation of the spin structure. A reorientation process is not necessarily associated with a proper thermodynamic phase boundary (see, e.g., rotation of a small ferromagnetic moment in  $\text{Eu}_2\text{CuSi}_3$  [28] and in  $\text{Gd}_2\text{In}_{0.97}\text{Si}_{2.97}$  [29] where similar humps in  $c_p$  are observed).

The magnetization data imply hysteresis between FC and ZFC measurements at low temperatures with bifurcation below  $T_N$ . Both the increase of magnetization and hysteresis further confirm the presence of a weak ferromagnetic component below  $T_N$ . The tiny peak in  $\chi_{\text{FC}}(B\|c)$  is typical of a ferromagnetic-like domain state signaling decrease of magnetic anisotropy when heating towards the transition temperature. This scenario is supported by the observations in larger fields which suppress all features mentioned above, i.e., jump in magnetization, bifurcation, tiny peak, and the hump at  $T^*$  [see Fig. 4(b)].

Several features appear in  $\chi(B\|ab)$  as demonstrated in Fig. 4(c): There is a kink at  $T_N$  indicating a very small increase of magnetization in the ordered phase. At  $T^*$ , there is a change in the slope as indicated by an inflection point in  $\chi$  vs  $T$ . In addition, we observe an anomaly at  $T^{**} \simeq 1.7$  K [see Fig. 4(c)]. Our data do not allow us to trace the field dependence  $T^{**}(B\|ab)$ . In contrast,  $T^*$  can be detected and it does not visibly change for small fields  $B \leq 0.1$  T and increases for higher fields.

Further information on the long-range ordered phase is obtained by estimating the actual jump size of the specific heat anomaly at  $T_N$ . It is derived from the data by an entropy-conserving method to  $\Delta c_p = 4.1(3)$  J/(mol K) [30]. This value is much smaller than the expected mean-field value for a  $S = 7/2$  equal-moment system [31] of  $\Delta c'_p = R \frac{5S(S+1)}{S^2+(S+1)^2} \simeq 20.1$  J/(mol K), with  $R$  being the gas constant [32]. Note that the actual jump size associated with the measured anomaly can be even smaller as it may be superimposed by critical fluctuations. The abovementioned mean-field result reduces to  $2/3$  of  $\Delta c'_p$  in the case of amplitude-modulated spin configurations in which the amplitude of the magnetic moment varies periodically from one site to another [33]. Both predicted values are much larger than the experimentally observed anomaly, which implies significant short-range magnetic order above  $T_N$  (as, e.g., suggested by the frustration parameter  $f \simeq 5$ ) and/or considerable spin disorder below  $T_N$ .

The magnetic entropy changes may be derived from the experimental specific heat data by subtracting the lattice contribution ( $c_p^{\text{phonon}}$ ) which yields the magnetic specific heat  $c_{\text{mag}}$ . Fitting the data well above  $T_N$  by an Einstein-Debye model yields the characteristic temperatures  $\Theta_D = 473$  K and

$\Theta_E = 850$  K and describes the data well for temperatures above 30 K (see Fig. S7 in the SM [24]) [34]. Integrating  $(c_p - c_p^{\text{ph}})/T$  yields the magnetic entropy changes of about  $17.8(2)$  J/(mol K), which agrees with the theoretical expectation value of  $R \ln 8 = 17.29$  J/(mol K). We note that only about 60% of the magnetic entropy is released at  $T_N$  while nearly 40% of the magnetic entropy is consumed between  $T_N$  and 20 K. This result implies significant short-range magnetic order persisting up to ten times the long-range ordering temperature. This is further confirmed by the fact that the experimentally observed magnetic susceptibility deviates from the high-temperature Curie-Weiss fit in the same temperature regime (see Fig. S2 in the SM [24]).

Notably, the mean-field description of entropy changes also implies the presence of a hump in  $c_p$  associated with low-energy excitations in the  $J = 7/2$  multiplet, at  $T/T_N \simeq 0.25$  [33,35]. Using  $T_N = 2.1$  K predicts such a hump at  $\sim 0.5$  K, i.e., below  $T^*$  (see Fig. S6 in the SM [24]). Such a Schottky-like anomaly is typically observed in Gd-based systems with some variation of the temperature of its maximum [36–40]. Comparison of experimental data with the prediction of mean-field theory is shown as Fig. S8 in the SM [24]. Due to the fact that  $T_N$  does not meet the mean-field prediction either, one might attribute  $T^*$  to multiplet effects. However, our observation that  $\chi(B\|c)$  decreases at  $T^*$  while  $\chi(B\|ab)$  increases rather suggests the scenario of partial rotation of ferromagnetic component towards the  $ab$  plane. The fact that  $T^*$  is also characterized by a broad hump in the specific heat [Fig. 4(a)] then indicates that the changes in the magnetization in the ordered phase are associated with anomalous entropy changes.

The effect of magnetic fields on the magnetic ground state is further illustrated by the isothermal magnetization  $M$  vs  $B$  and the associated magnetic susceptibility  $\partial M/\partial B$  at  $T = 2$  K [up to 14 T: Fig. 3(d)] and at  $T = 0.4$  K (up to 7 T: Fig. 5) as derived from the  $M(B)$  curves. From  $M(T = 2$  K), similar values of the saturation magnetization  $M_s$  for the different field directions confirm rather isotropic  $g$  factors:  $7.0(1)$  ( $B\|ab$ ) and  $6.9(1)$   $\mu_B/\text{f.u.}$  ( $B\|c$ ). The saturation fields amount to  $B_s^{ab} = 7.3(2)$  T and  $B_s^c = 8.4(2)$  T. We also note several features in the  $M(B)$  curves, the most prominent one appearing at around  $M_s/3$  for  $B\|c \simeq 2.9$  T.

At  $T = 0.4$  K, the anomalies in the magnetization curves are most pronounced as displayed in Fig. 5 (full  $M(B)$  curves covering  $-7$  T  $\leq B \leq 7$  T are shown as Fig. S3 in the SM [24]). The main features are as follows.

(i) There is a small ferromagnetic moment and magnetic hysteresis visible in the inset of Fig. 5(a) which show, for  $B\|c$ , a small remanent moment of  $0.14$   $\mu_B/\text{f.u.}$  and the critical field  $\simeq 60$  mT. No indication of hysteresis is found for  $B\|ab$ , which, however, displays s-shaped behavior around  $B = 0$  T as shown in the inset in Fig. 5(b) and by the broad peak in  $\partial M/\partial B\|ab$  centered at  $B = 0$  T.

(ii) For  $B\|c$ , there is a plateau-like feature in  $M$  centered at  $B_{c1} = 2.9$  T and a small jump in  $M$  at  $B_{c2} = 5.5$  T. Above  $B_{c2}$ ,  $M(B)$  features linear behavior which extrapolates to its saturation value at  $B_s \simeq 8.6$  T [41]. We also note a feature at  $B_{c1}^{\nabla} = 4.2$  T signaling the onset of the linear-in- $M$  regime and

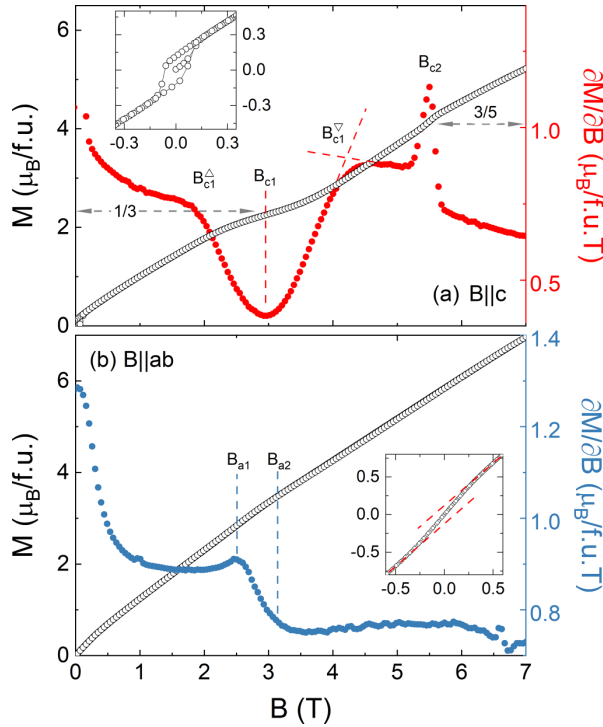


FIG. 5. Isothermal magnetization at  $T = 0.4$  K for (a) the  $B||c$  axis and (b) the  $B||ab$  plane (left ordinates) and corresponding magnetic susceptibilities  $\partial M/\partial B$  are shown (right ordinates). The full magnetization loop (from  $-7$  to  $+7$  T) is shown in Fig. S3 of the Supplemental Material [24]). Insets highlight the behavior around zero field. Horizontal dashed lines mark  $M_s/3$  and  $3M_s/5$ ; vertical lines show the anomaly fields as described in the text.

thus the upper limit of the plateau region while the plateau's lower edge is marked  $B_{c1}^\Delta$ .

(iii) For  $B||ab$ , there is a jump in  $\partial M/\partial B$  at  $B_{a1} \simeq 2.5$  T which is preceded by a tiny peak (i.e., a small jump in  $M$ ) at  $B_{a1}$  and followed by a linear regime in  $M$  for  $B > B_{a2}$ .

To summarize the main features, there is a clear magnetization plateau visible in  $M(B||c)$ , extending from  $B_{c1}^\Delta$  to  $B_{c1}^\nabla$  and centered at  $B_{c1}$ , which perfectly agrees with  $1/3$  of the saturation magnetization as determined at 2 K [cf. Fig. 3(d)]. Note that we find  $M_s$  rather independent of temperature in the accessible temperature regime so that  $M_s(2\text{ K}) \simeq M_s(0.4\text{ K})$ . A similar conclusion on the presence of a  $1/3$  magnetization plateau has been drawn from magnetization data at 1.8 K in Ref. [16]. In addition, there is a small jump in  $M$  at  $B_{c2}$  signaling a discontinuous phase transition at about  $3/5M_s$ . We also note that the tiny peak in  $\partial M/\partial B_{||ab}$  at  $B_{a1}$  appears at  $2/5$  of the saturation magnetization, and  $B_{a2}$  which signals the onset of a linear regime in  $M(B > B_{a2})$  appears at  $\simeq 1/2$  of  $M_s$ .

### C. Magnetic phase diagrams

Distinct anomalies in  $M$  vs  $B$  allow us to trace the temperature dependence of the phase boundaries associated with the critical fields marked in Fig. 5. Specifically, we have used the anomalies of the magnetic susceptibility shown in Fig. 6 to

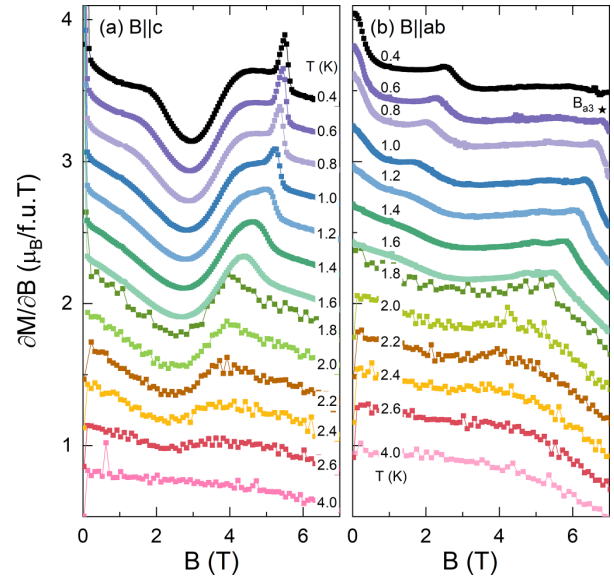


FIG. 6. Magnetic susceptibility  $\partial M/\partial B$  for (a)  $B||c$  and (b)  $B||ab$  at different temperatures. The curves are offset vertically by  $0.23 \mu_B/(f.u. \cdot T)$  for better visibility; the dashed line in panel (b) indicates the evolution of  $B_{a3}$ .

construct the magnetic phase diagrams. In addition, we have derived the saturation fields from our  $M(B, T \geq 1.8\text{ K})$  data up to 14 T (see Fig. 3(d) and Figs. S3 and S5 in the SM [24]) and from extrapolating the linear-in-field behavior at  $0.4\text{ K} \leq T \leq 1.8\text{ K}$ , as well as  $T_N(B)$ ,  $T^*(B)$ , and  $T^{**}(B)$  at low fields from  $M$  vs  $T$  measurements (see Fig. 4). The resulting phase diagrams are shown in Fig. 7. The following main features appear for  $B||c$ . Centered at  $B_{c1}$ , a  $1/3$  magnetization plateau is formed which starts to evolve at  $B_{c1}^\Delta$  and extends to  $B_{c1}^\nabla$ .  $B_{c1}$  is barely temperature dependent as it only slightly shifts to lower fields upon heating. Below about 1.2 K, there is a linear-in- $B$  regime of the magnetization following the AF I/plateau phase. Whether the AF I/AF I'/AF I'' boundaries signal proper thermodynamic phase transitions or crossover regimes is yet unclear. A sharp jump in  $M$  at  $B_{c2}$  clearly indicates a discontinuous phase transition and suggests a flip of the spin configuration. This jump is superimposed by a kink in  $M$  vs  $T$  as demonstrated by the peak and superimposed jump in  $\partial M/\partial B$  in Fig. 5. Upon heating, the sharp peak in  $\partial M/\partial B$  evolves to a broader feature in the temperature region where the upper boundary of the plateau phase ( $B_{c1}^\nabla$ ) merges with  $B_{c2}$ . Broadening and softening of the anomaly may indicate that the phase boundary evolves towards a continuous nature, which would suggest the presence of a tricritical point at  $\simeq 4$  T and  $\simeq 1.6$  K.

The Clausius-Clapeyron equation enables us to estimate the entropy changes appearing at the AF I'/AF II phase boundary [42]:

$$\Delta S_{c2} = -\Delta M_{c2} \frac{\partial B_{c2}}{\partial T}. \quad (1)$$

Using  $\Delta M(0.4\text{ K}) \simeq 0.11(1) \mu_B/f.u.$ , the analysis yields  $\Delta S_{c2} \simeq 0.15(3) \text{ J}/(\text{mol K})$ , at 0.4 K.

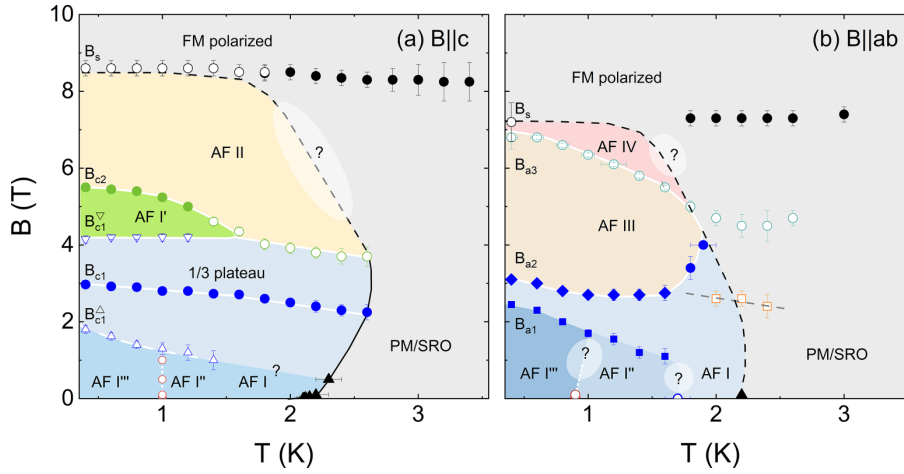


FIG. 7. Magnetic phase diagram of  $\text{GdInO}_3$  for  $B\parallel c$  and  $B\parallel ab$ .  $B_{a/ci}$  mark the critical fields as defined in Fig. 5 and in the text.  $B\parallel c$ : AF I: Low-field AF phase; 1/3 plateau phase centered around  $B_{c1}$  and confined by  $B_{c1}^\Delta$  and  $B_{c1}^\nabla$ . The latter marks the onset of a linear-in- $M$  regime AF I'. At  $B_{c2}$  a small jump in  $M$  appears before the polarized regime is achieved at  $B_s$ .  $B\parallel ab$ : At  $B = 0$  T, several features distinguish regions of different spin-orientation (AF I, AF I'', AF I'''). A clear phase boundary  $B_{a1}(T)$  separates AF I''' from the higher-field phase which may extend to AF I. Two AF phases (AF I and AF III) are separated by  $B_{a2}$ . A further kink in  $M$  marks the onset of a high-field but not fully polarized phase AF IV at  $B_{a3}$ . Several features appearing in the paramagnetic/short-range ordered phase (PM/SRO) are shown, too, as well as the regimes AF I, AF I'', and AF I'''. White areas mark regions where the phase boundaries are yet unclear.

As described above, for  $T > 1.2$  K, the sharp peak transforms into a much broader feature and  $B_{c2}$  is suppressed upon further heating. The saturation field towards the ferromagnetically polarized phase does not display strong temperature dependence and the saturation features can be traced well above the long-range ordered phase. We attribute this to significant short-range magnetic correlations above  $T_N$ . In contrast to  $B_s$ , magnetization measurements do not detect the phase boundary  $T_N(B > 4$  T), indicating that the magnetization in AF II and in the short-range ordered phase is very similar in this field regime. One may speculate about the phase boundary as suggested in Fig. 7(a).

We note that the magnetization  $M_c$  increases at  $T_N$  ( $\approx 0$  T), which already implies the observed positive initial field dependence of the associated phase boundary. Quantitatively, it may be estimated using the Ehrenfest equation:

$$\frac{\partial T_N}{\partial B} = -T_N \frac{\Delta M'}{\Delta c_p}. \quad (2)$$

Exploiting the experimentally determined jump in specific heat  $\Delta c_p$  from Fig. 4(a) and the change in slope of magnetization  $\Delta M' = \Delta(\partial M/\partial T)$  yields  $\partial T_N/\partial B\parallel c = 1.7(2)$  K/T, which is consistent with our data  $T_N(B \gtrsim 0$  T) shown in Fig. 7(a).

For  $B\parallel ab$  [Fig. 7(b)], we observe no sizable field dependence of  $T_N$  in small magnetic fields. This agrees with the observation of only a small increase of  $M_{ab}$  at  $T_N$ . The quantitative analysis in terms of the Ehrenfest relation [Eq. (2)] yields only  $\partial T_N/\partial B \approx 0.02(1)$  K/T. At zero field, two further anomalies in  $M(T)$  [Fig. 4(c)] indicate rotation of the ferromagnetic component. The related regimes in the phase diagram are labeled AF I'' and AF I''' and the nature of the boundaries is not clear [Fig 7(b)].

A small peak and a subsequent jump in  $\partial M/\partial B\parallel ab$  [see Fig. 5(b)] signal the appearance of the high-field phase AF III. From the fact that both anomalies  $B_{a1}$  and  $B_{a2}$  further separate upon heating, we conclude that the intermediate phase extends to the AF I regime at  $B = 0$  T. While AF I is separated by distinct anomalies from AF III around 2 K,  $B_{a1}$  cannot be traced up to  $T_N$ .  $T_N(B)$  cannot be well traced by our data either. In contrast, the upper phase boundary of AF III, i.e.,  $B_{a3}$ , is marked by clear anomalies in  $\partial M(B)/\partial B$  as indicated in Fig. 6, where associated kinks are visible for  $T \geq 0.6$  K. From the fact that  $B_s$  seems to be rather independent of temperature and clearly exceeds or is distinct from  $B_{a3}$ , we conclude the presence of the high-field phase AF IV [43]. The nature of AF IV is yet unknown. Note that again several features in  $M(B)$  extend into the short-range ordered/paramagnetic phase.

Finally, we discuss the phase diagram in the frame of potential spin configurations appearing in triangular-lattice spin systems (see, e.g., Refs. [19,20,44,45]). The ground-state spin configuration has not yet been determined experimentally. Potential candidates of the ground-state configuration are coplanar Y-type (as also discussed in Ref. [16]) or umbrella-type configurations. In both cases, finite-temperature  $uud$  phases may appear [45,46].

(i) Our experimental data imply the presence of a net magnetic moment. In the case of the Y-type configuration, the measured net moment would correspond to an angle of  $2\theta \approx 117^\circ$  between the upper spins in Fig. 8(a). An umbrella structure would feature a huge aperture outside the  $ab$  plane [see Fig. 8(b)]; the observed size of the canted moment would suggest an angle of  $\approx 1.2^\circ$  between the Gd moments and the  $ab$  plane [47]. The in-plane projections of the moments cancel out in this scenario. The data in Fig. 4 indicate partial rotation of the net moment towards the  $ab$  plane, yielding further



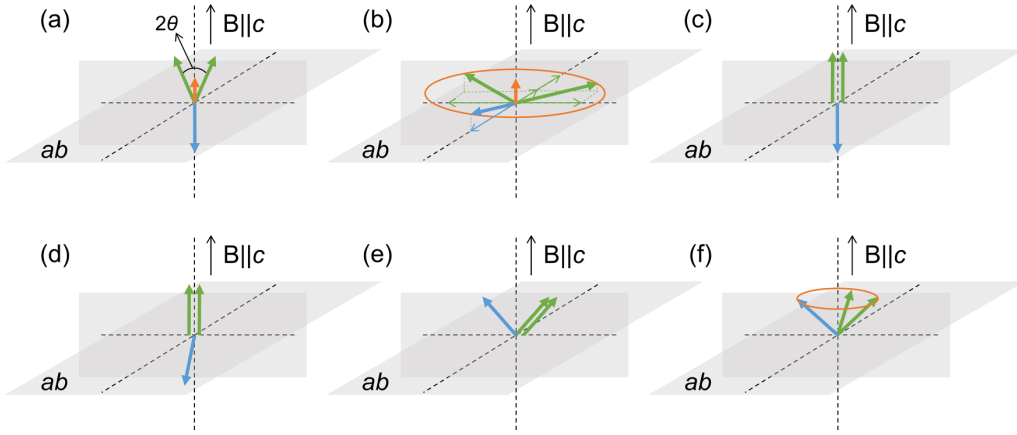


FIG. 8. Schematic diagram of possible spin configurations in  $\text{GdInO}_3$  in different magnetic fields. The green and blue arrows indicate the spin directions at the Gd1 and Gd2 positions, respectively, which correspond to the Gd atom positions in Fig. 2. The orange arrows indicate the net magnetic moment along the  $c$  axis. The angle between the upward spins in panel (a) is denoted by  $2\theta$ .

distortions of the abovementioned configurations. From Fig. 4(c) we conclude that this rotation appears in two steps at  $\simeq 1.7$  K and  $\simeq 1$  K, respectively. Small external magnetic field  $B\parallel c$  yields a ferromagnetic-like hysteresis [see Fig. 5(a)] with the  $c$  axis being the magnetic easy axis of the net moment.

(ii) Applying intermediate fields  $B\parallel c$  yields the formation of a collinear  $uud$  configuration [Fig. 8(c)], i.e., the plateau phase. At 0.4 K, the plateau region is centered at 2.9 T and extends from 1.9–4.2 T [Fig. 5(a)]. Our finding of a smeared-out and not completely flat plateau only for  $B\parallel c$  does not support the scenario of a classical Heisenberg triangular-lattice antiferromagnet (TLAF) with easy-axis anisotropy [48] as discussed, e.g., for  $\text{Na}_2\text{BaCo}(\text{PO}_4)_2$  [49],  $\text{Rb}_4\text{Mn}(\text{MoO}_4)_3$  [50],  $\text{GdPd}_2\text{Al}_3$  [51],  $\text{Ba}_3\text{MnNb}_2\text{O}_9$  [18], and  $\text{Ba}_3\text{NiSb}_2\text{O}_9$  [52]. The center and edges of the plateau phase do not strongly change upon heating. However, the plateau significantly blurs and no clear signature of  $B_{c1}^\Delta$  can be identified above  $\simeq 1.5$  K.

(iii) Above  $B_{c1}^\nabla$ , the linear increase in  $M$  implies breaking of the  $uud$  configuration and the continuous alignment of spins towards the field [Fig. 8(d)]. A similar behavior is predicted in Ref. [48]; in agreement with these numerical studies, phase AF I' is found to be destabilized in external fields  $B\parallel c$ .

(iv) In contrast to the predictions of the minimal TAF model [48], we observe an additional discontinuity at  $B_{c2}$  associated with a jump-like increase of magnetization. The jump is from about 4.1 to nearly  $4.2 \mu_B/\text{f.u.}$ , i.e., it starts at about 3/5 of the full saturation magnetization. In this magnetization regime, there are several possible scenarios which may account for such behavior. One of which includes discontinuous rotation of the  $uu$  moments from the easy direction towards a coplanar V-shaped structure which may evolve from the  $uud$  phase by decreasing the angle  $\angle(uu, d)$  as sketched in Fig. 8(e). However, our data do not allow to unambiguously resolve the spin configurations in this field range.

(v) For  $B\parallel ab$ , no plateau phase is formed. Instead, we observe a small kink and a jump in  $\partial M/\partial B$ , at  $B_{a1}$  and  $B_{a2}$  [see Fig. 5(b)]. Note that the magnetization at  $B_{a1}$  and  $B_{a2}$  amounts to  $2.79(5) \mu_B/\text{f.u.}$  and  $3.45(5) \mu_B/\text{f.u.}$ , respectively, which is

very similar to 2/5 and 1/2 of the saturation values. Due to the presence of several rotated spin arrangements (rotations at  $\simeq 1.7$  K and  $\simeq 1$  K), only rough speculations on the field effects are possible. The behavior of  $M(B\parallel ab)$  around  $B = 0$  T, however, shows that the net magnetic moment is rather smoothly aligned into the  $ab$  plane. The origin of the further distinct phases in the magnetic phase diagram Fig. 7(b) remains to be clarified.

In TLAFs with classical spins, both easy-axis anisotropy and easy-plane anisotropy can stabilize the  $uud$  phase at finite temperatures (see, e.g., Refs. [18,53]). The presence of the 1/3 plateau in  $\text{GdInO}_3$  implies that such easy-axis and easy-plane anisotropy, which lift geometric frustration, are relevant for driving the system into the  $uud$  configuration. Comparing the temperature evolution of the  $uud$  phase for  $B\parallel c$  with numerical studies [48] suggests that  $\text{GdInO}_3$  has a weak easy-axis anisotropy. This conclusion is corroborated by the absence of the 1/3 magnetization plateau for  $B\parallel ab$ . It is also in-line with model calculations of the magnetization of  $\text{GdInO}_3$  in Ref. [16] where weak easy-axis anisotropy  $D > 0$  and  $J_1 \geq J_2$  are suggested.

Anisotropy can arise from dipolar interactions between the  $\text{Gd}^{3+}$  moments within the filled honeycomb layer. Dipole-dipole interaction can be described by the following Hamiltonian [54]:

$$\mathcal{H}_{\text{dip}} = g^2 \mu_B^2 \sum_{i < j} [\mathbf{S}_i \mathbf{S}_j / r_{ij}^3 - 3(\mathbf{S}_i \mathbf{r}_{ij})(\mathbf{S}_j \mathbf{r}_{ji}) / r_{ij}^5], \quad (3)$$

with  $\mathbf{r}_{ij}$  being the vector between interacting paramagnetic centers and  $r_{ij}$  the distance between them, such that the dipolar anisotropy  $D_{\text{dip}}$  can be estimated as  $D_{\text{dip}} = E_{\text{dip}}/S^2 = \mu_B^2 p_{\text{eff}}^2 \mu_0 / 4\pi r^3 S^2$ . The resulting dipole-dipole energy amounts to  $E_{\text{dip}} = \mu_B^2 p_{\text{eff}}^2 \mu_0 / 4\pi r^3 = 0.78(2)$  K, with the weighted average  $r_{\text{ave}} = (2r_1 + r_2)/3 = 3.6753(5)$  calculated from the distances  $r_1 = 3.6813(5)$  and  $r_2 = 3.6633(5)$  from our structure refinement. This energy roughly corresponds to  $T^*$  and  $T^{**}$  where reorientation processes are observed. Similar anisotropy energies for  $\text{Gd}^{3+}$  systems were reported

in the literature for  $(Y_{1-x}Gd_x)_2Ti_2O_7$  [55] and  $Gd_2Ti_2O_7$  [56]. However, exchange interaction may be also relevant in this system, and its relevance in  $GdInO_3$  and in particular for the presence of the presumably anisotropy-related 3/5 discontinuity should be investigated by numerical studies.

#### IV. SUMMARY

By means of single crystals grown by the high-pressure optical floating-zone method, the magnetization process down to the mK regime and the magnetic phase diagrams of  $GdInO_3$  have been investigated. The system evolves long-range antiferromagnetic order at  $T_N = 2.1$  K and exhibits considerable magnetic frustration ( $|\Theta|/T_N \simeq 5$ ). The ground state features a small net magnetic moment along the crystallographic  $c$  direction which reorients upon cooling at  $T^{**} \simeq 1.7$  K and  $T^* \simeq 1$  K. A broad 1/3 plateau indicative of the  $uud$  spin configuration appears for  $B||c$  but is absent for  $B||ab$ , thereby suggesting easy-axis anisotropy. In this respect  $GdInO_3$  is a typical triangular-lattice material in which weak easy-axis

anisotropy of presumably dipolar nature breaks  $C_3$  symmetry and allows formation of the  $uud$  phase. In addition, a jump in magnetization at low temperatures signals a discontinuous transition to a high-field phase. There is evidence that the transition evolves a continuous nature upon heating via a possible tricritical point. Small energy and field scales in the accessible regimes render  $GdInO_3$  a well-suited example to study the phase diagram of a semiclassical frustrated hexagonal lattice in the presence of weak easy-axis anisotropy, e.g., by future neutron diffraction studies, to verify the actual spin configurations in the various thermodynamic phases.

#### ACKNOWLEDGMENTS

Support by Deutsche Forschungsgemeinschaft (DFG) under Germany's Excellence Strategy EXC2181/1-390900948 (The Heidelberg STRUCTURES Excellence Cluster) and through Project No. KL 1824/13-1 is gratefully acknowledged. N.Y. acknowledges support from a fellowship by the Chinese Scholarship Council (File No. 201906890005).

- 
- [1] A. Mercy, J. Bieder, J. Íñiguez, and P. Ghosez, *Nat. Commun.* **8**, 1677 (2017).
- [2] R. D. Sánchez, M. T. Causa, A. Caneiro, A. Butera, M. Vallet-Regi, M. J. Sayagués, J. González-Calbet, F. Garcia-Sanz, and J. Rivas, *Phys. Rev. B* **54**, 16574 (1996).
- [3] A. Ramirez, *J. Phys.: Condens. Matter* **9**, 8171 (1997).
- [4] M. Uehara, S. Mori, C. Chen, and S.-W. Cheong, *Nature (London)* **399**, 560 (1999).
- [5] C. N. R. Rao, A. Arulraj, P. N. Santosh, and A. K. Cheetham, *Chem. Mater.* **10**, 2714 (1998).
- [6] S. Uhlenbruck, R. Teipen, R. Klingeler, B. Büchner, O. Friedt, M. Hücker, H. Kierspel, T. Niemöller, L. Pinsard, A. Revcolevschi *et al.*, *Phys. Rev. Lett.* **82**, 185 (1999).
- [7] T. Choi, Y. Horibe, H. Yi, Y. J. Choi, W. Wu, and S.-W. Cheong, *Nat. Mater.* **9**, 253 (2010).
- [8] B. B. Van Aken, T. T. Palstra, A. Filippetti, and N. A. Spaldin, *Nat. Mater.* **3**, 164 (2004).
- [9] E. E. Gordon, X. Cheng, J. Kim, S.-W. Cheong, S. Deng, and M.-H. Whangbo, *Inorg. Chem.* **57**, 9260 (2018).
- [10] Y. Yu, N. Lin, H. Wang, R. Xu, H. Ren, and X. Zhao, *RSC Adv.* **10**, 4080 (2020).
- [11] B. Paul, S. Chatterjee, A. Roy, A. Midya, P. Mandal, V. Grover, and A. K. Tyagi, *Phys. Rev. B* **95**, 054103 (2017).
- [12] Y. Li, Y. Wang, W. Tan, W. Wang, J. Zhang, J. W. Kim, S.-W. Cheong, and X. Tao, *J. Mater. Chem. C* **6**, 7024 (2018).
- [13] L. Clark, G. Sala, D. D. Maharaj, M. B. Stone, K. S. Knight, M. T. Telling, X. Wang, X. Xu, J. Kim, Y. Li *et al.*, *Nat. Phys.* **15**, 262 (2019).
- [14] J. Kim, X. Wang, F.-T. Huang, Y. Wang, X. Fang, X. Luo, Y. Li, M. Wu, S. Mori, D. Kwok *et al.*, *Phys. Rev. X* **9**, 031005 (2019).
- [15] M. G. Kim, B. Winn, S. Chi, A. T. Savici, J. A. Rodriguez-Rivera, W. C. Chen, X. Xu, Y. Li, J. W. Kim, S. W. Cheong, and V. Kiryukhin, *Phys. Rev. B* **100**, 024405 (2019).
- [16] X. Yin, Y. Li, G. Wang, J. Hu, C. Xu, Q. Lu, Y. Zhong, J. Zhao, X. Zhao, Y. Zhang *et al.*, *Phys. Rev. B* **104**, 134432 (2021).
- [17] L. Seabra, T. Momoi, P. Sindzingre, and N. Shannon, *Phys. Rev. B* **84**, 214418 (2011).
- [18] M. Lee, E. S. Choi, X. Huang, J. Ma, C. R. Dela Cruz, M. Matsuda, W. Tian, Z. L. Dun, S. Dong, and H. D. Zhou, *Phys. Rev. B* **90**, 224402 (2014).
- [19] T. Susuki, N. Kurita, T. Tanaka, H. Nojiri, A. Matsuo, K. Kindo, and H. Tanaka, *Phys. Rev. Lett.* **110**, 267201 (2013).
- [20] L. E. Svistov, A. I. Smirnov, L. A. Prozorova, O. A. Petrenko, A. Micheler, N. Büttgen, A. Y. Shapiro, and L. N. Demianets, *Phys. Rev. B* **74**, 024412 (2006).
- [21] J. Rodríguez-Carvajal, *An Introduction to the Program FULLPROF 2000* (Laboratoire Leon Brillouin, CEA-CNRS, Saclay, France, 2001).
- [22] N. Wizen, G. Behr, F. Lipps, I. Hellmann, R. Klingeler, V. Kataev, W. Löser, N. Sato, and B. Büchner, *J. Cryst. Growth* **311**, 1273 (2009).
- [23] C. Neef, H. Wadepohl, H.-P. Meyer, and R. Klingeler, *J. Cryst. Growth* **462**, 50 (2017).
- [24] See Supplemental Material at <http://link.aps.org/supplemental/10.1103/PhysRevB.108.224403> for further information on the grown crystal and additional magnetization data.
- [25] W. Herggett, C. Neef, H. Wadepohl, H.-P. Meyer, M. M. Abdel-Hafiez, C. Ritter, E. Thauer, and R. Klingeler, *J. Cryst. Growth* **515**, 37 (2019).
- [26] W. Herggett, C. Neef, H.-P. Meyer, and R. Klingeler, *J. Cryst. Growth* **556**, 125995 (2021).
- [27] K. Momma and F. Izumi, *J. Appl. Crystallogr.* **44**, 1272 (2011).
- [28] C. D. Cao, R. Klingeler, H. Vinzelberg, N. Leps, W. Löser, G. Behr, F. Muranyi, V. Kataev, and B. Büchner, *Phys. Rev. B* **82**, 134446 (2010).
- [29] S. Chakraborty, S. Gupta, S. Pakhira, R. Choudhary, A. Biswas, Y. Mudryk, V. K. Pecharsky, D. D. Johnson, and C. Mazumdar, *Phys. Rev. B* **106**, 224427 (2022).
- [30] R. Ohlendorf, S. Spachmann, L. Fischer, K. Dey, D. Brunt, G. Balakrishnan, O. A. Petrenko, and R. Klingeler, *Phys. Rev. B* **103**, 104424 (2021).

- [31] Equal-moment systems are magnetic structures of equal-size moments such as Neel-type, helical, or cycloidal antiferromagnets.
- [32] A. H. Morrish, *The Physical Principles of Magnetism* (IEEE, Piscataway, NJ, 2001).
- [33] J. A. Blanco, D. Gignoux, and D. Schmitt, *Phys. Rev. B* **43**, 13145 (1991).
- [34] In Ref. [16] a more extended background fit with additional fitting parameters has been applied which yields similar yet slightly smaller entropy changes.
- [35] D. C. Johnston, *Phys. Rev. B* **91**, 064427 (2015).
- [36] D. C. Johnston, *J. Magn. Magn. Mater.* **535**, 168062 (2021).
- [37] S. Manni, S. L. Bud'ko, and P. C. Canfield, *Phys. Rev. B* **96**, 054435 (2017).
- [38] T. Kong, W. R. Meier, Q. Lin, S. M. Saunders, S. L. Bud'ko, R. Flint, and P. C. Canfield, *Phys. Rev. B* **94**, 144434 (2016).
- [39] E. Mun, S. Bud'ko, H. Ko, G. Miller, and P. Canfield, *J. Magn. Magn. Mater.* **322**, 3527 (2010).
- [40] H. Hidaka, K. Mizuuchi, E. Hayasaka, T. Yanagisawa, J. Ohara, and H. Amitsuka, *Phys. Rev. B* **102**, 174408 (2020).
- [41] Note that applying the same method at 1.8 K where the saturation field has been determined experimentally (see Fig. 3), i.e., extrapolating the linear regime at 1.8 K, yields a value of  $B_s$  which agrees well with the saturation field derived from the actual measurements up to 14 T at this temperature.
- [42] T. H. K. Barron and G. K. White, *Heat Capacity and Thermal Expansion at Low Temperatures*, The International Cryogenic Monograph Series (Kluwer Academic/Plenum, New York, 1999).
- [43] Extrapolating the experimental data  $M(B \leq 7\text{T})$  to higher fields as done for  $B\parallel c$  in order to estimate  $B_s$  only yields ambiguous results due to pronounced bending of  $M(B)$  in this regime. We, hence, do not apply this method for  $B\parallel ab$ .
- [44] T. Ono, H. Tanaka, H. Aruga Katori, F. Ishikawa, H. Mitamura, and T. Goto, *Phys. Rev. B* **67**, 104431 (2003).
- [45] O. A. Starykh, *Rep. Prog. Phys.* **78**, 052502 (2015).
- [46] C. Griset, S. Head, J. Alicea, and O. A. Starykh, *Phys. Rev. B* **84**, 245108 (2011).
- [47] For a sketch illustrating the calculation of the relevant angles, see Fig. S9 in the SM [24].
- [48] S. Miyashita, *J. Phys. Soc. Jpn.* **55**, 3605 (1986).
- [49] N. Li, Q. Huang, X. Yue, W. Chu, Q. Chen, E. Choi, X. Zhao, H. Zhou, and X. Sun, *Nat. Commun.* **11**, 4216 (2020).
- [50] R. Ishii, S. Tanaka, K. Onuma, Y. Nambu, M. Tokunaga, T. Sakakibara, N. Kawashima, Y. Maeno, C. Broholm, D. P. Gautreaux *et al.*, *Europhys. Lett.* **94**, 17001 (2011).
- [51] H. Kitazawa, H. Suzuki, H. Abe, J. Tang, and G. Kido, *Phys. B: Condens. Matter* **259-261**, 890 (1999).
- [52] Y. Shirata, H. Tanaka, T. Ono, A. Matsuo, K. Kindo, and H. Nakano, *J. Phys. Soc. Jpn.* **80**, 093702 (2011).
- [53] M. Lee, J. Hwang, E. S. Choi, J. Ma, C. R. Dela Cruz, M. Zhu, X. Ke, Z. L. Dun, and H. D. Zhou, *Phys. Rev. B* **89**, 104420 (2014).
- [54] A. Bencini and D. Gatteschi, *EPR of Exchange Coupled Systems* (Dover, Mineola, NY, 2012).
- [55] V. N. Glazkov, M. E. Zhitomirsky, A. I. Smirnov, H.-A. Krug von Nidda, A. Loidl, C. Marin, and J.-P. Sanchez, *Phys. Rev. B* **72**, 020409(R) (2005).
- [56] N. P. Raju, M. Dion, M. J. P. Gingras, T. E. Mason, and J. E. Greedan, *Phys. Rev. B* **59**, 14489 (1999).

## 1/3 plateau and 3/5 discontinuity in the magnetization and the magnetic phase diagram of hexagonal GdInO<sub>3</sub>

N. Yuan,<sup>1</sup> A. Elghandour,<sup>1</sup> W. Hergett,<sup>1</sup> R. Ohlendorf,<sup>1</sup> L. Gries,<sup>1</sup> and R. Klingeler<sup>1</sup>

<sup>1</sup>*Kirchhoff Institute of Physics, Heidelberg University,  
INF 227, D-69120 Heidelberg, Germany*

(Dated: January 9, 2024)

PACS numbers:

The Supplemental Material contains further information on the grown crystal, magnetization and specific heat data.

### I. STRUCTURE, VOLATILES, CRYSTAL ORIENTATION

TABLE I: Refined structural parameters for GdInO<sub>3</sub> ( $P6_3cm$ ) at room temperature. The refinement is performed based on the crystallographic information file COD No.7237332 [1, 2]

Atoms	Wyckoff position	$x$	$y$	$z$	Lattice Parameters(Å)	Reliability factors
Gd1	4b	0.33330	0.66670	0.03758	$a=6.3451(3)$	$R_p = 12.0 \%$
Gd2	2a	0.00000	0.00000	0.00810	$b=6.3451(3)$	$R_{wp} = 11.3 \%$
In1	6c	0.34237	0.66670	0.27392	$c=12.3408(9)$	$R_{exp} = 7.75 \%$
O1	6c	0.33245	0.00000	0.09612		$\chi^2 = 2.14$
O2	6c	0.39103	0.00000	0.43994		
O3	4b	0.66670	0.33330	0.27509		
O4	2a	0.00000	0.00000	0.30966		

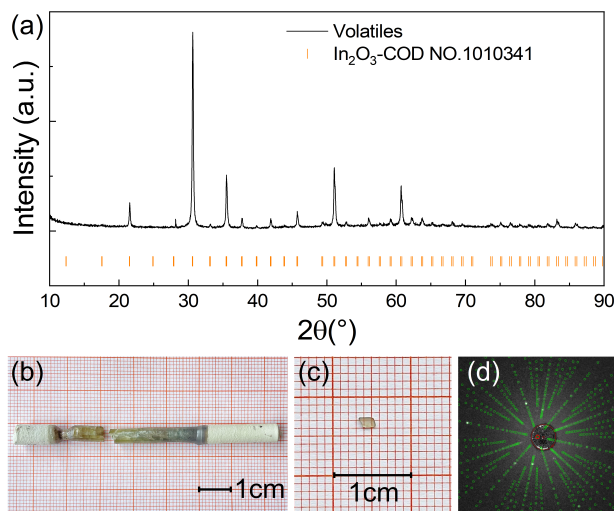


FIG. 1: (a) Powder XRD pattern of volatiles deposited on the growth chamber (see main manuscript text). Pictures of (b) the obtained GdInO<sub>3</sub> boule and (c) the oriented and cut sample used for magnetization and specific heat measurements. (d) Laue pattern of the GdInO<sub>3</sub> single crystal oriented along the (001) direction.



## II. MAGNETISATION

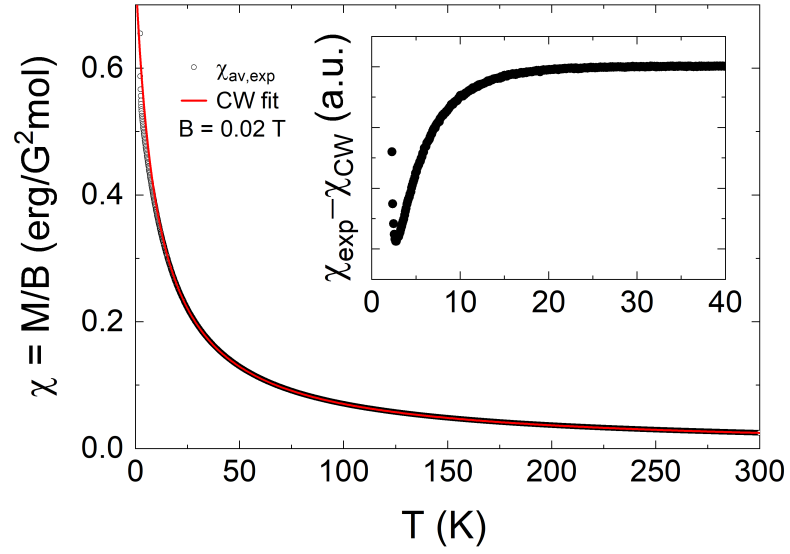


FIG. 2: Temperature dependence of the averaged static magnetic susceptibility  $\chi_{\text{av}} = (\chi_c + 2\chi_{ab})/3$  obtained at  $B = 0.02$  T and Curie-Weiss fit. Inset: Difference between the experimental data and the fit.

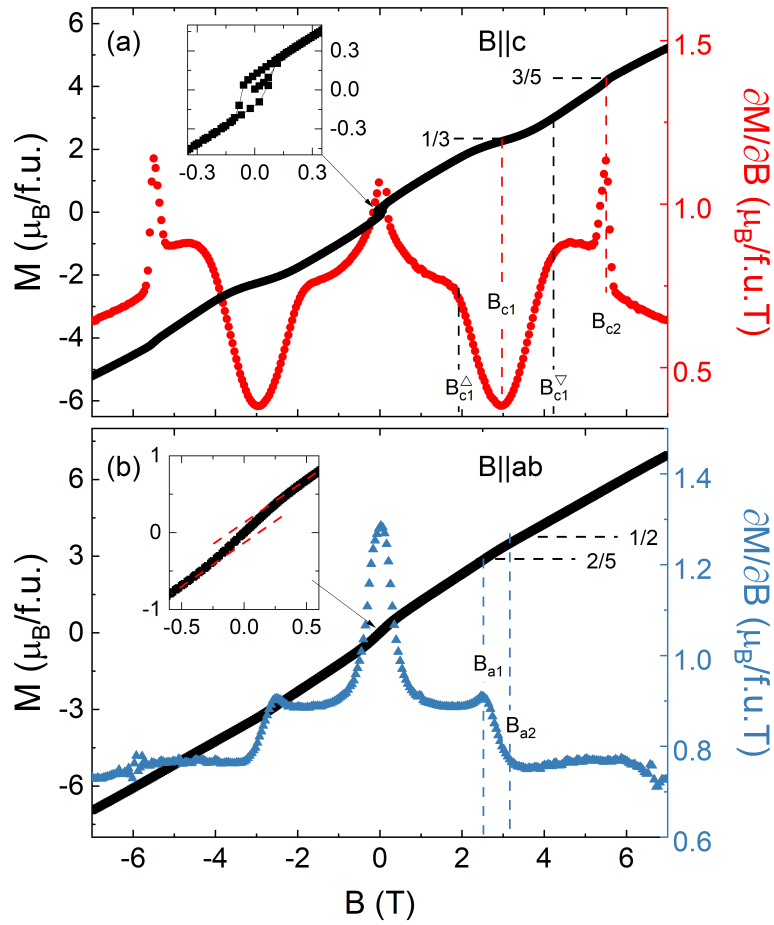


FIG. 3: Isothermal magnetization at  $T = 0.4$  K for (a)  $B||c$  axis and (b)  $B||ab$  plane. In addition, the corresponding magnetic susceptibilities  $\partial M/\partial B$  are shown (right ordinates). Insets highlight the behaviour around zero field. Horizontal dashed lines mark fractional values of the magnetization and vertical lines show the anomaly fields as described in the text of the main manuscript.

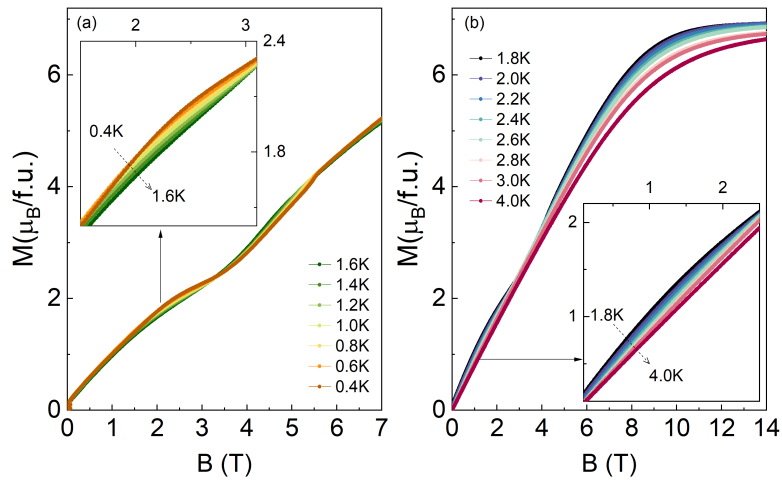


FIG. 4: Isothermal magnetization for  $B||c$  axis at (a) 0.4 K-1.6 K (0-7 T) and (b) 1.8 K-4.0 K (0-14 T).

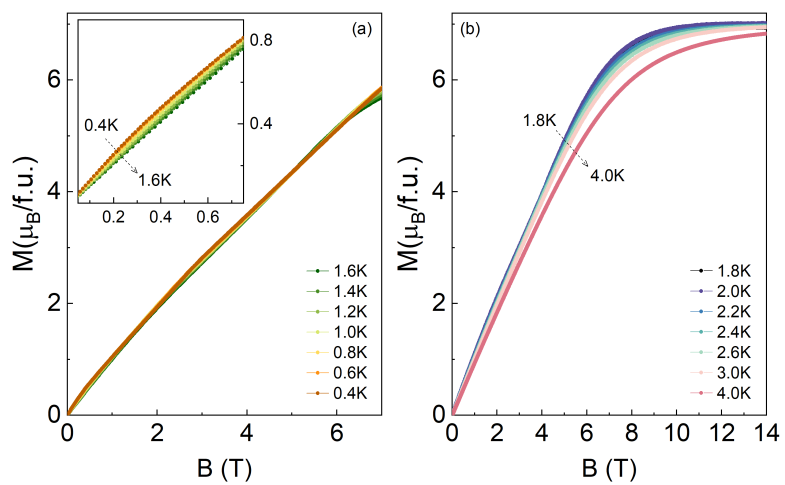


FIG. 5: Isothermal magnetization for  $B||ab$  axis at (a) 0.4 K-1.6 K (0-7 T) and (b) 1.8 K-4.0 K (0-14 T).

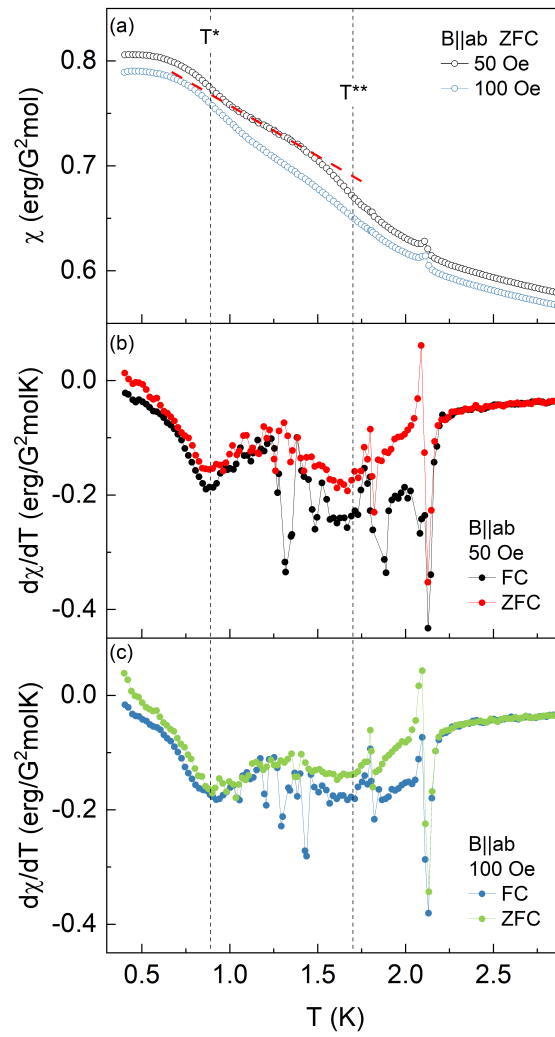


FIG. 6: (a) ZFC Magnetic susceptibility at 50 Oe and 100 Oe. (b) The derivative of magnetization for  $B||ab$  at 50 Oe. (c) The derivative of magnetization for  $B||ab$  at 100 Oe. The black dashed lines label the positions of  $T^*$  and  $T^{**}$  noted in the main text, and the red dashed lines mark the region between  $T^*$  and  $T^{**}$  where the susceptibility linearly varies with temperature.

### III. SPECIFIC HEAT AND PHONON BACKGROUND DETERMINATION AND SKETCHES OF THE SPIN CONFIGURATION

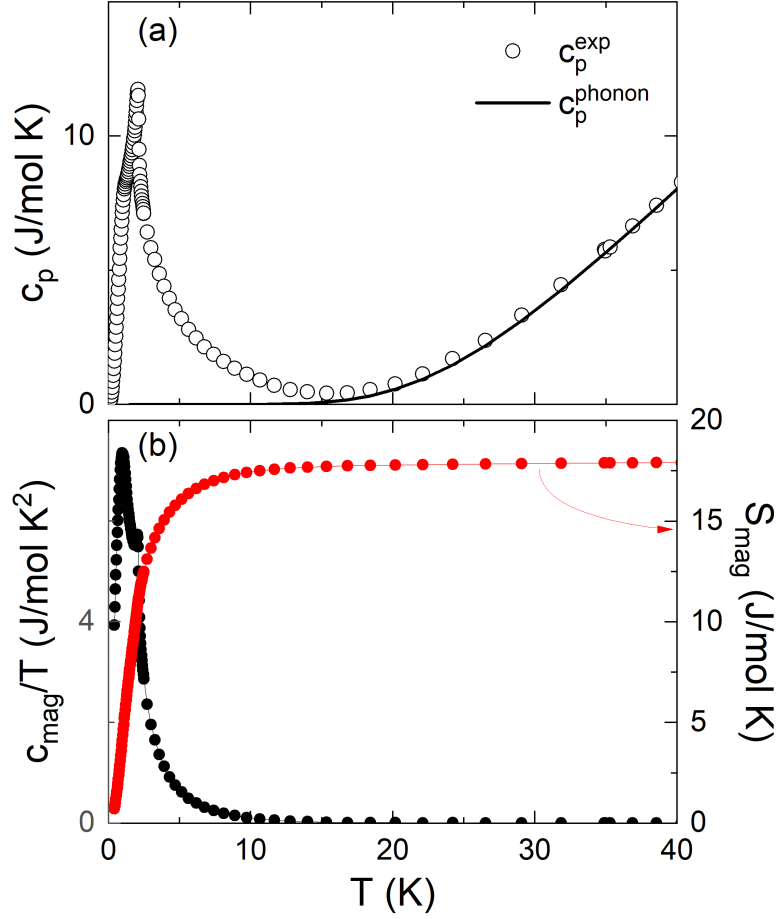


FIG. 7: Temperature dependence of specific heat of  $\text{GdInO}_3$  single crystal sample measured at  $B = 0$  T. The black line represents a phonon fit to the data based on one Debye and one Einstein mode according to Eq. 1. (b) Temperature dependence of  $c_{\text{mag}}/T$  as derived from subtracting the phonon specific heat from the experimental data and the calculated magnetic entropy  $S_{\text{mag}}$  (right ordinate).

The background specific heat capacity was fitted by phononic Debye and Einstein terms, as well as an electronic term, according to [3]:

$$c_p^{\text{ph}} = n_D D\left(\frac{T}{\Theta_D}\right) + n_E E\left(\frac{T}{\Theta_E}\right) \quad (1)$$

where  $n_D$  and  $n_E$  are constants,  $D(T/\Theta_D)$  and  $E(T/\Theta_E)$  are the Debye and Einstein functions with the Debye and Einstein temperatures  $\Theta_D$  and  $\Theta_E$ .

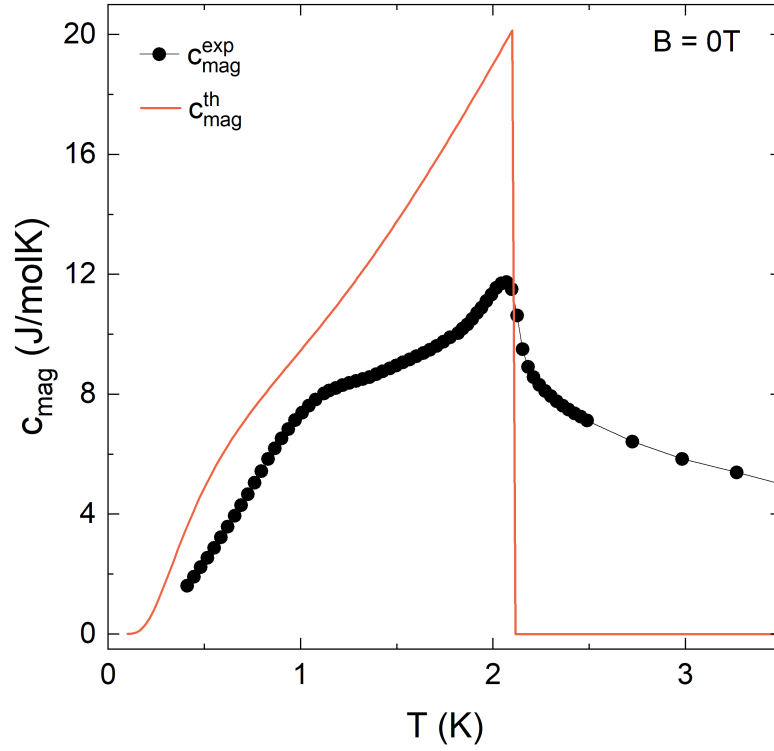


FIG. 8: Temperature dependence of the magnetic specific heat capacity  $c_{mag}$ . The solid red line represents the prediction of mean field theory [4–6] in Eq.2-Eq.7 for  $S = 7/2$  and  $T_N = 2.1$  K.

The mean field theory prediction of  $C_{mag}(T)$  is given by [4–6]:

$$\frac{C_{mag}(t)}{R} = \frac{3S\bar{\mu}_0^2(t)}{(S+1)t \left[ \frac{(S+1)t}{3B_S'(y_0(t))} - 1 \right]} \quad (2)$$

$$y_0(t) = \frac{3\bar{\mu}_0(t)}{(S+1)t} \quad (3)$$

$$B_S(y) = \frac{1}{2S} \left\{ (2S+1) \coth\left[(2S+1)\frac{y}{2}\right] - \coth\left(\frac{y}{2}\right) \right\} \quad (4)$$

$$B_S'(y_0) = \left[ \frac{dB_S(y)}{dy} \right]_{y=y_0} \quad (5)$$

$$t = \frac{T}{T_N} (B = 0) \quad (6)$$

where  $R$  is the gas constant,  $B_S(y)$  is the Brillouin function,  $\bar{\mu}_0(t)$  is the reduced ordered moment versus  $t$  in  $B = 0$ , which is determined by numerically solving the self-consistency equation:

$$\bar{\mu}_0(t) = B_S[y_0(t)] \quad (7)$$

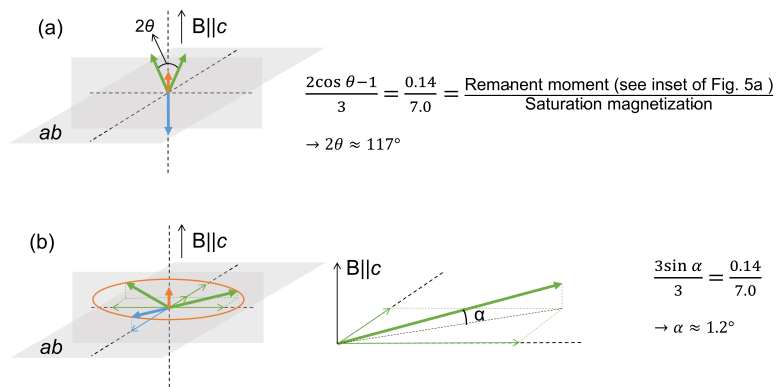


FIG. 9: Schematic calculation of the relevant angles in the main text Fig.8.

- 
- [1] Y. Li, Y. Wang, W. Tan, W. Wang, J. Zhang, J. W. Kim, S.-W. Cheong, and X. Tao, *Journal of Materials Chemistry C* **6**, 7024 (2018).  
[2] K. Momma and F. Izumi, *Journal of applied crystallography* **44**, 1272 (2011).  
[3] C. Kittel and P. McEuen, *Introduction to solid state physics* (John Wiley & Sons, 2018).  
[4] J. Blanco, D. Gignoux, and D. Schmitt, *Physical Review B* **43**, 13145 (1991).  
[5] D. C. Johnston, *Physical Review B* **91**, 064427 (2015).  
[6] D. C. Johnston, *Journal of Magnetism and Magnetic Materials* **535**, 168062 (2021).

## 3.2 TbInO<sub>3</sub>

### 3.2.1 Crystal Growth and Structural Characterization of TbInO<sub>3</sub>

Spin liquid, as a very special state in condensed matter physics, with potential applications in quantum computing [97], has attracted much attention from researchers in the recent years. Spin liquid is characterized by the lack of long-range order, highly entangled quantum states, etc [97, 98]. Experimentally, the properties of spin liquid states are usually revealed by neutron scattering [99], electron spin resonance (ESR) spectroscopy [13], and a combined consideration of anomalies in magnetism, specific heat, and thermal conductivity, etc. Representative materials include YbMgGaO<sub>4</sub> [13, 100], ZnCu<sub>3</sub>(OH)<sub>6</sub>Cl<sub>2</sub> [101], and  $\alpha$ -RuCl<sub>3</sub> [99, 102], etc. These studies have pointed out Kagome and triangular lattice structures as important platforms of searching for spin liquid, where special geometrical restraints between neighboring spins avoid the formation of conventionally ordered magnetic states. Complex spin arrangement also lead to complicated interactions between neighboring spins, resulting in a large number of locally entangled states in the system, all of which are factors favorable for the emergence of spin liquid. Therefore, TbInO<sub>3</sub> with the triangular lattice structure is of interest to researchers, and reports on its magnetic, electrical, and possibly spin liquid properties have appeared [36, 37, 103–106].

The magnetic atom Tb has two inequivalent sites in this structure, which is caused by the tilting of the InO<sub>5</sub> bipyramid centered on In<sup>3+</sup> [37]. Tb<sup>3+</sup> shows an undulating up-and-down arrangement in the *ab* plane and a honeycomb structure in the *c* axis. The crystal structure from the viewpoints of the *a* and *c* axis are depicted in Fig. 3.1 (a) and (b), respectively. Polycrystalline TbInO<sub>3</sub> was synthesized using a standard SSR method. Single crystal TbInO<sub>3</sub> was prepared via the high-pressure optical floating zone method (see Chapter 2). TbInO<sub>3</sub> decomposes during growth and loses In<sub>2</sub>O<sub>3</sub> components due to evaporation, resulting in the presence of gas bubbles in the melt zone. Several groups of growth parameters were experimented in this work, including O<sub>2</sub>/Ar pressure ranging from 30-50 bar, growth rates 5-20 mm/h, and gas flow rates 0.1-0.2 l/min. However, maintaining the stability of the melting zone for more than 1 hour was difficult under all these conditions, and the bubble issue was present in almost every growth. Finally, it was experimentally observed that adding excess In<sub>2</sub>O<sub>3</sub> (10% of stoichiometric ratio) to the raw material and growing at a rate of 5 mm/h noticeably decreased the number of bubbles and the frequency of bubble ruptures. Although this solution failed to completely



prevent the appearance of bubbles, it effectively extended the stabilization time of the melting zone. Fig. 3.2(a)-(c) show the grown crystal, the oriented and cut crystal as well as back reflection Laue diffraction pattern obtained along the  $c$  axis.  $\text{In}_2\text{O}_3$  volatiles were collected and confirmed by powder XRD (see Fig. 3.2(d)). The room temperature XRD pattern of polycrystalline  $\text{TbInO}_3$  as well as the rietveld refinement to the data are shown in Fig. 3.3 indicate the purity phase of  $\text{TbInO}_3$ , the refined structural parameters are shown as Table 3.1.

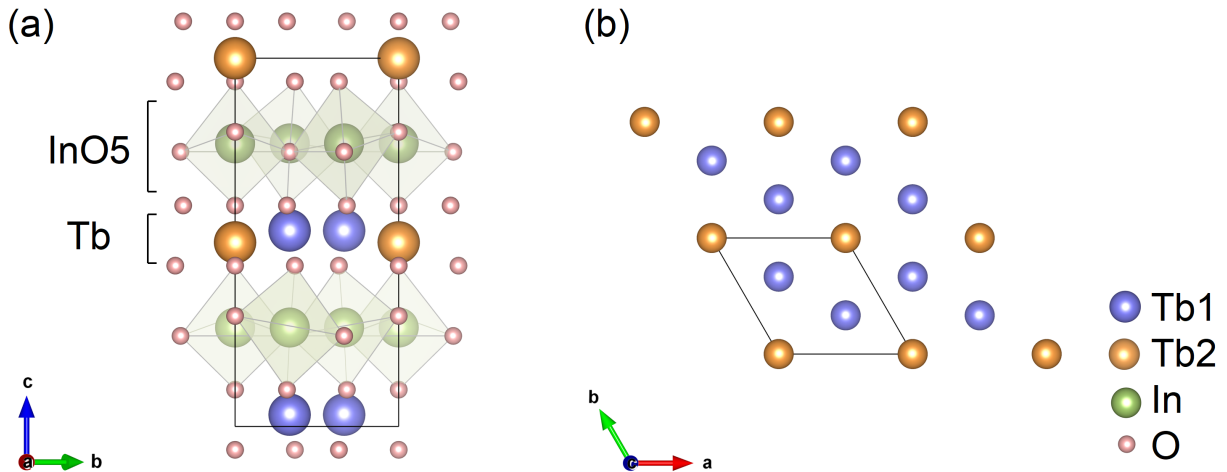


**Figure 3.1:** (a) Schematic of the crystal structure of  $\text{TbInO}_3$  along the  $[100]$  projection. (b) In-plane honeycomb arrangement of two inequivalent atomic sites of  $\text{Tb}^{3+}$  ions. The structure is created based on the crystallographic information file provided by the literature [105] and the image is made using the VESTA software [107].

**Table 3.1:** Selected structural parameters from the Rietveld refinement of the room temperature powder XRD data of  $\text{TbInO}_3$  ( $P6_3cm$ ). The refinement is performed based on the crystallographic information file provided by the literature [105].

Atoms	Wyckoff position	$x$	$y$	$z$	Lattice Parameters( $\text{\AA}$ )	Reliability factors
Tb1	$4b$	0.33330	0.66670	0.03210	$a=6.3186(3)$	$R_p = 12.9 \%$
Tb2	$2a$	0.00000	0.00000	-0.00004	$b=6.3186(3)$	$R_{wp} = 9.58 \%$
In1	$6c$	0.33400	0.00000	0.26873	$c=12.306(1)$	$R_{exp} = 9.16 \%$
O1	$6c$	0.31700	0.00000	0.10010		$\chi^2 = 1.09$
O2	$6c$	0.36540	0.00000	0.43670		
O3	$4b$	0.66670	0.33330	0.24600		
O4	$2a$	0.00000	0.00000	0.30000		

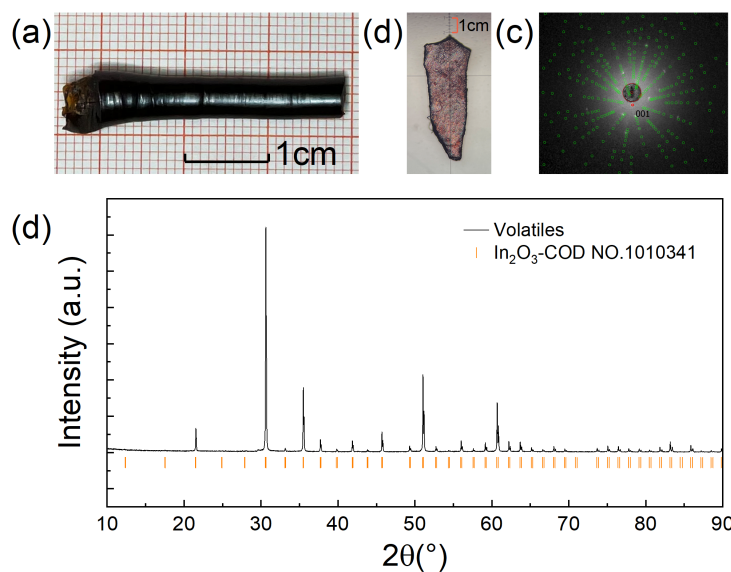


**Figure 3.2:** (a) Picture of the obtained  $\text{TbInO}_3$  boule and (b) the oriented and cut sample used for magnetization measurement. (c) Laue pattern of the  $\text{TbInO}_3$  single crystal oriented along the  $[001]$  direction. (d) Powder XRD pattern of volatiles  $\text{In}_2\text{O}_3$  deposited on the protection tube of growth.

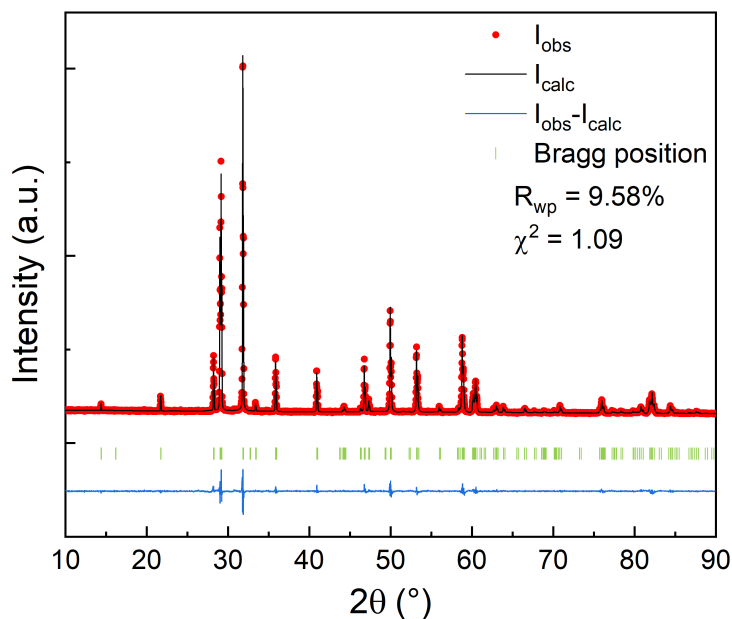


**Figure 3.3:** Room temperature XRD pattern and corresponding Rietveld refinement of polycrystalline  $\text{TbInO}_3$ . The observed diffraction pattern is shown in red, the calculated one in black, and the difference between them is shown in blue. Refinement is based on the hexagonal crystal system (space group  $P6_3cm$ , No. 185) of  $\text{TbInO}_3$  as a main phase. The vertical green bars show the expected Bragg positions. The refinement converged to  $R_p = 12.9\%$ ,  $R_{wp} = 9.58\%$ ,  $\chi^2 = 1.09$ .

---

### 3.2.2 Magnetic Susceptibility of TbInO<sub>3</sub>

Fig. 3.4(a) shows the temperature dependence of magnetic susceptibilities for both polycrystal ( $\chi_{pc}$ ) and single crystal ( $\chi_{ab}$  and  $\chi_c$ ), measured at  $B = 0.2$  T. The latter two distinct curves indicate magnetic anisotropy. The averaged susceptibility  $2/3\chi_{ab} + 1/3\chi_c$  is shown as the green line, which deviates slightly from  $\chi_{pc}$ . For  $B||ab$ , a larger susceptibility than that of the polycrystal is observed, conversely,  $\chi_c$  is significantly lower than  $\chi_{pc}$ . At 300 K, the non-overlapping  $\chi_{ab}$ , and  $\chi_c$  implicates the presence of anisotropy, as reported by L.Clark et al. [36] and J.Kim et al. [37]. Notably, no sign of long-range order is observed in the temperature region of 1.8-300 K. Both the zero field-cool (ZFC) and field-cool (FC) magnetic susceptibility are shown in the inset of Fig. 3.4(a). All ZFC curves are highly coincident with the FC curves, implying that no spin freezing exists for temperatures down to 1.8 K. Additionally, the measured temperature region were extended to 0.1 K (muon spin relaxation measurement) and 0.15 K (specific heat measurement) in the work presented by L.Clark et al. [36] and J.Kim et al. [37], respectively, and no signs of long-range order are observed in either case. The CW fitting were performed on the averaged susceptibility and  $\chi_{pc}$  data in the temperature region 20 K - 300 K, as shown in Fig. 3.4(b). The parameters obtained from the fit are listed in Table 3.2, where the value of the effective moment obtained for the fitted  $\chi_{pc}$  is slightly lower than the theoretical value  $\mu_{\text{eff}}^{\text{theo}} = 9.72 \mu_B$  (Tb<sup>3+</sup>:  $J = 6$ ,  $g = 3/2$ ). This is probably attributed to the addition of extra In<sub>2</sub>O<sub>3</sub> (10% of the stoichiometric ratio) in the synthesize of the polycrystalline samples to overcome the volatilization problem (see section 2.1.4 as well as section 3.2.1). Although extra 10% of In<sub>2</sub>O<sub>3</sub> is gradually lost during the synthesize of the polycrystals, a residual of 5% of In<sub>2</sub>O<sub>3</sub> is expected and this is not sufficient to be distinguished in polycrystalline XRD measurement (Fig. 3.3). Lastly, the difference between the temperature dependence of  $\chi_{ab}$  and  $\chi_c$  is illustrated in Fig. 3.4(c). The anisotropy ratio  $\chi_{ab}/\chi_c$  increases and then decreases upon cooling, reaching its peak value of 4.8, which differs from the reported results of 5.5 [36] and 6 [37] in the literature. The difference may originate from the discrepancy in quality of the single crystal samples but all three data confirm the highly anisotropic nature of the magnetic susceptibility in the measured temperature region. The possible role of anisotropic exchange interactions for TbInO<sub>3</sub> system was discussed in detail by L.Clark et al. [36] based on crystalline electric field analysis.

**Table 3.2:** The Weiss temperature ( $\Theta_W$ ), the effective magnetic moment ( $\mu_{\text{eff}}$ ), and diamagnetic constant background term  $\chi_0$  of  $\text{TbInO}_3$  obtained from the CW law.

	$\Theta_W$ (K)	$\mu_{\text{eff}}$ ( $\mu_B$ )	$\chi_0$ (erg/G <sup>2</sup> mol)
$\chi_{pc}$	-16(1)	9.4(1)	$2.59 \times 10^{-4}$
$2/3\chi_{ab}+1/3\chi_c$	-16(1)	9.9(2)	$5.08 \times 10^{-5}$

### 3.2.3 Summary

This section introduces  $\text{TbInO}_3$  single crystals prepared by the high-pressure floating zone method and its magnetization behavior. The growth instability caused by gas bubbles in the melt zone is effectively reduced by adding excess  $\text{In}_2\text{O}_3$  (10% of stoichiometric ratio) and applying a slower growth rate ( $< 5$  mm/h). The temperature dependence of magnetic susceptibilities for both polycrystal and single crystal clearly demonstrate the magnetic anisotropy. The CW analysis of  $\chi_{pc}$  data yields the effective moment  $\mu_{\text{eff}} = 9.40(5) \mu_B = 96.7\% \mu_{\text{eff}}^{\text{theo}}$ , which is attributed to the excess  $\text{In}_2\text{O}_3$  added in the synthesis of the polycrystalline samples. Also, the CW fitting gives Weiss temperature  $\Theta_W = -16.5(1)$  K, suggesting predominant antiferromagnetic exchange interactions. However, no long-range ordered is observed for temperatures down to 1.8 K. This result is consistent with literature [36, 37] with measured temperatures as low as 0.1 K, which implies that  $\text{TbInO}_3$  has considerable magnetic frustration parameter  $f$ . The anisotropy ratio  $\chi_{ab}/\chi_c$  also illustrates the magnetic anisotropy of  $\text{TbInO}_3$ . Although  $\chi_{ab}/\chi_c$  is slightly lower in value than the previously reported, the maximum value of  $\chi_{ab}/\chi_c$  exists near 13(1) K which is consistent with the literature. In summary,  $\text{TbInO}_3$  could potentially be a candidate material with spin liquid ground states, and high-quality, large-size single crystal samples are necessary for advanced studies.

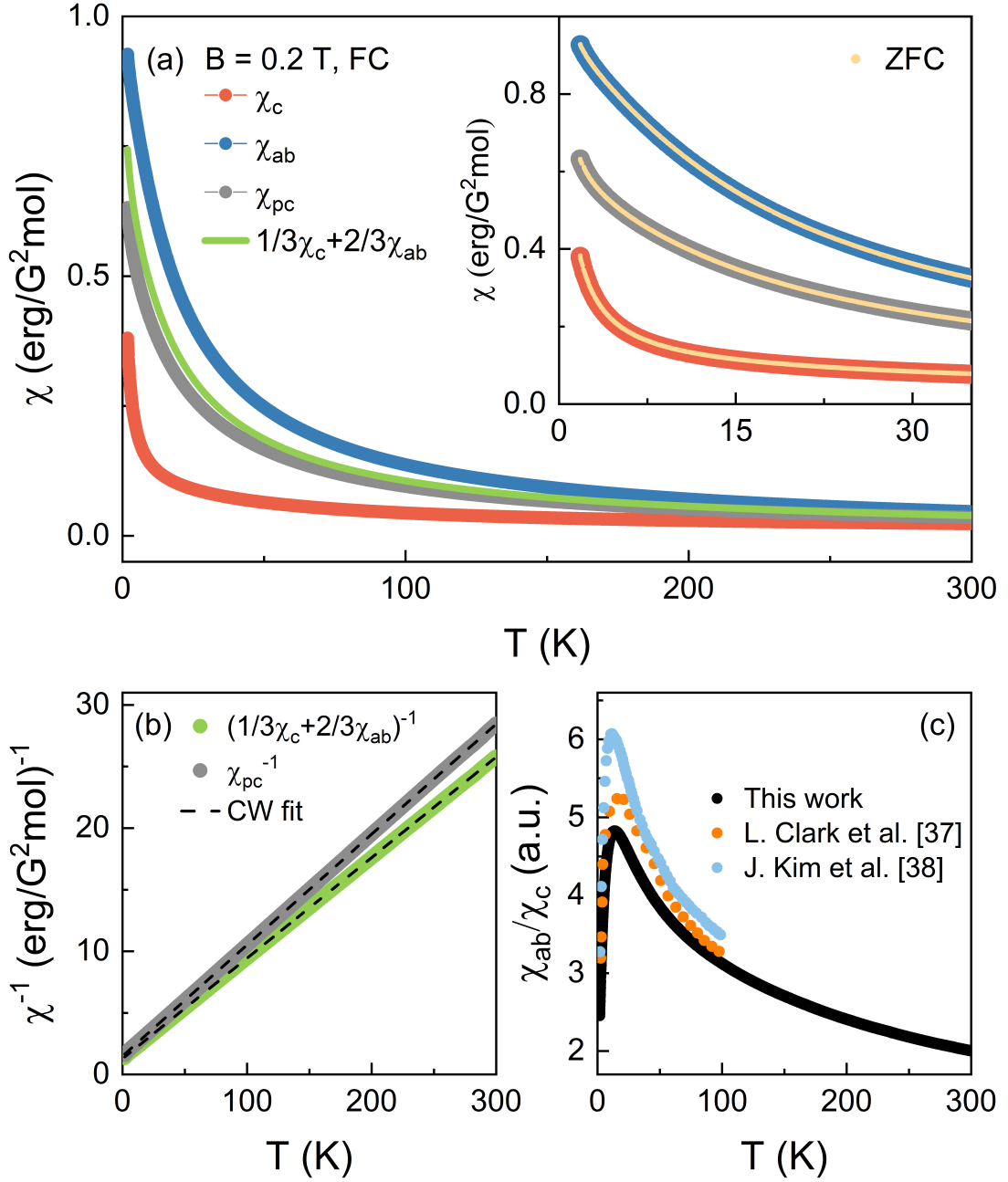


**Figure 3.4:** (a) Field-cooled (FC) magnetic susceptibility of TbInO<sub>3</sub> obtained at  $B = 0.2$  T. The gray, blue, and orange circles indicate data taken by using the polycrystal, the single crystal for  $B||ab$  plane and  $B||c$  axis, respectively. The green line indicates data calculated by  $2/3\chi_{ab} + 1/3\chi_c$ . Inset: The zero field-cooled (ZFC) and FC magnetic susceptibility at low temperatures. (b) Inverse of the  $\chi_{pc}$  (gray circle),  $2/3\chi_{ab} + 1/3\chi_c$  (green circle), and the CW fits (dashed black lines). (c) The temperature dependence of anisotropy ratio  $\chi_{ab}/\chi_c$ . The black, orange and blue circles indicate data obtained in this work, in the literature [36], and [37], respectively.



# 4

## Ruddlesden–Popper Trilayer Nickelates $\text{La}_4\text{Ni}_3\text{O}_{10}$

This chapter presents the single crystal growth and magnetic properties of the Ruddlesden–Popper nickelate  $\text{La}_4\text{Ni}_3\text{O}_{10}$ . This chapter has been published in the Journal of Crystal Growth [108].





---

The following chapter has been published: N. Yuan, A. Elghandour, J. Arneth, K. Dey, and R. Klingeler, “High-pressure crystal growth and investigation of the metal-to-metal transition of Ruddlesden–Popper trilayer nickelates  $\text{La}_4\text{Ni}_3\text{O}_{10}$ ”, *Journal of Crystal Growth*, vol. 627, p. 127–511, 2024 [108]. Copyright ©2024 Elsevier B.V.. All rights reserved. The preparation of the manuscript was completed by the first author **N. Yuan**, specifically:

- Single crystals were prepared by **N. Yuan**, including the orientation and cutting of single crystals.
- The data presented in the paper were measured and analyzed by **N. Yuan**, with the exception of the specific heat data measurements and analyses (Figs. 5-7). All figures and tables were made by **N. Yuan**.
- **A. Elghandour** measured the specific heat and participated in the discussion of these data.
- **K. Dey** contributed to the discussions during the single crystal preparation session and provided guidelines for equipment utilization.
- **J. Arneth** participated in the data discussion.
- **R. Klingeler** was responsible for the project, supervised the measurements, supported the data analysis and finalization of the manuscript.
- The manuscript draft was written by **N. Yuan**. Together with **R. Klingeler**, she revised and finished the manuscript, and communicated with the reviewers.
- All authors proofread the manuscript.





Contents lists available at ScienceDirect

Journal of Crystal Growth

journal homepage: [www.elsevier.com/locate/jcrysgro](http://www.elsevier.com/locate/jcrysgro)

# High-pressure crystal growth and investigation of the metal-to-metal transition of Ruddlesden–Popper trilayer nickelates $\text{La}_4\text{Ni}_3\text{O}_{10}$

Ning Yuan\*, Ahmed Elghandour, Jan Arneth, Kaustav Dey, Rüdiger Klingeler

Kirchhoff Institute of Physics, Heidelberg University, 69120 Heidelberg, Germany

## ARTICLE INFO

Communicated by T. Duffar

### Keywords:

A1. High-pressure optical Floating zone technique  
 A2. Crystal structure  
 A2. Single crystal growth  
 B1. Nickelate  
 B2. Magnetic materials

## ABSTRACT

Single crystals of Ruddlesden–Popper nickelates  $\text{La}_4\text{Ni}_3\text{O}_{10}$  were grown by means of the floating-zone technique at oxygen pressure of 20 bar. Our results reveal the effects of the annealing process under pressure on the crystal structure. We present the requirements for crystal growth and show how a reported ferromagnetic impurity phase can be avoided. The different growth and post-annealing processes result in two distinct phases  $P2_1/a$  and  $Bmab$  in which the metal-to-metal transitions occur at 152 K and 136 K, respectively.

## 1. Introduction

The recent discoveries of superconductivity in infinite-layer nickelates [1–8] have further demonstrated the position of nickelates as model systems to discover and decipher novel aspects of correlated electron physics. It is also the electronic similarity of the  $\text{Ni}^{1+}$  and  $\text{Cu}^{2+}$  electronic configurations which renders nickelates prime analogues to the high- $T_C$  superconducting cuprates and has raised a surge of interest to understand and modify the critical electronic features that determine electronic correlation and in particular superconductivity in nickelates. This has brought the Ruddlesden–Popper phases  $\text{La}_{n+1}\text{Ni}_n\text{O}_{3n+1}$  into the focus in which the valence of the Ni-ions and the electronic ground state can be tuned (see, e.g., [9–13]). Trilayer nickelates as reported at hand exhibit an unusual metal-to-metal transition (MMT) [14–20] with intertwined charge and spin orders developing at  $T_{\text{MM}}$  [21].

The crystal structure of Ruddlesden–Popper nickelates  $\text{R}_4\text{Ni}_3\text{O}_{10}$  is commonly described as an alternating arrangement of perovskite-like layers and rock-salt-like layers [9,22] and is often regarded as quasi-two-dimensional (2D). It exhibits a mixture of  $\text{Ni}^{2+}$  and  $\text{Ni}^{3+}$  ions with an average valence of +2.67 [14]. The space group details at room temperature and ambient pressure are still controversial and the debated four different space groups are discussed specifically in Refs. [17,18,23]. By means of high-resolution synchrotron and laboratory X-ray single-crystal diffraction studies Zhang et al. concluded that the formation of the  $P2_1/a$  (no. 14) and  $Bmab$  (no. 64) structures is closely related to the cooling rate after growth. The preparation of  $\text{La}_4\text{Ni}_3\text{O}_{10}$  compounds, especially of single crystals, is challenging

due to the required synthesis atmosphere of 20–30 bar oxygen pressure [9,18] and the pronounced tendency of phase mixture which is reported to be closely associated with slight variations of the oxygen content [20,24].

In this work, single crystals of  $\text{La}_4\text{Ni}_3\text{O}_{10}$  were successfully grown by the high-pressure optical floating-zone method under 20 bar oxygen pressure. We investigate the different growth and post-annealing processes resulting in two different phases, i.e.  $P2_1/a$  and  $Bmab$ , respectively, and report magnetic susceptibility and specific heat data. Our study shows sharp anomalies and marked anisotropy associated with the reported MMT in  $\text{La}_4\text{Ni}_3\text{O}_{10}$ . Using the here reported growth conditions avoids the formation of a previously reported ferromagnetic impurity phase.

## 2. Materials and experimental methods

Polycrystalline  $\text{La}_4\text{Ni}_3\text{O}_{10}$  was synthesized by a standard solid-state reaction. The raw materials  $\text{La}_2\text{O}_3$  (99.99%, Sigma-Aldrich) and  $\text{NiO}$  (99.998%, Alfa Aesar) powders were calcined at 900 °C and 1000 °C for 24 h to remove absorbed water. Stoichiometric amounts of the ingredients were mixed well in a mortar and calcined at 1050 °C for 24 h (air flow, ambient) with several intermediate grindings. The powder obtained is reground, packed in a rubber tube and isotropically pressed at 60 MPa in order to produce cylindrical rods with a length of 5–6 cm and a diameter of 5 mm as shown in Fig. 1a. The rods

\* Corresponding author.

E-mail address: [ning.yuan@kip.uni-heidelberg.de](mailto:ning.yuan@kip.uni-heidelberg.de) (N. Yuan).

<https://doi.org/10.1016/j.jcrysgro.2023.127511>

Received 10 October 2023; Received in revised form 20 November 2023; Accepted 25 November 2023

Available online 30 November 2023

0022-0248/© 2023 The Authors. Published by Elsevier B.V. This is an open access article under the CC BY-NC-ND license (<http://creativecommons.org/licenses/by-nc-nd/4.0/>).

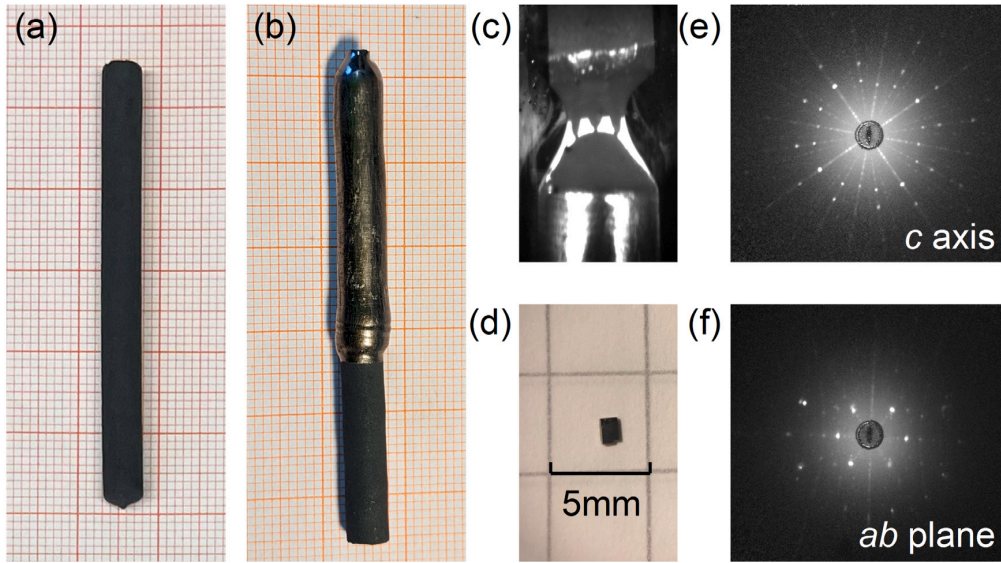


Fig. 1. Pictures of (a)  $\text{La}_4\text{Ni}_3\text{O}_{10}$  cylindrical polycrystalline rods, (b) the obtained  $\text{La}_4\text{Ni}_3\text{O}_{10}$  boule, (c) the melting-zone formed during the growth, and (d) the oriented and cut single crystal used for magnetic and calorimetric measurements. (e,f) Laue patterns of the  $\text{La}_4\text{Ni}_3\text{O}_{10}$  single crystal oriented along  $c$  axis and  $ab$  plane, respectively.

were annealed for 24 h at 1400 °C. It is notable that according to the thermodynamic analysis of the La–Ni–O system [25,26], only  $\text{La}_2\text{NiO}_4$  compounds can be synthesized at ambient pressure, and our experimental results are consistent with it. Single crystals of  $\text{La}_4\text{Ni}_3\text{O}_{10}$  were then successfully grown using the high-pressure optical floating-zone furnace (HKZ, SciDre) [27]. We employed a 5 kw Xenon arc lamp as the heat source, and 20 bar  $\text{O}_2$  atmosphere with an  $\text{O}_2$  flow rate maintained at 0.1 l/min. The volume of the HKZ inner sample chamber is approximately 23 ml. The composition of feed and seed rods are identical, both are polycrystalline  $\text{La}_4\text{Ni}_3\text{O}_{10}$ . To improve the homogeneity of the melting zone, counter-rotation of the feed and seed rods at 10 rpm is necessary. The feed rod was pulled at 6 mm/h and the seed rod was pulled at 4 mm/h to maintain the zone stability. Using an in-situ temperature measurement by means of a two-color pyrometer [28,29], the temperature of the melting zone during growth was determined to about 1650 °C. After the initial growth we performed a rapid cooling of the melting zone to avoid the precipitation of oxygen. In addition to crystals obtained from pristine boules grown as described above and further on labelled ‘S1’, we also applied a post-annealing procedure resulting in crystals labelled ‘S2’. The post-annealing was carried out in the HKZ furnace where the sample is held under the 20 bar oxygen pressure at 950 °C for 2 h, then quenched to room temperature following Ref. [18]. The latter process was achieved by quickly removing the rod out of focus.

The phase purity and crystallinity of the resulting materials were studied by powder X-ray diffraction (XRD) and the back-reflection Laue method. XRD was performed at room temperature by means of a Bruker D8 Advance ECO diffractometer using  $\text{Cu-K}\alpha$  radiation ( $\lambda = 1.5418 \text{ \AA}$ ). Data have been collected in the  $2\theta$  range of 10–90° with 0.02° step-size. Laue diffraction was done on a high-resolution X-ray Laue camera (Photonic Science). Magnetic studies in the temperature regime 1.8–350 K have been performed in a SQUID magnetometer (MPMS3, Quantum Design Inc.) following either field-cooled (FC) or zero-field-cooled (ZFC) protocols where the sample has been cooled down to lowest temperature in the actual measurement field or in zero magnetic field, respectively, before applying the external magnetic field at lowest temperature. Measurements of the specific heat have been performed in a Physical Properties Measurement System (PPMS, Quantum Design Inc.) utilizing a relaxation method.

### 3. Results

#### 3.1. Single crystal growth

$\text{La}_4\text{Ni}_3\text{O}_{10}$  single crystals were successfully grown under 20 bar oxygen pressure (see Fig. 1b for a picture of the as-grown boule). In order to maintain a stable melting zone, the feed rod must be pulled faster than the seed rod; optimized feed and seed rod velocities chosen for the experiment were 6 mm/h and 4 mm/h, respectively. The melting zone formed during the successful growth is shown in Fig. 1c. Using the same velocities for both rods resulted in the depletion of liquid in the melting zone, somehow similar as observed for  $\text{LaNiO}_3$  [28]. The inconsistent velocity setting results in wider diameter of the as-grown single crystal compared to the feed (see Fig. 1b) and in general entails a larger potential for cracking.

The procedure yields shiny boules from which single crystalline grains have been obtained, oriented, and cut (Fig. 1b and d). Crystals were obtained from both the pristine boule (S1) and the annealed one (S2). Figs. 1d–f show the oriented and cut crystal S2 as well as back-reflection Laue images obtained along the  $c$  axis and the  $ab$  plane, respectively. Similar sample dimension and Laue patterns have been obtained for crystal S1.

Powder X-ray diffraction was performed on several ground single crystals taken from the very vicinity of the oriented single crystal bulks in order to study phase purity of the grown single crystals. The resulting room temperature XRD pattern as well as the Rietveld refinements to the data presented in Fig. 2a,b indicate that the main phase is  $\text{La}_4\text{Ni}_3\text{O}_{10}$ . In addition, we observe a few Bragg peaks that do not correspond to  $\text{La}_4\text{Ni}_3\text{O}_{10}$  phases but are assigned to  $\text{La}_3\text{Ni}_2\text{O}_7$  impurities. We find that the annealing procedure under oxygen pressure leads to a notable reduction of the impurity phase, as shown in Fig. 2c,d.

#### 3.2. Magnetization

The in-plane and out-of-plane magnetization measurements performed on single crystal samples S1 and S2 shown in Fig. 3 provide further information on the quality of the single crystals and on potential impurity phases. The main features are sharp jumps or kinks in the static susceptibility  $\chi = M/B$  at  $T_{\text{MM}}^{\text{B}ab} = 152 \text{ K}$  and  $T_{\text{MM}}^{\text{P}2_1/a} = 136 \text{ K}$

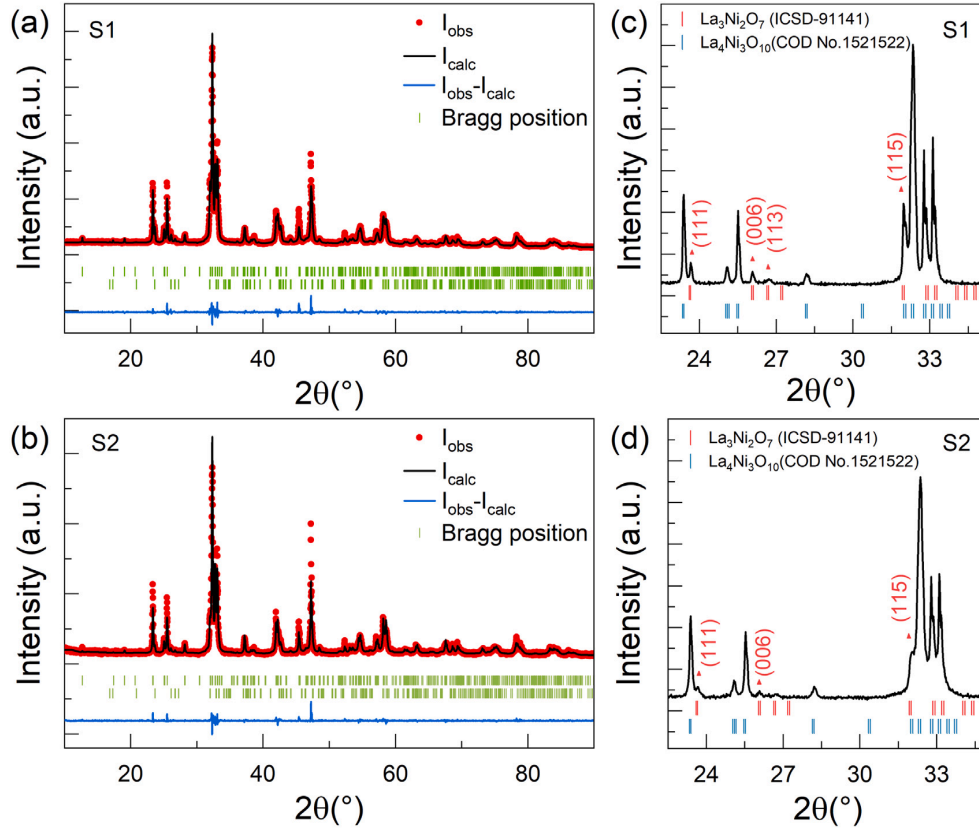


Fig. 2. Room temperature powder XRD patterns and corresponding Rietveld refinement [30] of ground  $\text{La}_4\text{Ni}_3\text{O}_{10}$  single crystals grown at 20 bar  $\text{O}_2$  pressure. S1 (a,c) and S2 (b,d) show results for pristine and annealed crystals, respectively (see the text). The observed diffraction pattern is shown in red, the calculated one in black, and the difference between them is shown in blue. The vertical green bars show the expected Bragg positions of  $\text{La}_4\text{Ni}_3\text{O}_{10}$  (COD no. 7237332 [31]) and  $\text{La}_3\text{Ni}_2\text{O}_7$  (ICSD no. 91141 [31]). The refinement converged to  $R_p = 15.9\%$ ,  $R_{wp} = 16.2\%$ ,  $\chi^2 = 5.7$  for S1 and  $R_p = 27.2\%$ ,  $R_{wp} = 24.8\%$ ,  $\chi^2 = 3.7$  for S2. (For interpretation of the references to colour in this figure legend, the reader is referred to the web version of this article.)

for the pristine S1 and the annealed S2, respectively. This result is consistent with previous reports [15–19,21,32] which imply that the MMT is characterized by an intertwined charge-magnetic ordering phenomenon.

We emphasize the absence of FC/ZFC hysteresis behaviour in the 1.8 to 350 K temperature interval (see Fig. 3); previously reported crystals show a pronounced anomaly in the susceptibility at around 50 K and strong differences between FC and ZFC susceptibilities, suggesting an unknown ferromagnetic component [18]. This component is absent in our crystals which confirms its extrinsic nature.<sup>1</sup> The absence of ferromagnetic impurities in our crystals is further confirmed by isothermal magnetization studies (see Fig. 4).

Despite the challenges and controversy regarding the determination of crystal structure of  $\text{La}_4\text{Ni}_3\text{O}_{10}$  by powder XRD analysis [17,18,23], the magnetic susceptibility data not only imply phase purity with respect to magnetic impurity phases, but also strongly suggest that the pristine crystal S1 exhibits *Bmab* structure while S2 exhibits  $P2_1/a$  structure. In particular, the very pronounced and sharp single anomalies exclude mixing of both phases in either of the single crystals. The very sharp jump in  $\chi_c$  at  $T_{\text{MM}}$  in S2 in particular indicates excellent crystallinity of the  $P2_1/a$  phase crystal. Zhang et al. [18] have identified the postgrowth cooling rate as a crucial parameter for obtaining a thermodynamically stable phase. The reported experiments on biphasic

$\text{La}_4\text{Ni}_3\text{O}_{10}$  crystals suggest that the *Bmab* structure can be transformed to  $P2_1/a$ . In our experiments we have performed rapid cooling of the as-grown boule as well as further high-pressure annealing. Our results show that the phase pure *Bmab* structure forms after rapid cooling while it completely transforms to  $P2_1/a$  upon heat treatment confirming the latter being the thermodynamically stable phase.

In general, the susceptibility data in Fig. 3 show (1) the continuous decrease of  $\chi$  upon cooling from 350 K towards  $T_{\text{MM}}$ , with a minimum in  $\chi_c$  at  $T_{\text{MM}}$  and a broad minimum in  $\chi_{\text{ab}}$  slightly below. (2) Pronounced anisotropy in the whole temperature range under study with  $\chi_{\text{ab}}/\chi_c = 1.42$  (S1) respectively 1.28 (S2), at 350 K. (3) A Curie–Weiss-like (CW-like) increase of the magnetic susceptibility  $\chi(T)$  at low temperatures which qualitatively corresponds to a Brillouin-like contribution to  $M(B, T = 2 \text{ K})$  (see Fig. 4 below).

Notably, the seemingly CW-like behaviour of magnetic susceptibility in both the  $P2_1/a$  (S1) and *Bmab* (S2) systems well below  $T_{\text{MM}}$  (see Fig. 3) cannot be described well in terms of the extended CW law  $\chi(T) = \frac{C}{T+\theta} + \chi_0$ , with  $C$  the Curie constant,  $\theta$  the Weiss temperature, and a temperature independent term  $\chi_0$ , in an extended temperature regime. This implies that at least one or even all these parameters change upon cooling. In an attempt to quantify these parameters at low temperature by restricting the CW fit to  $T < 10 \text{ K}$ , the data are reasonably well described by the parameters listed in Table 1. The small values of  $\theta$  imply the presence of very weakly coupled magnetic moments. When evaluating the Curie constant by assuming magnetic moments  $S = 1$  and  $g \approx 2$ , the data suggest 0.4 %/f.u. of such

<sup>1</sup> Within the error bars of the experiment, we obtain an upper limit of the ferromagnetic component being 25 times less than in Ref. [18].

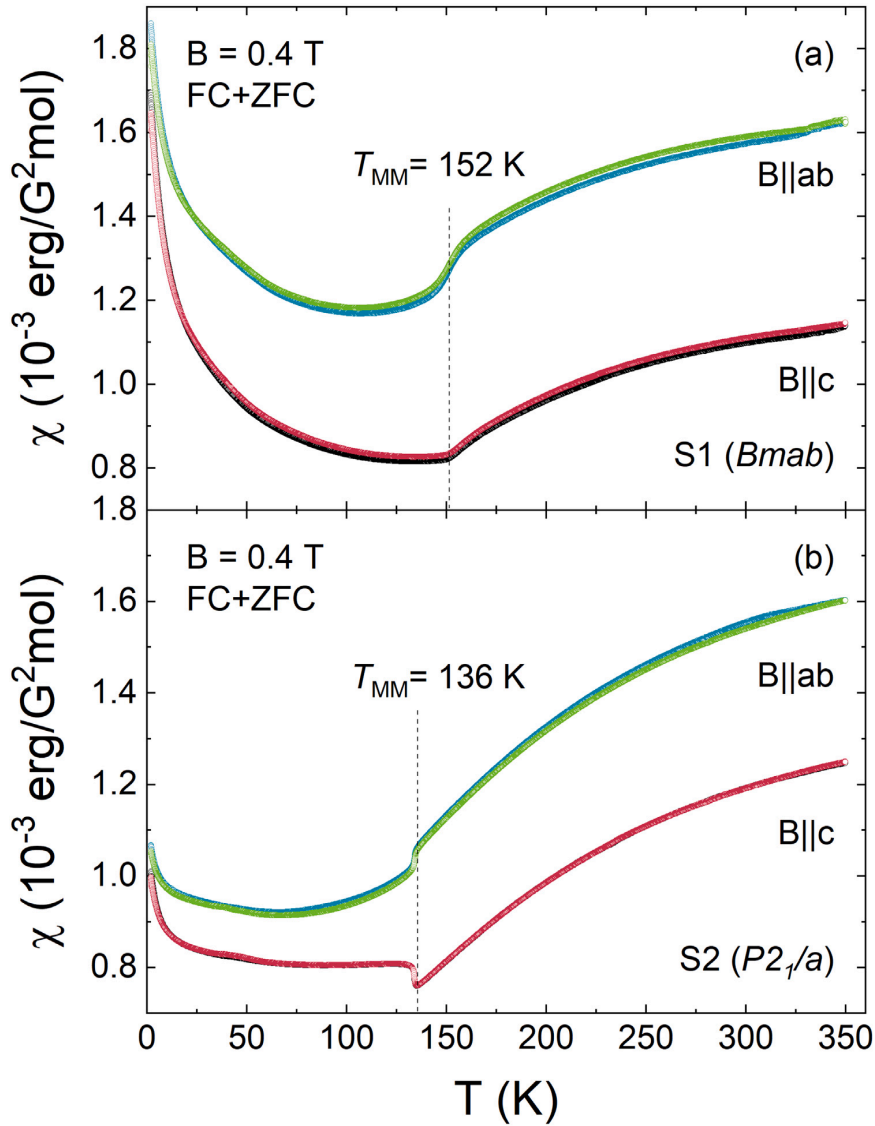


Fig. 3. Static magnetic susceptibility  $\chi = M/B$  vs.  $T$  measured at  $B = 0.4$  T of (a) the pristine crystal (S1:  $Bmab$ ) and (b) the annealed crystal (S2:  $P2_1/a$ ). For each field direction ( $B \parallel c$  and  $B \parallel ab$ ) both fc and zfc data are presented but do not show visible differences.

moments. The observed  $\chi(T)$  however also implies that the number of localized moments, their magnetic interaction and/or  $\chi_0$  change with temperature.

The isothermal magnetization (Fig. 4) shows rather linear behaviour in the high-field regime but also clear signatures of quasi-free spins as there is distinct right-bending in small fields. We attribute the linear behaviour to the response of the main magnetic phase. Considering these contributions,  $M(B)$  at  $T = 2$  K may be described by

$$M(B) = M_s \times B_S \left( \frac{g\mu_B SB}{k_B T} \right) + \chi_0 B. \quad (1)$$

Here,  $M_s$  is the saturation magnetization of the quasi-free moments,  $B_S$  the Brillouin function,  $S$  spin,  $k_B$  Boltzmann constant,  $\mu_B$  Bohr magneton,  $g$  the  $g$ -factor, and  $\chi_0$  the linear slope. Fitting the data yields the results listed in Table 1. The number of quasi-free spins obtained from this analysis through the parameter  $M_s$  is again in the  $\lesssim 1$  %-regime if assuming localized moments with  $S = 1$ . The obtained values of  $\chi_0$  are rather high with respect to the bare Sommerfeld model:

Using  $\gamma = 14.5(13.3)$  mJ/(molK<sup>2</sup>) for the  $Bmab$  ( $P2_1/a$ ) structured material [18], for non-correlated conduction electrons, one obtains  $\chi_P^{Bmab} \simeq 2.0 \times 10^{-4}$  erg/(G<sup>2</sup>mol) ( $\chi_P^{P2_1/a} \simeq 1.8 \times 10^{-4}$  erg/(G<sup>2</sup>mol)). Strong anisotropy of  $\partial M / \partial B$ , at  $B = 7$  T, already implies that magnetism of conduction electrons is however only one component determining the magnetic response in  $\text{La}_4\text{Ni}_3\text{O}_{10}$ .

### 3.3. Specific heat and $\partial T_{MM} / \partial B$

The specific heat of the single crystals under study shown in Figs. 5 and 6 confirms significant anomalous entropy changes at  $T_{MM}$ . While the anomaly of the  $P2_1/a$  structured crystal is typical for a first order transition, we conclude from the shape of the anomaly observed for the  $Bmab$  structure the discontinuous character of the MMT, too (see Fig. 5b). In an attempt to quantify the entropy changes  $\Delta S_{MM}$  associated with the MMT, a polynomial background was fitted to the data well below and above the specific heat anomaly as shown in Fig. 5a and



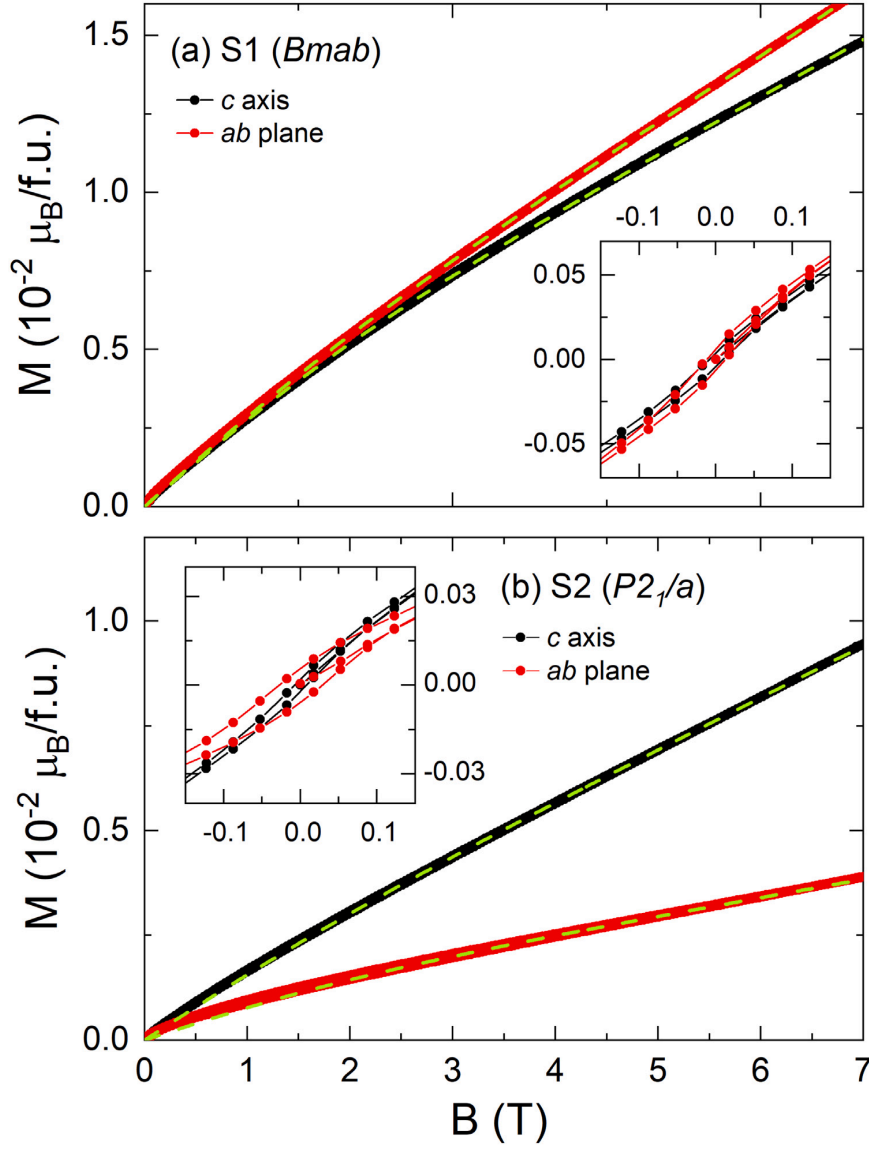


Fig. 4. Isothermal magnetization of (a) the pristine crystal (S1:  $Bmab$ ) and (b) the annealed crystal (S2:  $P2_1/a$ ), at  $T = 2$  K, for  $B \parallel c$  and  $B \parallel ab$  (both up- and down-sweeps are shown). Dashed lines extrapolate the linear high-field behaviour from which  $\chi_c$  and  $\chi_{ab}$  in Table 1 are derived. Insets:  $M$  vs.  $B$  for  $-0.15$  T  $\leq B \leq 0.15$  T. For a full  $M(B)$  curve ranging from  $-7$  T to  $+7$  T see the Supplemental Material [33].

Table 1

Fitting magnetization data in Figs. 3 and 4 (see the text).  $M_s$  and  $\chi$  are saturation magnetization of the quasi-free spins and linear slope derived from  $M(B, T = 2$  K).  $C$ ,  $\theta$ , and  $\chi_0$  are the Curie constant, Weiss temperature and temperature-independent susceptibility from fitting  $M(T)/B$  at  $T < 10$  K.

	$M_s^c$ $\mu_B/f.u.$	$\chi_c$ erg/(G <sup>2</sup> mol)	$C$ erg K/(G <sup>2</sup> mol)	$\theta$ K	$\chi_0$ erg/(G <sup>2</sup> mol)	$M_s^{ab}$ $\mu_B/f.u.$	$\chi_{ab}$ erg/(G <sup>2</sup> mol)	$C$ erg K/(G <sup>2</sup> mol)	$\theta$ K	$\chi_0$ erg/(G <sup>2</sup> mol)
S1( $Bmab$ )	$2.2 \times 10^{-3}$	$3.2 \times 10^{-3}$	$10 \times 10^{-3}$	9	$8 \times 10^{-4}$	$1.8 \times 10^{-3}$	$3.8 \times 10^{-3}$	$6 \times 10^{-3}$	7	$1.2 \times 10^{-3}$
S2( $P2_1/a$ )	$7.8 \times 10^{-4}$	$2.2 \times 10^{-3}$	$1.1 \times 10^{-3}$	3	$8 \times 10^{-4}$	$8.2 \times 10^{-4}$	$7.7 \times 10^{-4}$	$7 \times 10^{-4}$	3	$8 \times 10^{-4}$

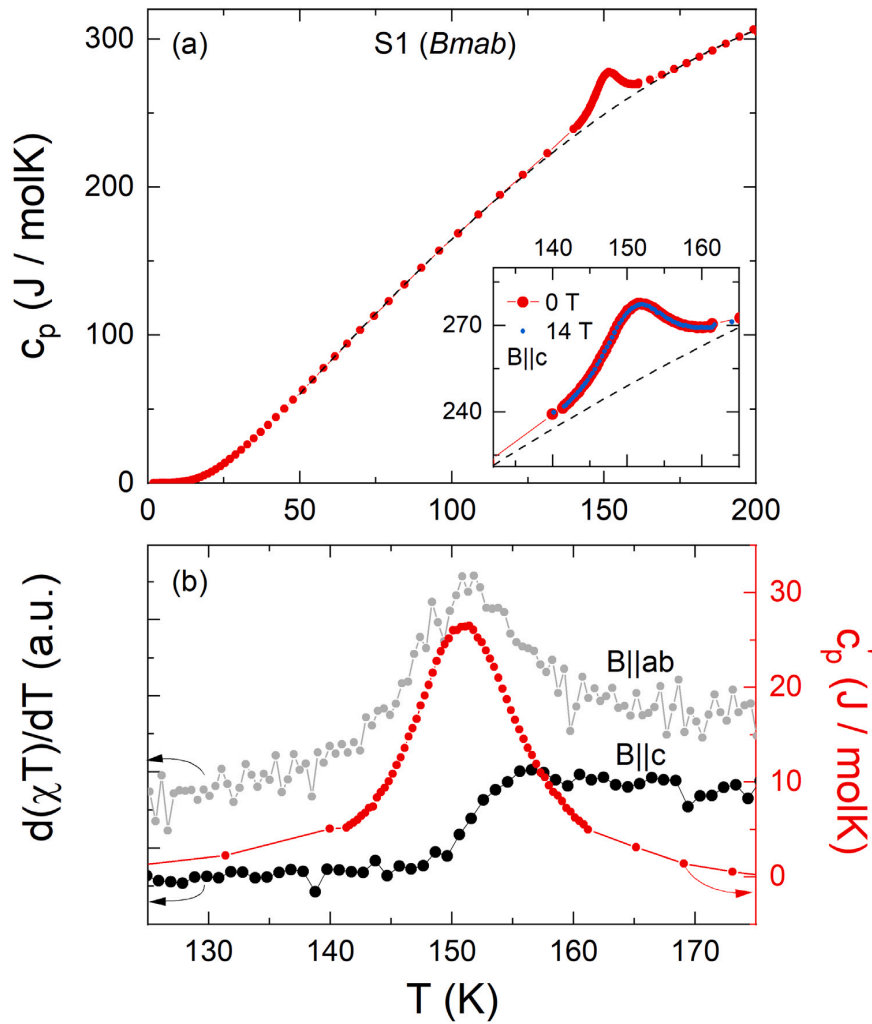


Fig. 5. (a) Specific heat capacity of the pristine crystal (S1:  $Bmab$ ). (b) Fisher's specific heat  $\partial(\chi T)/\partial T$  and anomalous contributions to the specific heat  $c_p'$  obtained by subtracting a polynomial background from the data (dashed line in (a)).

6a [34]. The background mainly reflects the phonon contribution. Due to the large size of the anomaly, using different temperature ranges for the determination of the background and/or choosing different fit functions does not change the result significantly. Subtracting the obtained background from the data yields the anomaly contribution to the specific heat  $c_p'$  as shown in Fig. 5b and 6b. Integrating  $c_p'/T$  yields the entropy changes  $\Delta S_{MM}$  listed in Table 2.

Our analysis implies that for both structures,  $Bmab$  and  $P2_1/a$ , the metal-to-metal transition is associated with similar entropy changes. The data also enable us to conclude about the field dependence of  $T_{MM}$  by exploiting the Clausius–Clapeyron equation

$$\frac{\partial T_{MM}}{\partial B} = -\frac{\Delta M}{\Delta S}. \quad (2)$$

Using the experimentally obtained jumps in  $M$  and  $S$  yields insignificant effects of magnetic fields on  $T_{MM}$  (see Table 2) which is experimentally confirmed by our measurements of the specific heat at  $B \parallel c = 14$  T (see the insets in Fig. 5a and 6a).

The obtained entropy changes are by ca. 20 % smaller than found for single crystal reported in Ref. [18] and ca. 40 % larger than recently determined from a  $P2_1/a$ -structured polycrystal [17]. A comparison of

Table 2  
Changes in entropy ( $\Delta S_{MM}$ ), magnetization ( $\Delta M$ , and  $\Delta(\partial M/\partial T)_{MM}$ ) at the MMT and field dependencies of  $T_{MM}$  calculated by means of Eq. (2).

	S1 ( $Bmab$ )	S2 ( $P2_1/a$ )
$\Delta S_{MM}$ (J/(mol K))	1.4(1)	1.6(1)
$\Delta M_{MM}^a$ ( $10^{-3}$ erg/(G <sup>2</sup> mol))	–	0.05(1)
$\Delta(\partial M/\partial T)_{MM}^a$ (erg/G <sup>2</sup> mol K)	–	0.006
$\Delta M_{MM}^{ab}$ ( $10^{-3}$ erg/(G <sup>2</sup> mol))	–0.15(2)	–0.05(1)
$ \partial T_{MM}^{ab}/\partial B $ (mK/T)	<0.01	<0.003

the anomalies is shown in Fig. 7. The data also imply slightly different ordering temperatures  $T_{MM}$  which is by 4.5 K lower for  $Bmab$  and 2.6 K larger for  $P2_1/a$  in Ref. [18] than found in our crystals.  $T_{MM}$  of the polycrystal perfectly agrees to our single crystal result [17]. These slight differences may be due to oxygen stoichiometry, which is considered a key parameter of electronic properties [24]. The fact that the specific heat and magnetic susceptibility anomalies at least for the  $P2_1/a$  system are much sharper in our crystal as compared to reported anomalies may be regarded as an indication that the crystals have particular excellent crystallinity.



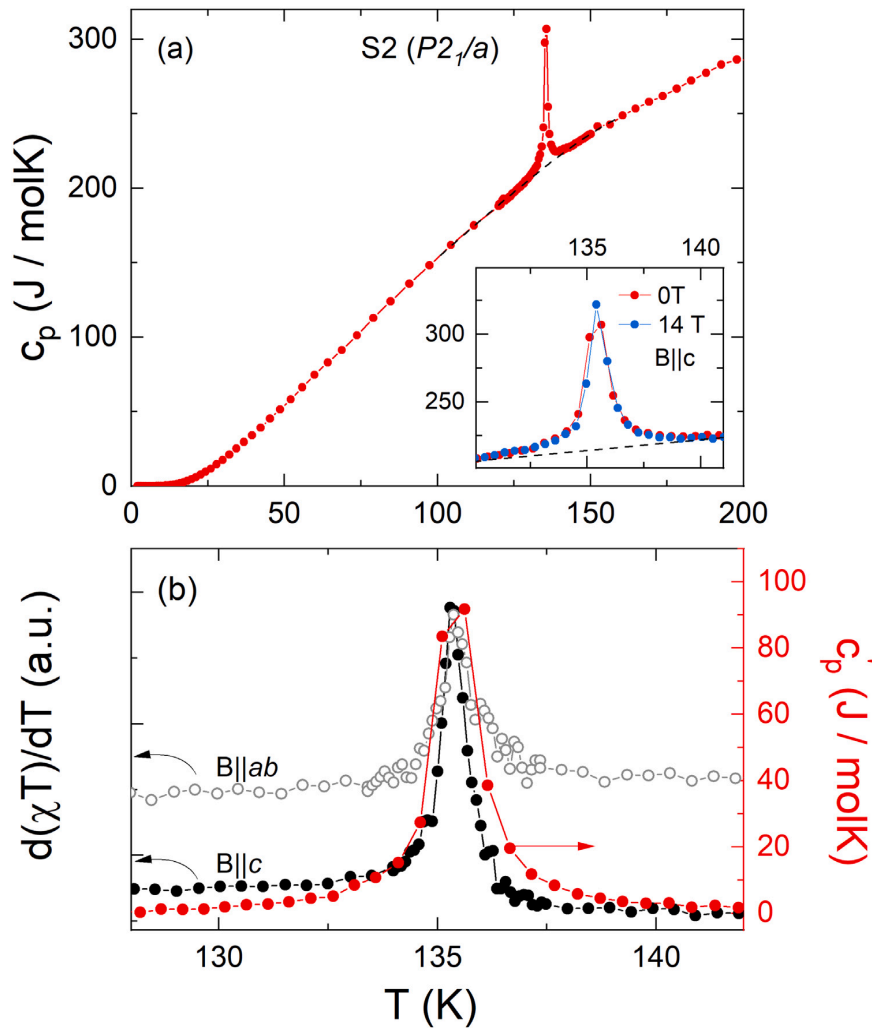


Fig. 6. (a) Specific heat capacity of the annealed crystal (S2:  $P2_1/a$ ). (b) Fisher's specific heat  $d(\chi T)/dT$  and anomalous contributions to the specific heat  $c'_p$  obtained by subtracting a polynomial background from the data (dashed line in (a)).

#### 4. Summary

$\text{La}_4\text{Ni}_3\text{O}_{10}$  single crystals were successfully grown and subsequently annealed at 20 bar oxygen pressure. Our specific heat and magnetization measurements imply  $P2_1/a$  and  $Bmab$  structured crystals, respectively, in which the metal-to-metal transitions occur at 152 K and 136 K. Sharp anomalies in the response functions imply highly crystalline samples and the thermodynamic and magnetic properties are analysed.

#### CRediT authorship contribution statement

**Ning Yuan:** Data curation, Writing – original draft. **Ahmed Elghandour:** Data curation. **Jan Arneth:** Data curation. **Kaustav Dey:** Methodology. **Rüdiger Klingeler:** Project administration, Supervision, Writing – review & editing.

#### Declaration of competing interest

The authors declare that they have no known competing financial interests or personal relationships that could have appeared to influence the work reported in this paper.

#### Data availability

Data will be made available on request.

#### Acknowledgements

The authors thank Ilse Glass for technical support. Support by the Deutsche Forschungsgemeinschaft (DFG), Germany under Germany's Excellence Strategy+ EXC2181/1-390900948 (The Heidelberg STRUCTURES Excellence Cluster) and through project KL1824/13-1 is gratefully acknowledged. N.Y. acknowledges fellowship by the Chinese Scholarship Council (File No. 201906890005).

#### Appendix A. Supplementary data

Supplementary material related to this article can be found online at <https://doi.org/10.1016/j.jcrysgro.2023.127511>. It contains the isothermal magnetization  $M$  vs.  $B$  of the pristine crystal ( $Bmab$ ) and the annealed crystal ( $P2_1/a$ ), at  $T = 2$  K and  $-7$  T  $\leq B \leq 7$  T for  $B \parallel c$  and  $B \parallel ab$ .

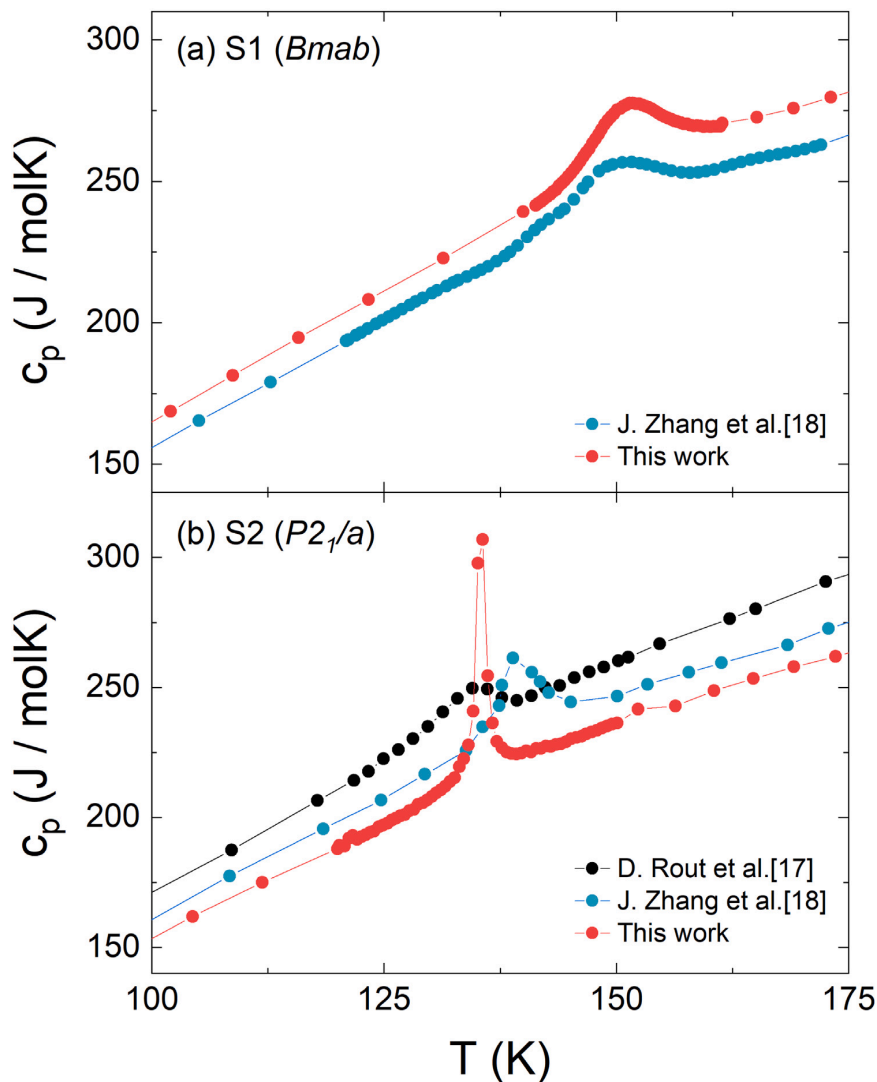


Fig. 7. Comparison of specific heat capacity of (a) the pristine crystal (S1:  $Bmab$ ) and (b) the annealed crystal (S2:  $P2_1/a$ ) with single crystal [18] and polycrystal [17] data reported in the literature.

## References

- [1] D. Li, K. Lee, B.Y. Wang, M. Osada, S. Crossley, H.R. Lee, Y. Cui, Y. Hikita, H.Y. Hwang, Superconductivity in an infinite-layer nickelate, *Nature* 572 (7771) (2019) 624–627.
- [2] D. Li, B.Y. Wang, K. Lee, S.P. Harvey, M. Osada, B.H. Goodge, L.F. Kourkoutis, H.Y. Hwang, Superconducting dome in  $\text{Nd}_{1-x}\text{Sr}_x\text{NiO}_2$  infinite layer films, *Phys. Rev. Lett.* 125 (2) (2020) 027001.
- [3] S. Zeng, C.S. Tang, X. Yin, C. Li, M. Li, Z. Huang, J. Hu, W. Liu, G.J. Omar, H. Jani, et al., Phase diagram and superconducting dome of infinite-layer  $\text{Nd}_{1-x}\text{Sr}_x\text{NiO}_2$  thin films, *Phys. Rev. Lett.* 125 (14) (2020) 147003.
- [4] Q. Gu, Y. Li, S. Wan, H. Li, W. Guo, H. Yang, Q. Li, X. Zhu, X. Pan, Y. Nie, et al., Single particle tunneling spectrum of superconducting  $\text{Nd}_{1-x}\text{Sr}_x\text{NiO}_2$  thin films, *Nat. Commun.* 11 (1) (2020) 6027.
- [5] M. Osada, B.Y. Wang, B.H. Goodge, K. Lee, H. Yoon, K. Sakuma, D. Li, M. Miura, L.F. Kourkoutis, H.Y. Hwang, A superconducting praseodymium nickelate with infinite layer structure, *Nano Lett.* 20 (8) (2020) 5735–5740.
- [6] M. Osada, B.Y. Wang, K. Lee, D. Li, H.Y. Hwang, Phase diagram of infinite layer praseodymium nickelate  $\text{Pr}_{1-x}\text{Sr}_x\text{NiO}_2$  thin films, *Phys. Rev. Mater.* 4 (12) (2020) 121801.
- [7] M. Osada, B.Y. Wang, B.H. Goodge, S.P. Harvey, K. Lee, D. Li, L.F. Kourkoutis, H.Y. Hwang, Nickelate superconductivity without rare-earth magnetism:  $(\text{La}, \text{Sr})\text{NiO}_2$ , *Adv. Mater.* 33 (45) (2021) 2104083.
- [8] S. Zeng, C. Li, L.E. Chow, Y. Cao, Z. Zhang, C.S. Tang, X. Yin, Z.S. Lim, J. Hu, P. Yang, et al., Superconductivity in infinite-layer nickelate  $\text{La}_{1-x}\text{Ca}_x\text{NiO}_2$  thin films, *Sci. Adv.* 8 (7) (2022) eabl9927.
- [9] M. Greenblatt, Ruddlesden-Popper  $\text{Ln}_{n+1}\text{Ni}_n\text{O}_{3n+1}$  nickelates: structure and properties, *Curr. Opin. Solid State Mater. Sci.* 2 (2) (1997) 174–183.
- [10] H. LaBollita, A.S. Botana, Electronic structure and magnetic properties of higher-order layered nickelates:  $\text{La}_{n+1}\text{Ni}_n\text{O}_{2n+2}$  ( $n = 4 - 6$ ), *Phys. Rev. B* 104 (2021) 035148.
- [11] M.-C. Jung, J. Kapeghian, C. Hanson, B. Pamuk, A.S. Botana, Electronic structure of higher-order Ruddlesden-Popper nickelates, *Phys. Rev. B* 105 (2022) 085150.
- [12] G.A. Pan, Q. Song, D. Ferenc Segedin, M.-C. Jung, H. El-Sherif, E.E. Fleck, B.H. Goodge, S. Doyle, D. Córdoba Carrizales, A.T. N'Diaye, P. Shafer, H. Paik, L.F. Kourkoutis, I. El Baggari, A.S. Botana, C.M. Brooks, J.A. Mundy, Synthesis and electronic properties of  $\text{Nd}_{n+1}\text{Ni}_n\text{O}_{3n+1}$  Ruddlesden-Popper nickelate thin films, *Phys. Rev. Mater.* 6 (2022) 055003.
- [13] J. Zhang, A. Botana, J. Freeland, D. Phelan, H. Zheng, V. Pardo, M. Norman, J. Mitchell, Large orbital polarization in a metallic square-planar nickelate, *Nat. Phys.* 13 (9) (2017) 864–869.
- [14] S. Kumar, Ø. Fjellvåg, A.O. Sjøstad, H. Fjellvåg, Physical properties of Ruddlesden-Popper ( $n = 3$ ) nickelate:  $\text{La}_3\text{Ni}_3\text{O}_{10}$ , *J. Magn. Magn. Mater.* 496 (2020) 165915.

- [15] B.-Z. Li, C. Wang, P. Yang, J. Sun, Y.-B. Liu, J. Wu, Z. Ren, J.-G. Cheng, G.-M. Zhang, G.-H. Cao, Metal-to-metal transition and heavy-electron state in  $\text{Nd}_4\text{Ni}_3\text{O}_{10-\delta}$ , *Phys. Rev. B* 101 (19) (2020) 195142.
- [16] S. Huangfu, G.D. Jakub, X. Zhang, O. Blacque, P. Puphal, E. Pomjakushina, F.O. von Rohr, A. Schilling, Anisotropic character of the metal-to-metal transition in  $\text{Pr}_4\text{Ni}_3\text{O}_{10}$ , *Phys. Rev. B* 101 (10) (2020) 104104.
- [17] D. Rout, S.R. Mudi, M. Hoffmann, S. Spachmann, R. Klingeler, S. Singh, Structural and physical properties of trilayer nickelates  $R_4\text{Ni}_3\text{O}_{10}$  ( $R = \text{La}, \text{Pr}$ , and  $\text{Nd}$ ), *Phys. Rev. B* 102 (19) (2020) 195144.
- [18] J. Zhang, H. Zheng, Y.-S. Chen, Y. Ren, M. Yonemura, A. Huq, J. Mitchell, High oxygen pressure floating zone growth and crystal structure of the metallic nickelates  $R_4\text{Ni}_3\text{O}_{10}$  ( $R = \text{La}, \text{Pr}$ ), *Phys. Rev. Mater.* 4 (8) (2020) 083402.
- [19] S. Huangfu, X. Zhang, A. Schilling, Correlation between the tolerance factor and phase transition in  $A_{3-x}B_x\text{Ni}_3\text{O}_{10}$  ( $A$  and  $B = \text{La}, \text{Pr}$ , and  $\text{Nd}$ ;  $x = 0, 1, 2$ , and  $3$ ), *Phys. Rev. Res.* 2 (3) (2020) 033247.
- [20] G. Wu, J. Neumeier, M. Hundley, Magnetic susceptibility, heat capacity, and pressure dependence of the electrical resistivity of  $\text{La}_3\text{Ni}_2\text{O}_7$  and  $\text{La}_4\text{Ni}_3\text{O}_{10}$ , *Phys. Rev. B* 63 (24) (2001) 245120.
- [21] J. Zhang, D. Phelan, A. Botana, Y.-S. Chen, H. Zheng, M. Krogstad, S.G. Wang, Y. Qiu, J. Rodriguez-Rivera, R. Osborn, et al., Intertwined density waves in a metallic nickelate, *Nat. Commun.* 11 (1) (2020) 6003.
- [22] Z. Zhang, M. Greenblatt, Synthesis, structure, and properties of  $\text{Ln}_4\text{Ni}_3\text{O}_{10-\delta}$  ( $\text{Ln} = \text{La}, \text{Pr}$ , and  $\text{Nd}$ ), *J. Solid State Chem.* 117 (2) (1995) 236–246.
- [23] D. Puggioni, J.M. Rondinelli, Crystal structure stability and electronic properties of the layered nickelate  $\text{La}_4\text{Ni}_3\text{O}_{10}$ , *Phys. Rev. B* 97 (11) (2018) 115116.
- [24] M. Carvalho, M. Cruz, A. Wattiaux, J. Bassat, F. Costa, M. Godinho, Influence of oxygen stoichiometry on the electronic properties of  $\text{La}_4\text{Ni}_3\text{O}_{10\pm\delta}$ , *J. Appl. Phys.* 88 (1) (2000) 544–549.
- [25] M. Zinkevich, N. Solak, H. Nitsche, M. Ahrens, F. Aldinger, Stability and thermodynamic functions of lanthanum nickelates, *J. Alloys Compd.* 438 (1–2) (2007) 92–99.
- [26] M. Zinkevich, F. Aldinger, Thermodynamic analysis of the ternary  $\text{La-Ni-O}$  system, *J. Alloys Compd.* 375 (1–2) (2004) 147–161.
- [27] C. Neef, H. Wadepohl, H.-P. Meyer, R. Klingeler, High-pressure optical floating-zone growth of  $\text{Li}(\text{Mn}, \text{Fe})\text{PO}_4$  single crystals, *J. Cryst. Growth* 462 (2017) 50–59.
- [28] K. Dey, W. Hergett, P. Telang, M.M. Abdel-Hafiez, R. Klingeler, Magnetic properties of high-pressure optical floating-zone grown  $\text{LaNiO}_3$  single crystals, *J. Cryst. Growth* 524 (2019) 125157.
- [29] W. Hergett, C. Neef, H. Wadepohl, H.-P. Meyer, M.M. Abdel-Hafiez, C. Ritter, E. Thauer, R. Klingeler, High-pressure optical floating-zone growth of  $\text{Li}_2\text{FeSiO}_4$  single crystals, *J. Cryst. Growth* 515 (2019) 37–43.
- [30] J. Rodríguez-Carvajal, An Introduction to the Program FullProf 2000 (Version July 2001), 2001.
- [31] C.D. Ling, D.N. Argyriou, G. Wu, J. Neumeier, Neutron diffraction study of  $\text{La}_3\text{Ni}_2\text{O}_7$ : Structural relationships among  $n = 1, 2$ , and  $3$  phases  $\text{La}_{n+1}\text{Ni}_n\text{O}_{3n+1}$ , *J. Solid State Chem.* 152 (2) (2000) 517–525.
- [32] H. Li, X. Zhou, T. Nummy, J. Zhang, V. Pardo, W.E. Pickett, J.F. Mitchell, D.S. Dessau, Fermiology and electron dynamics of trilayer nickelate  $\text{La}_4\text{Ni}_3\text{O}_{10}$ , *Nat. Commun.* 8 (1) (2017) 704.
- [33] N. Yuan, A. Elghandour, J. Arneth, R. Klingeler, The Supplemental Material contains the full  $M(B)$  curve ranging from  $-7$  T to  $7$  T, 2023.
- [34] R. Klingeler, J. Geck, R. Gross, L. Pinsard-Gaudart, A. Revcolevschi, S. Uhlenbruck, B. Büchner, Magnetism and the charge order transition in lightly doped  $\text{La}_{1-x}\text{Sr}_x\text{MnO}_3$ , *Phys. Rev. B* 65 (2002) 174404.

## High-pressure crystal growth and investigation of the metal-to-metal transition of Ruddlesden–Popper trilayer nickelates $\text{La}_4\text{Ni}_3\text{O}_{10}$

Ning Yuan<sup>a,\*</sup>, Ahmed Elghandour<sup>a</sup>, Jan Arneth<sup>a</sup>, Kaustav Dey<sup>a</sup>, Rüdiger Klingeler<sup>a</sup>

<sup>a</sup>Kirchhoff Institute of Physics, Heidelberg University, 69120 Heidelberg, Germany

### Abstract

The Supplemental Material contains the full  $M(B)$  curve ranging from -7 T to +7 T.

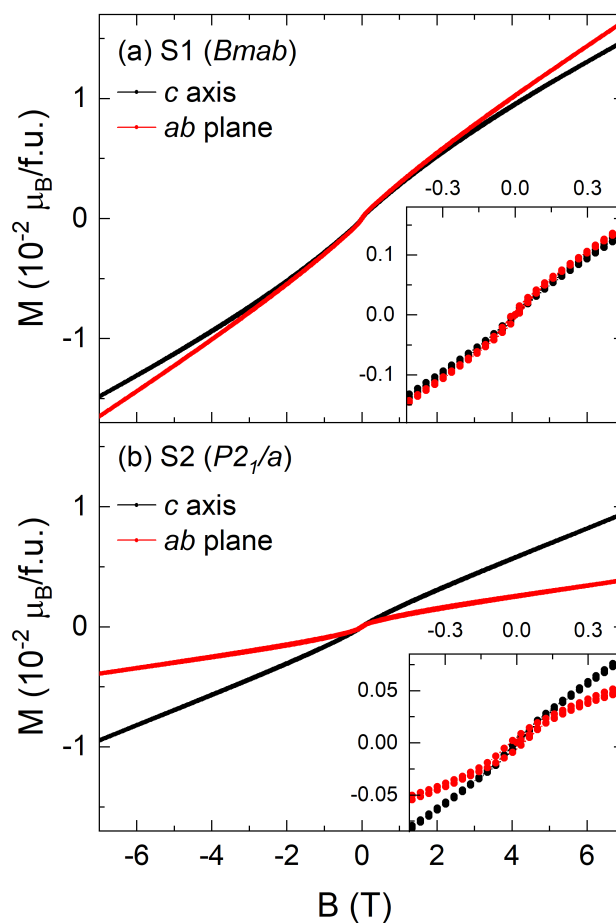


Figure 1: Magnetization of (a) the pristine crystal (S1: $Bmna$ ) and (b) the annealed crystal (S2: $P2_1/a$ ), at  $T = 2$  K, for  $B||c$  and  $B||ab$ . Insets:  $M$  vs.  $B$  for  $-0.45 \text{ T} \leq B \leq 0.45 \text{ T}$ .

\*Corresponding author

Email address: ning.yuan@kip.uni-heidelberg.de (Ning Yuan)

# 5

## Rare-Earth Orthochromites

This chapter presents three members of the rare-earth orthochromites ( $R\text{CrO}_3$ ),  $\text{ErCrO}_3$ ,  $\text{GdCrO}_3$ , and  $\text{SmCrO}_3$ . The focus of this chapter is on investigating the single crystal growth of  $\text{ErCrO}_3$ ,  $\text{GdCrO}_3$ , and  $\text{SmCrO}_3$ , as well as discussing the evolution of their magnetic ordering states under the influence of an external magnetic field along various crystallographic axes.



---

## 5.1 Introduction of $R\text{CrO}_3$

The interaction between transition metal and rare-earth magnetic moments holds significant importance in various research areas, notably in the field of permanent magnets, such as Sm-Co [113, 114] and Nd-Fe-B systems [65, 115, 116]. This interplay becomes particularly complex when two different magnetic sublattices are intertwined, giving rise to a diverse range of phenomena, including spin reorientation [117–121], solitonic lattices [122], emerging spin-phonon coupling [20], multiferroicity [123–128], spin switching [129, 130], and exchange bias behavior [131], etc. This chapter introduces three members  $\text{SmCrO}_3$ ,  $\text{ErCrO}_3$ , and  $\text{GdCrO}_3$  of  $R\text{CrO}_3$  ( $R$  = rare-earth element), a system characterized by two intertwined magnetic sublattices.

The rare-earth orthochromites  $R\text{CrO}_3$  exhibit the distorted perovskite structure due to the large radius of the rare-earth ions. The space group of  $R\text{CrO}_3$  is  $Pbnm$  or  $Pnma$  from the orthorhombic crystal system, and its crystal structure is shown in Fig. 5.1(a). Each unit cell of the distorted perovskite structure comprises four primitive cells, where  $\text{Cr}^{3+}$  and  $\text{O}^{2-}$  form the  $\text{CrO}_6$  octahedron.  $\text{Cr}^{3+}$  is located at the center of the octahedron, and  $\text{O}^{2-}$  occupies the in-plane and vertex positions depending on the O occupancy, respectively. These  $\text{CrO}_6$  octahedra are connected by co-vertex corners (see Fig. 5.1(b)), and rare-earth ions occupy the interstitial spaces within the  $\text{CrO}_6$  octahedral network. The distortion degree of perovskite lattice is usually described by the tolerance factor  $t$ , calculated by Eq. 5.1:

$$t = \frac{R_{\text{RE}} + R_{\text{O}}}{\sqrt{2}(R_{\text{Cr}} + R_{\text{O}})}. \quad (5.1)$$

where  $R_{\text{RE}}$ ,  $R_{\text{Cr}}$ , and  $R_{\text{O}}$  are the radii of  $R^{3+}$ ,  $\text{Cr}^{3+}$ , and  $\text{O}^{2-}$ , respectively. An ideal perovskite structure ( $\text{CaTiO}_3$ , cubic crystal system) is defined when  $t = 1$ . When  $t$  deviates from 1, it indicates that the ideal structure is distorted. The  $t$  of  $R\text{CrO}_3$  is always less than 1, and it varies with the radius of the rare-earth ions.

In  $R\text{CrO}_3$ , there are two kinds of magnetic subsystems, which are often called Cr sublattice and rare-earth sublattice [111, 112]. Since the magnetic properties of macroscopic matter are mainly determined by electronic magnetic moments [132], the magnetic properties of  $R\text{CrO}_3$  compounds are determined by the  $3d$  electrons of  $\text{Cr}^{3+}$  and the  $4f$  electrons of  $R^{3+}$ . Meanwhile, there are three kinds of interactions of  $\text{Cr}^{3+}$ - $\text{Cr}^{3+}$ ,  $R^{3+}$ - $\text{Cr}^{3+}$  and

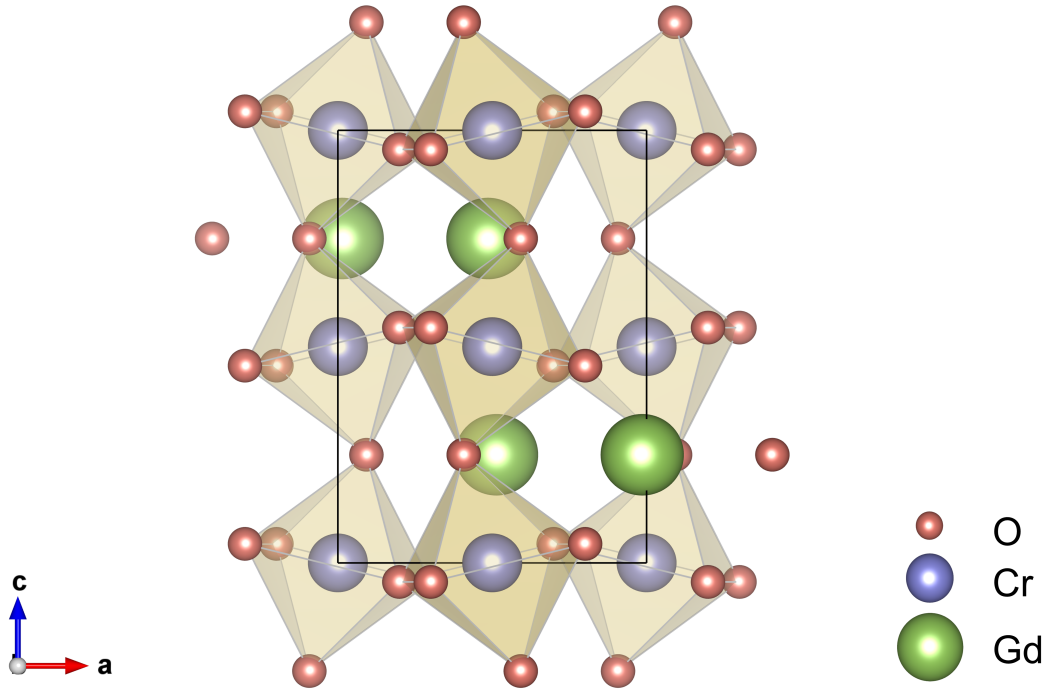


**Figure 5.1:** Schematic of the crystal structure of  $RCrO_3$  along the  $[010]$  projection. The structure is created based on the crystallographic information file (COD) No. 1533276 [109]. The image is made using the VESTA software [107].

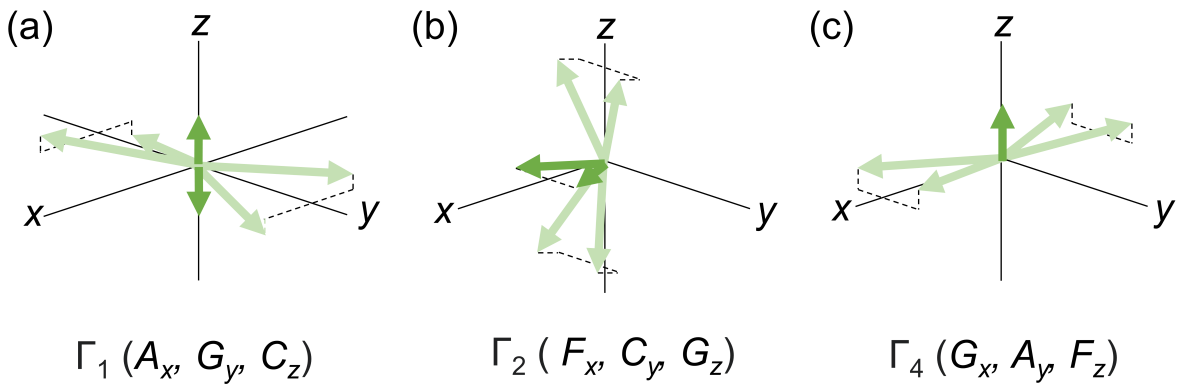


**Figure 5.2:** Schematics of possible spin configurations in  $RCrO_3$  [110–112]. The light and dark green arrows depict the  $Cr^{3+}$  and net magnetic moments, respectively, while  $R^{3+}$  moments are not shown. After [110]



---

$R^{3+}$ - $R^{3+}$  in  $RCrO_3$ , which are all functions of the temperature. Due to the distorted perovskite structure of  $RCrO_3$ , the presence of DM interactions is possible and causes the Cr sublattice to exhibit canted antiferromagnetic order [57–59]. In 1978, the physicist R. M. Hornreich has summarized previous work on  $RCrO_3$  proved only 3 spin configurations [111]:  $\Gamma_1$  ( $Cr^{3+}$ :  $A_x, G_y, C_z$ ;  $R^{3+}$ :  $O_x, O_y, C_z$ ),  $\Gamma_2$  ( $Cr^{3+}$ :  $F_x, C_y, G_z$ ;  $R^{3+}$ :  $F_x, C_y, O_z$ ) and  $\Gamma_4$  ( $Cr^{3+}$ :  $G_x, A_y, F_z$ ;  $R^{3+}$ :  $O_x, O_y, F_z$ ), shown in Fig. 5.2. Specifically, neighboring Cr magnetic moments are not perfectly co-linear (light green arrows). Instead, they exhibit tilted coupling, there can be weak ferromagnetic magnetic moments in certain directions (dark green arrows). For the  $\Gamma_1$  spin configuration, the system shows no net magnetic moment; In the case of the  $\Gamma_2$  spin configuration, the spin vectors of four  $Cr^{3+}$  superimpose a non-zero vector on the  $x$ -axis, resulting in a weak ferromagnetic magnetic moment along the  $x$ -axis (corresponding to the  $a$  axis of  $RCrO_3$  crystals); Meanwhile, for the  $\Gamma_4$  spin configuration, the spin vectors of four  $Cr^{3+}$  superimpose on the  $z$ -axis and creating a non-zero vector, so the magnetic moment is along the  $z$ -axis (corresponding to the  $c$  axis of the  $RCrO_3$  crystals).  $RCrO_3$  stabilize in a specific spin configuration under specific temperature/magnetic field environments. The different spin configurations might transform into each other depending on the interactions in the  $RCrO_3$  system, a phenomenon known as spin reorientation transition (SRT). The phase diagram of the  $RCrO_3$  has also been presented by R. M. Hornreich [111].

The long-range antiferromagnetic ordering (AF) temperature of the Cr sublattice ( $T_N^{Cr}$ ) falls within the range of 110 K to 280 K [111], whereas the rare-earth sublattice has an ordering temperature ( $T_N^R$ ) typically in the order of  $10^0$  K [133]. When the study focuses on the temperature region  $T > T_N^R$ , the rare-earth ions should be in a disordered state. However, induced by the Cr sublattice, the rare-earth ions will exhibit certain weak ferromagnetic moments at  $T > T_N^R$ . These moments are intrinsically aligned either parallel ( $R = Pr, Sm, Tb, Dy, Ho$ ) or antiparallel ( $R = Nd, Gd, Er, Tm, Yb$ ) to the  $Cr^{3+}$  magnetic moments [111]. This leads to diverse magnetization behaviors, such as compensation temperature, exchange bias, spin switching effect, and so on.

In addition, there has been a notable focus on studies related to multiferroics in recent years. The evolution of sizable spontaneous polarization has been shown in the magnetic ordered phase [134, 135], such as the dielectric anomalies observed in  $ErCrO_3$  and  $SmCrO_3$  correspond to the long-range AF ordering temperature  $T_N$  and  $T_{SR}$ ; The strong coupling between spontaneous magnetization and polarization in  $GdCrO_3$ . These investigations imply that  $ErCrO_3$ ,  $GdCrO_3$  and  $SmCrO_3$  exhibit both long-range AF order and ferroelectric

properties, which are temperature-correlated and the indicative of multiferroics [136].

In this chapter,  $\text{ErCrO}_3$ ,  $\text{GdCrO}_3$  and  $\text{SmCrO}_3$  single crystals are successfully grown by the high-pressure optical floating zone method (see Chapter 2 for more details). The obtained single crystals have been used to investigate the magnetic properties and study the effect of external magnetic field applied along the main crystallographic axis. In particular, the long-range magnetic order of the Cr-sublattice evolves at 132 K, 167 K and 192 K for  $\text{ErCrO}_3$ ,  $\text{GdCrO}_3$  and  $\text{SmCrO}_3$  respectively. For  $\text{ErCrO}_3$ , the high-temperature spin configuration is  $\Gamma_4$ , and the net magnetic moments of the system experience rotation within the  $ac$  plane at  $T = 19$  K before the complete establishment of the low-temperature  $\Gamma_1$  spin configuration.  $\text{GdCrO}_3$  exhibits  $\Gamma_4 - \Gamma_2$  SRT at 6 K, along with a magnetization compensation point at 144 K, accompanied by the phenomenon of spin switching.  $\text{SmCrO}_3$  undergoes the SRT around 33 K. The influence of the magnetic field on  $T_{\text{SR}}$  can be traced by isothermal magnetization measurement. Furthermore, distinct anomalies in the magnetization signal the appearance of  $\text{Sm}^{3+}$  order at 3 K. Therefore, complete magnetic phase diagrams of  $\text{SmCrO}_3$  for  $B||a$  and  $B||c$  have been investigated.

## 5.2 $R\text{CrO}_3$ Sample Details

Single crystals of  $R\text{CrO}_3$  ( $R = \text{Er, Gd, Sm}$ ) were successfully grown using the high-pressure optical floating zone furnace (HKZ, SciDre), detailed sample preparation methods are described in Chapter 2. The powder X-ray diffraction on the ground  $\text{ErCrO}_3$ ,  $\text{GdCrO}_3$  and  $\text{SmCrO}_3$  single crystals as well as the Rietveld refinement to the data are shown in Fig. 5.3- Fig. 5.5 and Table 5.1. The  $R\text{CrO}_3$  ( $R = \text{Er, Gd, Sm}$ ) belongs to the  $Pbnm$  ( $Pnma$ ) space group, and the cell volume gradually increases as the radius of the rare-earth ions increases. The discrepancy between the experimental and calculated patterns is quite small, with the reliability factor being only  $R_{wp} = 14.1\%$  for  $\text{ErCrO}_3$ ,  $R_{wp} = 9.97\%$  for  $\text{GdCrO}_3$  and  $R_{wp} = 13.3\%$  for  $\text{SmCrO}_3$ , which indicates that the single-phase nature of crystals, and the results are consistent with the reported results [61, 137, 138]. Fig. 5.6-Fig. 5.8 show the Laue pattern of three single crystal samples used for the magnetic measurement. The X-ray incidence and diffraction centers (black diffuse spots in the center region of the figure) are coincident, and the diffraction patterns of each crystallographic axis of  $a$ ,  $b$ , and  $c$  have obvious characteristics, with sharply defined and clear diffraction spots, indicating that the crystals are well crystallised.

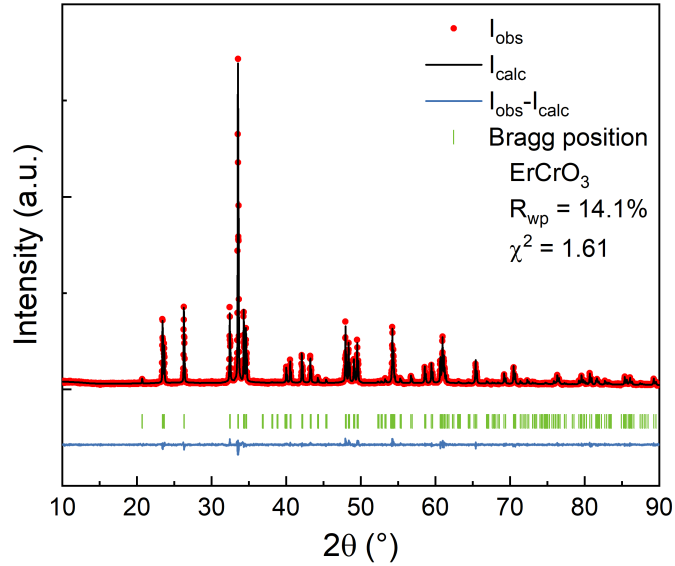


**Figure 5.3:** Room temperature powder XRD patterns and corresponding Rietveld refinement [93] of ground  $\text{ErCrO}_3$  single crystals. The observed diffraction pattern is shown in red, the calculated one in black, and the difference between them is shown in blue. The vertical green bars show the expected Bragg positions of  $\text{ErCrO}_3$  (COD No. 1008159 [139]).

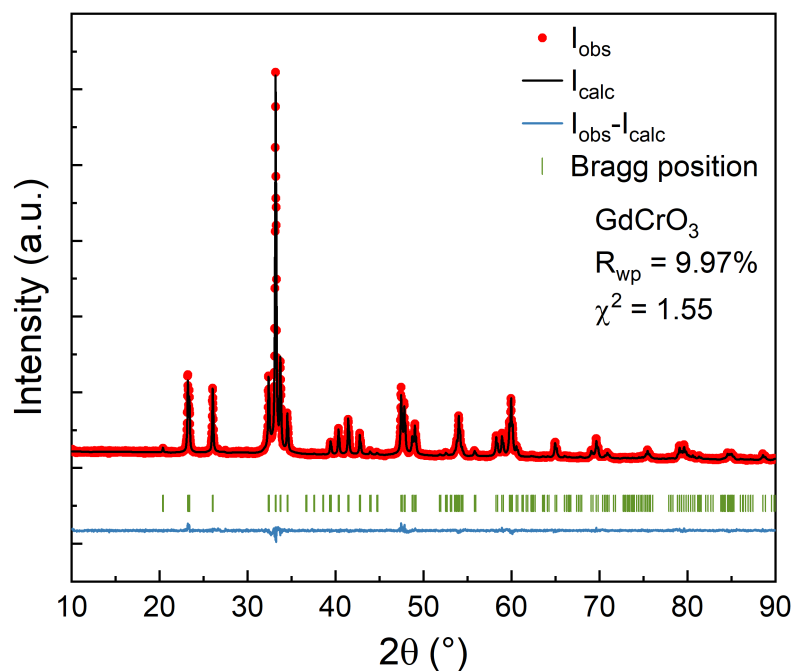


**Figure 5.4:** Room temperature powder XRD patterns and corresponding Rietveld refinement [93] of ground GdCrO<sub>3</sub> single crystals. The observed diffraction pattern is shown in red, the calculated one in black, and the difference between them is shown in blue. The vertical green bars show the expected Bragg positions of GdCrO<sub>3</sub> (COD No. 1533276 [109]).

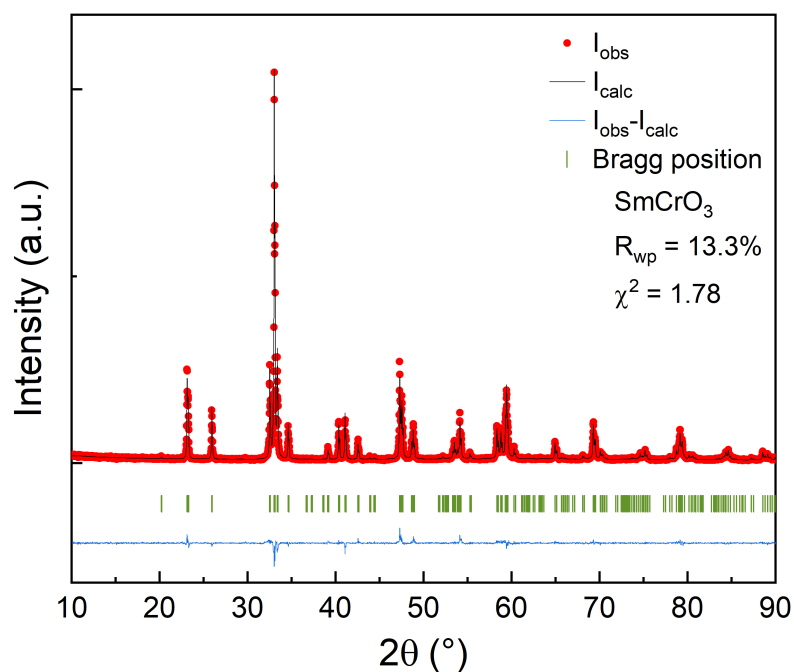


**Figure 5.5:** Room temperature powder XRD patterns and corresponding Rietveld refinement [93] of ground SmCrO<sub>3</sub> single crystals. The observed diffraction pattern is shown in red, the calculated one in black, and the difference between them is shown in blue. The vertical green bars show the expected Bragg positions of SmCrO<sub>3</sub> (ICSD No. 5988 [140]).

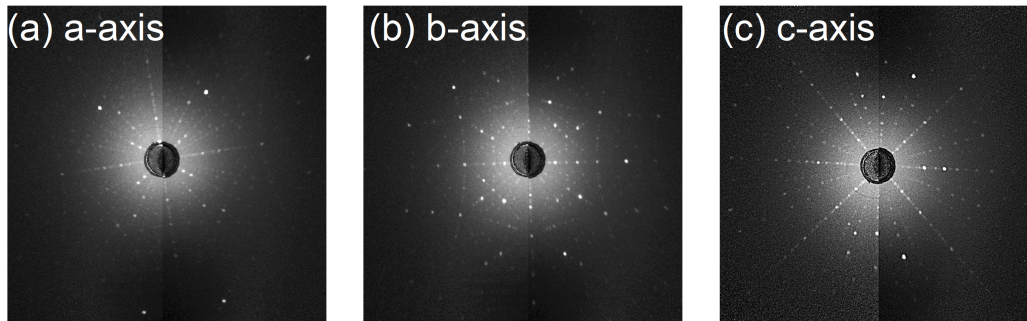


**Figure 5.6:** Laue pattern of the  $\text{ErCrO}_3$  single crystal oriented along the  $[100]$ ,  $[010]$  and  $[001]$  direction respectively.

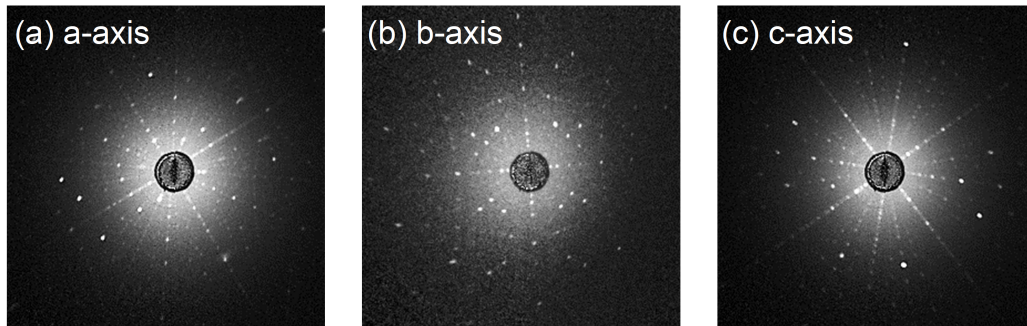


**Figure 5.7:** Laue pattern of the  $\text{GdCrO}_3$  single crystal oriented along the  $[100]$ ,  $[010]$  and  $[001]$  direction respectively.

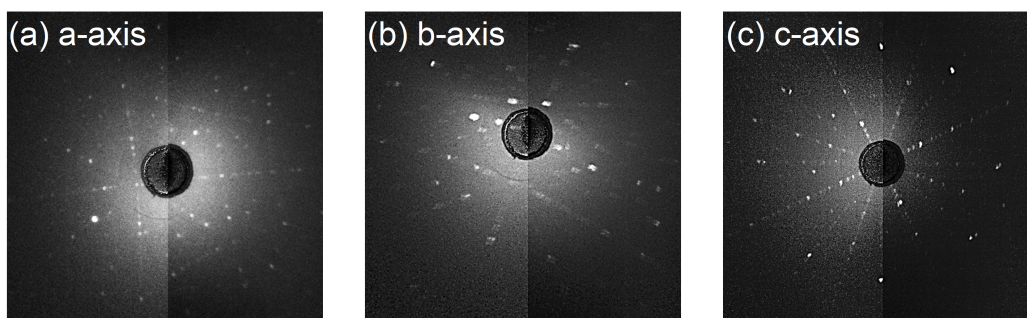


**Figure 5.8:** Laue pattern of the  $\text{SmCrO}_3$  single crystal oriented along the  $[100]$ ,  $[010]$  and  $[001]$  direction respectively.

**Table 5.1:** Selected structural parameters from the Rietveld refinement of the room temperature powder XRD data of  $R\text{CrO}_3$  ( $R = \text{Er, Gd, Sm}$ ) (space group No.62 *Phm*). The refinement is performed based on the crystallographic information file COD No. 1008159 [139] ( $\text{ErCrO}_3$ ), COD No. 1533276 [109] ( $\text{GdCrO}_3$ ), and ICSD No. 5988 [140] ( $\text{SmCrO}_3$ ).

$R\text{CrO}_3$	$R$ Ionic radii [141, 142] Unit cell volume	Atoms	Wyckoff position	$x$	$y$	$z$	Lattice parameters	Reliability factors
$\text{ErCrO}_3$	1.144 Å 216.59(1) Å <sup>3</sup>	Er	4c	-0.01834	0.06725	0.25000	$a = 5.2225(5)$ Å	$R_{wp} = 14.1$ %
		Cr	4b	0.50000	0.00000	0.00000	$b = 5.5159(4)$ Å	$\chi^2 = 1.61$
		O1	4c	0.09217	0.47030	0.25000	$c = 7.5186(6)$ Å	
$\text{GdCrO}_3$	1.193 Å 223.16(1) Å <sup>3</sup>	O2	8d	-0.31576	0.30539	0.04815	$\alpha = \beta = \gamma = 90^\circ$	
		Gd	4c	0.98461	0.05853	0.25000	$a = 5.3117(5)$ Å	$R_{wp} = 9.97$ %
		Cr	4b	0.00000	0.50000	0.00000	$b = 5.5247(6)$ Å	$\chi^2 = 1.55$
$\text{SmCrO}_3$	1.219 Å 225.63(2) Å <sup>3</sup>	O1	4c	0.10536	0.46061	0.25000	$c = 7.6046(7)$ Å	
		O2	8d	0.70232	0.28889	0.04995	$\alpha = \beta = \gamma = 90^\circ$	
		Sm	4c	-0.01030	0.05048	0.25000	$a = 5.3646(1)$ Å	$R_{wp} = 13.3$ %
$\text{SmCrO}_3$	225.63(2) Å <sup>3</sup>	Cr	4b	0.50000	0.00000	0.00000	$b = 5.5025(4)$ Å	$\chi^2 = 1.78$
		O1	4c	0.08780	0.47970	0.25000	$c = 7.6437(4)$ Å	
		O2	8d	-0.29000	0.28510	0.04340	$\alpha = \beta = \gamma = 90^\circ$	

---

## 5.3 Magnetization

### 5.3.1 ErCrO<sub>3</sub>

ErCrO<sub>3</sub> single crystals have a significant magnetic anisotropy, which can be clearly observed in the temperature dependence of the static magnetic susceptibility  $\chi$  for  $B||a$  and  $B||c$  at  $B = 0.01$  T, as shown in Fig. 5.9. The onset of long-range AF order at  $T_N = 132$  K. For  $B||c$ , a remarkable increase of  $\chi_c$  is observed after  $T < 132$  K, in comparison to the signs of a weak increase of  $\chi_a$ <sup>1</sup> and the not visible increase of  $\chi_b$ , suggesting that the sizable net magnetic moments are well ordered in the  $c$  axis. It is consistent with all previous theoretical [111, 112], polycrystals [137], and single crystal reports on ErCrO<sub>3</sub> [60, 143–147]. As seen in Fig. 5.10(a),  $\chi_a$ ,  $\chi_b$ , and  $\chi_c$  though different are very similar in the high-temperature region. The temperature dependence of the magnetic susceptibility obeys the Curie-Weiss (CW)-like behavior above 132 K, as shown by  $\chi^{-1}(T)$  in Fig. 5.10(b). The CW fitting was performed on  $a$ ,  $b$ , and  $c$  axis in temperature region 250 - 400 K (at  $B = 1$  T), respectively. The effective moment  $\mu_{\text{eff}}$ , Weiss temperature  $\Theta_W$ , and diamagnetic constant background term  $\chi_0$  obtained from the CW fitting are listed in Table 5.2. The lower value from  $B||a(b)$  compared to the theoretical values  $10.334 \mu_B^2$  might be due to a slight angular deviation between the measured magnetic field direction and the crystal orientation. This deviation is caused by the cutting of the crystal or by the sample mounting during the measurement, and an angular deviation of about  $5^\circ$  is unavoidable in experiments. The higher  $\mu_{\text{eff}}$  value from  $B||c$  might be influenced by the spin-orbit coupling effect, as the Er<sup>3+</sup> with a high orbital angular momentum  $L = 6$ .

Likewise, in the scenario of canted antiferromagnets, a so-called Moriya model may be applied which incorporates the antisymmetric exchange interaction (DM interaction) based on the classical Curie-Weiss law. [58]. Moriya's model states that along the easy axis, the susceptibility adheres to the CW law. Nevertheless, in the direction perpendicular to the easy axis, the susceptibility can be described by the following Eq. 5.2:

$$\chi = \frac{N_A \mu_{\text{eff}}^2}{3k_B(T - \Theta_W)} \frac{(T - T_0)}{(T - T_N^{\text{Cr}})}. \quad (5.2)$$

---

<sup>1</sup> Below  $T_N$ , there is only a very small anomaly in  $\chi_a$  which is only 4 % of the one in  $\chi_c$ . This is within the error bars of the crystal orientation and the cutting process.

<sup>2</sup>  $\mu_{\text{eff}} = \sqrt{\mu_{\text{Er}}^2 + \mu_{\text{Cr}}^2}$ ;  $\mu_{\text{Er}} = g\mu_B \sqrt{J(J+1)} = 9.58 \mu_B$  ( $J = 15/2$ ,  $g = 6/5$ );  $\mu_{\text{Cr}} = 3.873 \mu_B$  ( $J = 3/2$ ,  $g = 2$ ).

$$T_0 = \frac{2J_e Z S(S+1)}{3k_B}, \quad (5.3)$$

$$T_N^{\text{Cr}} = \frac{2J_e Z S(S+1)}{3k_B} \left[ 1 + \left( \frac{D}{2J_e} \right)^2 \right]^{1/2}, \quad (5.4)$$

with the Avogadro number  $N_A$ , the Boltzman constant  $k_B$ , the Weiss temperature  $\Theta_W$ , fitted parameter  $T_0$ , the Néel temperature for Cr ordering  $T_N^{\text{Cr}}$ , symmetric (antisymmetric) exchange interactions between  $\text{Cr}^{3+}$  ions  $J_e(D)$ , spin quantum number  $S$ . Here,  $Z = 6$  represents the coordination number of  $\text{Cr}^{3+}$  concerning other  $\text{Cr}^{3+}$  [148, 149],  $S = 3/2$  of  $\text{Cr}^{3+}$ . The fitting results (at  $B = 0.01$  T) are listed in Table 5.2 and denote by solid red line in Fig. 5.10(c). Obviously, the fitting for  $1/\chi_c$  is superior to  $1/\chi_a$  and  $1/\chi_b$  due to the fact that the  $\frac{(T-T_0)}{(T-T_N^{\text{Cr}})}$  term in Eq. 5.2 describes the behavior near  $T_N$ , which causes the sharp drop in  $1/\chi$ . Below 133 K, the magnetic moments of the system are ordering in the  $c$  axis, therefore  $1/\chi_a$ , and in particular  $1/\chi_b$  lacks this sharp drop. In earlier studies of polycrystalline samples [148, 149], the Moriya model provided satisfactory results. A. McDannald et al. reported the temperature dependence of the inverse susceptibility ( $1/\chi$ ) for  $\text{DyCrO}_3$  and  $\text{Dy}_{0.7}\text{R}_{0.3}\text{CrO}_3$  ( $R = \text{Y}, \text{Er}, \text{and Ho}$ ), in which the fitting results given by the CW law and the Moriya model were identical [148]. The similar comparison between the fitting results obtained by the CW law and the Moriya model is also reported by Shiqi Yin et al. for  $\text{HoCrO}_3$  and  $\text{Ho}_{0.67}\text{Tm}_{0.33}\text{CrO}_3$  ( $R = \text{Tm and Gd}$ ) [149]. However, in this analysis for  $\text{ErCrO}_3$  single crystal, the fit obtained by CW law is superior to the Moriya model. Despite this, the value of  $J_e$  and  $D$  may be estimated by Eq. 5.3 and Eq. 5.4, as presented in Table 5.2.

**Table 5.2:** Comparison of the Weiss-temperature ( $\Theta_W$ ) and the effective magnetic moment ( $\mu_{\text{eff}}$ ) of  $\text{ErCrO}_3$  obtained from the CW law and Moriya model [58] (Eq. 5.2- 5.4). The resulting fits to the data are shown in Figs. 5.10 (b) and (c).

	Magnetic Field	$\mu_{\text{eff}}$ $\mu_B$	$\Theta_W$ K	$\chi_0$ $\text{erg G}^{-2} \text{mol}^{-1}$	$T_N^{\text{Cr}}$ K	$T_0$ K	$J_e$ K	$D$ K
CW law (Fig. 5.10 (b))	$B  a$	10.1(2)	-31(1)	$-3.40 \times 10^{-7}$				
	$B  b$	10.1(2)	-62(2)	$-4.19 \times 10^{-8}$				
	$B  c$	10.5(2)	7(1)	$1.49 \times 10^{-6}$				
Moriya model (Fig. 5.10 (c))	$B  a$	10.5(1)	-47(1)	-	132.6(1)	132.8(1)	$8.84(1)k_B$	$0.97(2)k_B$
	$B  b$	10.6(1)	-62(1)	-	133.0(1)	133.0(1)	$8.87(1)k_B$	-
	$B  c$	10.4(1)	3(1)	-	130.7(1)	130.5(1)	$8.70(1)k_B$	$0.96(2)k_B$



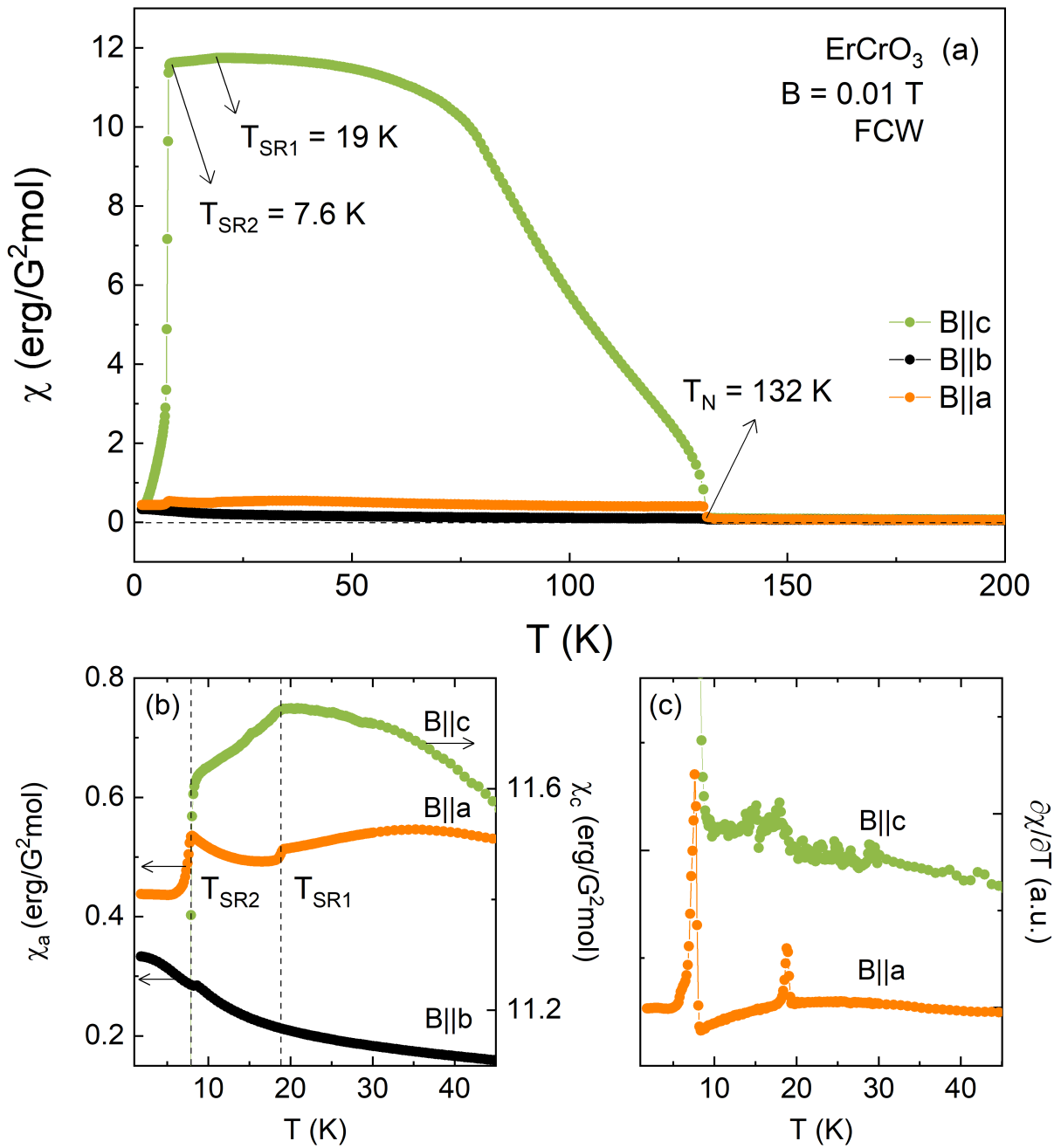


**Figure 5.9:** (a) Temperature dependence of the static magnetic susceptibility  $\chi = M/B$ , obtained at  $B = 0.01$  T applied along the crystallographic  $a$  ( $B||a$ ),  $b$  ( $B||b$ ), and  $c$  axis ( $B||c$ ) for ErCrO<sub>3</sub>. (b) Static magnetic susceptibility and (c) its derivative for  $B||a$  and  $B||c$  at  $B = 0.01$  T and  $T \leq 45$  K.  $T_N$ ,  $T_{SR1}$ , and  $T_{SR2}$  have been determined as described in the text.

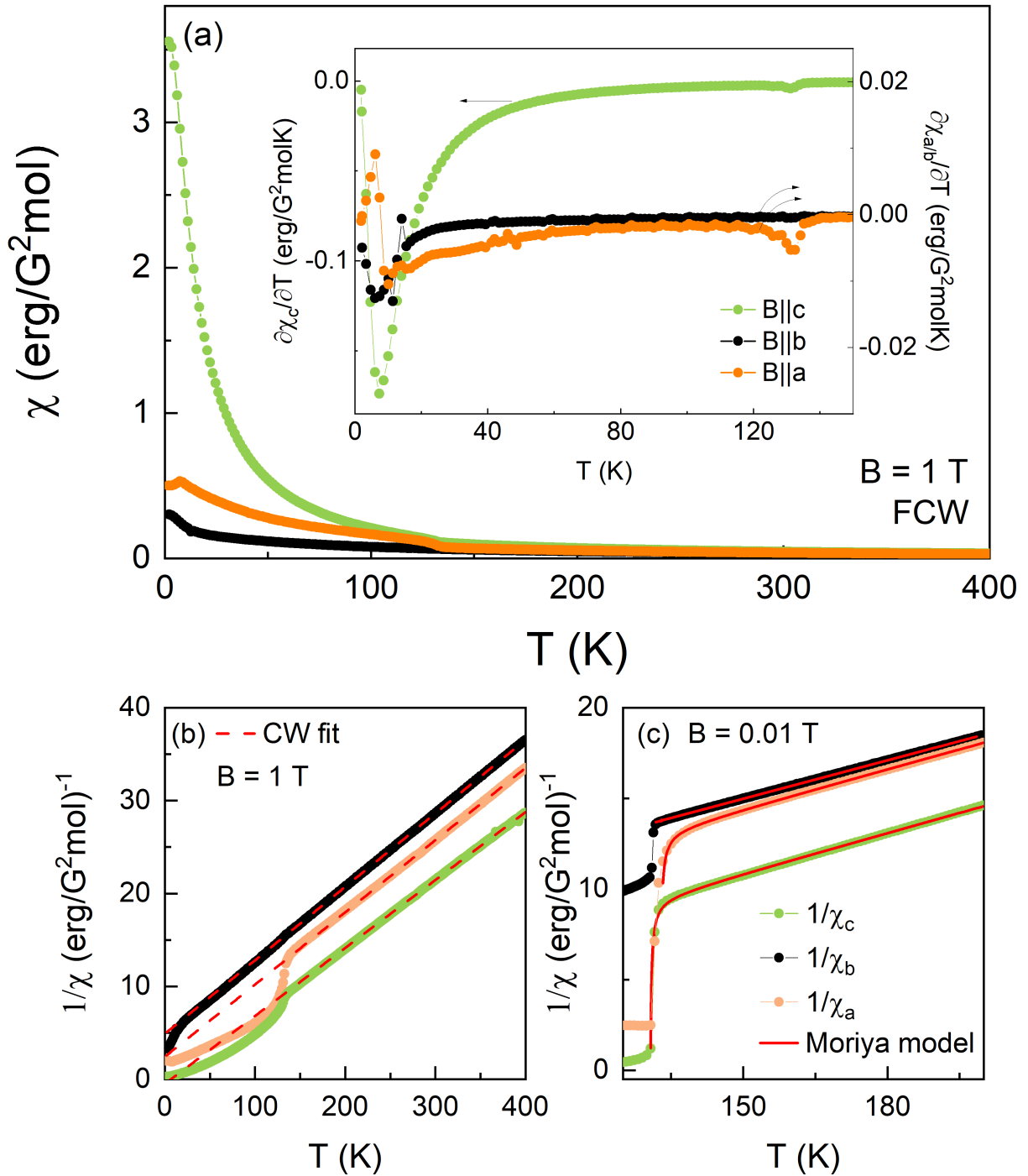


**Figure 5.10:** (a) Temperature dependence of the static magnetic susceptibility  $\chi = M/B$ , obtained at  $B = 1$  T for  $B||a$ ,  $B||b$ , and  $B||c$  axis of ErCrO<sub>3</sub>. Inset: Corresponding temperature derivative. (b) Inverse static susceptibility obtained at  $B = 1$  T for  $B||a$ ,  $B||b$ , and  $B||c$  axis and fitted by the CW law (dashed red line). (c) Inverse static susceptibility obtained at  $B = 0.02$  T for  $B||a$ ,  $B||b$ , and  $B||c$  axis and fitted by Eq. 5.2 (solid red line).

Upon cooling,  $\chi_c$  reaches a maximum value of 11.74(1) erg/G<sup>2</sup>mol around  $T_{\text{SR1}} = 19$  K then followed by a gentle decrease (see Fig. 5.9(b)). Meanwhile,  $\chi_a$  slowly increases below  $T_{\text{SR1}}$ , suggesting rotation of the net magnetic moments from the  $c$  to the  $a$  axis,  $\chi_b$  maintains a gentle upward trend. However, with  $T < T_{\text{SR2}} = 7.6$  K, a final steep decrease in  $\chi_c$  is observed, coinciding with a decrease in  $\chi_a$  (see Fig. 5.9(b)). The derivative of both  $\chi_c$  and  $\chi_a$  at  $B = 0.01$  T clearly show two peaks, as shown in Fig. 5.9(c). The anomalous peak in the low-temperature region can still be traced at  $B = 1$  T, as shown in the inset of Fig. 5.10(a). Until cooling down to 1.8 K, there is no net magnetic moment in any of the three  $a$ ,  $b$ , and  $c$  axis, this is further illustrated by the magnetic-field dependence of magnetization at  $T = 1.8$  K, as shown in Fig. 5.11. No indication of hysteresis is seen for three different axis near  $B = 0$  T (see inset of Fig. 5.11(b)), which represent no sign of net magnetic moments at  $T = 1.8$  K. Overall, the data suggest an evolution of SRT from  $\Gamma_4 (G_x, A_y, F_z)$  to  $\Gamma_1 (A_x, G_y, C_z)$ . At the highest measured field of 7 T, the magnetization is not saturated for all three directions. Taking the theoretical value of  $g$ -factor = 6/5,  $S = 15/2$  of  $\text{Er}^{3+}$  should achieve a saturated magnetization of 9  $\mu_B$  or larger. At 7 T, distinctly differing values of  $M_c = 7.2(1)$   $\mu_B/\text{f.u.}$ ,  $M_a = 4.0(1)$   $\mu_B/\text{f.u.}$ , and  $M_b = 3.4(1)$   $\mu_B/\text{f.u.}$  for three axes were obtained.

The effect of magnetic fields on the alignment of net magnetic moments at low temperatures is also illustrated by the isothermal magnetization  $M$  vs.  $B$  and the associated magnetic susceptibility  $\partial M/\partial B$  at  $T = 1.8$  K. As shown in Fig. 5.11(c), for  $B||c$ , there is a plateau-like feature of  $M$  in the range  $-0.07$  T  $< B < 0.07$  T, which also exhibits the broad asymmetric peak in  $\partial M/\partial B||c$  centered at  $B = 0.07$  T, marked as  $B_c$  on Fig. 5.11(c). The magnetization curves of the three directions  $a$ ,  $b$ , and  $c$  coincide well for  $B < B_c$ . With  $B$  larger than  $B_c$ ,  $M_a$  and  $M_b$  gradually separate as the magnetic field increases, but  $M_c$  increases rapidly and linearly up to 0.45 T. This suggests an accumulation of the net magnetic moments along the  $c$  axis after  $B > 0.07$  T. For  $B||a$ , a slight deviation from a linear increase in  $M_a$  near  $B = 0$  T is manifested by a broadening of the peak in  $\partial M/\partial B||a$  centered around 1.8 T (see Fig. 5.11(d)), and followed by a linear growth of  $M_a$  at  $B > 3.1$  T. Overall, the magnetization of  $\text{ErCrO}_3$  system is contributed by the weakly ferromagnetic magnetic moments of transition metal ions and the induced net magnetic moments of rare-earth ions, as well as the paramagnetic magnetic moments of rare-earth ions. For  $B||a$ , the magnetization curve is S-shaped at 1.8 K, which implies a weakly ferromagnetic state on the  $a$  axis.  $M_b(B)$  curve exhibits a linearly increasing diagonal, which is typically an antiferromagnetic behavior. Meanwhile, for  $B||c$ , there is a larger

increasing slope in the magnetization curve at small fields, which is due to the paramagnetic effective magnetic moments of rare-earth ions. Fig. 5.12 illustrates the variation of  $B_c$  with temperature. With increasing temperature,  $B_c$  shifting to lower temperatures and disappear at  $T = 8$  K, which is above the spin reorientation temperature of 7.6 K as shown in Fig. 5.9.

The magnetization measurements on the  $\text{ErCrO}_3$  single crystal studied at hand clearly present the SRT from  $\Gamma_4 (G_x, A_y, F_z)$  ( $T > T_{\text{SR}}$ ) to  $\Gamma_1 (A_x, G_y, C_z)$  ( $T < T_{\text{SR}}$ ), which is generally consistent with previous reports [60, 137, 144]. More specifically, S. Yano et al. provided the magnetic structure of  $\text{ErCrO}_3$  at 5 K and 25 K through neutron diffraction analysis [60].  $\text{ErCrO}_3$  exhibits two spin configurations  $\Gamma_1$  ( $T = 5$  K) and  $\Gamma_4$  ( $T = 25$  K), i.e., at low temperatures, no net magnetic moments are observed in all three  $a$ ,  $b$ , and  $c$  axis, whereas the net magnetic moments align along the  $c$  axis in the high-temperature region. This is consistent with the results of this work; however, a rotation of the net magnetic moments within the  $ac$  plane near 19 K is observed (see Fig. 5.9), which was not reported in previous studies. Furthermore, the reported values of  $T_{\text{SR}}$  are inconsistent. For example, Su et al.'s report on polycrystalline sample states that  $T_{\text{SR}} = 22$  K [137]; L. Yin's report on single crystals prepared by the flux method indicates that the reorientation is accomplished in two steps, occurring at 10.2 K and 6.0 K [144]; whereas S. Yano's report on single crystals prepared by the floating zone method suggests that the reorientation occurs at 9.3 K-10 K [60]. The variation of  $T_{\text{SR}}$  could be attributed to the quality of sample synthesized using various methods. Nevertheless, the noticeable rotation of the net magnetic moments around 19 K also clearly depicted in the derivative of the magnetic susceptibility (Fig. 5.9(c)) alongside the absence of any anomalies in  $\chi_b$  around 19 K. Therefore, the net magnetic moments rotation should take place only in the  $ac$  plane. The ordering of the  $\text{Er}^{3+}$  moment at low temperatures may follows the SRT, although it is impractical to distinguish the temperatures at which  $\text{Er}^{3+}$  ordering and the reorientation phase transition occur based on the current data alone. The results presented in this work illustrate the magnetic anisotropy of  $\text{ErCrO}_3$  and suggest that the net magnetic moments of the system undergo rotation in the  $ac$  plane before the low-temperature  $\Gamma_1$  spin configuration fully develops.

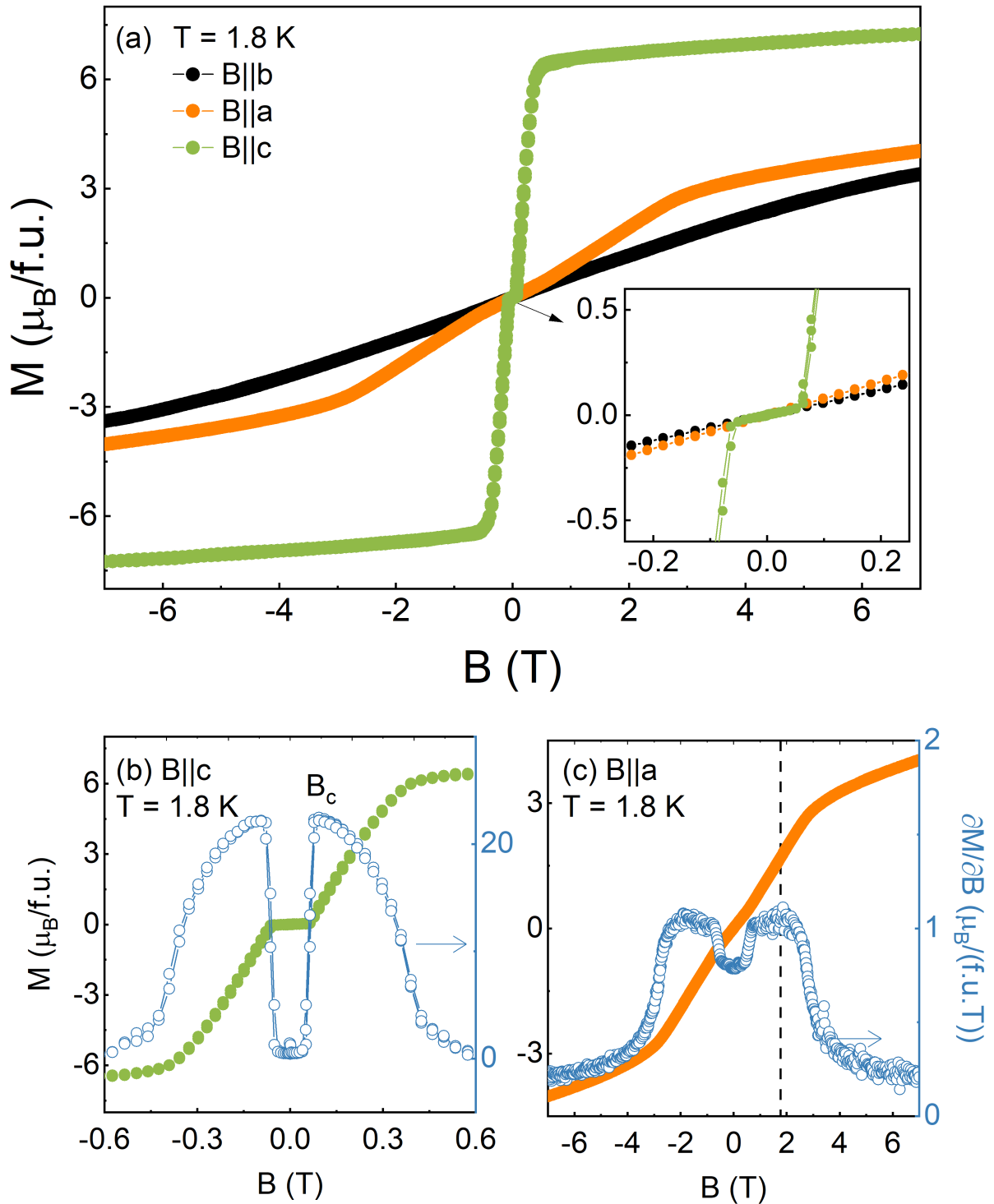


**Figure 5.11:** (a) Isothermal magnetization at  $T = 1.8$  K for  $B||a$ ,  $B||b$ , and  $B||c$  axis of  $\text{ErCrO}_3$ . The inset highlights the behaviour around zero field. (b) Isothermal magnetization at  $T = 1.8$  K for  $B||c$  axis (left ordinate) and corresponding magnetic susceptibility  $\partial M/\partial B_{||c}$  (right ordinate), the critical field  $B_c$  as described in the text. (c) Isothermal magnetization at  $T = 1.8$  K for  $B||a$  axis (left ordinate) and corresponding magnetic susceptibility  $\partial M/\partial B_{||a}$  (right ordinate), the dashed line shows the critical field  $B_a$  as described in the text.

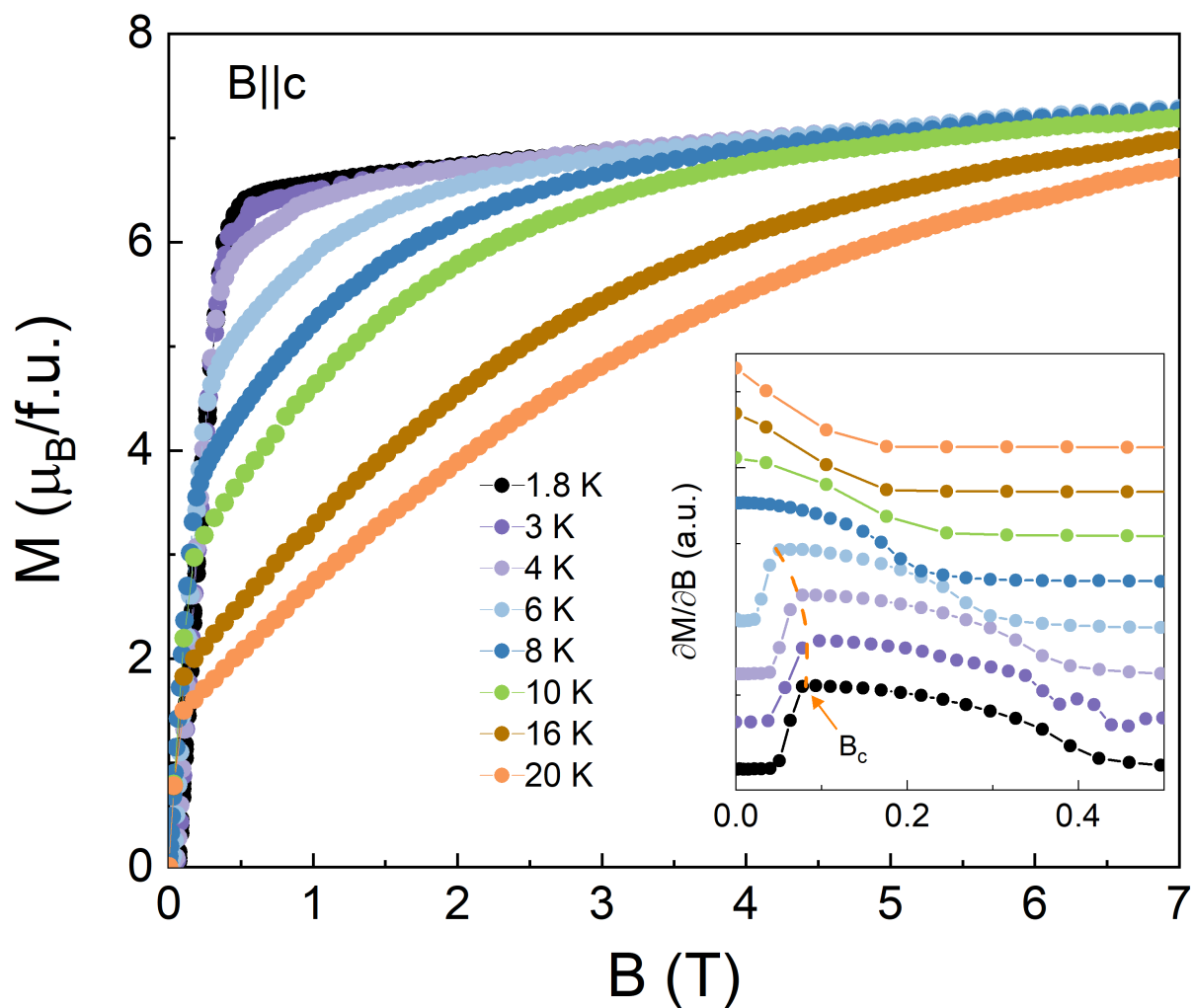


**Figure 5.12:** (a) Isothermal magnetization for  $B \parallel c$  of  $\text{ErCrO}_3$  at different temperatures. Inset: Magnetic susceptibility  $\partial M / \partial B \parallel c$ . The dashed line indicates the evolution of  $B_c$ .

---

## 5.3.2 GdCrO<sub>3</sub>

### 5.3.2.1 Magnetization $M(T, B)$

GdCrO<sub>3</sub> single crystals display the complex magnetization behavior and exhibit pronounced magnetic anisotropy. Specifically, the magnetic anisotropy is characterized by the difference between the temperature-dependent static magnetic susceptibility strengths  $\chi_a$ ,  $\chi_b$ , and  $\chi_c$  ( $B = 0.01$  T), as illustrated in Fig. 5.13. For  $B \parallel c$ , there is a marked increase in  $\chi_c$  below  $T < 167$  K, whereas the increases in  $\chi_a$  and  $\chi_b$  are not as pronounced (inset of Fig. 5.13(a)), implying that the long-range AF ordering occurs at  $T_N = 167$  K and the net magnetic moments are effectively aligned in the  $c$  axis for  $T < 167$  K. The temperature dependence of the magnetic susceptibility obeys a CW-like behavior above 167 K, as shown by  $\chi^{-1}(T)$  in Fig. 5.14(a). The CW fitting was performed on  $c$  axis in temperature region 200 - 300 K (at  $B = 0.02$  T). The effective moment  $\mu_{\text{eff}} = 8.7(1) \mu_B$ , Weiss temperature  $\Theta_W = -17(1)$  K and diamagnetic constant background term  $\chi_0 = 5.43 \times 10^{-4}$  erg/G<sup>2</sup>mol are obtained from the CW fitting, which is consistent with previous reports [62, 63, 150, 151] and the theoretical value<sup>3</sup>. The fit based on Eq. 5.2 is also displayed in Fig. 5.14(b) (solid red line), which yields  $\mu_{\text{eff}} = 8.8(1) \mu_B$ ,  $\Theta_W = -25(2)$  K,  $J = 11.13(1) k_B$  and  $D = 0.84(2) k_B^4$ .

From the inset of Fig. 5.13(a) it is also notice that GdCrO<sub>3</sub> exhibits a susceptibility jump behavior around 160 K, which also known as spin switching effect [62, 129, 130, 151, 152]. The absolute value of  $\chi_c$  is analogous before and after the jump, and the negative  $\chi_c$  persists until 144 K, which has been defined as the magnetization compensation temperature  $T_{\text{comp}}$  in numerous reports [62, 63, 151]. Following  $T < T_{\text{comp}} = 144$  K,  $\chi_c$  reverts to a positive value and steadily increases until approximately 6 K, reaching a peak value of 7.10(1) erg/G<sup>2</sup>mol, and finally it descends quickly.  $\chi_a$  and  $\chi_b$  are almost coincident in the high-temperature region until about 65 K where they gradually separate, and  $\chi_a$  continues to increase until reaches the maximum value of 6.72(1) erg/G<sup>2</sup>mol at  $T < T_{\text{SR}} = 6$  K. However,  $\chi_b(T)$  curve shows an upward tail only in the low-temperature region, and  $\chi_b$  is significantly lower than  $\chi_a$  and  $\chi_c$  (Fig. 5.13(b)). This result suggests that a rotation of the net magnetic moments from the  $c$  axis to  $a$  axis occurred at  $T < T_{\text{SR}} = 6$  K, namely,

---

<sup>3</sup>  $\mu_{\text{eff}} = \sqrt{\mu_{\text{Gd}}^2 + \mu_{\text{Cr}}^2}$ ;  $\mu_{\text{Gd}} = g\mu_B \sqrt{J(J+1)} = 7.93 \mu_B$  ( $J = 7, g = 2$ );  $\mu_{\text{Cr}} = 3.873 \mu_B$  ( $J = 3/2, g = 2$ ).

<sup>4</sup> Since the  $\frac{(T-T_0)}{(T-T_N)^{\text{Cr}}}$  term in Eq. 5.2 describes the behavior near  $T_N$ , only  $1/\chi_c$  is analyzed here.

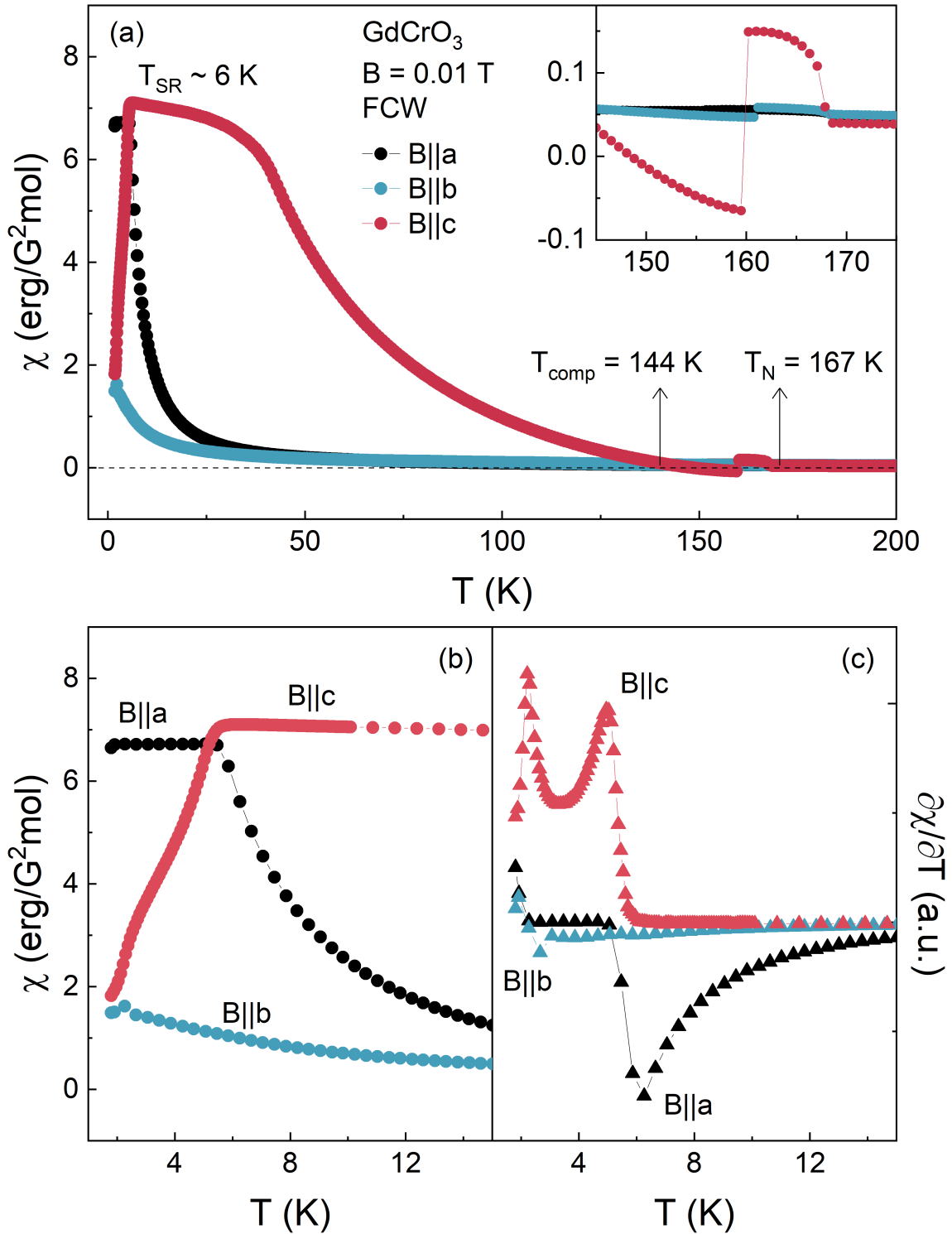


**Figure 5.13:** (a) Temperature dependence of the static magnetic susceptibility  $\chi = M/B$ , obtained at  $B = 0.01$  T for  $B||a$ ,  $B||b$ , and  $B||c$  of GdCrO<sub>3</sub>. (b) Static magnetic susceptibility and (c) its derivative for  $B||a$ ,  $B||b$ , and  $B||c$  at  $B = 0.01$  T and at  $T < 15$  K.  $T_N$ ,  $T_{SR}$ , and  $T_{comp}$  have been determined as described in the text.



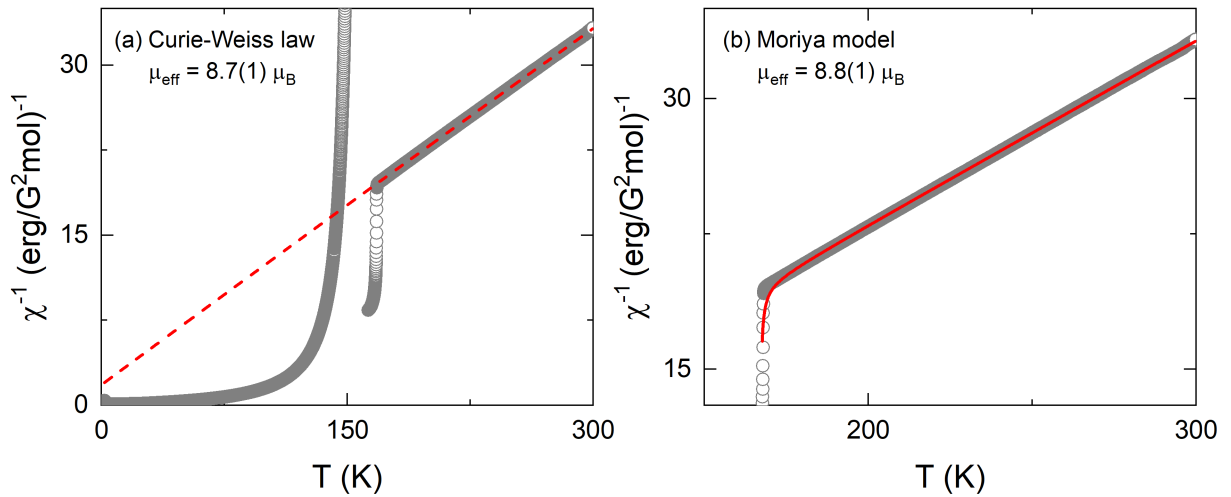


**Figure 5.14:** Inverse static susceptibility  $\chi = M/B$ , obtained at  $B = 0.02$  T for  $B||c$  of  $\text{GdCrO}_3$  and fitted by (a) the CW law (dashed red line) and (b) Moriya model Eq. 5.2 (solid red line).

$\text{GdCrO}_3$  undergoes the SRT from  $\Gamma_4$  ( $G_x, A_y, F_z$ ) to  $\Gamma_2$  ( $F_x, C_y, G_z$ ) spin configuration, which is consistent with previous reports [61–63, 150, 151].

The low-temperature spin configuration is also illustrated by the isothermal magnetization  $M$  vs.  $B$  at  $T = 1.8$  K. As shown in Fig. 5.15, the magnetization curve for  $B||a$  at 1.8 K displays an S-shaped pattern, indicating a weakly ferromagnetic state along the  $a$  axis. The  $M_b(B)$  curve demonstrates a linearly increasing diagonal, characteristic of typical antiferromagnetic behavior. Meanwhile, for  $B||c$ ,  $M_c$  exhibits a gradual increase in the range of  $-0.2$  T  $< B < 0.2$  T, beyond which it undergoes a notable change in the rate of increment. The anomalies on both  $M_a$  and  $M_c$  can also be observed by the derivative curve, which is marked by a broad peak in  $\partial M/\partial B_{||a}$  centered at  $B_a = 0.59(1)$  T (Fig. 5.16(a)) and a sharp peak in  $\partial M/\partial B_{||c}$  centered at  $B_c = 0.24(1)$  T (Fig. 5.16(b)), respectively. Fig. 5.16(c) and (d) illustrate the isothermal magnetization  $M$  vs.  $B$  at different temperatures. Both  $B_a$  and  $B_c$  show variations with temperatures. While  $B_a$  and  $B_c$  may not be evident in the isothermal magnetization results, these anomalies can be traced in the temperature dependence of the relative length changes of  $\text{GdCrO}_3$ , which measurements were conducted along the crystallographic  $a$ ,  $b$ , and  $c$  axis under an applied magnetic field. These anomalies correspond to multiple phase boundaries of the low-temperature AFM phase, which have been discussed in detail by Marius Säubert in his M.S. thesis [153]. Remarkably, a signal of  $\text{Gd}^{3+}$  ordering is observed around 2.2 K. This signal is clearly represented on the magnetic susceptibility  $\partial M/\partial B$  (Fig. 5.13(c)), which is

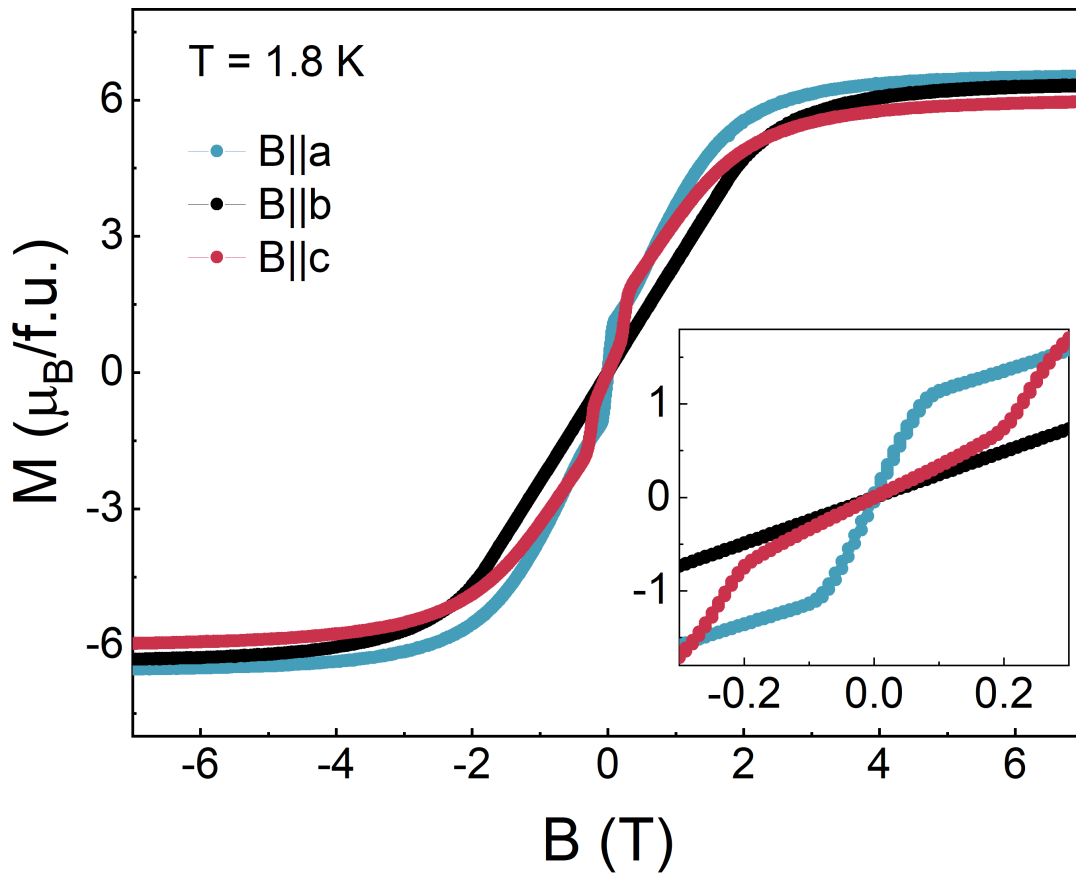


**Figure 5.15:** Isothermal magnetization at  $T = 1.8$  K for  $B||a$ ,  $B||b$ , and  $B||c$  axis of  $\text{GdCrO}_3$ . The inset highlights the behaviour around zero field.

also confirmed by the specific heat results [153].

### 5.3.2.2 Spin Switching Behavior of $\text{GdCrO}_3$

To delve deeper into the spin switching effect, measurements were conducted to examine the dependency between the switching temperature  $T_{\text{sw}}$  and the applied magnetic field. Additionally, the magnetization results obtained from the FCW (Field-Cooling Warming) and FCC (Field-Cooling Cooling) modes (refer to Chapter 2 for a detailed explanation of FCW and FCC measurement) are compared. Fig. 5.17(a) and its enlarged view in Fig. 5.17(b) illustrate the magnetization behavior in the FCW mode, while Fig. 5.17(c) and its magnified version in Fig. 5.17(d) corresponds to the measurements conducted under the FCC mode. Initially, as the measurements involve a warming process (FCW), for  $\text{GdCrO}_3$ , with  $T < T_{\text{SR}} = 6$  K, the  $\text{Gd}^{3+}$  moment is polarized by the weak antiferromagnetic component of the  $\text{Cr}^{3+}$  [112], maintaining an antiparallel arrangement with  $\text{Cr}^{3+}$ , the two

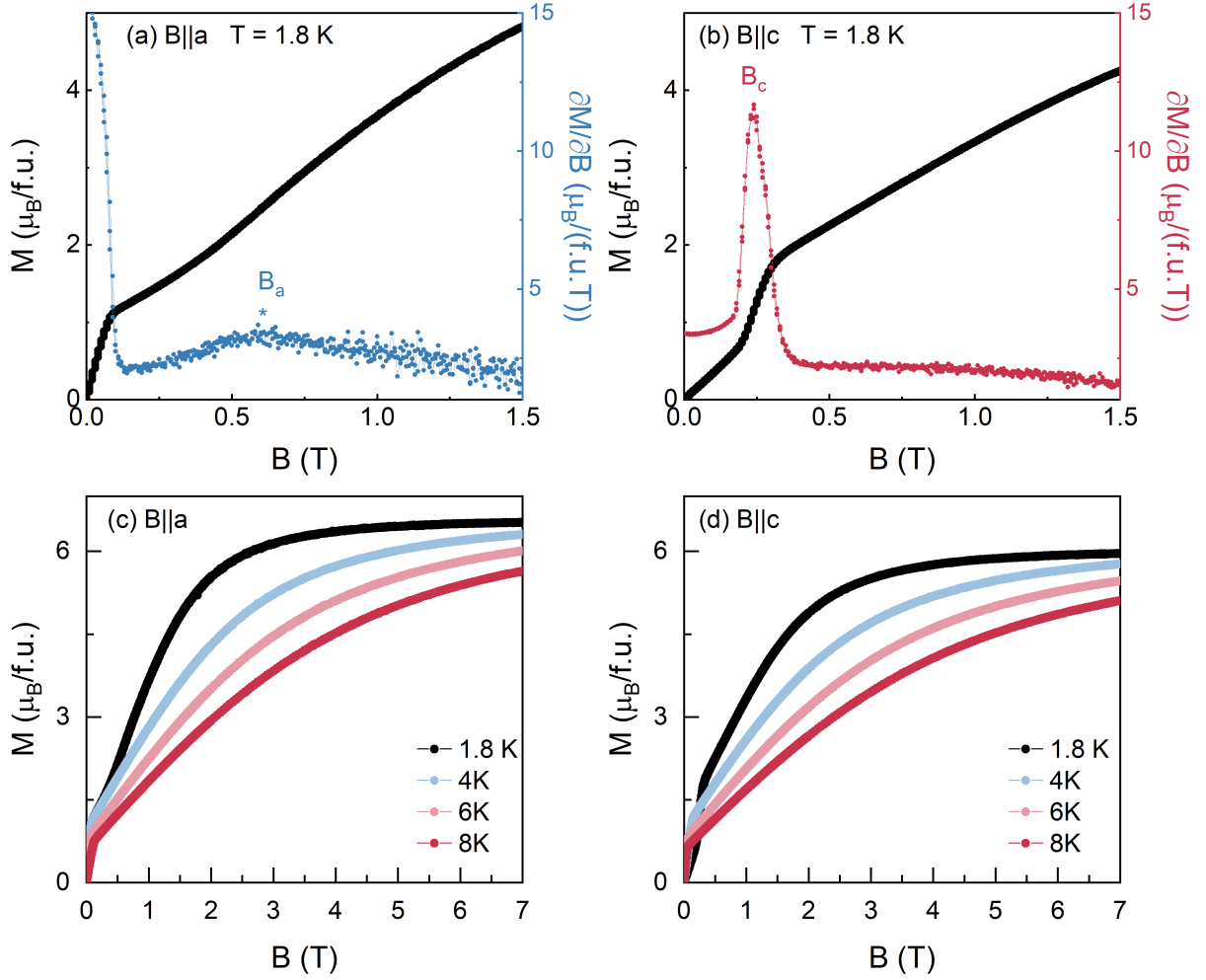


**Figure 5.16:** (a) Isothermal magnetization at  $T = 1.8$  K for  $B||a$  axis (left ordinate) and corresponding magnetic susceptibility  $\partial M/\partial B_{||a}$  (right ordinate) of GdCrO<sub>3</sub>. (b) Isothermal magnetization at  $T = 1.8$  K for  $B||c$  axis (left ordinate) and corresponding magnetic susceptibility  $\partial M/\partial B_{||c}$  (right ordinate) of GdCrO<sub>3</sub>. The critical field  $B_a$  and  $B_c$  as described in the text. (c) Isothermal magnetization for  $B||a$  axis and (d)  $B||c$  axis at different temperatures.

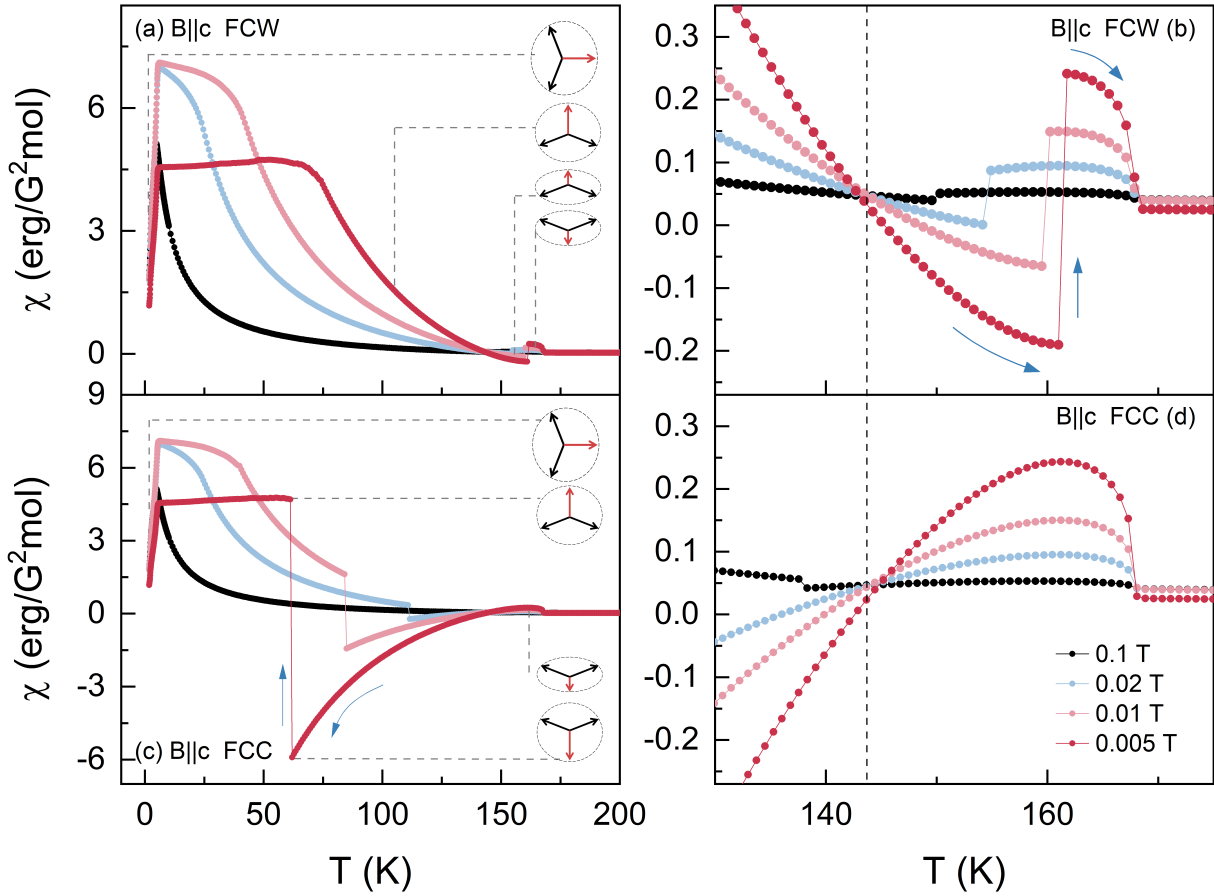


**Figure 5.17:** Temperature dependence of the static magnetic susceptibility  $\chi = M/B$  obtained with different fields for  $B||c$  of  $\text{GdCrO}_3$  from (a-b) the FCW process and (c-d) the FCC process, respectively. The combination of circles and arrows in (a) and (c) illustrates the relative positions of  $\text{Gd}^{3+}$  and  $\text{Cr}^{3+}$  magnetic moments. The blue arrows indicate the (b) warming or (c) cooling processes. The dashed line in (b) and (d) marks the position of  $T_{\text{comp}}$ .

---

moments are arranged along the  $a$  axis (as illustrated in Fig. 5.17(a)). In the temperature range of  $6 \text{ K} < T < 161 \text{ K}$ , the antiparallel alignment persists, but now they align in the  $c$  axis, leading to an overall increase in magnetization with increasing temperature. Both magnetic moments of  $\text{Gd}^{3+}$  and  $\text{Cr}^{3+}$  reverse simultaneously at  $T_{\text{sw}} = 162 \text{ K}$  ( $B = 0.005 \text{ T}$ ), and the relative anti-parallelism of  $\text{Gd}^{3+}$  and  $\text{Cr}^{3+}$  moments persists, resulting in a change of the  $\chi_c$  value from negative to positive. The switching temperature,  $T_{\text{sw}}$  gradually moves to lower temperatures with an increased magnetic field, displaying a weak signal when  $B = 0.1 \text{ T}$ . During measurements accompanied by a cooling process (FCC), however, a brief increase in  $\chi_c$  is observed after  $T < T_{\text{N}} = 167 \text{ K}$ , followed by a continuous decrease until  $\chi_c$  becomes less than zero (see Fig. 5.17(c)). This negative magnetization behavior persists down to  $62 \text{ K}$  at  $B = 0.005 \text{ T}$  with  $\chi_c$  reaching  $-5.90(1) \text{ erg/G}^2\text{mol}$ , preceded by a jump in susceptibility. The  $T_{\text{sw}}$  around  $62 \text{ K}$  gradually shifts to higher temperatures as the magnetic field increases, with faint signs of it still present at  $B = 0.1 \text{ T}$ . In summary, the spin switching effect observed in  $\text{GdCrO}_3$  is intricately tied to the magnetization histories. Specifically, around  $T_{\text{comp}} = 144 \text{ K}$ , the  $T_{\text{sw}}$  on FCW and FCC curves are positioned on the left and right sides of  $T_{\text{comp}}$ , respectively. Both  $T_{\text{sw}}$  on FCW and FCC curves move in the direction of  $T_{\text{comp}}$  with an increase in the magnetic field until  $B > 0.1 \text{ T}$ , after which it becomes unobservable. Building on previous classifications and discussions on spin switching effect [129, 130], it is established that this phenomenon is closely linked to whether rare-earth ions and transition metal ions inherently tend to align in an antiparallel manner. In the case of  $\text{GdCrO}_3$ , the sign of  $\chi_c$  is opposite before and after the spin switching occurs, but its absolute value is numerically close. Hence, the  $\text{Gd}^{3+}$  magnetic moment consistently maintains an antiparallel alignment with the  $\text{Cr}^{3+}$  moment.

Also the temperature dependence of the remanent magnetization ( $M_r$ ) along the  $c$  axis is investigated. The measurements were conducted at  $B = 0 \text{ T}$  during three different FC sequence, as depicted in Fig. 5.18(a), the arrow indicates the starting position of the measurement:

- Sequence 1, FC with  $B = 1 \text{ T}$  to  $T = 130 \text{ K} < T_{\text{comp}}$  (black):  
The magnetic moment of  $\text{Gd}^{3+}$  aligns with the cooling field, resulting in a positive value of  $M_r$  at the initial temperature  $130 \text{ K}$ . As the temperature decreases, the  $\text{Gd}^{3+}$  magnetic moment increases under the influence of the internal field ( $B_{\text{I}}$ ) originating from the ordered  $\text{Cr}^{3+}$  spins.
- Sequence 2, FC with  $B = 1 \text{ T}$  to  $T = 160 \text{ K} > T_{\text{comp}}$  (green):  
At the initial temperature  $160 \text{ K}$ , the  $\text{Cr}^{3+}$  moment dominates (positive  $B_{\text{I}}$ ) and the

$\text{Gd}^{3+}$  moment is aligned antiparallel to it, with the absolute value still increasing as the temperature decreases.

- Sequence 3, FC with  $B = 1 \text{ T}$  to  $T = 1.8 \text{ K} < T_{\text{comp}}$  (orange).

The remarkable spin switching behavior observed in  $\text{GdCrO}_3$  finds its explanation in the model proposed by Cooke et al. [154]. This model considers the canted FM moment of  $\text{Cr}^{3+}$  spins, resulting from DM interactions, along with the opposite paramagnetic moments arising from antiferromagnetic interactions between  $\text{Cr}^{3+}$  and  $\text{Gd}^{3+}$  spins. The temperature dependence of magnetization can be described by the Eq. 5.5:

$$M = M_{\text{Cr}} + \frac{C_{\text{Gd}}(B - B_{\text{I}})}{T + \Theta_{\text{W}}}. \quad (5.5)$$

with the canted magnetization of  $\text{Cr}^{3+}$ :  $M_{\text{Cr}}$ , the Curie constant:  $C_{\text{Gd}}$ , the internal exchange field generated by the ordered  $\text{Cr}^{3+}$ :  $B_{\text{I}}$ , and the Weiss constant:  $\Theta_{\text{W}}$ . Note that  $B_{\text{I}}$  is in opposed direction to  $M_{\text{Cr}}$ . The analysis based on I. Fita [62] shows that, spin switching is caused by an instantaneous fall in the Zeeman energy  $E_{\text{Z}}$ , see Eq. 5.6. Meanwhile, the report from I. Fita [62] also indicates that  $E_{\text{Z}}$  should reach a maximum  $E_{\text{Z1}}$  and a minimum  $E_{\text{Z2}}$  when the spin configuration achieves the negative magnetization state ( $E_{\text{Z1}}$ ), and when the magnetization is parallel to applied magnetic field  $B$  ( $E_{\text{Z2}}$ ), respectively.

$$E_{\text{Z}} = -M \cdot B. \quad (5.6)$$

$$E_{\text{Z1}} = -\left[M_{\text{Cr}} + \frac{C_{\text{Gd}}(B - B_{\text{I}})}{T + \Theta_{\text{W}}}\right] \cdot B. \quad (5.7)$$

$$E_{\text{Z2}} = -\left[-M_{\text{Cr}} + \frac{C_{\text{Gd}}(B - B_{\text{I}})}{T + \Theta_{\text{W}}}\right] \cdot B. \quad (5.8)$$

$$\Delta E = -2\left[M_{\text{Cr}} - \frac{C_{\text{Gd}}B_{\text{I}}}{T + \Theta_{\text{W}}}\right] \cdot B_{\text{sw}}. \quad (5.9)$$

Therefore  $T_{\text{comp}}$  is obtained from  $M_{\text{Cr}} - \frac{C_{\text{Gd}}B_{\text{I}}}{T + \Theta_{\text{W}}} = 0$ :

$$T_{\text{comp}} = \frac{C_{\text{Gd}}B_{\text{I}}}{M_{\text{Cr}}} - \Theta_{\text{W}}. \quad (5.10)$$

$B_{\text{sw}}$  is obtained by when  $M = B = 0$  in Eq. 5.5 and taking into account  $T_{\text{comp}}$ :

$$B_{\text{sw}} = \pm \frac{\Delta E}{2M_{\text{Cr}}} \cdot \frac{(T + \Theta_{\text{W}})}{T - T_{\text{comp}}}. \quad (5.11)$$

---

with “ + ” for the temperature region  $T > T_{\text{comp}}$ , and “ - ” for the  $T < T_{\text{comp}}$ .

Taking the theoretical values of the Gd-ordered temperature of 2.3 K and the effective magnetic moment of  $7.94 \mu_{\text{B}}$ , the fitting results according to Eq. 5.5 are shown as the red line in Fig. 5.18(a), which yields the  $M_{\text{Cr}} = 236(1)$  erg/Gmol,  $B_{\text{I}} = 0.43(1)$  T for Sequence 1 and  $M_{\text{Cr}} = 242(1)$  erg/Gmol,  $B_{\text{I}} = 0.43(1)$  T for Sequence 2. Therefore  $T_{\text{comp}} = 139(1)$  K according to Eq. 5.10, which is lower than the experience result  $T_{\text{comp}} = 144$  K (Fig. 5.13). The  $T_{\text{sw}}$  of FCC measurement at various magnetic fields can also be determined from Fig. 5.17(c). The  $T_{\text{sw}}$  represented by the black data points in Fig. 5.18(b), by fitting according to Eq. 5.11 yields  $T_{\text{comp}} = 148(1)$  K,  $\Delta E = 3.11(6) \times 10^4$  erg/mol (for Sequence 1) and  $\Delta E = 3.17(7) \times 10^4$  erg/mol (for Sequence 2). The  $T_{\text{comp}}$  obtained from Eq. 5.5 and Eq. 5.11 are slightly elevated because the impact of the sample’s demagnetization factor is not considered in the fitting process.

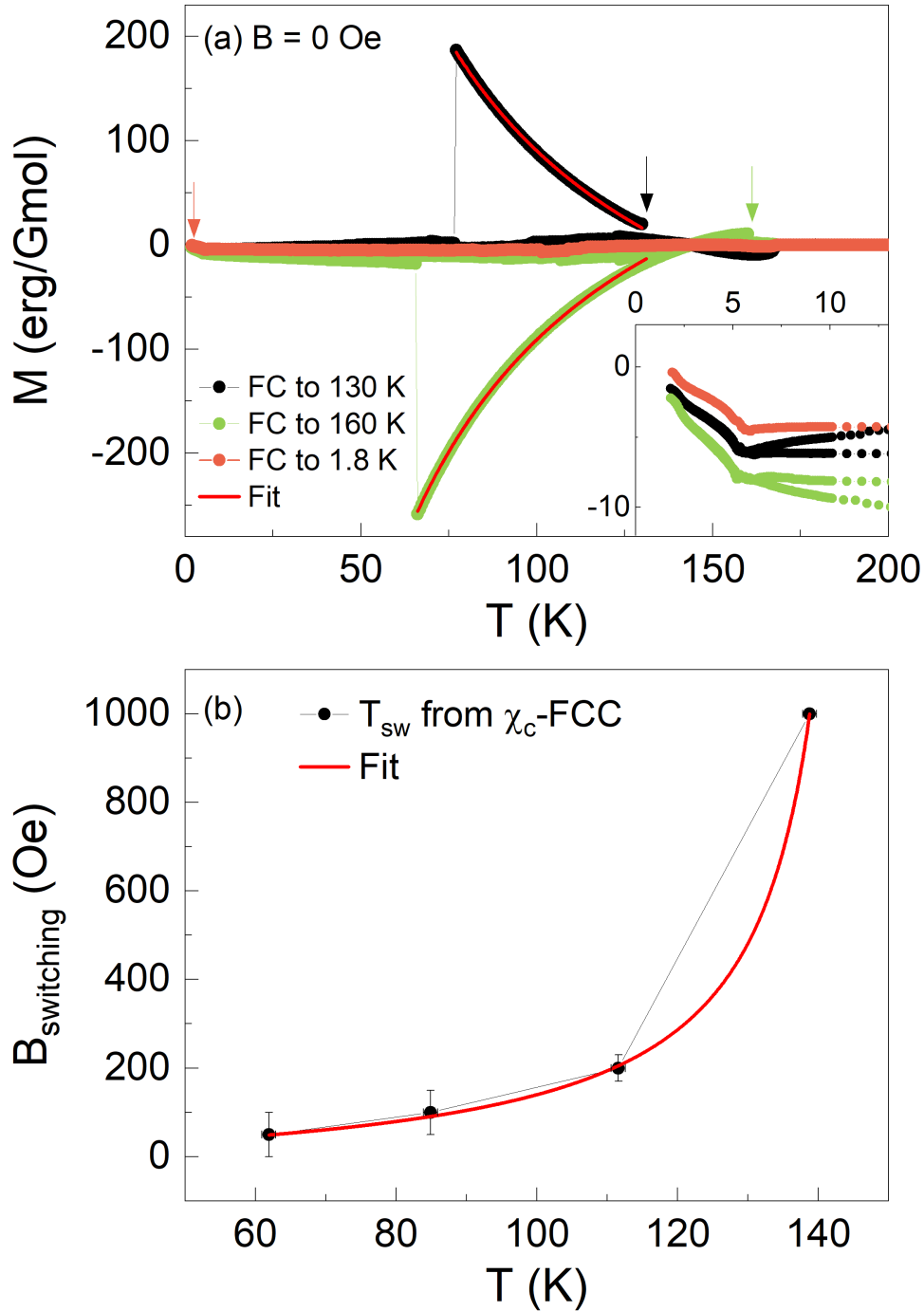


**Figure 5.18:** (a) The remanent magnetization  $M_r$  of  $\text{GdCrO}_3$  measured along the  $c$  axis at  $B = 0$  T by the three FC ( $B = 1$  T) sequences as described in text. Each of the three colored arrows corresponds to the starting position of the measurement. The red lines represent the outcome of fitting by Eq. 5.5. Inset highlights the behavior of low-temperature region. (b) The dependence of  $T_{\text{sw}}$  on  $B_{\text{sw}}$  as read from Fig. 5.18(b) and the fitting result (red line) via Eq. 5.11.



---

### 5.3.3 SmCrO<sub>3</sub>

#### 5.3.3.1 Magnetization $M(T, B)$

Analogous to ErCrO<sub>3</sub> and GdCrO<sub>3</sub>, the SmCrO<sub>3</sub> single crystals also show pronounced magnetic anisotropy, as shown in Fig. 5.19. The long-range AF ordering starts at  $T_N = 192$  K accompanied by a significant increase in  $\chi_c$ , which is consistent with previous studies on polycrystals [121, 134, 155]. Above 350 K, the variation of magnetic susceptibility with temperature presents a CW like behavior as demonstrated by  $\chi_c^{-1}(T)$  in Fig. 5.20 (red line). Fitting the data obtained at 1 T yields the effective moment  $\mu_{\text{eff}} = 3.5(1) \mu_B$ , Weiss temperature  $\Theta_W = -375(3)$  K and diamagnetic constant background term  $\chi_0 = -2.55 \times 10^{-11}$  erg/G<sup>2</sup>mol. The  $\mu_{\text{eff}}$  is lower than those reported previously [121, 138, 156], but much closer to the theoretical value  $3.96 \mu_B^5$ . The fit based on Eq. 5.2 is also displayed in Fig. 5.20 (blue line), which yields  $\mu_{\text{eff}} = 3.6(1) \mu_B$ ,  $\Theta_W = -435(2)$  K,  $J = 12.84(1) k_B$  and  $D = 1.54(2) k_B$ . Upon cooling below  $T_N$ ,  $\chi_c$  reaches a maximum value of  $1.91(1)$  erg/G<sup>2</sup>mol at approximately 73 K and subsequently decreasing sharply at  $T_{\text{SR}} \approx 33$  K. Meanwhile,  $\chi_a$  increases rapidly and  $\chi_b$  also increase, suggesting the net magnetic moments in the system tend to align along the  $c$  axis for  $T_{\text{SR}} < T < T_N^6$ , while they rotate from the  $c$  axis to the  $ab$  plane for  $T < T_{\text{SR}}$ .

The rotation of the small ferromagnetic moment from the  $c$  axis towards  $ab$  plane is confirmed by isothermal magnetization data in Fig. 5.21. At  $T = 1.8$  K, the  $M_a$  ( $M_b$ ) data evidence a small remanent moment of  $0.013 \mu_B/\text{f.u.}$  ( $0.0049 \mu_B/\text{f.u.}$ ) and hysteresis of about 0.1 T (0.14 T). In contrast, there is no hysteresis for  $B||c$ , which further confirmed the rotation of the net magnetic moments. The linearly increased magnetization with increasing magnetic field reveals the AFM behaviour. Moreover, at the maximum value of the 7 T field,  $M_c$  ( $M_b$ ) is about 48% (58%) of  $M_a$ , while none of the three  $M_c$ ,  $M_b$  and  $M_a$  are saturated at the 7 T field. At  $T = 20$  K, there is a kink feature around  $B_c = 6.4(1)$  T, which presents as a broad peak on  $\partial M/\partial B||c$ , as seen in Fig. 5.21(b). Similar feature around  $B_a = 2.3(1)$  T is shown for  $B||a$  at  $T = 40$  K (Fig. 5.21(c)). This work presumes that with increasing magnetic field when  $B||c$ , a field-induced SRT with the net magnetic

---

<sup>5</sup>  $\mu_{\text{eff}} = \sqrt{\mu_{\text{Sm}}^2 + \mu_{\text{Cr}}^2}$ ;  $\mu_{\text{Sm}} = g\mu_B \sqrt{J(J+1)} = 0.845 \mu_B$  ( $J = 5/2$ ,  $g = 2/7$ );  $\mu_{\text{Cr}} = 3.873 \mu_B$  ( $J = 3/2$ ,  $g = 2$ ).

<sup>6</sup> For  $T_{\text{SR}} < T < T_N$ , there is only a very small anomaly in  $\chi_a$  ( $\chi_b$ ) which is only 2.3 % (3.8 %) of the one in  $\chi_c$ , and this is within the error bars of the crystal orientation and the cutting process so that the data presented in this work do not imply a net spin component  $\perp c$  axis.

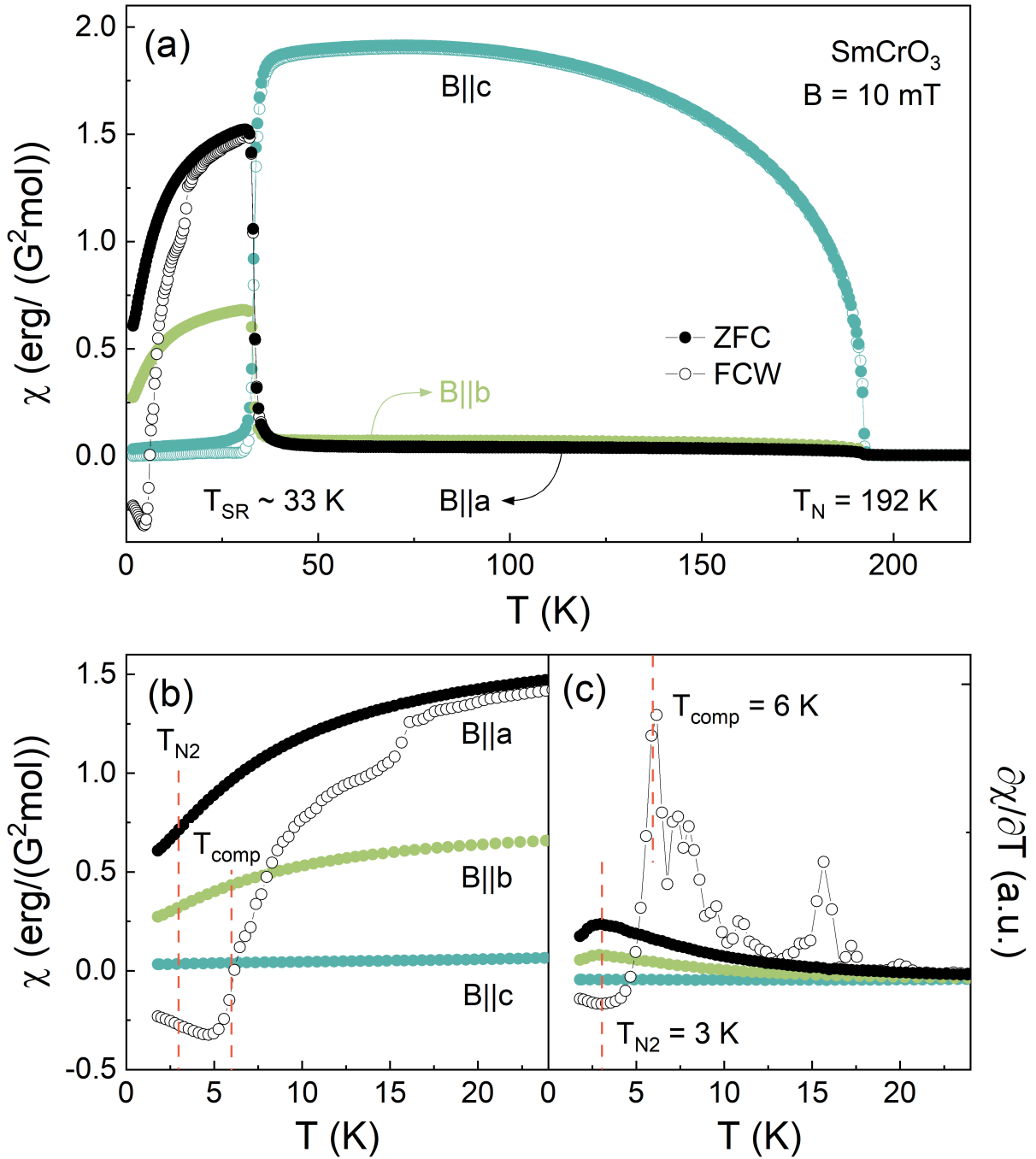


**Figure 5.19:** (a) Temperature dependence of the static magnetic susceptibility  $\chi = M/B$ , obtained at  $B = 0.01$  T for  $B||a$ ,  $B||b$ , and  $B||c$  of SmCrO<sub>3</sub>. ZFC and FCW data are represented by open and solid circles, respectively. (b) Static magnetic susceptibility and (c) its derivative for  $B||c$ ,  $B||b$ , and  $B||a$  at  $B = 0.01$  T and at  $T \leq 30$  K.  $T_N$ ,  $T_{N2}$ , and  $T_{comp}$  have been determined as described in the text.

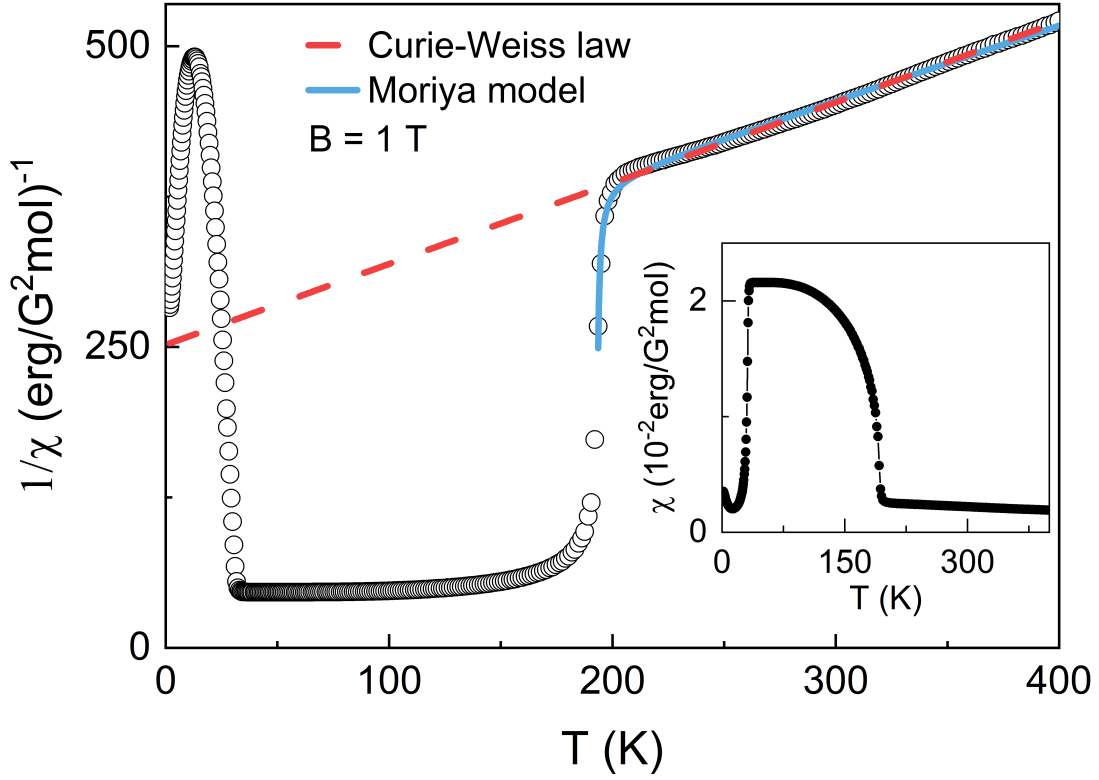


**Figure 5.20:** Inverse static susceptibility  $\chi = M/B$ , obtained at  $B = 1$  T applied for  $B||c$  of  $\text{SmCrO}_3$  fitted by the CW law and Moriya model Eq. 5.4. Inset: Temperature dependence of the static magnetic susceptibility  $\chi = M/B$ , obtained at  $B = 1$  T applied for  $B||c$  (FCW).

moments rotated from  $ab$  plane to  $c$  axis is undergoing centered around  $B_c = 6.4(1)$  T, and the net magnetic moments rotated from  $c$  axis to  $ab$  plane is evolving centered on  $B_a = 2.3(1)$  T for  $B||a$ . In the following,  $M_a$  and  $M_c$  are compared primarily.

To visualize the reorientation region, a series of magnetic hysteresis loop is shown in Fig. 5.22(a)-(e) for  $B||c$  and (f)-(j) for  $B||a$ . At  $T < T_{\text{SR}}$ , no hysteresis loop is observed for  $B||c$ , Fig. 5.22(a) shows the standard linear AFM behaviour at 10 K, and the line becomes an S-shaped curve without hysteresis for  $T = 35$  K, finally a rectangular hysteresis loop is observed for  $T > T_{\text{SR}}$ . Additionally, the remanent magnetic moments  $M_r^a$  and  $M_r^c$  can be derived from a series of hysteresis loops. The temperature dependence of  $M_r^a$  and  $M_r^c$  are shown in Fig. 5.23(a). The dashed line marks the position of the SRT which is determined from Fig. 5.19. Notably, the moment at  $T < T_{\text{SR}}$  is smaller than  $T > T_{\text{SR}}$ , implies the presence of a finite weak ferromagnetic moment along the  $b$  axis in  $T < T_{\text{SR}}$ . Hence, for  $T > T_{\text{SR}}$ , the measured value  $\chi_c$  is approximately equal to the total net magnetic moments  $M'$  in the system. For  $T < T_{\text{SR}}$ , the measured values  $\chi_a$  ( $\chi_b$ ) can be considered as the projection of  $M'$  on the  $a$  ( $b$ ) axis. Thus, the angle  $\alpha$  between  $M_r^a$  and  $M'$  at  $T < T_{\text{SR}}$  can

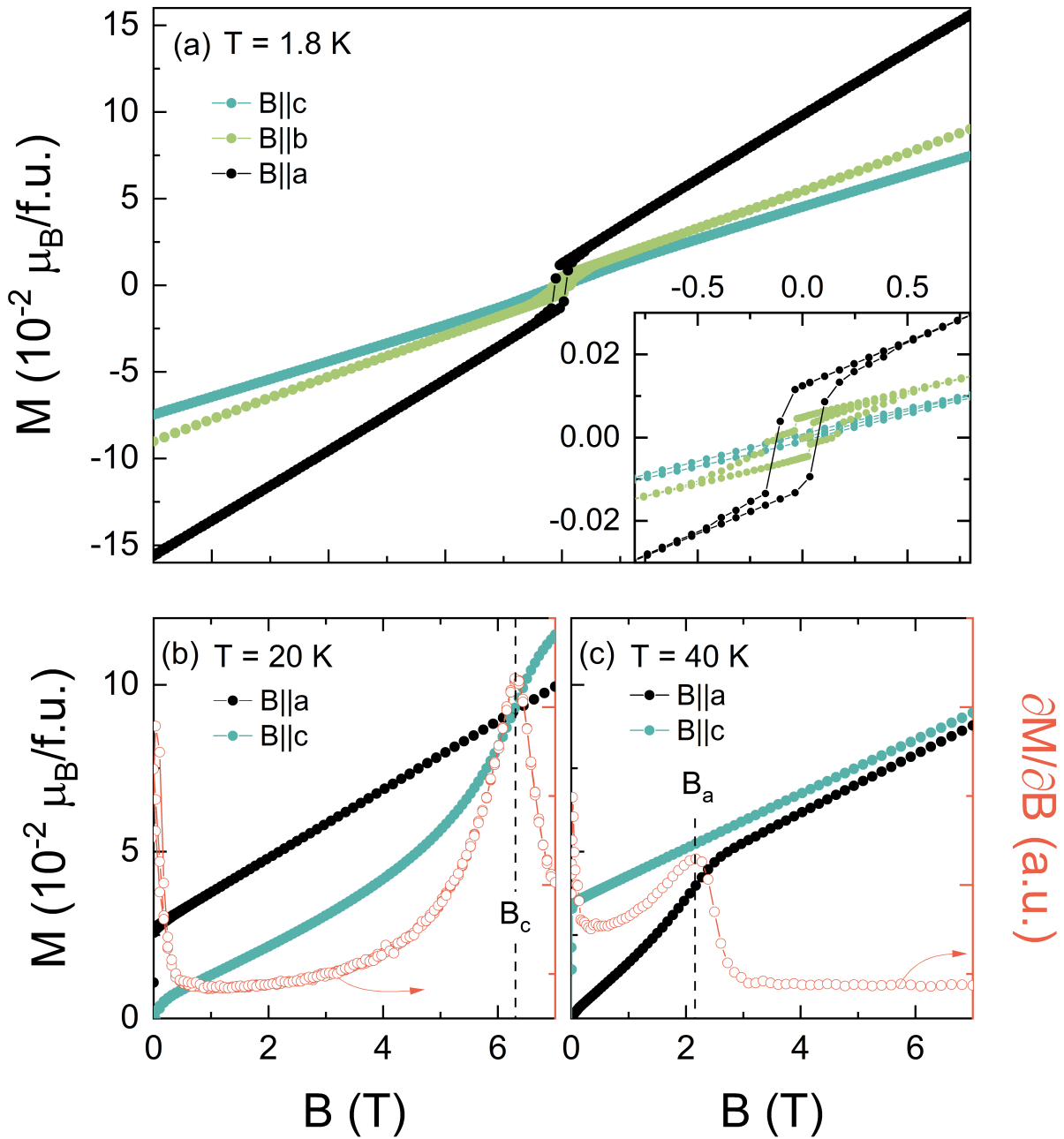


**Figure 5.21:** (a) Isothermal magnetization at  $T = 1.8$  K for  $B||c$ ,  $B||b$ , and  $B||a$  axis of  $\text{SmCrO}_3$ . The inset highlights the behaviour around zero field. Isothermal magnetization (b) at  $T = 20$  K for  $B||c$  axis (left ordinate) and corresponding magnetic susceptibility  $\partial M/\partial B_{||c}$  (right ordinate), (c) at  $T = 40$  K for  $B||a$  axis (left ordinate) and corresponding magnetic susceptibility  $\partial M/\partial B_{||a}$  (right ordinate). The dashed lines indicate the critical field  $B_c$  and  $B_a$  as described in the text.

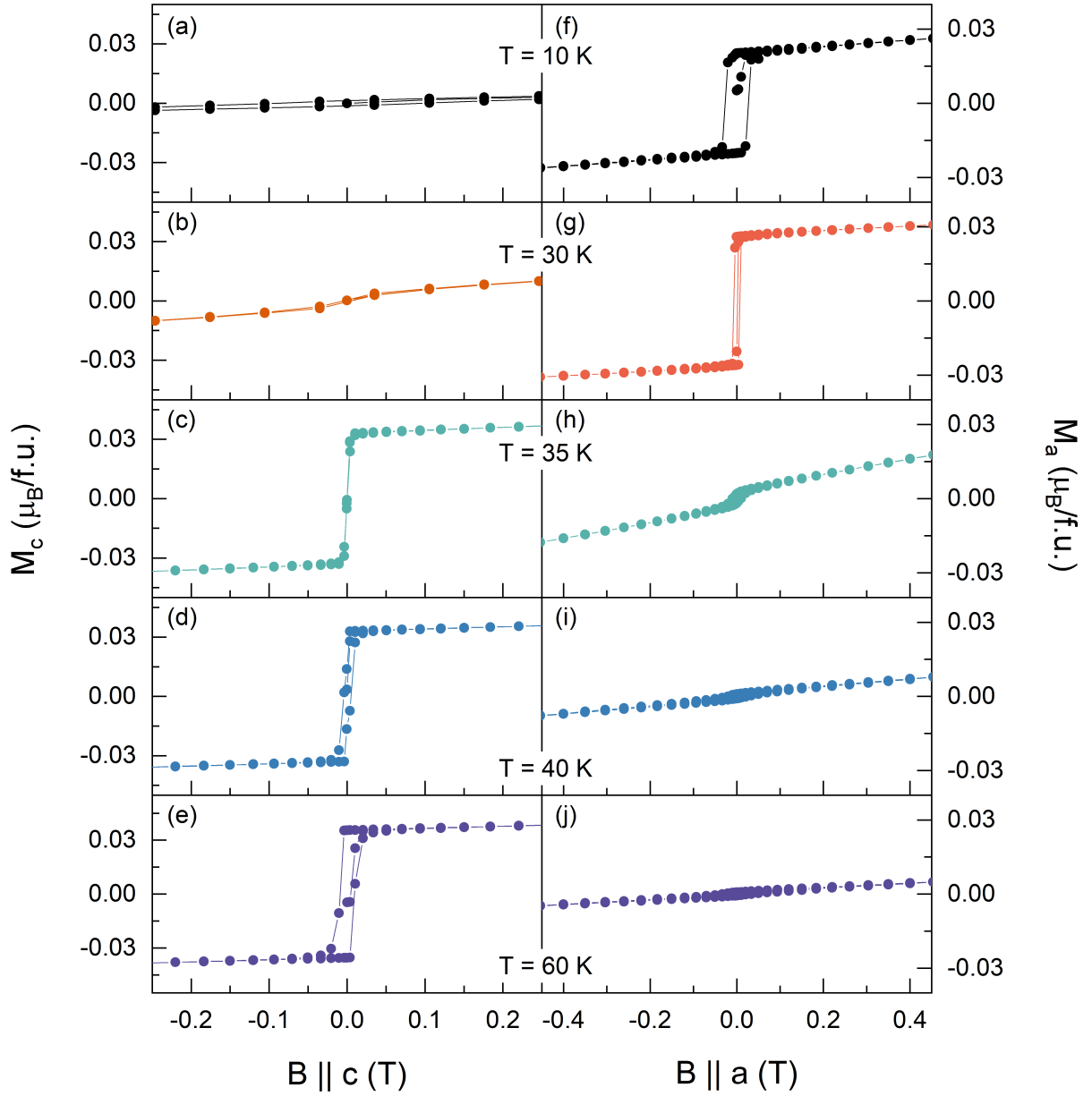


**Figure 5.22:** Isothermal magnetization at different temperatures for (a-e)  $B||c$  axis and (f-j)  $B||a$  axis of  $\text{SmCrO}_3$ .

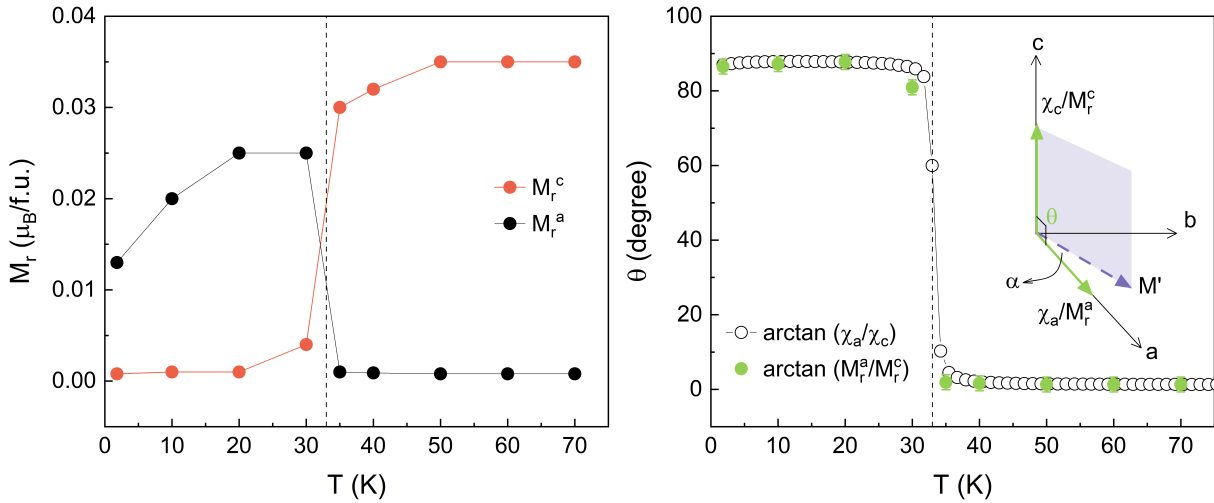


**Figure 5.23:** (a) Temperature dependence of the remanent magnetic moment  $M_r^a$  and  $M_r^c$  read from isothermal magnetization. (b) The temperature dependence of rotation angle  $\theta$ . Open black circles: calculated  $\theta$  from the static magnetic susceptibility  $\chi = M/B$  obtained at  $B = 0.01$  T for  $B||a$  and  $B||c$ . Solid green circles: calculated  $\theta$  from  $M_r^a$  and  $M_r^c$  obtained from isothermal magnetization.  $a$ ,  $b$ , and  $c$  in the schematic indicate the crystallographic axis direction, with all three perpendicular to each other. The description of  $\alpha$ ,  $\theta$  and  $M'$  is given in the text. Dashed lines mark the center of the SRT.

be estimated to be approximately  $24^\circ$ . More on magnetization behavior for  $B||b$  is not measured in this work.

The rotation of the net magnetic moments can also be visualized as the temperature dependence of rotation angle  $\theta$  [157] (see Fig. 5.23(b)):

$$\theta = \arctan\left(\frac{M_r^a}{M_r^c}\right). \quad (5.12)$$

$\theta$  can be estimated from  $\chi_c/\chi_a$  or  $M_r^a/M_r^c$ , both results are shown in Fig. 5.23(b) as the open and solid circle respectively. The two estimates are highly overlapping. Here,  $\theta$  characterizes the rotation of the magnetic moment in the  $ac$  plane, whereas the actual rotation plane of  $M'$  might be approximated by the purple plane illustrated in Fig. 5.23(b). Thus,  $\theta = 90^\circ$  merely represents the alignment of the magnetic moment in the  $ab$  plane. In summary, the weak ferromagnetic moments are mainly aligned along the  $c$  axis when  $T > T_{SR}$ , implying the spin configuration is  $\Gamma_4$ . For  $T < T_{SR}$ , the magnetic moments rotate from the  $c$  axis to  $ab$  plane, exhibiting a  $\Gamma_2$ -dominated spin configuration, and a mixture of multiple spin configurations may be present. Additional measurements, such as neutron diffraction on single crystals, are required to clarify this result.

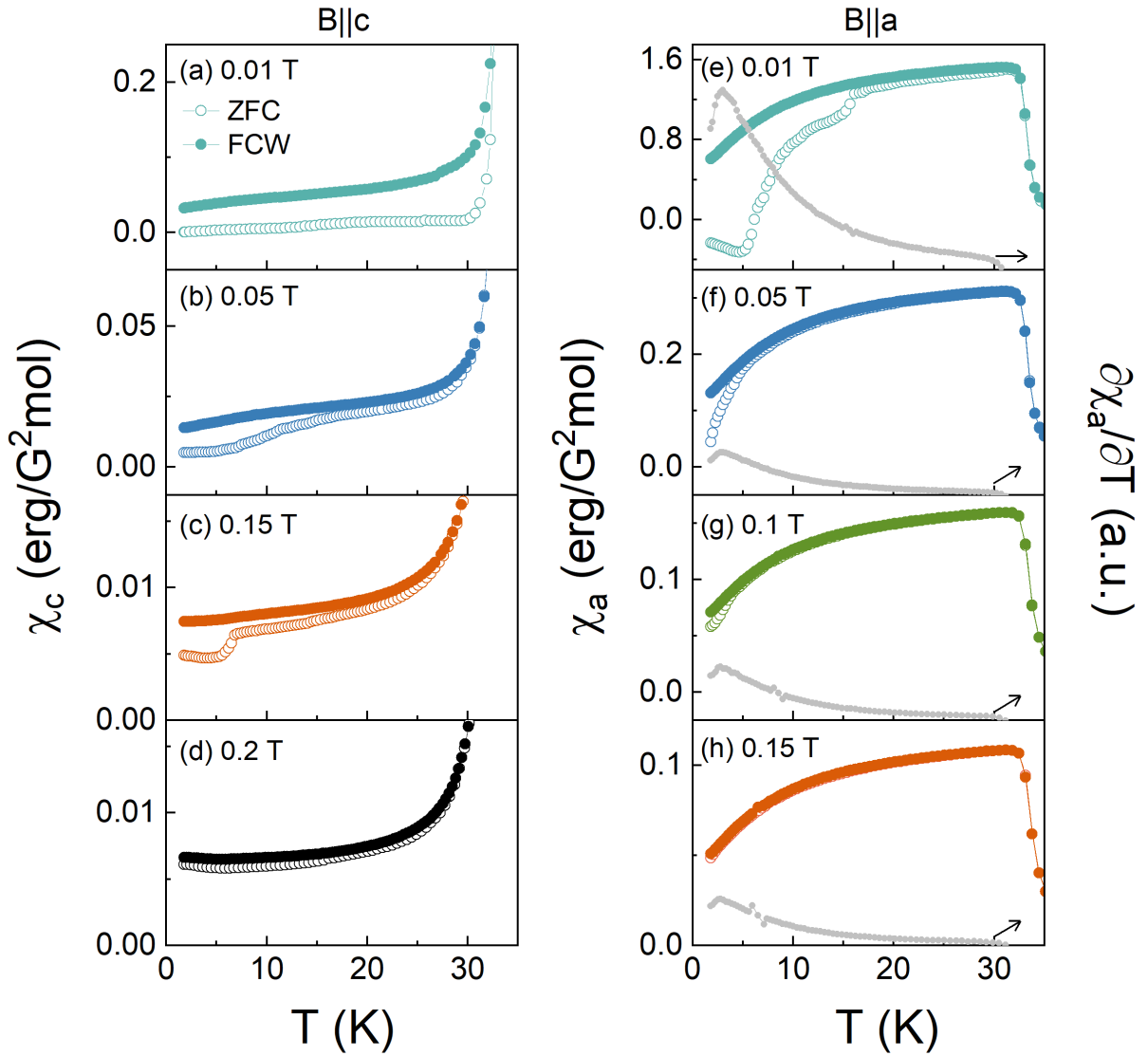


**Figure 5.24:** Temperature dependence of the static magnetic susceptibility  $\chi = M/B$ , obtained at different fields applied along the crystallographic (a-d)  $c$  axis and (e-f)  $a$  axis of  $\text{SmCrO}_3$ , respectively. ZFC and FCW data are labeled with open and solid circles and the grey solid circles indicate the derivative of susceptibilities for  $B||a$  (right ordinates).

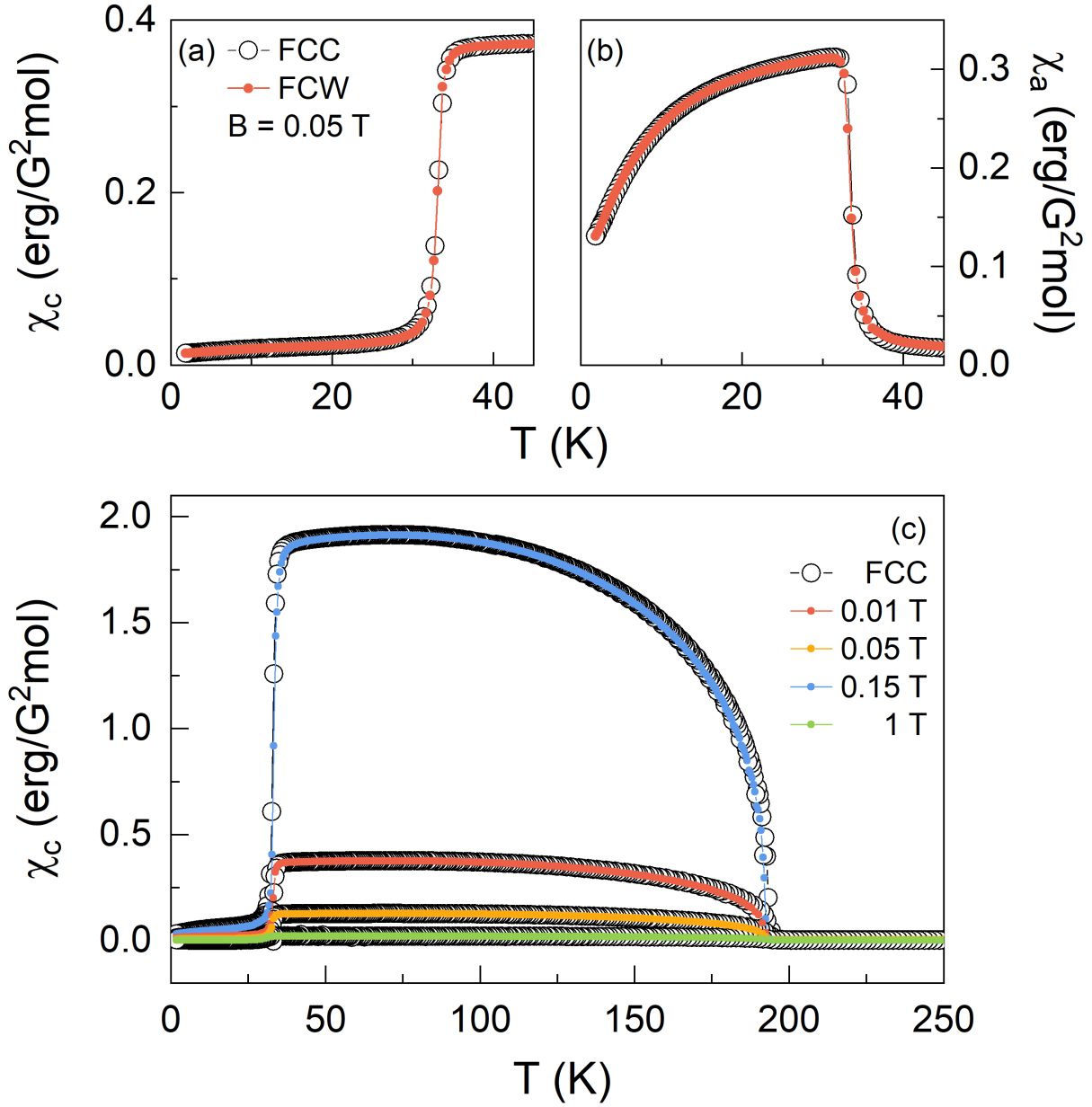


**Figure 5.25:** Temperature dependence of the static magnetic susceptibility  $\chi = M/B$ , obtained at  $B = 0.05$  T applied along the crystallographic (a)  $c$  axis and (b)  $a$  axis of  $\text{SmCrO}_3$ . (c) Static magnetic susceptibility  $\chi_c^{\text{FCC}}$  (open circles) and  $\chi_c^{\text{FCW}}$  (solid circles) at different external magnetic fields up to 1 T.



Upon cooling, there is a pronounced hysteresis between the  $\chi_a$  data obtained after FC and ZFC<sup>7</sup>, confirms the presence of the weak ferromagnetic component in the  $ab$  plane (see Fig. 5.19(b)). Although this bifurcation is also present in  $\chi_c$ , it is only about 7(1)% of the  $\chi_a$  ( $\sim 30$  K). Particularly,  $\chi_c^{\text{ZFC}} = 0$  at compensation point around  $T_{\text{comp}} = 6$  K, with negative  $\chi_c^{\text{ZFC}}$  at lower temperature. At  $T_{\text{comp}}$ , the magnetic moments of  $\text{Sm}^{3+}$  and  $\text{Cr}^{3+}$  are of equal magnitude and opposite directions, offsetting each other and leading to  $\chi = 0$ . The persistent decrease of  $\chi_a$  in the low-temperature region implicates the ordering of  $\text{Sm}^{3+}$ , which can be clearly observed for  $T_{\text{N}2} = 3$  K in the derivative  $\partial\chi_a/\partial T$ . The tail of the  $\chi_a^{\text{ZFC}}$  also suggests the antiparallel arrangement of  $\text{Sm}^{3+}$  and  $\text{Cr}^{3+}$  magnetic moments.

To further discuss the influence of magnetization histories on  $\text{SmCrO}_3$ , Fig. 5.24 present the effect of magnetic field on the static magnetic susceptibility  $\chi_c$  and  $\chi_a$ , where the FCW and ZFC curves are labeled with solid and open circles, respectively. At low magnetic fields ( $B < 0.2$  T), the bifurcation between the  $\chi_{\text{FCW}}$  and  $\chi_{\text{ZFC}}$  vanishes with increasing magnetic fields, suggesting the effect of the internal field caused by the  $\text{Cr}^{3+}$  sublattice is hidden by increased measurement fields. Due to various competitive interactions between the  $\text{Cr}^{3+}$  and  $\text{Sm}^{3+}$  moments, short-range ordered ferromagnetic compositions may exist at low temperatures, as illustrated by the presence of both the bifurcation and the kink of  $\chi_a^{\text{ZFC}}$  at around 16 K. An additional remark is that one may attribute the bifurcation behavior of the  $\chi_c^{\text{FCW}}$  and  $\chi_c^{\text{ZFC}}$  to the orientation and cutting errors of the single crystal sample, which causes the angle of the  $a$ ,  $c$  axis to deviate severely from 90 degrees. However, it is worth noting that at  $B = 0.015$  T, the  $\chi_c^{\text{FCW}}$  and  $\chi_c^{\text{ZFC}}$  bifurcate (see Fig. 5.24(c)), while the  $\chi_a^{\text{FCW}}$  and  $\chi_a^{\text{ZFC}}$  are highly overlapped, and  $\chi_a$  is an order of magnitude larger than  $\chi_c$  at  $B = 0.015$  T (see Fig. 5.24(h)), which rules out the possibility that the angle between  $a$  and  $c$  axis is seriously off by 90 degrees. In addition, the signal of  $\text{Sm}^{3+}$  ordering  $T_{\text{N}2} = 3$  K can be traced on the  $d\chi/dT$ , and the corresponding derivative of susceptibility are indicated by gray solid circles in Fig. 5.24(e)-(h).

There has been controversy about the type of SRT for  $\text{SmCrO}_3$ , between Tripathi et al. [158] and Sau et al. [138] giving the magnetic structure probed by neutron diffraction. The former concluded that the low-temperature spin configuration is  $\Gamma_1$  and the latter suggested  $\Gamma_2$ . The reason for this debate may be that the high neutron absorption of  $^{149}\text{Sm}$ , one of the Sm isotope in natural Sm compounds, makes it challenging to determine the spin structure of  $\text{SmCrO}_3$  by neutron diffraction [138, 158]. However, the data of

<sup>7</sup> The applied magnetic field was zeroed out by using the oscillation mode at room temperature before ZFC measurement begins. Hence the remnant field is  $< 10^{-3}$  T.

SmCrO<sub>3</sub> single crystal sample presented in this work show that the spin configuration at low temperatures is not strictly  $\Gamma_1$  or  $\Gamma_2$ , instead it may be a mixed or in-homogeneous spin configurations. Additionally, the discussion from Sau et al. [156] on whether the SRT is first- or second-order nature pointed out that, for the DC susceptibility measurement, two hysteresis regions were noticeable in the FCC and FCW cycles. Sau et al. concluded that hysteresis regions implied the SRT was composed of two steps, continuous rotation and discontinuous jump, with the former being second-order behavior and the latter responding to a first-order nature of SRT. The data presented in this work, instead, show distinctly opposite results, with a highly overlapping between FCC and FCW cycle measurements and no hysteresis regions for either  $\chi_a$  or  $\chi_c$ , which indicates the continuous transition of spins. Nevertheless, only the magnetization data from this work are not sufficient to answer the question of whether SRT is first- or second-order phase transition, and further low-temperature specific heat analysis is essential.

### 5.3.3.2 Magnetic Phase Diagrams

The isothermal magnetization and magnetic susceptibility  $\partial M/\partial B$  for  $B||c$  between 20 K and 32 K is shown in Figs. 5.26(a) and (b). For  $T < T_{SR}$ , the temperature dependence of the field-induced SRT boundaries could be traced. As the temperature decreases,  $B_c$  continuously increases up to  $T = 20$  K after which it is no longer traceable beyond the upper limit of the measured field (7 T). To illustrate the location of the field-induced SRT in more detail, its upper and lower limits are labeled  $B_c^\nabla$  and  $B_c^\Delta$ , respectively (as shown in the inset of Fig. 5.26(a)), the experimentally obtained jumps in  $M$  between  $B_c^\nabla$  and  $B_c^\Delta$  is denoted as  $\Delta M$ . For  $B||a$ , the analogous feature is exhibited in Fig. 5.27. The distinct anomalies on  $\partial M/\partial B_{||c}$  and  $\partial M/\partial B_{||a}$  are marked as  $B_c$  and  $B_a$ , respectively, corresponding to the center of the field-induced SRT. Based on  $B_c$  and  $B_a$ , combined with  $T_N$ ,  $T_{N2}$ ,  $T_{SR}$ , and  $T_{comp}$  from  $M$  vs.  $T$  measurements, Fig. 5.28 illustrate the phase diagrams for  $0 < B < 7$  T applied along the  $a$  axis and  $c$  axis.

- For  $B||c$ , applying magnetic fields up to 7 T,  $T_N$  is only slightly shifts to higher temperatures. The phase boundary at  $T_N = 192$  K separates the paramagnetic (PM) phase and the antiferromagnetic (AFM) phase. Whereas the increase in the magnetic field significantly affects the  $T_{SR}$ . The AF II phase persists until 33 K at low field, the phase boundary starting at  $T = 33$  K and moves toward the high field with decreasing temperature, which signaling the field-induced SRT, i.e., the weak net

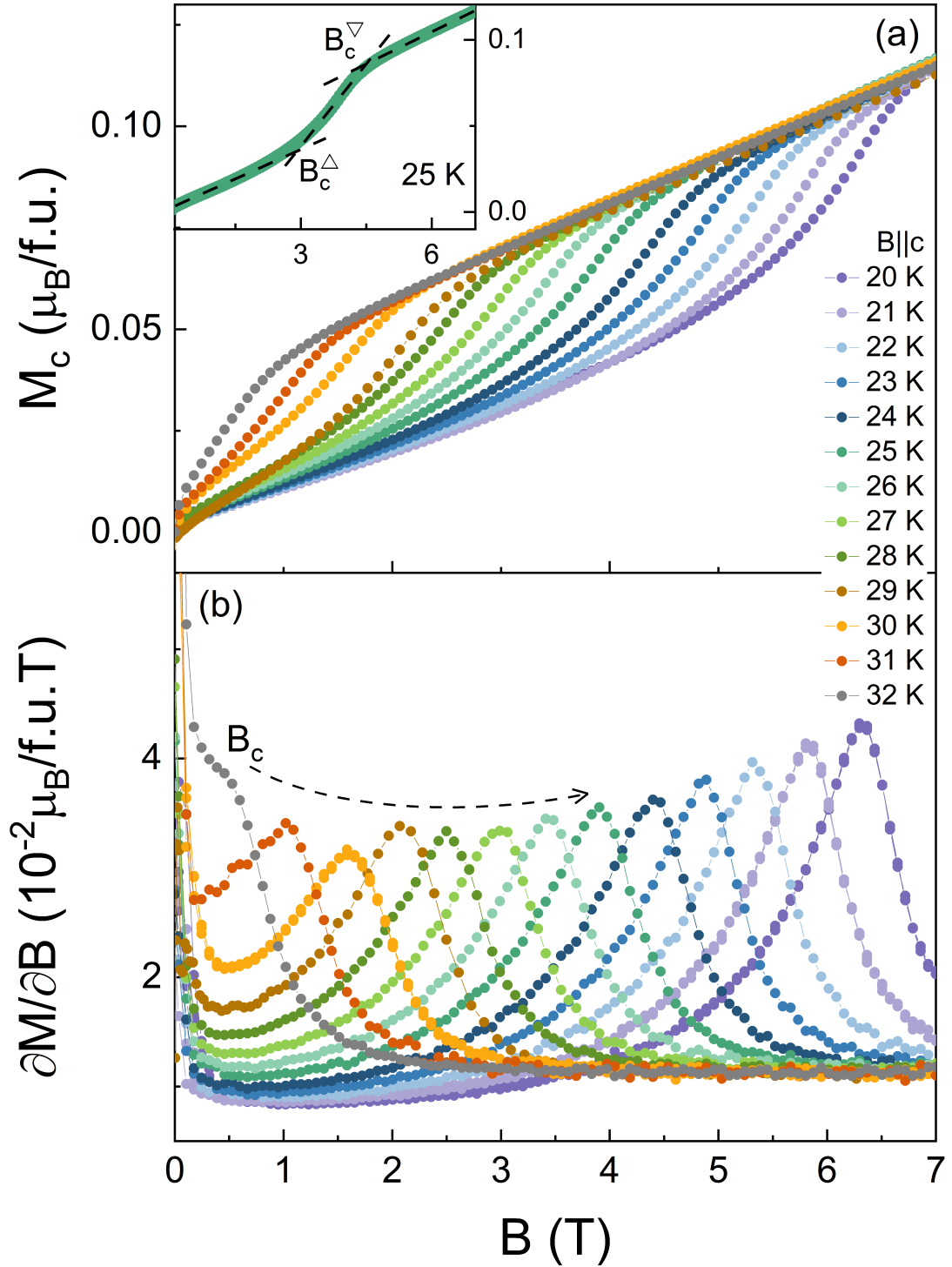


**Figure 5.26:** (a) Isothermal magnetization and (b) magnetic susceptibility  $\partial M/\partial B_{\parallel c}$  for  $B_{\parallel c}$  of  $\text{SmCrO}_3$  at different temperatures. Inset highlights the behaviour at 25 K.  $B_c^\nabla$  and  $B_c^\Delta$  are marked the upper and lower limits of field-induced SRT. The dashed line in (b) indicates the evolution of  $B_c$ .

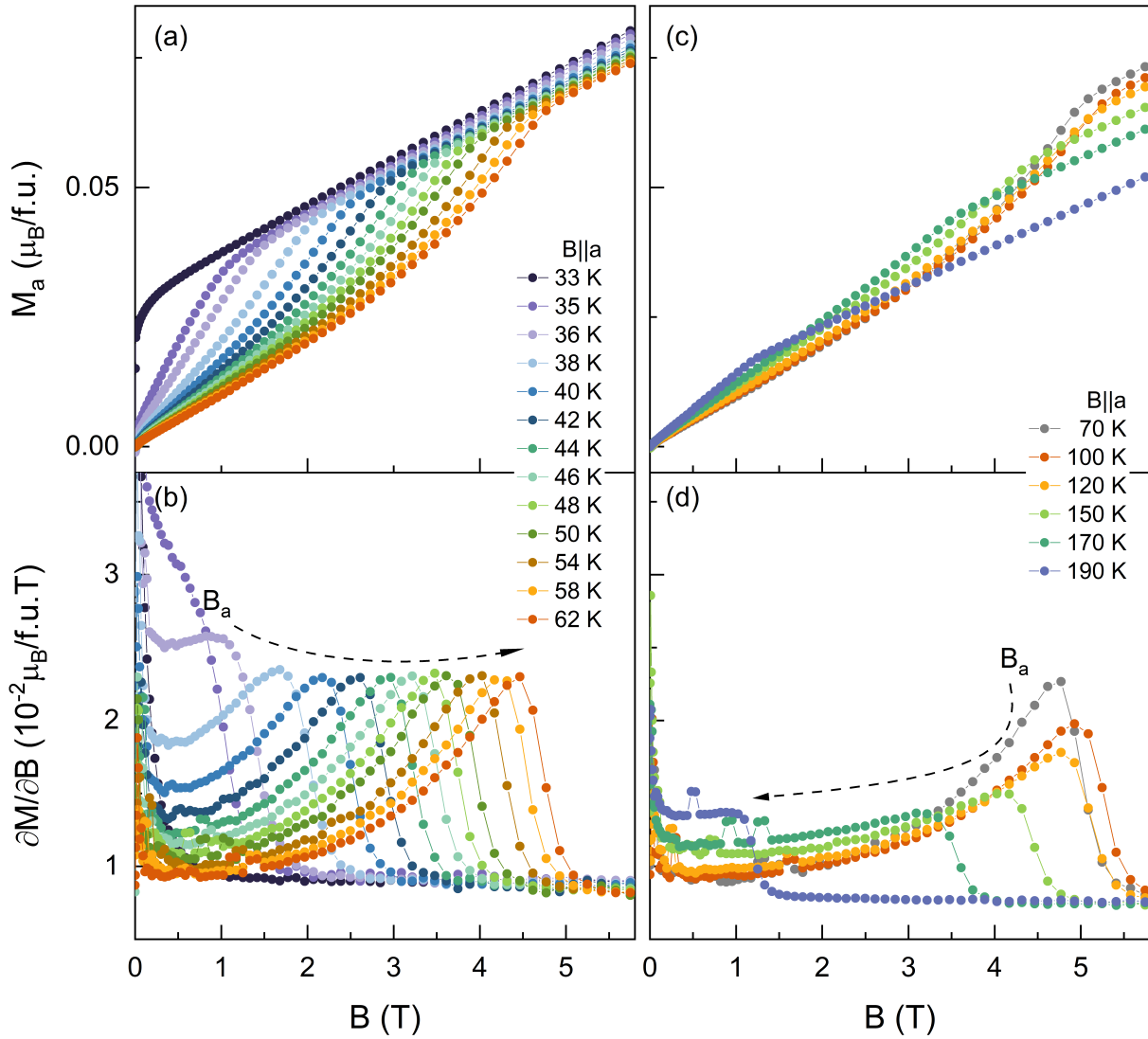


**Figure 5.27:** (a-b) Isothermal magnetization and (c-d) magnetic susceptibility  $\partial M/\partial B_{\parallel a}$  for  $B \parallel a$  of  $\text{SmCrO}_3$  at different temperatures. The dashed line in (c-d) indicates the evolution of  $B_a$ .

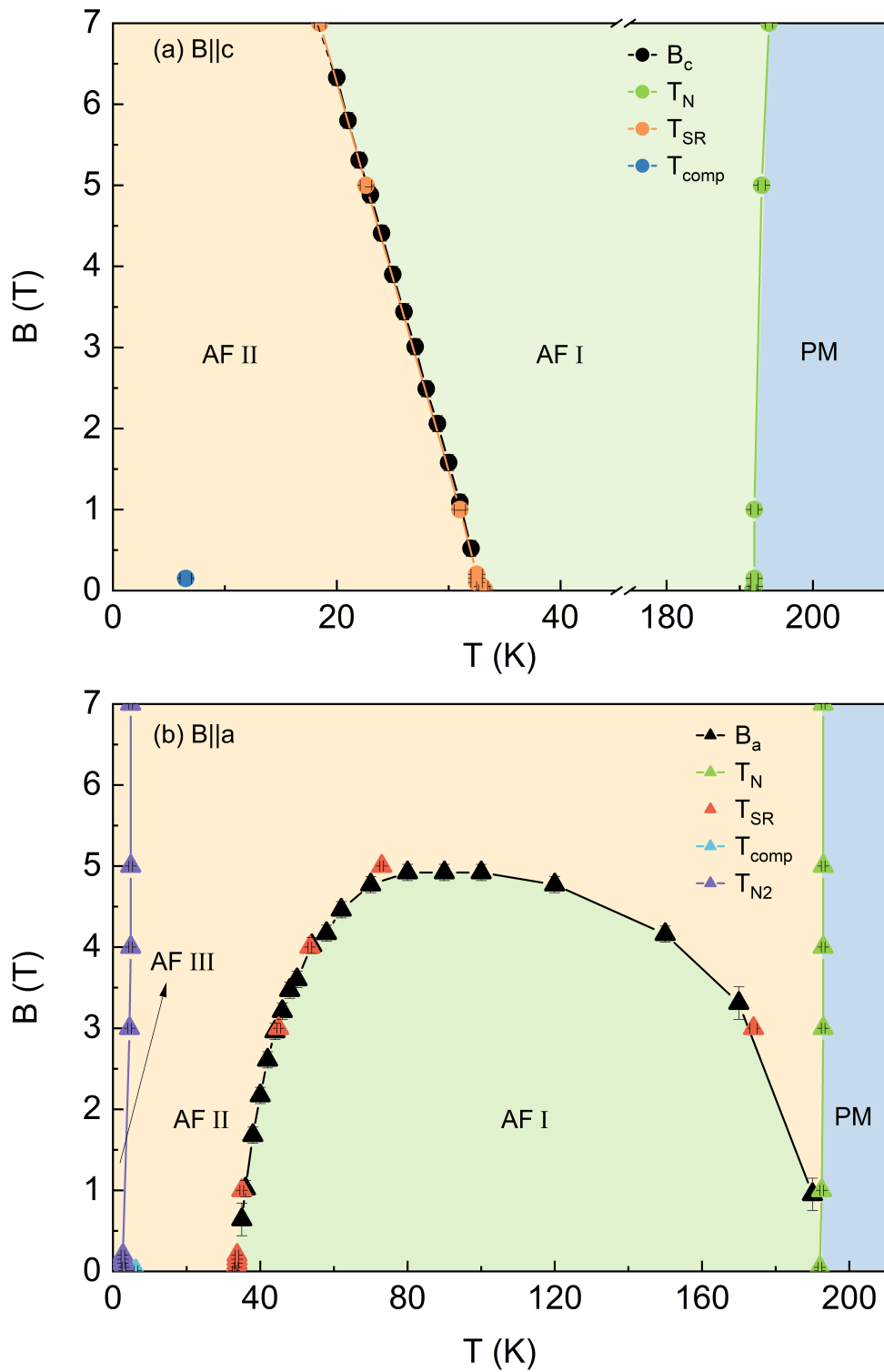


**Figure 5.28:** Magnetic phase diagram of  $\text{SmCrO}_3$  showing the respective ordering phenomena for (a)  $B \parallel c$  and (b)  $B \parallel a$ . PM: Paramagnetic phase; AF I: Antiferromagnetic phase with net magnetic moments are along the  $c$  axis ( $\Gamma_4$ ); AF II: Antiferromagnetic phase with net magnetic moments ordered in  $ab$  plane; AF III: Antiferromagnetic phase with  $\text{Sm}^{3+}$  ordering.

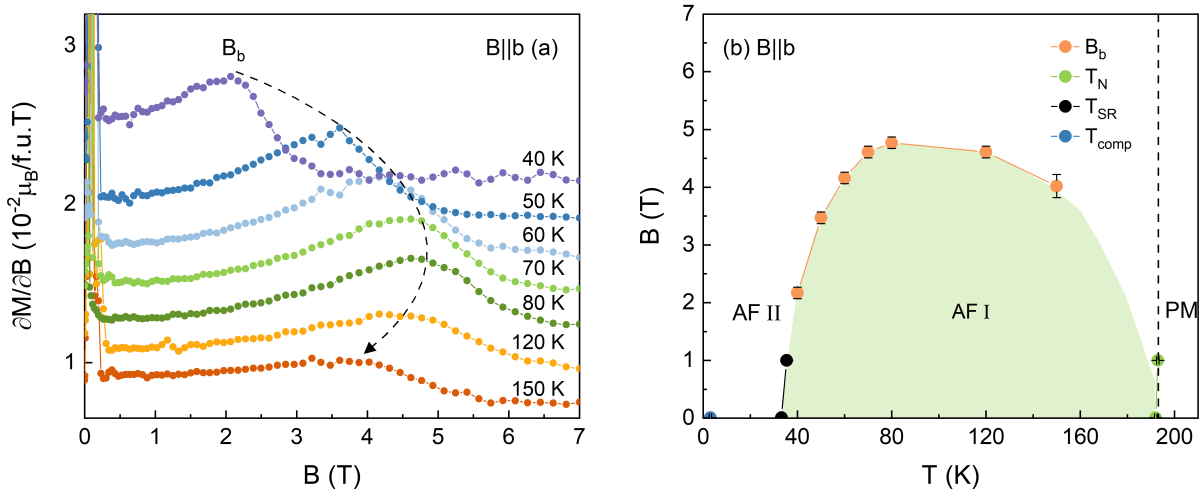


**Figure 5.29:** (a) Magnetic susceptibility  $\partial M/\partial B_{||b}$  for  $B_{||b}$  of  $\text{SmCrO}_3$  at different temperatures. The dashed line indicates the evolution of  $B_b$ . The curves are offset vertically by  $2.2 \times 10^{-3} \mu_B/\text{f.u.}$  for better visibility. (b) Magnetic phase diagram of  $B_{||b}$  for  $\text{SmCrO}_3$ . PM: Paramagnetic phase; AF I: Antiferromagnetic phase with net magnetic moments are along the  $c$  axis ( $\Gamma_4$ ); AF II: Antiferromagnetic phase with net magnetic moments ordered in the  $ab$  plane.

magnetic moments of the canted  $\text{Cr}^{3+}$  sublattice rotate from the  $ab$  plane (AFM II) to  $c$  axis (AFM I). There exists a compensation point at  $T_{\text{comp}} = 6$  K, which is induced by the antiparallel alignment of magnetic moment between  $R^{3+}$  and transition metal ion  $M^{3+}$ , as demonstrated in several homogeneous systems, e.g.,  $\text{GdCrO}_3$  ( $T_{\text{comp}} = 144$  K, 100 Oe) [62, 151],  $\text{ErFeO}_3$  ( $T_{\text{comp}} = 46$  K, 100 Oe) [152, 159],  $\text{SmFeO}_3$  ( $T_{\text{comp}} = 3.9$  K, 300 Oe) [130, 160],  $\text{NdFeO}_3$  ( $T_{\text{comp}} = 7.6$  K, 100 Oe) [129].

- For  $B_{||a}$ , starting at  $B = 0$  T and AF III,  $\text{Sm}^{3+}$  ordering at the lower temperatures of  $T < 3$  K with  $\text{Sm}^{3+}$  aligned antiparallel to  $\text{Cr}^{3+}$ , the net magnetic moments of the  $\text{Cr}^{3+}$  sublattice are well ordered in  $ab$  plane. Due to the effect of the  $\text{Cr}^{3+}$  sublattice, more specifically the  $\text{Cr}^{3+}$ - $\text{Sm}^{3+}$  interactions,  $T_{\text{comp}}$  is also visible around 6 K. For  $T > T_{\text{SR}}$ , the phase boundary between AF II and AF I is presented clearly, which can be traced by the anomaly peak of  $\partial M/\partial B_{||a}$  (Fig. 5.27) until the temperature rises to  $T_N$ . Within magnetic fields up to 7 T, the long-range AF ordered temperature  $T_N$  is barely varied.
- For  $B_{||b}$ , magnetic susceptibilities  $\partial M/\partial B_{||b}$  at different temperatures and magnetic phase diagram is shown in Fig. 5.29, where the distinct anomalies on  $\partial M/\partial B_{||b}$  is marked as  $B_b$ . This result shows that  $B_b$  evolves with the magnetic field (temperature) in a similar way as  $B_a$ .

---

Back in 1974, T. Yamaguchi gave a theoretical framework for field-induced SRT [112], in which the temperature-dependent effective field dominates the SRT magnetization process, arising from isotropic/antisymmetric/anisotropic-symmetric exchange interactions between  $R^{3+}$  and  $\text{Cr}^{3+}$ , following the direction of the weakly ferromagnetic component of  $\text{Cr}^{3+}$ , and acting mainly on the  $\text{Cr}^{3+}$ . Similar experimental results have been reported for  $\text{Dy}_{0.5}\text{Pr}_{0.5}\text{FeO}_3$  [161],  $\text{YFeO}_3$  [162],  $\text{GdFeO}_3$  [163], and  $\text{ErCrO}_3$  [164]. This has been explained in previous experiment studies as a result of the subsequent enhancement of the anisotropy effective field [161]. At higher temperatures, this effective field competes less intensely with the external magnetic field, and thus behaves as a shift of  $B_c$  towards lower fields.

Furthermore, the determination of  $\Delta M_{\text{SR}/c}$  and  $\Delta M_{\text{SR}/a}$  is shown in Fig. 5.30 (a)-(b).  $\Delta M_{\text{SR}/c}$  is not readable anymore after  $T > 28$  K, while  $\Delta M_{\text{SR}/a}$  could be traced up to  $T_N$ . The variation of the jump in magnetization  $\Delta M_{\text{SR}}$  and associated entropy jump  $\Delta S_{\text{SR}}$  with magnetic field and temperature are shown in Fig. 5.30 (c)-(d), where  $\Delta S_{\text{SR}}$  can be calculated by Clausius-Clapeyron equation 5.13, which enables us to estimate the entropy changes appearing at the AF I/AF II phase boundary [165]:

$$\Delta S_{\text{SR}} = -\Delta M \times \frac{\partial B}{\partial T}. \quad (5.13)$$

Therefore, the estimated magnetic entropy change for  $T_{\text{SR}} = 33$  K at  $B = 0$  T is  $\Delta S_{\text{SR}} = 0.04(1)$  J/(molK). Additional information, such as the temperature dependence of entropy in the  $\text{SmCrO}_3$  system and the first/second order nature of the SRT in  $\text{SmCrO}_3$ , is worth determining by further specific heat measurements.

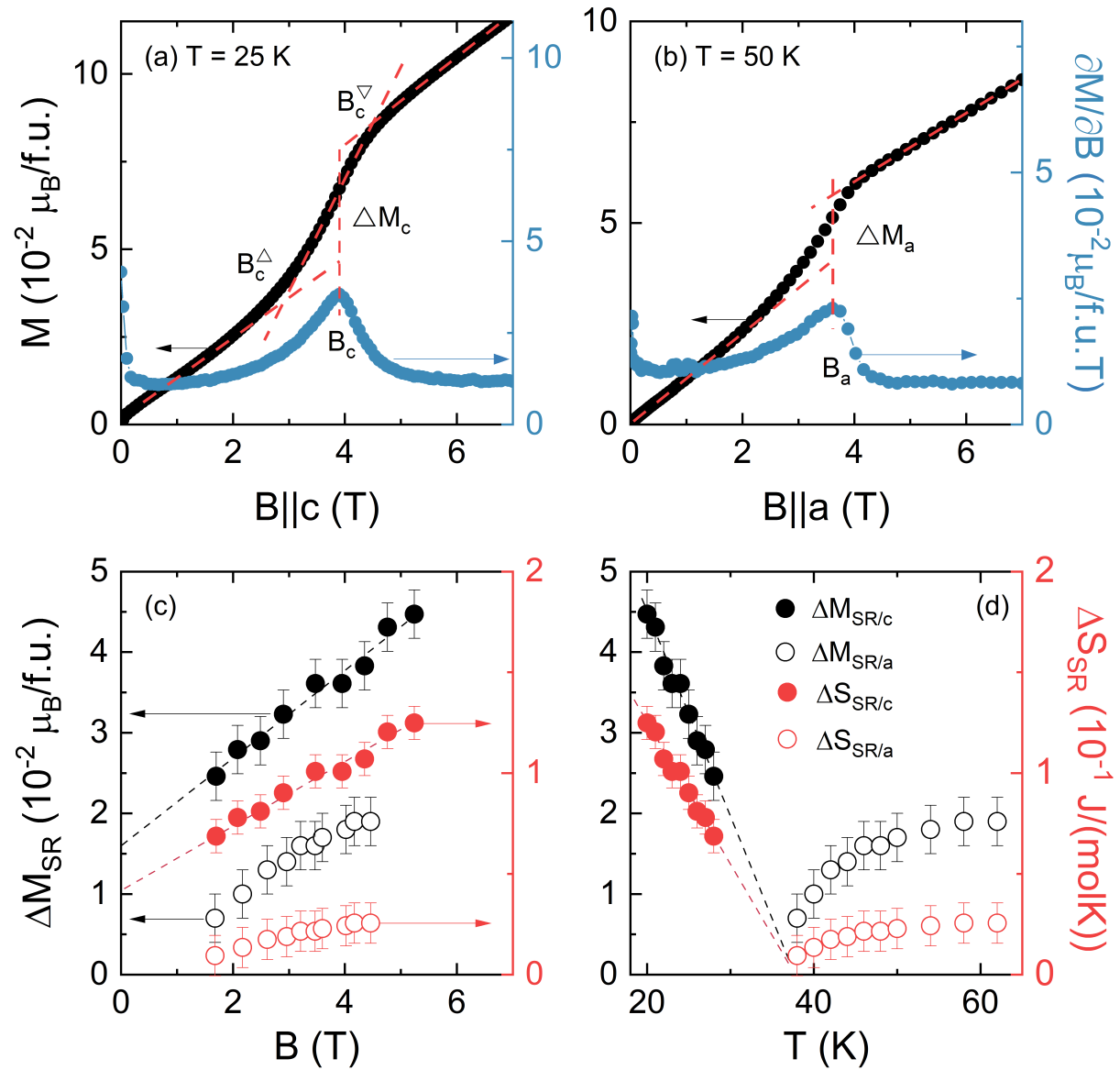


**Figure 5.30:** Determination of jump in magnetization  $\Delta M_{\text{SR}}$  at the SRT for (a)  $B||c$  and (b)  $B||a$  of SmCrO<sub>3</sub>. Dependence of  $\Delta M_{\text{SR}}$  and associated entropy jump  $\Delta S_{\text{SR}}$  (obtained from Eq. 5.13) on (c) magnetic fields and (d) temperatures. Dashed lines are guides to the eye.



---

## 5.4 Summary

This chapter introduces three single crystals of rare-earth orthochromites, namely  $\text{ErCrO}_3$ ,  $\text{GdCrO}_3$ , and  $\text{SmCrO}_3$ . The magnetization process for three single crystals and the magnetic phase diagrams of  $\text{SmCrO}_3$ , are thoroughly investigated. Firstly,  $\text{ErCrO}_3$  develops long-range AF order at  $T_N = 132$  K. The magnetization data clearly present the  $\Gamma_4$  ( $G_x, A_y, F_z$ )- $\Gamma_1$  ( $A_x, G_y, C_z$ ) SRT of  $\text{ErCrO}_3$  below 7.6 K, with the rotation of net magnetic moments within the  $ac$  plane at  $T = 19$  K. Secondly,  $\text{GdCrO}_3$  exhibits long-range AF order at  $T_N = 167$  K for  $\text{Cr}^{3+}$  sublattice and  $T_{N2} = 2.2$  K for  $\text{Gd}^{3+}$  sublattice.  $\text{GdCrO}_3$  exhibits  $\Gamma_4 - \Gamma_2$  SRT at 6 K, along with a magnetization compensation point at 144 K, accompanied by the phenomenon of spin switching. Based on the spin switching model proposed by Cooke et al. [154], the temperature dependence of the remanent magnetization ( $M_r$ ) along the  $c$  axis, and the internal exchange field  $B_I$  generated by the ordered  $\text{Cr}^{3+}$  are discussed. Finally, the  $\text{SmCrO}_3$  develops long-range AF order at  $T_N = 192$  K for  $\text{Cr}^{3+}$  sublattice and  $T_{N2} = 3$  K for  $\text{Sm}^{3+}$  sublattice, as well as the spin reorientation transition at  $T_{\text{SR}} = 33$  K, when the net magnetic moments within the system undergo a rotation between the  $c$  and  $ab$  plane. This indicates that the spin configuration is  $\Gamma_4$  for  $T > T_{\text{SR}}$ , while it is dominated by  $\Gamma_2$  for  $T < T_{\text{SR}}$ . The presented results are not in complete agreement with previous experimental reports on polycrystals, however, to more precisely determine the low-temperature spin configuration, neutron diffraction of single crystals is essential, and therefore preparing large-sized single crystals is necessary. This work also identifies the presence of a field-induced SRT of  $\text{SmCrO}_3$  for magnetic fields applied along the  $c$  and  $a$  axis, tracking the variation of critical field  $B_c$  and  $B_a$  with temperature. In conclusion, the complete magnetic phase diagram for magnetic fields ranging from 0 to 7 T is established. Notably, all single crystals of  $\text{ErCrO}_3$ ,  $\text{GdCrO}_3$ , and  $\text{SmCrO}_3$  exhibit significant magnetic anisotropy. This work not only serves as a crucial reference for growing single crystals of  $R\text{CrO}_3$  under high-pressure conditions, but also provides essential support for studying the complex magnetic interactions and magneto-electric coupling involving the  $4f$  electrons of  $R^{3+}$  and  $3d$  electrons of  $\text{Cr}^{3+}$  in orthochromites.



# 6

## Overall Summary



---

The objective of this study is to experimentally investigate the synthesis and magnetic properties of three specific systems within the class of strongly correlated materials: the rare-earth indates  $\text{GdInO}_3$  and  $\text{TbInO}_3$ , the Ruddlesden–Popper nickelates  $\text{La}_4\text{Ni}_3\text{O}_{10}$ , and the rare-earth orthochromites  $\text{ErCrO}_3$ ,  $\text{GdCrO}_3$ , and  $\text{SmCrO}_3$ . All single crystals in this study were grown under an oxygen/argon pressure of 20–45 bar using the high-pressure floating zone furnace (HKZ, SciDre). This study outlines the challenges associated with single crystal growth, encompassing issues like volatilization, bubble aggregation in the melting zone, and weak surface tension of the melt, and emphasizes the role of high-pressure in addressing these challenges. The magnetization measurements were primarily conducted using the MPMS3, including the  $^3\text{He}$  quantum extension to cover the temperature range 0.4–400 K.

Firstly, the magnetic phase diagram of the frustrated magnet  $\text{GdInO}_3$  is determined.  $\text{GdInO}_3$  has a centered honeycomb lattice structure crystallizing in the  $P6_3cm$  space group. Its key features include: (a) Development of long-range magnetic order below  $T_N = 2.1$  K from a short-range-ordered paramagnetic phase, with a frustration parameter  $f = \frac{|\Theta|}{T_N} \sim 5$ . The magnitude of the specific heat jump at  $T_N$ , amounts to  $\Delta c_p = 4.1(3)$  J/(molK), which is significantly smaller than the anticipated mean-field value of 20.1 J/(molK) (for an  $S = 7/2$  system). (b) The ground state exhibits a small net magnetic moment along the crystallographic  $c$  axis, which undergoes reorientation upon cooling at  $T^{**} = 1.7$  K and  $T^* = 1$  K. (c) A broad  $1/3$  plateau indicative of the up-up-down spin configuration appears for  $B||c$  but is absent for  $B||ab$ , suggesting easy-axis anisotropy. (d) At  $T = 0.4$  K, a small jump in magnetization for  $B||c$  occurs at about  $3/5$  of the saturation magnetization, indicating a discontinuous phase transition to a high-field phase. The possible tricritical point is discussed. Overall,  $\text{GdInO}_3$  serves as a suitable example for studying the phase diagram of a semiclassical frustrated hexagonal magnetic system. Conversely,  $\text{TbInO}_3$  shares a similar structure with  $\text{GdInO}_3$ , the variation of  $\chi_c$  and  $\chi_{ab}$  clearly indicates the magnetic anisotropy. The Curie-Weiss fitting of the polycrystal gives Weiss temperature  $\Theta_W = -16(1)$  K, suggesting the antiferromagnetic exchange interactions, although no indication of long-range ordering is observed down to 1.8 K. Therefore,  $\text{TbInO}_3$  is of great interest in searching spin-liquid ground states.

The second part of this work discusses the Ruddlesden–Popper nickelates  $\text{La}_4\text{Ni}_3\text{O}_{10}$ , characterized by alternating perovskite-like layers and rock-salt-like layers. The presence of both  $\text{Ni}^{2+}$  and  $\text{Ni}^{3+}$  ions results in an average valence of +2.67. Single crystal growth of  $\text{La}_4\text{Ni}_3\text{O}_{10}$  and post-annealing under 20 bar oxygen pressure yield two different phases,

namely  $P2_1/a$  and  $Bmab$ , respectively. Both magnetic and specific heat measurements reveal sharp anomalies and marked anisotropy associated with the reported metal-to-metal transition in  $\text{La}_4\text{Ni}_3\text{O}_{10}$ .

Thirdly,  $\text{ErCrO}_3$ ,  $\text{GdCrO}_3$ , and  $\text{SmCrO}_3$  belong to the distorted perovskite structure-type and have the space group  $Pbnm$ . This structure exhibits two magnetic subsystems ( $\text{Cr}^{3+}$  and  $R^{3+}$  sublattice) and three types of magnetic interactions (between  $\text{Cr}^{3+}$ - $\text{Cr}^{3+}$ ,  $R^{3+}$ - $\text{Cr}^{3+}$ , and  $R^{3+}$ - $R^{3+}$ ). Dzyaloshinskii-Moriya interaction induces canted antiferromagnetism in the Cr sublattice, with ordering temperatures of  $T_N = 132$  K, 167 K, and 192 K for  $\text{ErCrO}_3$ ,  $\text{GdCrO}_3$ , and  $\text{SmCrO}_3$ , respectively. As the radius of the rare-earth ions increases, the antiferromagnetic ordering temperature of the system shifts to higher temperatures. All three single crystals display significant magnetic anisotropy and spin reorientation transition (SRT). Specifically,  $\text{ErCrO}_3$  presents the  $\Gamma_4 (G_x, A_y, F_z)$ - $\Gamma_1 (A_x, G_y, C_z)$  SRT, with the net magnetic moments of the system rotating within the  $ac$ -plane ( $7.6 \text{ K} < T < 19 \text{ K}$ ) before the low-temperature  $\Gamma_1$  spin configuration is fully formed ( $T < 7.6 \text{ K}$ ).  $\text{GdCrO}_3$  undergoes the  $\Gamma_4 (G_x, A_y, F_z)$ - $\Gamma_2 (F_x, C_y, G_z)$  SRT at 6 K. The negative magnetization, a compensation point at 144 K, and spin switching behavior of  $\text{GdCrO}_3$  are discussed in this work. The appearance of these behaviors is based on the feature that two magnetic sublattices of  $\text{Gd}^{3+}$  and  $\text{Cr}^{3+}$  are arranged antiparallel to each other.  $T_{\text{sw}}$  is closely related to the magnetization histories and modulated by the external magnetic field. For FCW (FCC) mode,  $T_{\text{sw}} = 162 \text{ K}$  (62 K) at  $B = 0.005 \text{ T}$ , and it gradually shifts to lower (higher) temperatures with an increased magnetic field. Additionally, anomalies in  $\partial M/\partial B_{\parallel c}$  and  $\partial M/\partial B_{\parallel a}$  suggest the boundaries of multiple low-temperature AFM phases. For  $\text{SmCrO}_3$ ,  $T_{\text{SR}} = 33 \text{ K}$  and the spin configuration is  $\Gamma_2$  for  $T_{\text{SR}} < T < T_N$ , while the low-temperature spin configuration remains controversial. For  $T < T_{\text{SR}}$ , the data presented in this work show that the net magnetic moment is rotated from the  $c$  axis towards the  $ab$  plane, suggesting likely mixed or inhomogeneous spin configurations at low temperatures. The field-induced SRT in  $\text{SmCrO}_3$  has been determined by isothermal magnetization measurements. Based on the magnetization jumps on the SRT phase boundary (AF I/AF II) and applying the Clausius-Clapeyron equation, yields a small entropy change of  $\Delta S_{\text{SR}} = 0.04(1) \text{ J}/(\text{molK})$ . These significant anomalies exist in  $\partial M/\partial B_{\parallel c}$  and  $\partial M/\partial B_{\parallel a}$  triggered a discussion of the  $\text{SmCrO}_3$  magnetic phase diagrams.

In short, this work delineates magnetic studies of six single crystal oxides across three material systems. All these materials demonstrate complex magnetization behavior and remarkable magnetic anisotropy at low temperatures. The preparation of single crystals

---

is essential for accurately discussing magnetic anisotropy. In this work, the optical floating-zone method is employed to grow single crystals, emphasizing the essential role of high-pressure techniques in exploring the single crystal of novel quantum materials.





# Appendix

## A.1 $\text{LiMn}_2\text{O}_4$

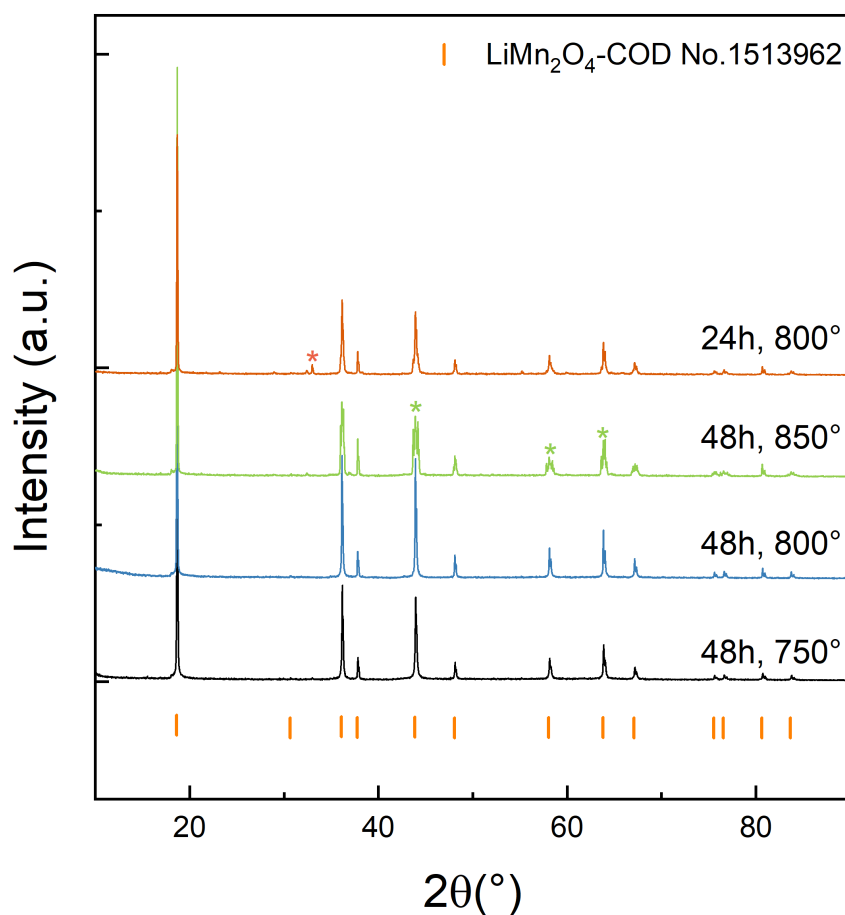


**Figure 6.1:** Room temperature XRD pattern of polycrystalline  $\text{LiMn}_2\text{O}_4$  obtained from different synthesis temperatures.

Polycrystalline  $\text{LiMn}_2\text{O}_4$  was synthesized by the standard solid-state reaction method, with synthesis conditions referred to several reports [167–169]. Stoichiometric amounts of  $\text{Li}_2\text{CO}_3$  (99%, Sigma-Aldrich) and  $\text{Mn}_2\text{CO}_3$  (99.9%, Sigma-Aldrich) were mixed well

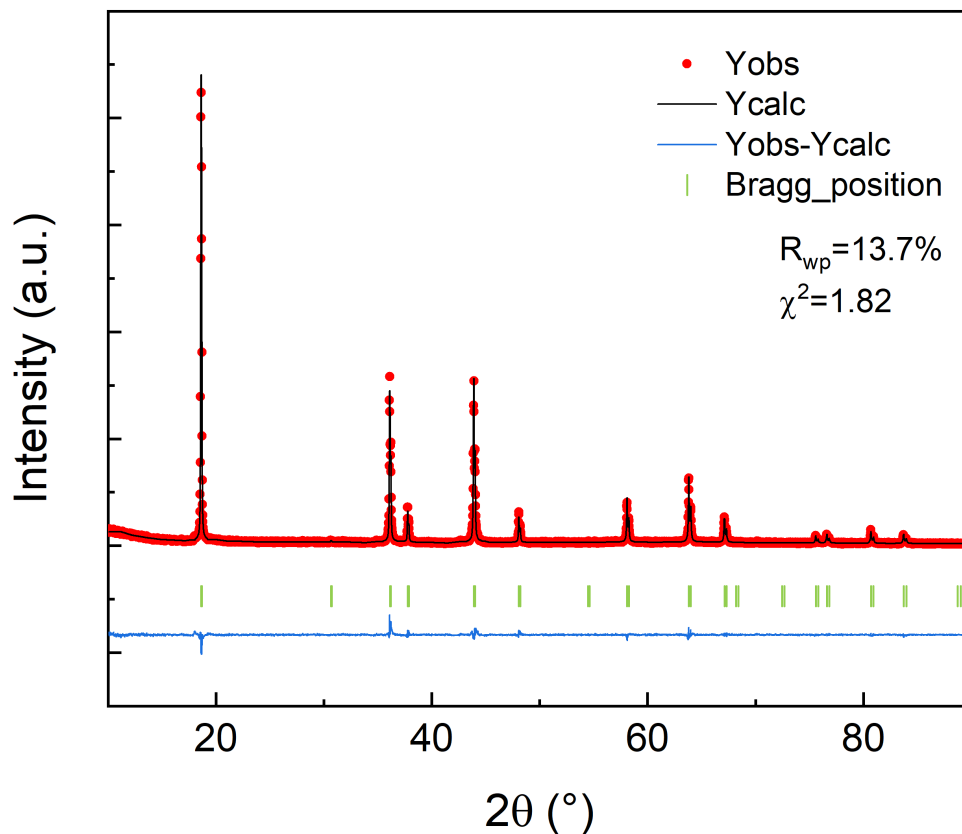


**Figure 6.2:** Room temperature XRD pattern and corresponding Rietveld refinement [93] of polycrystalline  $\text{LiMn}_2\text{O}_4$ . The observed diffraction pattern is shown in red, the calculated one in black, and the difference between them is shown in blue. The vertical green bars show the expected Bragg positions (COD NO.1513962 [166]). The refinement converged to  $R_p = 11.5\%$ ,  $R_{wp} = 13.7\%$ ,  $\chi^2 = 1.82$ .

in a mortar and calcined at  $500^\circ\text{C}$  for 1 h (round 1) and 2 h (round 2) with intermediate grinding (air flow, ambient), then calcined at  $800^\circ\text{C}$  for 48 h (round 3, air flow, ambient). When the sintering temperature  $< 750^\circ\text{C}$  or the sintering time is insufficient, the product contains the impurity  $\text{Mn}_2\text{O}_3$ . Conversely, at a sintering temperature of  $850^\circ\text{C}$ , the product contains the impurity  $\text{Mn}_3\text{O}_4$ . The compounds sintered at  $750^\circ\text{C}$  and  $800^\circ\text{C}$  for 48 h have proved to be pure phases (see Fig. 6.1). The Rietveld refinement was performed on XRD data of polycrystalline  $\text{LiMn}_2\text{O}_4$  sintered at  $800^\circ\text{C}$  for 48 h. The result presented in Fig. 6.2 is indicate the purity phase of  $\text{LiMn}_2\text{O}_4$ , the refined structural parameters are shown as Table A.1. Scanning electron microscopy (SEM) image of  $\text{LiMn}_2\text{O}_4$  sintered at  $800^\circ\text{C}$  for 48 h is shown in Fig. 6.3, the morphology is powdery with particles approximately  $1\mu\text{m}$  in size.

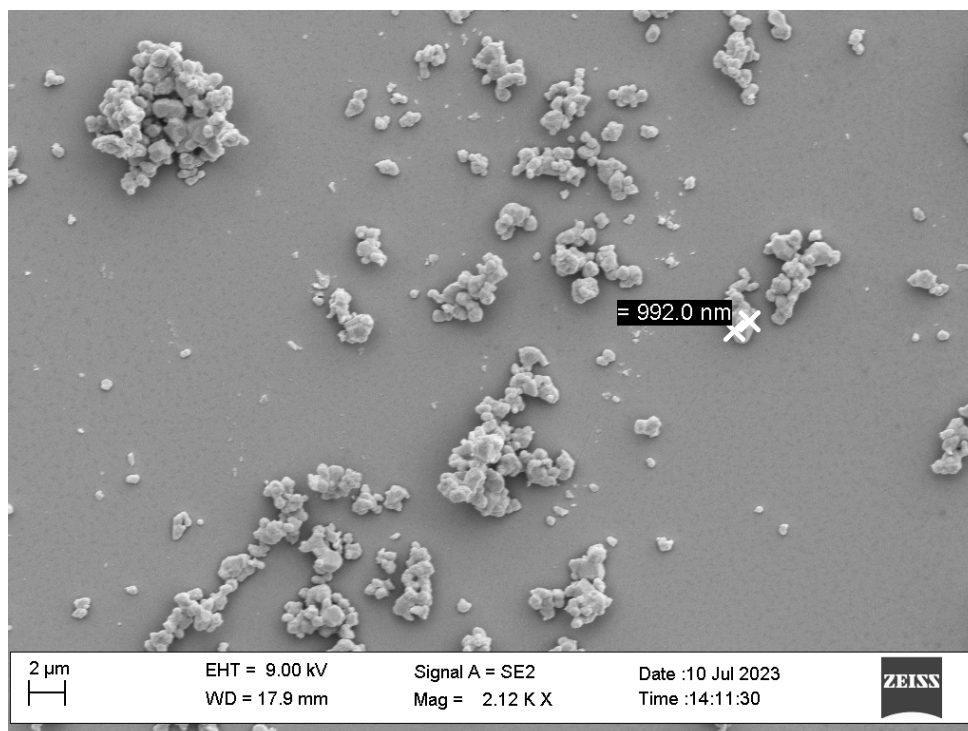


**Figure 6.3:** SEM image of  $\text{LiMn}_2\text{O}_4$  sintered at  $800^\circ\text{C}$  for 48 h.

**Table A.1:** Selected structural parameters from the Rietveld refinement of the room temperature powder XRD data of  $\text{LiMn}_2\text{O}_4$  ( $Fd\bar{3}m$ ). The refinement is performed based on the crystallographic information file COD NO.1513962.

Atoms	Wyckoff position	$x$	$y$	$z$	Lattice Parameters( $\text{\AA}$ )	Reliability factors
Li1	$8a$	0.12500	0.12500	0.12500	$a=8.2426(1)$	$R_p=11.5\%$
Mn1	$16d$	0.50000	0.50000	0.50000	$b=8.2426(1)$	$R_{wp}=13.7\%$
O1	$32e$	0.26257	0.26257	0.26257	$c=8.2426(1)$	$\chi^2=1.82$

## A.2 Additional Tables

**Table A.2:** Summary of the triangular lattice antiferromagnets (TLAFs) for which magnetization plateau behavior is experimentally observed.

Materials	$S$	Space group	Magnetization plateau
GdPd <sub>2</sub> Al <sub>3</sub> [170]	7/2	$P6/mmm$	1/3
RbFe(MoO <sub>4</sub> ) <sub>2</sub> [35, 171, 172]	5/2	$P\bar{3}m1$	1/3
Rb <sub>4</sub> Mn(MoO <sub>4</sub> ) <sub>3</sub> [173]	5/2	$P6_3/mmc$	1/3
Ba <sub>3</sub> NiSb <sub>2</sub> O <sub>9</sub> [174]	1	$P6_3/mmc$	1/3, $\sqrt{3}/3$
Ba <sub>3</sub> CoSb <sub>2</sub> O <sub>9</sub> [34, 175, 176]	1/2	$P6_3/mmc$	1/3, 3/5
Ba <sub>3</sub> NiNb <sub>2</sub> O <sub>9</sub> [177]	1/2	$P\bar{3}m1$	1/3, 1/2, 2/3, $\sqrt{3}/3$
Cs <sub>2</sub> CuBr <sub>4</sub> [178, 179]	1/2	$Pnma$	1/3, 1/2, 5/9, 2/3
CuFeO <sub>2</sub> [180–182]	5/2	$R\bar{3}m$	1/3
CsYbSe <sub>2</sub> [183]	1/2	$R\bar{3}m$	1/3
Ni <sub>3</sub> V <sub>2</sub> O <sub>8</sub> [184, 185]	1	$Cmca$	1/3
CsFe(SO <sub>4</sub> ) <sub>2</sub> [171, 172]	5/2	$P\bar{3}m1$	1/3
Ba <sub>3</sub> MnNb <sub>2</sub> O <sub>9</sub> [33]	5/2	$P\bar{3}m1$	1/3

**Table A.3:** The chemicals used in this work.

Chemical	Formula	Assay	Source
Lithium carbonate	Li <sub>2</sub> CO <sub>3</sub>	99%	Sigma-Aldrich
Chromium(III) oxide	Cr <sub>2</sub> O <sub>3</sub>	99.6%	Alfa Aesar
Manganese(II) carbonate	Mn <sub>2</sub> CO <sub>3</sub>	99.9%	Sigma-Aldrich
Nickel(II) oxide	NiO	99.998%	Alfa Aesar
Indium(III) oxide	In <sub>2</sub> O <sub>3</sub>	99.9%	Alfa Aesar
Lanthanum(III) oxide	La <sub>2</sub> O <sub>3</sub>	99.99%	Sigma-Aldrich
Samarium(III) oxide	Sm <sub>2</sub> O <sub>3</sub>	99.9%	Alfa Aesar
Gadolinium(III) oxide	Gd <sub>2</sub> O <sub>3</sub>	99.9%	Alfa Aesar
Terbium(III, IV) oxide	Tb <sub>4</sub> O <sub>7</sub>	99.9%	Alfa Aesar
Erbium(III) oxide	Er <sub>2</sub> O <sub>3</sub>	99.9%	Alfa Aesar

# List of Tables

2.1	The synthesize temperatures and growth parameters of the single crystal samples prepared in this work. . . . .	30
3.1	Selected structural parameters from the Rietveld refinement of the room temperature powder XRD data of $\text{TbInO}_3$ ( $P6_3cm$ ). The refinement is performed based on the crystallographic information file provided by the literature [105]. . . . .	57
3.2	The Weiss temperature ( $\Theta_W$ ), the effective magnetic moment ( $\mu_{\text{eff}}$ ), and diamagnetic constant background term $\chi_0$ of $\text{TbInO}_3$ obtained from the CW law. . . . .	60
5.1	Selected structural parameters from the Rietveld refinement of the room temperature powder XRD data of $R\text{CrO}_3$ ( $R = \text{Er, Gd, Sm}$ ) (space group No.62 $Pbnm$ ). The refinement is performed based on the crystallographic information file COD No. 1008159 [139] ( $\text{ErCrO}_3$ ), COD No. 1533276 [109] ( $\text{GdCrO}_3$ ), and ICSD No. 5988 [140] ( $\text{SmCrO}_3$ ). . . . .	86
5.2	Comparison of the Weiss-temperature ( $\Theta_W$ ) and the effective magnetic moment ( $\mu_{\text{eff}}$ ) of $\text{ErCrO}_3$ obtained from the CW law and Moriya model [58] (Eq. 5.2- 5.4). The resulting fits to the data are shown in Figs. 5.10 (b) and (c). . . . .	88
A.1	Selected structural parameters from the Rietveld refinement of the room temperature powder XRD data of $\text{LiMn}_2\text{O}_4$ ( $Fd\bar{3}m$ ). The refinement is performed based on the crystallographic information file COD NO.1513962.	131
A.2	Summary of the triangular lattice antiferromagnets (TLAFs) for which magnetization plateau behavior is experimentally observed. . . . .	132

Extra table from the publications:

- Table I (Section 3.1): Growth parameters and phase analysis from the Rietveld refinement of the room temperature powder XRD data of GdInO<sub>3</sub> single crystals from the literature [30, 31] and reported at hand (HKZ). 40
- Table SI (Section 3.1): Refined structural parameters for GdInO<sub>3</sub> (*P6<sub>3</sub>cm*) at room temperature. The refinement is performed based on the crystallographic information file COD No.7237332 [31, 107]. 48
- Table 1 (Chapter 4): Fitting magnetization data in Fig.3 and 4 (see the text).  $M_s$  and  $\chi$  are saturation magnetization of the quasi-free spins and linear slope derived from  $M(B, T = 2 \text{ K})$ .  $C$ ,  $\Theta$ , and  $\chi_0$  are the Curie constant, Weiss temperature and temperature-independent susceptibility from fitting  $M(T)/B$  at  $T < 10 \text{ K}$ . 71
- Table 2 (Chapter 4): Changes in entropy ( $\Delta S_{\text{MM}}$ ), magnetization ( $\Delta M$ , and  $\Delta(\partial M/\partial T)_{\text{MM}}$ ) at the MMT and field dependencies of  $T_{\text{MM}}$  calculated by means of Eq.(2). 72

# List of Publications

**N. Yuan**, A. Elghandour, W. Hergett, R. Ohlendorf, L. Gries, R. Klingeler, 1/3 plateau and 3/5 discontinuity in the magnetization and the magnetic phase diagram of hexagonal GdInO<sub>3</sub>, *Physical Review B*, Volume 108, October 2023, 224403.  
<https://doi.org/10.1103/PhysRevB.108.224403>

**N. Yuan**, A. Elghandour, K. Dey, J. Arneth, R. Klingeler, High-pressure crystal growth and investigation of the metal-to-metal transition of Ruddlesden–Popper trilayer nickelates La<sub>4</sub>Ni<sub>3</sub>O<sub>10</sub>, *Journal of Crystal Growth*, Volume 627, February 2024, 127511.  
<https://doi.org/10.1016/j.jcrysgro.2023.127511>





# Bibliography

- [1] E. Morosan, D. Natelson, A. H. Nevidomskyy, and Q. Si, “Strongly correlated materials”, *Advanced Materials*, vol. 24, no. 36, pp. 4896–4923, 2012.
- [2] B. Keimer and J. Moore, “The physics of quantum materials”, *Nature Physics*, vol. 13, no. 11, pp. 1045–1055, 2017.
- [3] P. A. Lee, N. Nagaosa, and X.-G. Wen, “Doping a Mott insulator: Physics of high-temperature superconductivity”, *Reviews of modern physics*, vol. 78, no. 1, p. 17, 2006.
- [4] T. Moriya and K. Ueda, “Spin fluctuations and high temperature superconductivity”, *Advances in Physics*, vol. 49, no. 5, pp. 555–606, 2000.
- [5] S. Koohpayeh, D. Fort, and J. Abell, “The optical floating zone technique: A review of experimental procedures with special reference to oxides”, *Progress in Crystal Growth and Characterization of Materials*, vol. 54, no. 3-4, pp. 121–137, 2008.
- [6] K. Yamada, C. Lee, K. Kurahashi, J. Wada, S. Wakimoto, S. Ueki, H. Kimura, Y. Endoh, S. Hosoya, G. Shirane, *et al.*, “Doping dependence of the spatially modulated dynamical spin correlations and the superconducting-transition temperature in  $\text{La}_{2-x}\text{Sr}_x\text{CuO}_4$ ”, *Physical Review B*, vol. 57, no. 10, p. 6165, 1998.
- [7] Z. Zou, J. Ye, K. Oka, and Y. Nishihara, “Superconducting  $\text{PrBa}_2\text{Cu}_3\text{O}_x$ ”, *Physical review letters*, vol. 80, no. 5, p. 1074, 1998.
- [8] K. Ross, T. Proffen, H. Dabkowska, J. Quilliam, L. Yaraskavitch, J. Kycia, and B. Gaulin, “Lightly stuffed pyrochlore structure of single-crystalline  $\text{Yb}_2\text{Ti}_2\text{O}_7$  grown by the optical floating zone technique”, *Physical Review B*, vol. 86, no. 17, p. 174424, 2012.
- [9] B. Sacépé, J. B. Oostinga, J. Li, A. Ubaldini, N. J. Couto, E. Giannini, and A. F. Morpurgo, “Gate-tuned normal and superconducting transport at the surface of a topological insulator”, *Nature communications*, vol. 2, no. 1, p. 575, 2011.
- [10] K. Kimura, S. Nakatsuji, J. Wen, C. Broholm, M. Stone, E. Nishibori, and H. Sawa, “Quantum fluctuations in spin-ice-like  $\text{Pr}_2\text{Zr}_2\text{O}_7$ ”, *Nature communications*, vol. 4, no. 1, p. 1934, 2013.
- [11] J. A. Paddison, M. Daum, Z. Dun, G. Ehlers, Y. Liu, M. B. Stone, H. Zhou, and M. Mourigal, “Continuous excitations of the triangular-lattice quantum spin liquid  $\text{YbMgGaO}_4$ ”, *Nature Physics*, vol. 13, no. 2, pp. 117–122, 2017.

- [12] Y. Li, D. Adroja, R. I. Bewley, D. Voneshen, A. A. Tsirlin, P. Gegenwart, and Q. Zhang, “Crystalline electric-field randomness in the triangular lattice spin-liquid  $\text{YbMgGaO}_4$ ”, *Physical review letters*, vol. 118, no. 10, p. 107 202, 2017.
- [13] Y. Li, G. Chen, W. Tong, L. Pi, J. Liu, Z. Yang, X. Wang, and Q. Zhang, “Rare-earth triangular lattice spin liquid: a single-crystal study of  $\text{YbMgGaO}_4$ ”, *Physical review letters*, vol. 115, no. 16, p. 167 203, 2015.
- [14] J. Ruff, B. Gaulin, J. Castellan, K. Rule, J. Clancy, J. Rodriguez, and H. Dabkowska, “Structural fluctuations in the spin-liquid state of  $\text{Tb}_2\text{Ti}_2\text{O}_7$ ”, *Physical review letters*, vol. 99, no. 23, p. 237 202, 2007.
- [15] X. Yu, Y. Onose, N. Kanazawa, J. H. Park, J. Han, Y. Matsui, N. Nagaosa, and Y. Tokura, “Real-space observation of a two-dimensional skyrmion crystal”, *Nature*, vol. 465, no. 7300, pp. 901–904, 2010.
- [16] M. Hirschberger, T. Nakajima, S. Gao, L. Peng, A. Kikkawa, T. Kurumaji, M. Kriener, Y. Yamasaki, H. Sagayama, H. Nakao, *et al.*, “Skyrmion phase and competing magnetic orders on a breathing kagomé lattice”, *Nature communications*, vol. 10, no. 1, p. 5831, 2019.
- [17] K. Dey, W. Hergett, P. Telang, M. M. Abdel-Hafiez, and R. Klingeler, “Magnetic properties of high-pressure optical floating-zone grown  $\text{LaNiO}_3$  single crystals”, *Journal of Crystal Growth*, vol. 524, p. 125 157, 2019.
- [18] J. Zhang, H. Zheng, Y. Ren, and J. Mitchell, “High-pressure floating-zone growth of perovskite nickelate  $\text{LaNiO}_3$  single crystals”, *Crystal Growth & Design*, vol. 17, no. 5, pp. 2730–2735, 2017.
- [19] H. Guo, Z. Li, L. Zhao, Z. Hu, C. Chang, C.-Y. Kuo, W. Schmidt, A. Piovano, T. Pi, O. Sobolev, *et al.*, “Antiferromagnetic correlations in the metallic strongly correlated transition metal oxide  $\text{LaNiO}_3$ ”, *Nature communications*, vol. 9, no. 1, p. 43, 2018.
- [20] M. C. Weber, M. Guennou, D. M. Evans, C. Toulouse, A. Simonov, Y. Kholina, X. Ma, W. Ren, S. Cao, M. A. Carpenter, *et al.*, “Emerging spin–phonon coupling through cross-talk of two magnetic sublattices”, *Nature communications*, vol. 13, no. 1, p. 443, 2022.
- [21] C. Kloc, S.-W. Cheong, and P. Matl, “Floating-zone crystal growth of perovskite manganites with colossal magnetoresistance”, *Journal of crystal growth*, vol. 191, no. 1-2, pp. 294–297, 1998.
- [22] S. Angappane, M. Pattabiraman, G. Rangarajan, K. Sethupathi, and V. Sastry, “Electron magnetic resonance study in a single crystal of the colossal magnetoresistance manganite  $\text{Nd}_{0.5}\text{Sr}_{0.5}\text{MnO}_3$ ”, *Physical Review B*, vol. 69, no. 9, p. 094 437, 2004.
- [23] S. Loffland, S. Bhagat, K. Ghosh, R. Greene, S. Karabashev, D. Shulyatev, A. Arsenov, and Y. Mukovskii, “Magnetic transition and electronic transport in colossal magnetoresistance perovskites”, *Physical Review B*, vol. 56, no. 21, p. 13 705, 1997.

- [24] S. Uhlenbruck, R. Teipen, R. Klingeler, B. Büchner, O. Friedt, M. Hücker, H. Kierspel, T. Niemöller, L. Pinsard, A. Revcolevschi, *et al.*, “Interplay between charge order, magnetism, and structure in  $\text{La}_{0.875}\text{Sr}_{0.125}\text{MnO}_3$ ”, *Physical review letters*, vol. 82, no. 1, p. 185, 1999.
- [25] E. Ruff, S. Krohns, M. Lilienblum, D. Meier, M. Fiebig, P. Lunkenheimer, and A. Loidl, “Conductivity contrast and tunneling charge transport in the vortexlike ferroelectric domain patterns of multiferroic hexagonal  $\text{YMnO}_3$ ”, *Physical Review Letters*, vol. 118, no. 3, p. 036 803, 2017.
- [26] Q. Zhang, G. Tan, L. Gu, Y. Yao, C. Jin, Y. Wang, X. Duan, and R. Yu, “Direct observation of multiferroic vortex domains in  $\text{YMnO}_3$ ”, *Scientific reports*, vol. 3, no. 1, p. 2741, 2013.
- [27] B. Lorenz, “Hexagonal manganites—( $\text{RMnO}_3$ ): class (I) multiferroics with strong coupling of magnetism and ferroelectricity”, *International Scholarly Research Notices*, vol. 2013, 2013.
- [28] E. E. Gordon, X. Cheng, J. Kim, S.-W. Cheong, S. Deng, and M.-H. Whangbo, “Nonequivalent Spin Exchanges of the Hexagonal Spin Lattice Affecting the Low-Temperature Magnetic Properties of  $\text{RInO}_3$  ( $R = \text{Gd}, \text{Tb}, \text{Dy}$ ): Importance of Spin–Orbit Coupling for Spin Exchanges between Rare-Earth Cations with Nonzero Orbital Moments”, *Inorganic Chemistry*, vol. 57, no. 15, pp. 9260–9265, 2018.
- [29] Y. Yu, N. Lin, H. Wang, R. Xu, H. Ren, and X. Zhao, “First principles study of ferroelectric hexagonal compounds  $\text{RInO}_3$  ( $R = \text{Dy}, \text{Er}, \text{and Ho}$ ): electronic structure, optical and dielectric properties”, *RSC Advances*, vol. 10, no. 7, pp. 4080–4086, 2020.
- [30] X. Yin, Y. Li, G. Wang, J. Hu, C. Xu, Q. Lu, Y. Zhong, J. Zhao, X. Zhao, Y. Zhang, *et al.*, “Magnetic properties of the quasi two-dimensional centered honeycomb antiferromagnet  $\text{GdInO}_3$ ”, *Physical Review B*, vol. 104, no. 13, p. 134 432, 2021.
- [31] Y. Li, Y. Wang, W. Tan, W. Wang, J. Zhang, J. W. Kim, S.-W. Cheong, and X. Tao, “Laser floating zone growth of improper geometric ferroelectric  $\text{GdInO}_3$  single crystals with  $Z_6$  topological defects”, *Journal of Materials Chemistry C*, vol. 6, no. 26, pp. 7024–7029, 2018.
- [32] L. Seabra, T. Momoi, P. Sindzingre, and N. Shannon, “Phase diagram of the classical Heisenberg antiferromagnet on a triangular lattice in an applied magnetic field”, *Physical Review B*, vol. 84, no. 21, p. 214 418, 2011.
- [33] M. Lee, E. Choi, X. Huang, J. Ma, C. D. Cruz, M. Matsuda, W. Tian, Z. Dun, S. Dong, and H. Zhou, “Magnetic phase diagram and multiferroicity of  $\text{Ba}_3\text{MnNb}_2\text{O}_9$ : A spin-5/2 triangular lattice antiferromagnet with weak easy-axis anisotropy”, *Physical Review B*, vol. 90, no. 22, p. 224 402, 2014.
- [34] T. Susuki, N. Kurita, T. Tanaka, H. Nojiri, A. Matsuo, K. Kindo, and H. Tanaka, “Magnetization process and collective excitations in the  $S = 1/2$  triangular-lattice Heisenberg antiferromagnet  $\text{Ba}_3\text{CoSb}_2\text{O}_9$ ”, *Physical Review Letters*, vol. 110, no. 26, p. 267 201, 2013.

- [35] L. Svistov, A. Smirnov, L. Prozorova, O. Petrenko, A. Micheler, N. Büttgen, A. Y. Shapiro, and L. Demianets, “Magnetic phase diagram, critical behavior, and two-dimensional to three-dimensional crossover in the triangular lattice antiferromagnet  $\text{RbFe}(\text{MoO}_4)_2$ ”, *Physical Review B*, vol. 74, no. 2, p. 024 412, 2006.
- [36] L. Clark, G. Sala, D. D. Maharaj, M. B. Stone, K. S. Knight, M. T. Telling, X. Wang, X. Xu, J. Kim, Y. Li, *et al.*, “Two-dimensional spin liquid behaviour in the triangular-honeycomb antiferromagnet  $\text{TbInO}_3$ ”, *Nature Physics*, vol. 15, no. 3, pp. 262–268, 2019.
- [37] J. Kim, X. Wang, F.-T. Huang, Y. Wang, X. Fang, X. Luo, Y. Li, M. Wu, S. Mori, D. Kwok, *et al.*, “Spin Liquid State and Topological Structural Defects in Hexagonal  $\text{TbInO}_3$ ”, *Physical Review X*, vol. 9, no. 3, p. 031 005, 2019.
- [38] D. Li, K. Lee, B. Y. Wang, M. Osada, S. Crossley, H. R. Lee, Y. Cui, Y. Hikita, and H. Y. Hwang, “Superconductivity in an infinite-layer nickelate”, *Nature*, vol. 572, no. 7771, pp. 624–627, 2019.
- [39] D. Li, B. Y. Wang, K. Lee, S. P. Harvey, M. Osada, B. H. Goodge, L. F. Kourkoutis, and H. Y. Hwang, “Superconducting dome in  $\text{Nd}_{1-x}\text{Sr}_x\text{NiO}_2$  infinite layer films”, *Physical Review Letters*, vol. 125, no. 2, p. 027 001, 2020.
- [40] S. Zeng, C. S. Tang, X. Yin, C. Li, M. Li, Z. Huang, J. Hu, W. Liu, G. J. Omar, H. Jani, *et al.*, “Phase diagram and superconducting dome of infinite-layer  $\text{Nd}_{1-x}\text{Sr}_x\text{NiO}_2$  thin films”, *Physical Review Letters*, vol. 125, no. 14, p. 147 003, 2020.
- [41] Q. Gu, Y. Li, S. Wan, H. Li, W. Guo, H. Yang, Q. Li, X. Zhu, X. Pan, Y. Nie, *et al.*, “Single particle tunneling spectrum of superconducting  $\text{Nd}_{1-x}\text{Sr}_x\text{NiO}_2$  thin films”, *Nature communications*, vol. 11, no. 1, p. 6027, 2020.
- [42] M. Osada, B. Y. Wang, B. H. Goodge, K. Lee, H. Yoon, K. Sakuma, D. Li, M. Miura, L. F. Kourkoutis, and H. Y. Hwang, “A superconducting praseodymium nickelate with infinite layer structure”, *Nano letters*, vol. 20, no. 8, pp. 5735–5740, 2020.
- [43] M. Osada, B. Y. Wang, K. Lee, D. Li, and H. Y. Hwang, “Phase diagram of infinite layer praseodymium nickelate  $\text{Pr}_{1-x}\text{Sr}_x\text{NiO}_2$  thin films”, *Physical Review Materials*, vol. 4, no. 12, p. 121 801, 2020.
- [44] M. Osada, B. Y. Wang, B. H. Goodge, S. P. Harvey, K. Lee, D. Li, L. F. Kourkoutis, and H. Y. Hwang, “Nickelate superconductivity without rare-earth magnetism:  $(\text{La},\text{Sr})\text{NiO}_2$ ”, *Advanced Materials*, vol. 33, no. 45, p. 2 104 083, 2021.
- [45] S. Zeng, C. Li, L. E. Chow, Y. Cao, Z. Zhang, C. S. Tang, X. Yin, Z. S. Lim, J. Hu, P. Yang, *et al.*, “Superconductivity in infinite-layer nickelate  $\text{La}_{1-x}\text{Ca}_x\text{NiO}_2$  thin films”, *Science advances*, vol. 8, no. 7, eabl9927, 2022.
- [46] M. Greenblatt, “Ruddlesden-Popper  $\text{Ln}_{n+1}\text{Ni}_n\text{O}_{3n+1}$  nickelates: structure and properties”, *Current Opinion in Solid State and Materials Science*, vol. 2, no. 2, pp. 174–183, 1997.

- [47] Z. Zhang and M. Greenblatt, “Synthesis, structure, and properties of  $\text{Ln}_4\text{Ni}_3\text{O}_{10-\delta}$  (Ln = La, Pr, and Nd)”, *Journal of solid state chemistry*, vol. 117, no. 2, pp. 236–246, 1995.
- [48] S. Kumar, Ø. Fjellvåg, A. O. Sjøstad, and H. Fjellvåg, “Physical properties of Ruddlesden-Popper ( $n = 3$ ) nickelate:  $\text{La}_4\text{Ni}_3\text{O}_{10}$ ”, *Journal of Magnetism and Magnetic Materials*, vol. 496, p. 165 915, 2020.
- [49] B.-Z. Li, C. Wang, P. Yang, J. Sun, Y.-B. Liu, J. Wu, Z. Ren, J.-G. Cheng, G.-M. Zhang, and G.-H. Cao, “Metal-to-metal transition and heavy-electron state in  $\text{Nd}_4\text{Ni}_3\text{O}_{10-\delta}$ ”, *Physical Review B*, vol. 101, no. 19, p. 195 142, 2020.
- [50] S. Huangfu, G. D. Jakub, X. Zhang, O. Blacque, P. Puphal, E. Pomjakushina, F. O. von Rohr, and A. Schilling, “Anisotropic character of the metal-to-metal transition in  $\text{Pr}_4\text{Ni}_3\text{O}_{10}$ ”, *Physical Review B*, vol. 101, no. 10, p. 104 104, 2020.
- [51] D. Rout, S. R. Mudi, M. Hoffmann, S. Spachmann, R. Klingeler, and S. Singh, “Structural and physical properties of trilayer nickelates  $R_4\text{Ni}_3\text{O}_{10}$  ( $R = \text{La, Pr, and Nd}$ )”, *Physical Review B*, vol. 102, no. 19, p. 195 144, 2020.
- [52] J. Zhang, H. Zheng, Y.-S. Chen, Y. Ren, M. Yonemura, A. Huq, and J. Mitchell, “High oxygen pressure floating zone growth and crystal structure of the metallic nickelates  $R_4\text{Ni}_3\text{O}_{10}$  ( $R = \text{La, Pr}$ )”, *Physical Review Materials*, vol. 4, no. 8, p. 083 402, 2020.
- [53] S. Huangfu, X. Zhang, and A. Schilling, “Correlation between the tolerance factor and phase transition in  $\text{A}_{4-x}\text{B}_x\text{Ni}_3\text{O}_{10}$  (A and B = La, Pr, and Nd;  $x = 0, 1, 2,$  and  $3$ )”, *Physical Review Research*, vol. 2, no. 3, p. 033 247, 2020.
- [54] G. Wu, J. Neumeier, and M. Hundley, “Magnetic susceptibility, heat capacity, and pressure dependence of the electrical resistivity of  $\text{La}_3\text{Ni}_2\text{O}_7$  and  $\text{La}_4\text{Ni}_3\text{O}_{10}$ ”, *Physical Review B*, vol. 63, no. 24, p. 245 120, 2001.
- [55] D. Puggioni and J. M. Rondinelli, “Crystal structure stability and electronic properties of the layered nickelate  $\text{La}_4\text{Ni}_3\text{O}_{10}$ ”, *Physical Review B*, vol. 97, no. 11, p. 115 116, 2018.
- [56] J. Zhang, D. Phelan, A. Botana, Y.-S. Chen, H. Zheng, M. Krogstad, S. G. Wang, Y. Qiu, J. Rodriguez-Rivera, R. Osborn, *et al.*, “Intertwined density waves in a metallic nickelate”, *Nature communications*, vol. 11, no. 1, p. 6003, 2020.
- [57] I. Dzyaloshinsky, “A thermodynamic theory of “weak” ferromagnetism of antiferromagnetics”, *Journal of physics and chemistry of solids*, vol. 4, no. 4, pp. 241–255, 1958.
- [58] T. Moriya, “Anisotropic superexchange interaction and weak ferromagnetism”, *Physical review*, vol. 120, no. 1, p. 91, 1960.
- [59] A. Moskvin, “Dzyaloshinskii–Moriya coupling in 3D insulators”, *Condensed Matter*, vol. 4, no. 4, p. 84, 2019.
- [60] S. Yano, C.-W. Wang, Y. Zhu, K. Sun, and H.-F. Li, “Magnetic structure and phase transition in a single crystal of  $\text{ErCrO}_3$ ”, *Physical Review B*, vol. 108, no. 17, p. 174 406, 2023.

- [61] M. Tripathi, T. Chatterji, H. Fischer, R. Raghunathan, S. Majumder, R. Choudhary, and D. Phase, “Role of local short-scale correlations in the mechanism of negative magnetization”, *Physical Review B*, vol. 99, no. 1, p. 014 422, 2019.
- [62] I. Fita, R. Puzniak, A. Wisniewski, and V. Markovich, “Spin switching and unusual exchange bias in the single-crystalline GdCrO<sub>3</sub> compensated ferrimagnet”, *Physical Review B*, vol. 100, no. 14, p. 144 426, 2019.
- [63] I. Fita, R. Puzniak, and A. Wisniewski, “Pressure-tuned spin switching in compensated GdCrO<sub>3</sub> ferrimagnet”, *Physical Review B*, vol. 103, no. 5, p. 054 423, 2021.
- [64] S. Blundell, *Magnetism in condensed matter*. OUP Oxford, 2001.
- [65] J. M. Coey, *Magnetism and magnetic materials*. Cambridge university press, 2010.
- [66] S. H. Simon, *The Oxford solid state basics*. OUP Oxford, 2013.
- [67] P. Coleman, *Introduction to many-body physics*. Cambridge University Press, 2015.
- [68] R. C. O’handley, *Modern magnetic materials: principles and applications*. Wiley, 2000.
- [69] A. Ramirez, “Strongly geometrically frustrated magnets”, *Annual Review of Materials Science*, vol. 24, no. 1, pp. 453–480, 1994.
- [70] R. Moessner and A. P. Ramirez, “Geometrical frustration”, *Physics Today*, vol. 59, no. 2, pp. 24–29, 2006.
- [71] L. Balents, “Spin liquids in frustrated magnets”, *nature*, vol. 464, no. 7286, pp. 199–208, 2010.
- [72] M. Collins and O. Petrenko, “Review/synthèse: triangular antiferromagnets”, *Canadian journal of physics*, vol. 75, no. 9, pp. 605–655, 1997.
- [73] O. A. Starykh, “Unusual ordered phases of highly frustrated magnets: a review”, *Reports on Progress in Physics*, vol. 78, no. 5, p. 052 502, 2015.
- [74] R. Rosenberg, *Principles of Physical Chemistry*. Oxford University Press, 1977.
- [75] V. I. Anisimov, J. Zaanen, and O. K. Andersen, “Band theory and Mott insulators: Hubbard U instead of Stoner I”, *Physical Review B*, vol. 44, no. 3, p. 943, 1991.
- [76] E. Dagotto, “Correlated electrons in high-temperature superconductors”, *Reviews of Modern Physics*, vol. 66, no. 3, p. 763, 1994.
- [77] J. Hubbard, “Electron Correlations in Narrow Energy Bands”, *Proceedings of the Royal Society of London. Series A, Mathematical and Physical Sciences*, vol. 276, no. 1365, pp. 238–257, 1963. (visited on 02/29/2024).
- [78] H. Schmalzried, “Treatise on Solid State Chemistry: Volume 4 Reactivity of Solids”, in *Solid-State Reactions*, N. B. Hannay, Ed. Boston, MA: Springer US, 1976, pp. 233–279.
- [79] H. A. Dabkowska and A. B. Dabkowski, “Crystal Growth of Oxides by Optical Floating Zone Technique”, in *Springer Handbook of Crystal Growth*, G. Dhanaraj, K. Byrappa, V. Prasad, and M. Dudley, Eds. Berlin, Heidelberg: Springer Berlin Heidelberg, 2010, pp. 367–391.

- [80] S. S. I. D. GmbH, *High Pressure Crystal Growth Furnace Manual*, ScIDre, 2012.
- [81] D. Hurler, *Handbook of Crystal Growth: Bulk crystal growth. 2* (Handbook of Crystal Growth: Bulk Crystal Growth). North-Holland, 1994.
- [82] A. Mühlbauer, “Innovative induction melting technologies: A historical review”, in *International Scientific Colloquium, Modelling for Material Processing*, vol. 13, 2006, p. 20.
- [83] D. Souptel, “Crystal growth and perfection of selected intermetallic and oxide compounds”, 2005.
- [84] D. Souptel, W. Löser, and G. Behr, “Vertical optical floating zone furnace: principles of irradiation profile formation”, *Journal of crystal growth*, vol. 300, no. 2, pp. 538–550, 2007.
- [85] S. S. Dossa and J. J. Derby, “Modeling optical floating zone crystal growth in a high-pressure, single-lamp furnace”, *Journal of Crystal Growth*, vol. 591, p. 126 723, 2022.
- [86] C. Lan, “Three-dimensional simulation of floating-zone crystal growth of oxide crystals”, *Journal of crystal growth*, vol. 247, no. 3-4, pp. 597–612, 2003.
- [87] N. Pistawala, D. Rout, K. Saurabh, R. Bag, K. Karmakar, L. Harnagea, and S. Singh, “Crystal growth of quantum materials: A review of selective materials and techniques”, *Bulletin of Materials Science*, vol. 45, pp. 1–20, 2022.
- [88] S. Sakata, W. Itoyama, I. Fujii, and K. Iishi, “Preparation of low-temperature  $\text{Li}_3\text{VO}_4$  single crystal by floating zone technique”, *Journal of crystal growth*, vol. 135, no. 3-4, pp. 555–560, 1994.
- [89] D. K. Unruh and T. Z. Forbes, “X-ray diffraction techniques”, *Analytical geomicrobiology: a handbook of instrumental techniques*, pp. 215–237, 2019.
- [90] A. A. Bunaciu, E. G. UdrişTioiu, and H. Y. Aboul-Enein, “X-ray diffraction: instrumentation and applications”, *Critical reviews in analytical chemistry*, vol. 45, no. 4, pp. 289–299, 2015.
- [91] O. H. Seeck and B. Murphy, *X-ray Diffraction: Modern Experimental Techniques*. CRC Press, 2015.
- [92] H. M. Rietveld, “The rietveld method”, *Physica Scripta*, vol. 89, no. 9, p. 098 002, 2014.
- [93] J. Rodríguez-Carvajal, *An introduction to the program FullProf 2000 (Version July 2001)*, 2001.
- [94] Q. Design, *MPMS 3 user’s manual*, Quantum Design, 2016.
- [95] N. Yuan, A. Elghandour, W. Hergett, R. Ohlendorf, L. Gries, and R. Klingeler, “ $1/3$  plateau and  $3/5$  discontinuity in the magnetization and the magnetic phase diagram of hexagonal  $\text{GdInO}_3$ ”, *Physical Review B*, vol. 108, no. 22, p. 224 403, 2023.
- [96] Rahel Ohlendorf, “Electron Spin Resonance Studies on Frustrated Low Dimensional  $\text{PbCuSeO}_4(\text{OH})_2$  and  $\text{GdInO}_3$ ”, Master thesis, Heidelberg University, 2023.

- [97] L. Savary and L. Balents, “Quantum spin liquids: a review”, *Reports on Progress in Physics*, vol. 80, no. 1, p. 016 502, 2016.
- [98] Y. Zhou, K. Kanoda, and T.-K. Ng, “Quantum spin liquid states”, *Reviews of Modern Physics*, vol. 89, no. 2, p. 025 003, 2017.
- [99] A. Banerjee, J. Yan, J. Knolle, C. A. Bridges, M. B. Stone, M. D. Lumsden, D. G. Mandrus, D. A. Tennant, R. Moessner, and S. E. Nagler, “Neutron scattering in the proximate quantum spin liquid  $\alpha$ - $\text{RuCl}_3$ ”, *Science*, vol. 356, no. 6342, pp. 1055–1059, 2017.
- [100] Z. Zhu, P. Maksimov, S. R. White, and A. Chernyshev, “Disorder-induced mimicry of a spin liquid in  $\text{YbMgGaO}_4$ ”, *Physical review letters*, vol. 119, no. 15, p. 157 201, 2017.
- [101] P. Khuntia, M. Velazquez, Q. Barthélemy, F. Bert, E. Kermarrec, A. Legros, B. Bernu, L. Messio, A. Zorko, and P. Mendels, “Gapless ground state in the archetypal quantum kagome antiferromagnet  $\text{ZnCu}_3(\text{OH})_6\text{Cl}_2$ ”, *Nature Physics*, vol. 16, no. 4, pp. 469–474, 2020.
- [102] P. Czajka, T. Gao, M. Hirschberger, P. Lampen-Kelley, A. Banerjee, J. Yan, D. G. Mandrus, S. E. Nagler, and N. Ong, “Oscillations of the thermal conductivity in the spin-liquid state of  $\alpha$ - $\text{RuCl}_3$ ”, *Nature Physics*, vol. 17, no. 8, pp. 915–919, 2021.
- [103] T. S. Jung, X. Xu, J. Kim, B. H. Kim, H. J. Shin, Y. J. Choi, E.-G. Moon, S.-W. Cheong, and J. H. Kim, “Unconventional room-temperature carriers in the triangular-lattice Mott insulator  $\text{TbInO}_3$ ”, *Nature Physics*, vol. 19, no. 11, pp. 1611–1616, 2023.
- [104] M. Kim, B. Winn, S. Chi, A. Savici, J. Rodriguez-Rivera, W. Chen, X. Xu, Y. Li, J. Kim, S.-W. Cheong, *et al.*, “Spin-liquid-like state in pure and Mn-doped  $\text{TbInO}_3$  with a nearly triangular lattice”, *Physical Review B*, vol. 100, no. 2, p. 024 405, 2019.
- [105] C. Min, Y. Wu, Y. Li, C. Zhou, S.-W. Cheong, X. Lu, T. Zhou, and L. Zhang, “Structural and Improper Ferroelectric Properties of  $\text{TbInO}_3$  Single Crystal Grown by Laser Floating Zone”, *Crystals*, vol. 13, no. 2, p. 287, 2023.
- [106] M. Ye, X. Xu, X. Wang, J. Kim, S.-W. Cheong, and G. Blumberg, “Crystal-field excitations and vibronic modes in the triangular-lattice spin-liquid candidate  $\text{TbInO}_3$ ”, *Physical Review B*, vol. 104, no. 8, p. 085 102, 2021.
- [107] K. Momma and F. Izumi, “VESTA 3 for three-dimensional visualization of crystal, volumetric and morphology data”, *Journal of applied crystallography*, vol. 44, no. 6, pp. 1272–1276, 2011.
- [108] N. Yuan, A. Elghandour, J. Arneth, K. Dey, and R. Klingeler, “High-pressure crystal growth and investigation of the metal-to-metal transition of Ruddlesden–Popper trilayer nickelates  $\text{La}_4\text{Ni}_3\text{O}_{10}$ ”, *Journal of Crystal Growth*, vol. 627, p. 127 511, 2024.
- [109] Z. Zaitseva and A. Litvin, “Specification of crystal structure of neodymium and gadolinium chromite, Dop Ak Nauk Ukr RSR Ser B-Geol Khim”, *Biol Nauk*, pp. 994–997, 1978.



- [110] R. White, “Review of recent work on the magnetic and spectroscopic properties of the rare-earth orthoferrites”, *Journal of Applied Physics*, vol. 40, no. 3, pp. 1061–1069, 1969.
- [111] R. Hornreich, “Magnetic interactions and weak ferromagnetism in the rare-earth orthochromites”, *Journal of magnetism and magnetic materials*, vol. 7, no. 1-4, pp. 280–285, 1978.
- [112] T. Yamaguchi, “Theory of spin reorientation in rare-earth orthochromites and orthoferrites”, *Journal of Physics and Chemistry of Solids*, vol. 35, no. 4, pp. 479–500, 1974.
- [113] J. Herbst, “ $R_2\text{Fe}_{14}\text{-B}$  materials: Intrinsic properties and technological aspects”, *Reviews of Modern Physics*, vol. 63, no. 4, p. 819, 1991.
- [114] M. Sagawa, S. Hirosawa, H. Yamamoto, S. Fujimura, and Y. Matsuura, “Nd-Fe-B permanent magnet materials”, *Japanese journal of applied physics*, vol. 26, no. 6R, p. 785, 1987.
- [115] R. Perkins and S. Strässler, “Interpretation of the magnetic properties of pseudobinary  $\text{Sm}_2(\text{Co}, \text{M})_{17}$  compounds. I. Magnetocrystalline anisotropy”, *Physical Review B*, vol. 15, no. 1, p. 477, 1977.
- [116] K. Buschow, “Intermetallic compounds of rare-earth and 3d transition metals”, *Reports on Progress in Physics*, vol. 40, no. 10, p. 1179, 1977.
- [117] A. Kimel, A. Kirilyuk, A. Tsvetkov, R. Pisarev, and T. Rasing, “Laser-induced ultrafast spin reorientation in the antiferromagnet  $\text{TmFeO}_3$ ”, *Nature*, vol. 429, no. 6994, pp. 850–853, 2004.
- [118] K. Yamaguchi, T. Kurihara, Y. Minami, M. Nakajima, and T. Suemoto, “Terahertz time-domain observation of spin reorientation in orthoferrite  $\text{ErFeO}_3$  through magnetic free induction decay”, *Physical review letters*, vol. 110, no. 13, p. 137 204, 2013.
- [119] W. Zhao, S. Cao, R. Huang, Y. Cao, K. Xu, B. Kang, J. Zhang, and W. Ren, “Spin reorientation transition in dysprosium-samarium orthoferrite single crystals”, *Physical Review B*, vol. 91, no. 10, p. 104 425, 2015.
- [120] Y. Su, J. Zhang, L. Li, B. Li, Y. Zhou, D. Deng, Z. Chen, and S. Cao, “Temperature dependence of magnetic properties and change of specific heat in perovskite  $\text{ErCrO}_3$  chromites”, *Applied Physics A*, vol. 100, pp. 73–78, 2010.
- [121] X. Qian, L. Chen, S. Cao, and J. Zhang, “A study of the spin reorientation with t–e orbital hybridization in  $\text{SmCrO}_3$ ”, *Solid state communications*, vol. 195, pp. 21–25, 2014.
- [122] S. Artyukhin, M. Mostovoy, N. P. Jensen, D. Le, K. Prokes, V. G. De Paula, H. N. Bordallo, A. Maljuk, S. Landsgesell, H. Ryll, *et al.*, “Solitonic lattice and Yukawa forces in the rare-earth orthoferrite  $\text{TbFeO}_3$ ”, *Nature materials*, vol. 11, no. 8, pp. 694–699, 2012.

- [123] Y. Tokunaga, Y. Taguchi, T.-h. Arima, and Y. Tokura, “Electric-field-induced generation and reversal of ferromagnetic moment in ferrites”, *Nature Physics*, vol. 8, no. 11, pp. 838–844, 2012.
- [124] Y. Tokunaga, N. Furukawa, H. Sakai, Y. Taguchi, T.-h. Arima, and Y. Tokura, “Composite domain walls in a multiferroic perovskite ferrite”, *Nature materials*, vol. 8, no. 7, pp. 558–562, 2009.
- [125] E. Hassanpour, M. C. Weber, Y. Zemp, L. Kürten, A. Bortis, Y. Tokunaga, Y. Taguchi, Y. Tokura, A. Cano, T. Lottermoser, *et al.*, “Interconversion of multiferroic domains and domain walls”, *Nature Communications*, vol. 12, no. 1, p. 2755, 2021.
- [126] Y. Su, L. Li, Z. Xing, Z. Feng, D. Deng, B. Kang, S. Cao, and J. Zhang, “Study of Magnetism and specific-heat properties for multiferroic  $\text{YCrO}_3$  chromites”, in *2011 International Symposium on Applications of Ferroelectrics (ISAF/PFM) and 2011 International Symposium on Piezoresponse Force Microscopy and Nanoscale Phenomena in Polar Materials*, IEEE, 2011, pp. 1–4.
- [127] J.-S. Zhou, J. Alonso, V. Pomjakushin, J. B. Goodenough, Y. Ren, J.-Q. Yan, and J.-G. Cheng, “Intrinsic structural distortion and superexchange interaction in the orthorhombic rare-earth perovskites  $\text{RCrO}_3$ ”, *Physical Review B*, vol. 81, no. 21, p. 214 115, 2010.
- [128] J. R. Sahu, C. R. Serrao, and C. Rao, “Modification of the multiferroic properties of  $\text{YCrO}_3$  and  $\text{LuCrO}_3$  by Mn substitution”, *Solid state communications*, vol. 145, no. 1-2, pp. 52–55, 2008.
- [129] S. Yuan, W. Ren, F. Hong, Y. Wang, J. Zhang, L. Bellaiche, S. Cao, and G. Cao, “Spin switching and magnetization reversal in single-crystal  $\text{NdFeO}_3$ ”, *Physical Review B*, vol. 87, no. 18, p. 184 405, 2013.
- [130] S. Cao, H. Zhao, B. Kang, J. Zhang, and W. Ren, “Temperature induced spin switching in  $\text{SmFeO}_3$  single crystal”, *Scientific reports*, vol. 4, no. 1, p. 5960, 2014.
- [131] S. Huang, G. Zerihun, Z. Tian, S. Yuan, G. Gong, C. Yin, and L. Wang, “Magnetic exchange bias and high-temperature giant dielectric response in  $\text{SmCrO}_3$  ceramics”, *Ceramics International*, vol. 40, no. 9, pp. 13 937–13 943, 2014.
- [132] A. H. Morrish, *The physical principles of magnetism*. IEEE Inc., 2001.
- [133] T. Yamaguchi and K. Tsushima, “Magnetic symmetry of rare-earth orthochromites and orthoferrites”, *Physical review B*, vol. 8, no. 11, p. 5187, 1973.
- [134] B. Rajeswaran, D. Khomskii, A. Zvezdin, C. Rao, and A. Sundaresan, “Field-induced polar order at the Néel temperature of chromium in rare-earth orthochromites: Interplay of rare-earth and Cr magnetism”, *Physical Review B*, vol. 86, no. 21, p. 214 409, 2012.
- [135] K. P. Meher, A. Wahl, A. Maignan, C. Martin, and O. I. Lebedev, “Observation of electric polarization reversal and magnetodielectric effect in orthochromites: A comparison between  $\text{LuCrO}_3$  and  $\text{ErCrO}_3$ ”, *Physical Review B*, vol. 89, no. 14, p. 144 401, 2014.

- [136] D. Khomskii, “Classifying multiferroics: Mechanisms and effects”, *Physics*, vol. 2, p. 20, 2009.
- [137] Y. Su, J. Zhang, B. Li, B. Kang, Q. Yu, C. Jing, and S. Cao, “The dependence of magnetic properties on temperature for rare earth  $\text{ErCrO}_3$  chromites”, *Ceramics International*, vol. 38, S421–S424, 2012.
- [138] T. Sau, P. Yadav, S. Sharma, R. Raghunathan, P. Manuel, V. Petricek, U. Deshpande, and N. Lalla, “High-resolution time of flight neutron diffraction and magnetization studies of spin reorientation and polar transitions in  $\text{SmCrO}_3$ ”, *Physical Review B*, vol. 103, no. 14, p. 144 418, 2021.
- [139] E. Bertaut and J. Mareschal, “Etude de la structure magnetique des chromites d’erbium et de neodyme par diffraction neutronique”, *Solid State Communications*, vol. 5, no. 2, pp. 93–97, 1967.
- [140] M. Tripathi, R. Choudhary, D. Phase, T. Chatterji, and H. Fischer, “Evolution of magnetic phases in  $\text{SmCrO}_3$ : A neutron diffraction and magnetometric study”, *Physical Review B*, vol. 96, no. 17, p. 174 421, 2017.
- [141] Y. Zhu, P. Zhou, K. Sun, and H.-F. Li, “Structural evolution of single-crystal  $\text{RECrO}_3$  ( $\text{RE} = \text{Y}, \text{Eu-Lu}$ ) orthochromates”, *Journal of Solid State Chemistry*, vol. 313, p. 123 298, 2022.
- [142] *Webelements*, <https://www.webelements.com/>, 2023.
- [143] Y. Zhu, J. Xia, S. Wu, K. Sun, Y. Yang, Y. Zhao, H. W. Kan, Y. Zhang, L. Wang, H. Wang, *et al.*, “Crystal growth engineering and origin of the weak ferromagnetism in antiferromagnetic matrix of orthochromates from te orbital hybridization”, *Iscience*, vol. 25, no. 4, 2022.
- [144] L. Yin, J. Yang, P. Tong, X. Luo, C. Park, K. Shin, W. Song, J. Dai, K. Kim, X. Zhu, *et al.*, “Role of rare earth ions in the magnetic, magnetocaloric and magnetoelectric properties of  $\text{RCrO}_3$  ( $R = \text{Dy}, \text{Nd}, \text{Tb}, \text{Er}$ ) crystals”, *Journal of Materials Chemistry C*, vol. 4, no. 47, pp. 11 198–11 204, 2016.
- [145] R. Courths, S. Hübner, J. Pelzl, and L. Van Uitert, “Optical measurements in single crystal  $\text{ErCrO}_3$ ”, *Zeitschrift fuer Physik*, vol. 249, pp. 445–455, 1972.
- [146] V. A. Sanina, B. K. Khannanov, E. I. Golovenchits, and M. Shcheglov, “Electric polarization in  $\text{ErCrO}_3$  induced by restricted polar domains”, *Physics of the Solid State*, vol. 61, pp. 370–378, 2019.
- [147] A. Jablunovskis, E. Chukalina, L. Yin, and M. Popova, “High-Resolution Spectroscopy of the  $\text{ErCrO}_3$  Crystal: A New Phase Transition?”, *JETP Letters*, vol. 118, no. 2, pp. 92–99, 2023.
- [148] A. McDannald, L. Kuna, M. Seehra, and M. Jain, “Magnetic exchange interactions of rare-earth-substituted  $\text{DyCrO}_3$  bulk powders”, *Physical Review B*, vol. 91, no. 22, p. 224 415, 2015.
- [149] S. Yin, M. S. Seehra, C. J. Guild, S. L. Suib, N. Poudel, B. Lorenz, and M. Jain, “Magnetic and magnetocaloric properties of  $\text{HoCrO}_3$  tuned by selective rare-earth doping”, *Physical Review B*, vol. 95, no. 18, p. 184 421, 2017.

- [150] Y. Zhu, P. Zhou, T. Li, J. Xia, S. Wu, Y. Fu, K. Sun, Q. Zhao, Z. Li, Z. Tang, *et al.*, “Enhanced magnetocaloric effect and magnetic phase diagrams of single-crystal  $\text{GdCrO}_3$ ”, *Physical Review B*, vol. 102, no. 14, p. 144 425, 2020.
- [151] L. Yin, J. Yang, X. Kan, W. Song, J. Dai, and Y. Sun, “Giant magnetocaloric effect and temperature induced magnetization jump in  $\text{GdCrO}_3$  single crystal”, *Journal of Applied Physics*, vol. 117, no. 13, 2015.
- [152] X. Ma, W. Fan, G. Zhao, H. Chen, C. Wang, B. Kang, Z. Feng, J.-Y. Ge, W. Ren, and S. Cao, “Low field control of spin switching and continuous magnetic transition in an  $\text{ErFeO}_3$  single crystal”, *Physical Chemistry Chemical Physics*, vol. 24, no. 2, pp. 735–742, 2022.
- [153] Marius Säubert, “Untersuchung von  $\text{GdCrO}_3$  mittels hochauflösender Kapazitätsdilatometrie und Charakterisierungsmessungen am PPMS”, Master thesis, Heidelberg University, 2024.
- [154] A. Cooke, D. Martin, and M. Wells, “Magnetic interactions in gadolinium orthochromite,  $\text{GdCrO}_3$ ”, *Journal of Physics C: Solid State Physics*, vol. 7, no. 17, p. 3133, 1974.
- [155] M. Tripathi, R. Choudhary, and D. Phase, “Phase coexistence and the magnetic glass-like phase associated with the Morin type spin reorientation phase transition in  $\text{SmCrO}_3$ ”, *RSC advances*, vol. 6, no. 93, pp. 90 255–90 262, 2016.
- [156] T. Sau, S. Sharma, P. Yadav, R. Baumbach, T. Siegrist, A. Banerjee, and N. Lalla, “First-order nature of the spin-reorientation phase transition in  $\text{SmCrO}_3$ ”, *Physical Review B*, vol. 106, no. 6, p. 064 413, 2022.
- [157] Y. B. Bazaliy, L. Tsymbal, G. Kakazei, A. Izotov, and P. Wigen, “Spin-reorientation in  $\text{ErFeO}_3$ : Zero-field transitions, three-dimensional phase diagram, and anisotropy of erbium magnetism”, *Physical Review B*, vol. 69, no. 10, p. 104 429, 2004.
- [158] M. Tripathi, R. Choudhary, D. Phase, T. Chatterji, and H. Fischer, “Evolution of magnetic phases in  $\text{SmCrO}_3$ : A neutron diffraction and magnetometric study”, *Physical Review B*, vol. 96, no. 17, p. 174 421, 2017.
- [159] R. Huang, S. Cao, W. Ren, S. Zhan, B. Kang, and J. Zhang, “Large rotating field entropy change in  $\text{ErFeO}_3$  single crystal with angular distribution contribution”, *Applied Physics Letters*, vol. 103, no. 16, 2013.
- [160] L. Marshall, J.-G. Cheng, J.-S. Zhou, J. Goodenough, J.-Q. Yan, and D. Mandrus, “Magnetic coupling between  $\text{Sm}^{3+}$  and the canted spin in an antiferromagnetic  $\text{SmFeO}_3$  single crystal”, *Physical Review B*, vol. 86, no. 6, p. 064 417, 2012.
- [161] H. Wu, S. Cao, M. Liu, Y. Cao, B. Kang, J. Zhang, and W. Ren, “Twofold spin reorientation and field-induced incomplete phase transition in single-crystal  $\text{Dy}_{0.5}\text{Pr}_{0.5}\text{FeO}_3$ ”, *Physical review B*, vol. 90, no. 14, p. 144 415, 2014.
- [162] X. Lin, J. Jiang, Z. Jin, D. Wang, Z. Tian, J. Han, Z. Cheng, and G. Ma, “Terahertz probes of magnetic field induced spin reorientation in  $\text{YFeO}_3$  single crystal”, *Applied Physics Letters*, vol. 106, no. 9, 2015.

- [163] M. Das, S. Roy, and P. Mandal, “Giant reversible magnetocaloric effect in a multiferroic  $\text{GdFeO}_3$  single crystal”, *Physical Review B*, vol. 96, no. 17, p. 174405, 2017.
- [164] K. Toyokawa, S. Kurita, and K. Tsushima, “Spectroscopic study of the field-induced spin reorientation in  $\text{ErCrO}_3$ ”, *Physical Review B*, vol. 19, no. 1, p. 274, 1979.
- [165] T. H. K. Barron and G. K. White, *Heat Capacity and Thermal Expansion at Low Temperatures* (The International Cryogenic Monograph Series). Kluwer Academic / Plenum Publishers, 1999.
- [166] A. Mosbah, A. Verbaere, and M. Tournoux, “Phases  $\text{LiMn}_2\text{O}_4$  rattachees au type spinelle”, *Materials research bulletin*, vol. 18, no. 11, pp. 1375–1381, 1983.
- [167] D. Ahn and M. Song, “Variations of the Electrochemical Properties of  $\text{LiMn}_2\text{O}_4$  with Synthesis Conditions”, *Journal of the Electrochemical Society*, vol. 147, no. 3, p. 874, 2000.
- [168] X. Zhou, M. Chen, M. Xiang, H. Bai, and J. Guo, “Solid-state combustion synthesis of spinel  $\text{LiMn}_2\text{O}_4$  using glucose as a fuel”, *Ceramics International*, vol. 39, no. 5, pp. 4783–4789, 2013.
- [169] X. Zhou, M. Chen, H. Bai, C. Su, L. Feng, and J. Guo, “Preparation and electrochemical properties of spinel  $\text{LiMn}_2\text{O}_4$  prepared by solid-state combustion synthesis”, *Vacuum*, vol. 99, pp. 49–55, 2014.
- [170] H. Kitazawa, H. Suzuki, H. Abe, J. Tang, and G. Kido, “High-field magnetization of triangular lattice antiferromagnet:  $\text{GdPd}_2\text{Al}_3$ ”, *Physica B: Condensed Matter*, vol. 259, pp. 890–891, 1999.
- [171] T. Inami, Y. Ajiro, and T. Goto, “Magnetization process of the triangular lattice antiferromagnets,  $\text{RbFe}(\text{MoO}_4)_2$  and  $\text{CsFe}(\text{SO}_4)_2$ ”, *Journal of the Physical Society of Japan*, vol. 65, no. 8, pp. 2374–2376, 1996.
- [172] A. Smirnov, H. Yashiro, S. Kimura, M. Hagiwara, Y. Narumi, K. Kindo, A. Kikkawa, K. Katsumata, A. Y. Shapiro, and a. L. Demianets, “Triangular lattice antiferromagnet  $\text{RbFe}(\text{MoO}_4)_2$  in high magnetic fields”, *Physical Review B*, vol. 75, no. 13, p. 134412, 2007.
- [173] R. Ishii, S. Tanaka, K. Onuma, Y. Nambu, M. Tokunaga, T. Sakakibara, N. Kawashima, Y. Maeno, C. Broholm, D. P. Gautreaux, *et al.*, “Successive phase transitions and phase diagrams for the quasi-two-dimensional easy-axis triangular antiferromagnet  $\text{Rb}_4\text{Mn}(\text{MoO}_4)_3$ ”, *EPL (Europhysics Letters)*, vol. 94, no. 1, p. 17001, 2011.
- [174] Y. Shirata, H. Tanaka, T. Ono, A. Matsuo, K. Kindo, and H. Nakano, “Quantum magnetization plateau in spin-1 triangular-lattice antiferromagnet  $\text{Ba}_3\text{NiSb}_2\text{O}_8$ ”, *Journal of the Physical Society of Japan*, vol. 80, no. 9, p. 093702, 2011.
- [175] Y. Shirata, H. Tanaka, A. Matsuo, and K. Kindo, “Experimental realization of a spin-1/2 triangular-lattice Heisenberg antiferromagnet”, *Physical review letters*, vol. 108, no. 5, p. 057205, 2012.

- [176] D. Yamamoto, G. Marmorini, and I. Danshita, “Microscopic model calculations for the magnetization process of layered triangular-lattice quantum antiferromagnets”, *Physical review letters*, vol. 114, no. 2, p. 027 201, 2015.
- [177] J. Hwang, E. Choi, F. Ye, C. D. Cruz, Y. Xin, H. Zhou, and P. Schlottmann, “Successive magnetic phase transitions and multiferroicity in the spin-one triangular-lattice antiferromagnet  $\text{Ba}_3\text{NiNb}_2\text{O}_9$ ”, *Physical Review Letters*, vol. 109, no. 25, p. 257 205, 2012.
- [178] T. Ono, H. Tanaka, H. A. Katori, F. Ishikawa, H. Mitamura, and T. Goto, “Magnetization plateau in the frustrated quantum spin system  $\text{Cs}_2\text{CuBr}_4$ ”, *Physical Review B*, vol. 67, no. 10, p. 104 431, 2003.
- [179] N. A. Fortune, S. T. Hannahs, Y. Yoshida, T. Sherline, T. Ono, H. Tanaka, and Y. Takano, “Cascade of magnetic-field-induced quantum phase transitions in a spin-1/2 triangular-lattice antiferromagnet”, *Physical review letters*, vol. 102, no. 25, p. 257 201, 2009.
- [180] F. Wang and A. Vishwanath, “Spin phonon induced collinear order and magnetization plateaus in triangular and kagome antiferromagnets: Applications to  $\text{CuFeO}_2$ ”, *Physical review letters*, vol. 100, no. 7, p. 077 201, 2008.
- [181] T. Lummen, C. Strohm, H. Rakoto, A. Nugroho, and P. van Loosdrecht, “High-field recovery of the undistorted triangular lattice in the frustrated metamagnet  $\text{CuFeO}_2$ ”, *Physical Review B*, vol. 80, no. 1, p. 012 406, 2009.
- [182] T. Nakajima, N. Terada, S. Mitsuda, and R. Bewley, “Spin-driven bond order in a 1/5-magnetization plateau phase in the triangular lattice antiferromagnet  $\text{CuFeO}_2$ ”, *Physical Review B*, vol. 88, no. 13, p. 134 414, 2013.
- [183] J. Xing, L. D. Sanjeewa, J. Kim, G. Stewart, A. Podlesnyak, and A. S. Sefat, “Field-induced magnetic transition and spin fluctuations in the quantum spin-liquid candidate  $\text{CsYbSe}_2$ ”, *Physical Review B*, vol. 100, no. 22, p. 220 407, 2019.
- [184] R. Chen, J. Wang, Z. Ouyang, Z. He, S. Wang, L. Lin, J. Liu, C. Lu, Y. Liu, C. Dong, *et al.*, “Magnetic field induced ferroelectricity and half magnetization plateau in polycrystalline  $R_2\text{V}_2\text{O}_7$  ( $R = \text{Ni}, \text{Co}$ )”, *Physical Review B*, vol. 98, no. 18, p. 184 404, 2018.
- [185] I. Cabrera, M. Kenzelmann, G. Lawes, Y. Chen, W. Chen, R. Erwin, T. Gentile, J. Leao, J. Lynn, N. Rogado, *et al.*, “Coupled magnetic and ferroelectric domains in multiferroic  $\text{Ni}_3\text{V}_2\text{O}_8$ ”, *Physical review letters*, vol. 103, no. 8, p. 087 201, 2009.

# Acknowledgement

First and foremost, I would like to express my sincere gratitude to my supervisor, Prof. Dr. Rüdiger Klingeler. Thank you for welcoming me into the F25 group at Heidelberg University. I am grateful for every discussion on the data you provided, for your support and encouragement, and for your patience and sincerity throughout this journey. Secondly, I would like to thank Prof. Dr. Maurits Haverkort for graciously accepting the role of the second referee.

I am deeply appreciative of all the members of the F25 group, past and present. Thank each of you for all the assistance given to me and for your kindness. I would not be able to complete this work without your support.

To all my friends in Heidelberg, thank you for the precious moments we've shared and for your company during holidays and vacations. It's my pleasure to meet you all in a foreign land. Thanks to my friends in China for motivating me to pursue this Physics PhD.

Thanks to my parents Tiehong Li, Zhihua Yuan, and my family, for your unwavering support. Thank you for honoring my decisions. Special thanks to my cousin Yi'an Li for her company over the past 20+ years.

Recalling my arrival in Germany, I could not have foreseen that I would spend 1,223 days away from home due to the epidemic. However, I could not have anticipated receiving such assistance and kindness from a place over 7,000 kilometers away from my hometown, for which I am eternally grateful.

Lastly, I express my deepest gratitude to my grandma, Guilan Yao, and my grandpa, Yulin Li. Thank you for your eternal love and wisdom. I will always miss you.